08:09:28 OCA PAD AMENDMENT - PROJECT HEADER INFORMATION 01/07/92

Active

Project #: B-10-635 Cost share #: B-10-361 Rev #: 14
Center # : R5956-0A0 Center shr #: OCA file #:
Work type : RES
Contract#: A210824-03 Mod #: LTR DTD 911219 Document : PO
Prime #: Contract entity: GTRC

Subprojects ? : Y CFDA: N/A
Main project #: PE #: N/A

Project unit: OIP Unit code: 03.010.200
Project director(s):
SUMMERS C J PSL (404)894-3420

Sponsor/division names: POLAROID CORPORATION /
Sponsor/division codes: 215 / 016

Award period: 850401 to 930101 (performance) 930101 (reports)

Sponsor amount	New this change	Total to date
Contract value	0.00	608,015.00
Funded	0.00	608,015.00
Cost sharing amount		30,600.00

Does subcontracting plan apply ?: N

Title: HIGH PERFORMANCE PHOTODIODES

PROJECT ADMINISTRATION DATA

OCA contact: Ina R. Lashley 894-4820

Sponsor technical contact

KENNETH MALONEY
(617)577-2046

POLAROID CORPORATION
565 TECHNOLOGY SQUARE
CAMBRIDGE, MA 02139

Sponsor issuing office

JOEL MORRISON
(617)577-3179

POLAROID CORPORATION
PURCHASING OFFICE, 9TH FLOOR
565 TECHNOLOGY SQUARE
CAMBRIDGE, MA 02139

Security class (U,C,S,TS) : U ONR resident rep. is ACO (Y/N): N
Defense priority rating : N/A N/A supplemental sheet
Equipment title vests with: Sponsor GIT

Administrative comments -
POLAROID LETTER DATED 12/19/91, FROM KEN MALONEY, AUTHORIZES A NO-COST EXTENSION TO 1/1/93.

GEORGIA INSTITUTE OF TECHNOLOGY
OFFICE OF CONTRACT ADMINISTRATION

NOTICE OF PROJECT CLOSEOUT

Closeout Notice Date 05/09/95

Project No. B-10-635 Center No. R5956-0A0

Project Director SUMMERS C J School/Lab OIP

Sponsor POLAROID CORPORATION/

Contract/Grant No. A210824-03 Contract Entity GTRC

Prime Contract No.

Title HIGH PERFORMANCE PHOTODIODES

Effective Completion Date 930101 (Performance) 930101 (Reports)

Closeout Actions Required:	Y/N	Date Submitted
Final Invoice or Copy of Final Invoice	Y	
Final Report of Inventions and/or Subcontracts	Y	
Government Property Inventory & Related Certificate	N	
Classified Material Certificate	N	
Release and Assignment	N	
Other	N	

Comments

Subproject Under Main Project No.

Continues Project No.

Distribution Required:

Project Director	Y
Administrative Network Representative	Y
GTRI Accounting/Grants and Contracts	Y
Procurement/Supply Services	Y
Research Property Managment	Y
Research Security Services	N
Reports Coordinator (OCA)	Y
GTRC	Y
Project File	Y
Other	N
	N

NOTE: Final Patent Questionnaire sent to PDPI.

B-10-635 (A-4233)

GEORGIA TECH RESEARCH INSTITUTE
GEORGIA INSTITUTE OF TECHNOLOGY
ATLANTA, GEORGIA 30332

GTRI

September 9, 1985

Dr. Kenneth A. Maloney
Polaroid Corporation
Microelectronics/Materials Center
21 Osborn Street, Dept. 775
Cambridge, Massachusetts 02139

Dear Ken:

I enclose progress reports for July and August which effectively constitute the first quarterly report, as we have discussed. In October I hope to send you the second quarterly report which will bring us closer to the original schedule.

The MBE growth runs are proceeding and we intend to have sufficient data by the end of September to warrant the beginning of the experimental effort.

Sincerely,

Christopher J. Summers
Chief,
Physical Sciences Division

CJS:bg

Enclosure

Progress Report

High Performance Photodiodes

Polaroid Corporation

July 1985

Pursuant to the discussion on July 15th with members of Polaroid's technical staff a careful review of the existing information on noise theory in photodetectors was made. Specifically, the paper entitled "Multiplication Noise in Uniform Avalanche Diodes", by R.J. McIntyre was examined and the argument traced step by step. This paper determines the spectral density of the noise generated in a uniform APD. The noise is predominantly "shot noise" arising from the randomly occuring ionization events within the active region of the diode. In other words, random spatially occuring ionization events give rise to fluctuation in the gain which produces the noise in the device. The noise is of shot noise origin since each ionization event is random and considered instantaneous. The statistical variation of the multiplication rate from the average carrier multiplication rate is responsible for the increased noise.

McIntyre finds that if the electron, α , and hole, β , ionization rates are approximately equal then the excess noise factor is a maximum. Consequently for low noise performance in a uniform APD it is essential that α and β be vastly different.

An alternative means of reducing the excess noise factor is to design a device in which carrier multiplication (electrons) can occur at only a small number of discrete locations in the device such as in a photomultiplier. In a photomultiplier the variability of the number of electrons generated per detected photon is minimized since multiplication occurs only at fixed grids within the device. Existing photomultipliers however are large and cumbersome producing a need for a compact solid state device. Recent work by Capasso, Williams and Tsang suggests that a solid state photomultiplier can be made using a graded gap superlattice APD. The

excess noise in this device will be lower than in a conventional APD since the variability, and hence the gain fluctuation, of the number of electrons generated per photon is reduced.

The excess noise factor can be express as

$F_e = \langle N_m^2 \rangle / \langle N_m \rangle^2$

where N_m is the mean electron count or the total number of electrons generated at the output of an m-stage device.

If the device balances as a photomultiplier then the excess noise factor can be expressed as

$$F_e = \frac{2}{(1+P)} \qquad P>0$$

for an infinite stage device. P is the probability that a primary electron will generate a secondary electron at each stage. Clearly if P=1 or P=0 F_e=1. At either of these two extremes the device is completely deterministic, no random fluctuations exist, and hence the excess noise vanishes.

It is important to note that to produce a noiseless solid state APD it is necessary to fulfill two conditions: 1) the hole ionization rate in the device should be essentially nonexistent and 2) the gain per stage should be 2, P=1. If these conditions can be met or reasonably met an extremely low noise detector can be produced.

Dr. K. Brennan
Dr. C.J. Summers

Progress Report

High Performance Photodiodes

Polaroid Corporation

August 1985

As discussed in the report for July 1985, low noise performance of avalanche photodiode detectors can be achieved in uniform structures if the hole ionization rate vanishes. This condition is also of importance to low noise performance in a solid state photomultiplier. The GaAs/AlGaAs material system has been chosen as a potential candidate for low noise, superlattice APDs. It is therefore important to know the hole impact ionization rate as a function of applied electric field in both bulk GaAs and AlGaAs alloys.

Recent experimental work by Bulman et al. [1] has yielded the bulk ionization coefficients of both electrons and holes in GaAs. Figure 1 illustrates the electron ionization rate as a function of inverse electric field in bulk GaAs. Both the calculations (using the ensemble, many particle, Monte Carlo technique) and the experimental measurements are for fields applied along the 100 crystallographic direction at 300 K. Figure 2 shows the hole ionization rate in bulk $Al_{0.45}$ $Ga_{0.55}$ As and in bulk GaAs as a function of inverse electric field. No experimental measurements of the hole impact ionization rate in AlGaAs alloys presently exist. The calculations presented here of the hole ionization rate in the AlGaAs are the first reliable determination of the bulk ionization rate. These calculations were made using the full details of the $Al_{0.45}$ $Ga_{0.55}$ As band structure in an ensemble Monte Carlo program.

First the hole ionization rate in bulk GaAs was calculated and compared to the existing experimental data. Then the program was modified to include the AlGaAs band structure, the phonon scattering rate in AlGaAs,

and the modified ionization threshold energy (equal to the energy threshold, in the GaAs plus the energy gap change). The hole ionization rate in both the <100> and <111> directions is presented in Figure 2. As can be seen from this diagram, the hole ionization rate becomes very large at high applied electric fields, ~400 kV/cm, in bulk $Al_{0.45}$ $Ga_{0.55}$ As. Below ~33 kV/cm the hole ionization rate is negligible in bulk $Al_{0.45}$ $Ga_{0.55}$ As. Therefore for low noise detectors made using the GaAs/AlGaAs material system it is necessary to operate these devices at voltages such that the electric field within any long (>500Å) AlGaAs region be below 333kV/cm.

[1] G.E. Bulman, V.M. Robbins, K.F. Brennan, K. Hess, and G.E. Stillman, IEEE Electron Dev. Lett., EDL-4, 181 (1983).

Dr. K. Brennan
Dr. C.J. Summers

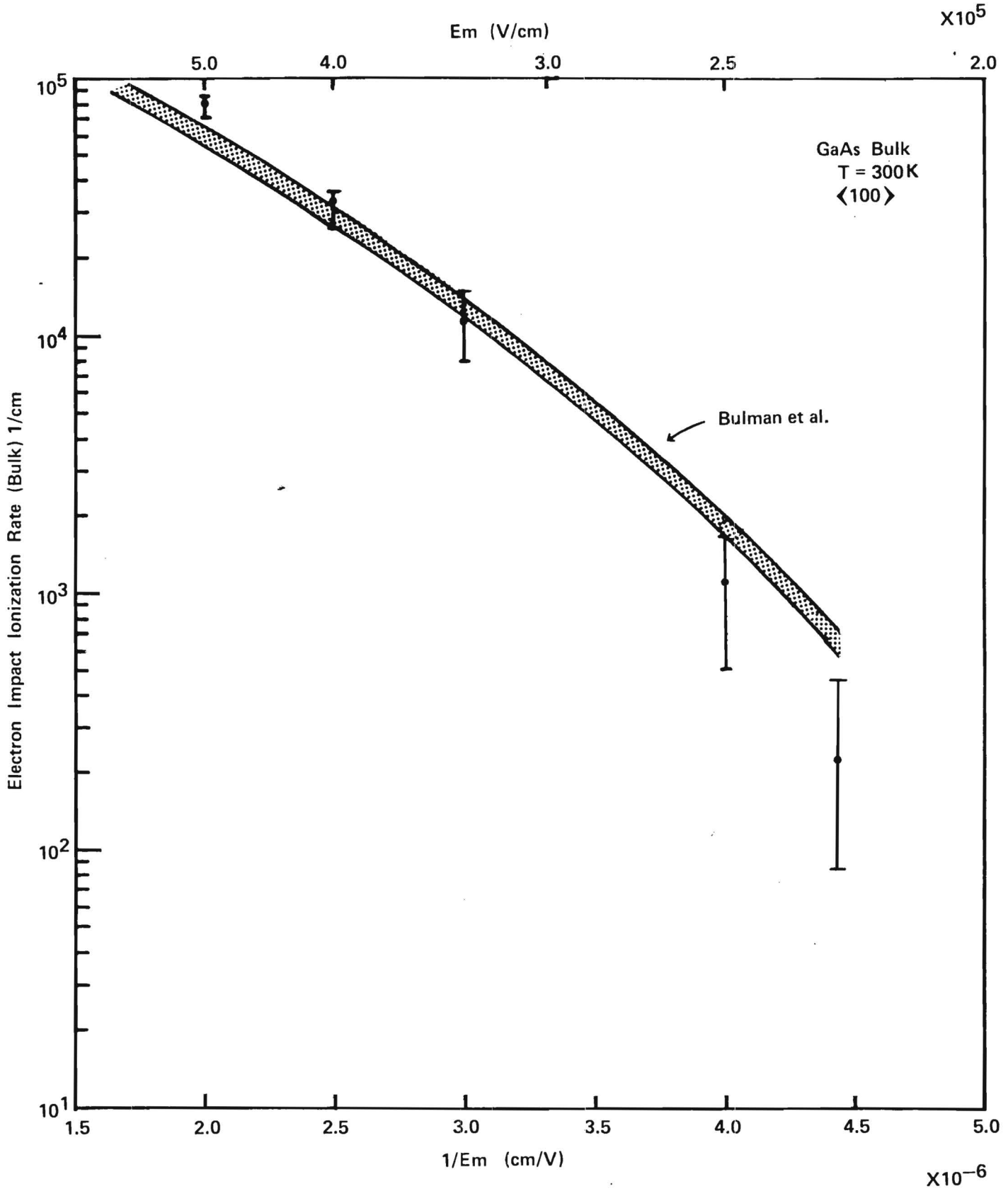
Em (V/cm)
X10^5
5.0
4.0
3.0
2.5
2.0
10^5
10^4
10^3
10^2
10^1
GaAs Bulk
T = 300K
⟨100⟩
Bulman et al.
Electron Impact Ionization Rate (Bulk) 1/cm
1.5
2.0
2.5
3.0
3.5
4.0
4.5
5.0
1/Em (cm/V)
X10^-6

Figure 1

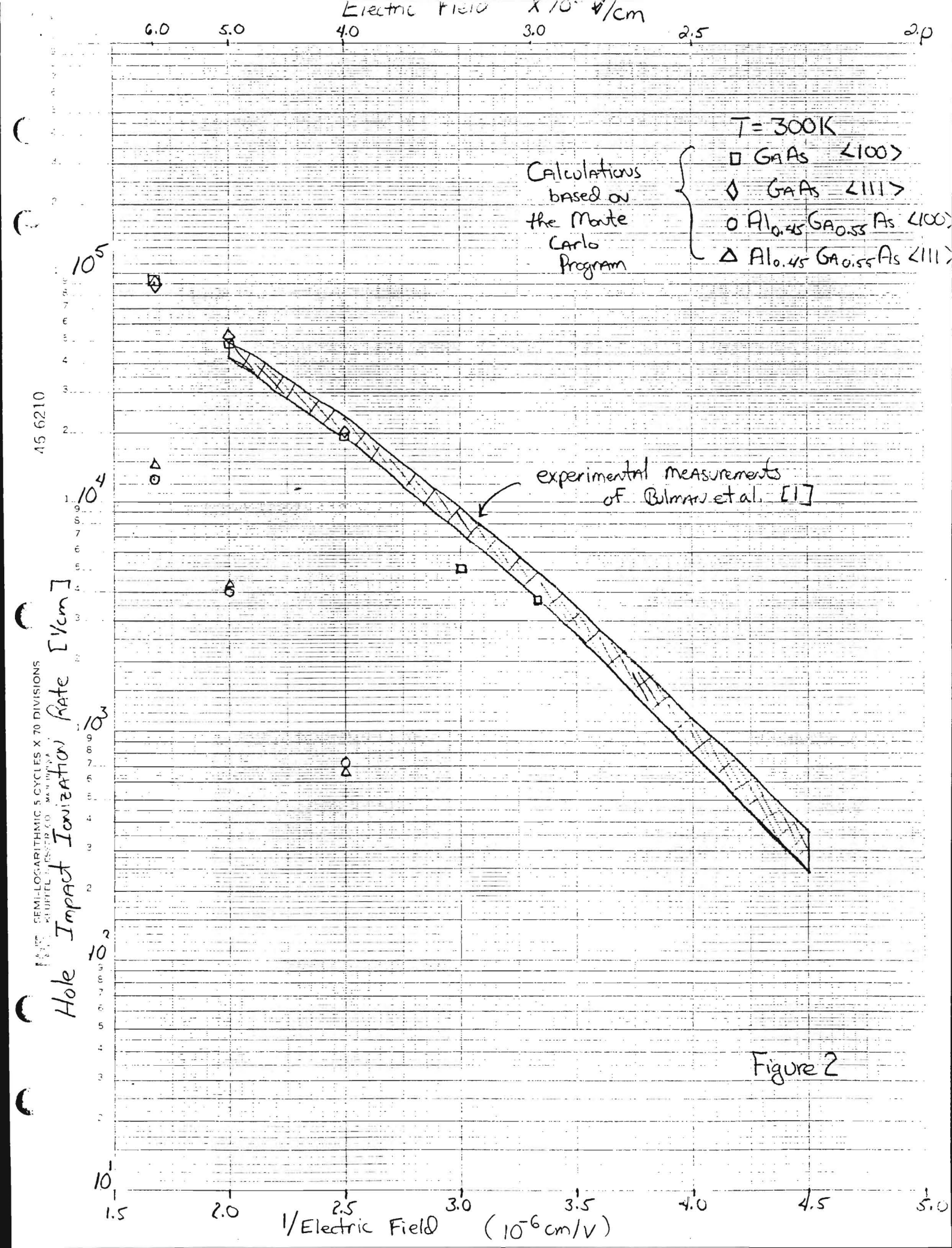
Electric Field x 10⁵ V/cm
6.0
5.0
4.0
3.0
2.5
2.0
T = 300K
□ GaAs <100>
◇ GaAs <111>
○ Al0.45 Ga0.55 As <100>
△ Al0.45 Ga0.55 As <111>
Calculations based on the Monte Carlo Program
experimental measurements of Bulman et al. [1]
Hole Impact Ionization Rate [1/cm]
10⁵
10⁴
10³
10²
10¹
1/Electric Field (10⁻⁶ cm/V)
1.5
2.0
2.5
3.0
3.5
4.0
4.5
5.0
SEMI-LOGARITHMIC 5 CYCLES X 70 DIVISIONS
15 6210

Figure 2

B-10-635

~~IN CONFIDENCE~~

2

IN CONFIDENCE

HIGH PERFORMANCE PHOTODIODES

Quarterly Report No. 2
Report Period: 1 July 1985 - 30 September 1985

Project No. A-4233

Prepared for:

Dr. Kenneth A. Maloney
Polaroid Corporation
Microelectronics/Materials Center
21 Osborn Street, Dept. 775
Cambridge, MA 02139

by

Dr. C. J. Summers and Dr. K. Brennan
Georgia Institute of Technology
Atlanta, GA 30332

THEORY OF THE DOPED QUANTUM WELL SUPERLATTICE APD: A NEW SOLID-STATE PHOTOMULTIPLIER

Kevin Brennan
School of Electrical Engineering
and
Microelectronics Research Center
Georgia Institute of Technology
Atlanta, Georgia 30332-0250

ABSTRACT

A new superlattice avalanche photodiode structure consisting of repeated unit cells formed from a p-i-n $Al_{0.45}Ga_{0.55}As$ region immediately followed by near intrinsic GaAs and $Al_{0.45}Ga_{0.55}As$ layers is examined using an ensemble Monte Carlo calculation. The effects of various device parameters, such as the high field layer width, GaAs well width, low field AlGaAs layer width, and applied electric field on the electron and hole ionization coefficients is analyzed. In addition, the fraction of electrons which ionize in a spatially deterministic way, at the same place in each stage of the device, is determined. As is well known, completely noiseless amplification can be achieved if each electron ionizes in each stage of the device at precisely the same location while no holes ionize anywhere within the device. A comparison is made between the doped quantum well device and other existing superlattice APDs such as the quantum well and staircase APDs. It is seen that the doped quantum well device most nearly approximates photomultiplier-like behavior when applied to the GaAs/AlGaAs material system amongst the three devices. In addition, it is determined that none of the devices, when made from GaAs and AlGaAs, fully mimic ideal photomultiplier-like performance. As the fraction

of electron ionizations per stage of the device is increased, through variations in the device geometry and applied electric field, the hole ionization rate invariably increases. It is expected that ideal performance can be more closely achieved in a material system in which the conduction band edge discontinuity is a greater fraction of the band gap energy in the narrow band gap semiconductor.

I. INTRODUCTION

Optical detectors, such as those used in lightwave communications systems, must provide high gain at low noise for optimal system performance. The sensitivity of optical detectors is primarily limited by the thermal (Johnson) noise of the load resistor and the shot noise of the junction detector itself [1]. The Johnson noise can be reduced by making the load resistance very large but this limits the frequency response of the detector [1]. For wide band width applications, the Johnson noise contribution can be made negligible by use of some internal gain mechanism which amplifies the signal current without increasing the thermal noise. The avalanche multiplication or impact ionization process provides a means of enhancing signal current without further increase in thermal noise. However, additional shot noise is introduced by the avalanche process.

The noise performance of uniform avalanche photodiodes was found by McIntyre [2] to depend upon the ratio of the electron to hole ionization coefficients. The noise is predominantly shot noise arising from the randomly occurring ionization events within the active region of the APD. The random spatially occurring ionization events cause fluctuation in the gain. This fluctuation in the multiplication rate from the average carrier multiplication rate is responsible for the increased noise [3]. McIntyre [2] found that if the electron, α, and hole, β, ionization rates are approximately equal, then the excess noise factor is a maximum. Consequently, for low noise performance in an APD, it is essential that α and β be vastly different.

For short wavelength detectors, $\lambda \sim 1.06$ μm, APDs made from silicon can be used since the electron to hole ionization rates ratio is large, ~20 [4,5]. Detectors sensitive over a wide range of wavelengths are necessarily made from

many different material systems, particularly the III-V semiconductor compounds and related alloys. In most of these materials however, the bulk ionization rates, electrons and holes, are roughly equal [3]. Therefore, low noise, high gain photodetectors for long wavelength operation require novel device structures in which the carrier ionization rate can be artificially increased.

Chin et al. [6] first proposed a means of artificially enhancing the electron to hole ionization coefficients through use of a superlattice structure consisting of alternating thin layers of GaAs and $Al_xGa_{1-x}As$. The relatively large difference between the conduction and valence band edge discontinuities, as well as the difference in the electron and hole ionization mean free paths [7], can be exploited to selectively heat the electron distribution more than the hole distribution. Recent experimental measurements [8,9] confirm the predicted enhancement in the electron ionization rate in quantum well superlattice APDs. The observed enhancement of the electron ionization rate in these structures can be explained from general considerations [10] as follows. In a structure with a periodic electric field, the electron and hole ionization rates are enhanced above their respective values in the absence of the periodic modulation as a result of the strong nonlinear (exponential) dependence of α and β on the field and the existence of a threshold energy in the impact ionization process [11]. The hole ionization rate enhancement observed in the quantum well APD [8,9] is much less than the corresponding electron ionization increase for two reasons. The conduction band edge discontinuity is significantly larger than the valence band offset [12,13], thus the electrons gain a larger kinetic energy boost from the heterointerface than the holes. More importantly, the hole energy relaxation

rate is much larger than the electron relaxation rate for the average carrier energies, less than 0.80 eV, at the applied fields used in the measurements. Consequently, the holes relax faster to their steady state energy after crossing over the heterobarrier resulting in fewer that survive to "lucky-drift" to energies high enough where impact ionization can occur [14,15]. Calculations [16,17] reveal that, depending upon the applied electric field, well and barrier widths, and well depth (band edge offset), the electron ionization rate can be much larger than the corresponding hole ionization rate.

Alternative device schemes, such as the graded gap staircase [18], channeling [19], and doped quantum well [20], APDs have recently been proposed. The channeling APD consists of alternating layers of GaAs and $Al_{0.45}Ga_{0.55}As$ which are doped n and p type, respectively. Upon application of a reverse bias, both transverse and longitudinal electric field components are produced. The transverse field acts to sweep the holes out of the GaAs layer into the $Al_{0.45}Ga_{0.55}As$ layers while confining the electrons within the GaAs. As originally proposed [19], the efficiency of the channeling APD depends upon how effectively the electrons are confined within the GaAs and how effectively the holes are swept out into the adjacent AlGaAs layers. Recent theoretical work [21] has shown that the largest enhancement in α arises in an undoped structure such that the carriers are free to transfer between the layers. Nevertheless, electron ionization events in the channeling APD occur completely at random spatially giving a full shot noise spectrum.

The graded gap staircase APD [18] is different from the channeling APD in that the ionization events occur only at the end of each stage of the device. In a photomultiplier, the variability of the number of electrons generated per

detected photon is minimized since multiplication occurs only at fixed grids within the device. Capasso et al. [18] suggest that a solid state multiplier can be made using the staircase APD. The excess noise in this device will be lower than in a conventional uniform APD and structures such as the channeling APD, where ionization events occur completely at random, since the variability and, hence, the gain fluctuation of the number of electrons generated per photon is reduced. It is expected, however, that a staircase APD made from the GaAs/AlGaAs material system will not behave like a photomultiplier since the conduction band edge offset is not a sufficiently large enough fraction of the energy gap in GaAs. An alternative to the staircase device, the doped quantum well APD [20], is presented herein which more nearly approximates photomultiplier-like behavior.

II. NOISE PROPERTIES OF AVALANCHE PHOTODIODES

The excess noise factor, the standard measure of the avalanche noise, can be expressed as [22]

$$Fe = \langle N_m^2 \rangle / \langle N_m \rangle^2 \tag{1}$$

where N_m is the mean electron count or the total number of electrons generated at the output of an m-stage device, $\langle N_m^2 \rangle$ is the second moment of the gain random variable for a single event at the input, and $\langle N_m \rangle$ is the square of the mean gain. Matsuo et al. [22] have shown that the excess noise factor can be expressed in terms of the mean and the variance of N_m, the electron count that results from a single primary event, as

$$Fe = 1 + \left[\mathrm{Var}(N_m) / \langle N_m \rangle^2 \right] . \tag{2}$$

If there is no spatial fluctuation in the multiplication, then the variance of N_m, $\mathrm{Var}(N_m)$, must be zero and Fe = 1, the minimum noise factor possible. In order to make a completely noiseless detector, it is then necessary that there be no fluctuation in the multiplication; the multiplication must be completely deterministic.

The mean electron count in a photomultiplier-like device, one in which the gain occurs at a specific spatial location in each stage, can be expressed as [18,22]

$$\langle N_m \rangle = (1 + P)^m \quad m \geq 1 \tag{3}$$

where P is the probability that an incident electron impact ionizes at the output of each stage in an m stage device. For an ideal, noiseless device, P = 1 (unity probability that at each stage each incident electron will ionize) and $\langle N_m \rangle = 2^m$. Fe can be written in terms of P as [22]

$$Fe = 1 + \left[(1 - P)/(1 + P)\right]\left[1 - (1 + P)^{-m}\right] . \tag{4}$$

From Eq. (4) when P = 1, Fe = 1 and the device is completely noiseless. For P > 0, Fe is always less than 2.

In the limit as $m \to \infty$, Eq. (4) becomes

$$Fe = 2./(1. + P) . \tag{5}$$

If P = 1, $F_e = 1$. When P is equal to zero, the limit $m \to \infty$, does not exist in Eq. (4), but it can clearly be seen that Eq. (4) reduces to $F_e = 1$ before the limit is taken. At either of these two extremes the device is completely deterministic, no random fluctuations exist, and hence, the excess noise

vanishes. The case P = 0 is uninteresting since there is no gain and the device is band width limited. The most desirable device is then one which optimizes P, one in which P = 1. Therefore, to produce a noiseless solid state APD, it is necessary to fulfill two conditions: (1) the hole ionization rate in the device should be essentially zero, and (2) the gain per stage of the device should be 2, P = 1. If these two conditions are met or reasonably met, an extremely low noise detector can be produced.

III. DESCRIPTION OF THE DEVICE AND MODEL

The device studied herein, originally proposed by Blauvelt et al. [20], is presented in Figure 1. The intrinsic region of the p-i-n diode consists of a superlattice whose basic unit cell consists of five layers made from two different materials of very different band gap energies, such as GaAs and $Al_{0.45}Ga_{0.55}As$. By doping the layers as shown, p+ i n+ ($Al_{0.45}Ga_{0.55}As$) followed by near intrinsic GaAs and $Al_{0.45}Ga_{0.55}As$ layers, the electric field profile can be made asymmetric in the unit cell (Figure 1). If the device is reverse biased, such that electrons are injected from the high field side (left side in Figure 1) and holes from the low field side, the electrons are accelerated by a much greater field than the holes before transferring into the GaAs layer. The combined action of the high field and subsequent injection over the heterobarrier produces very hot electrons within the narrow gap material (GaAs) such that impact ionization can occur. Conversely, the holes undergo little heating within the low field ($Al_{0.45}Ga_{0.55}As$) layer before being injected into the narrow gap (GaAs) region and few (if any) ionization events result. The holes, of course, also drift through the high field p-i-n region but then enter the low field AlGaAs layer where the band gap is much

larger than in the GaAs layer, and again the hole ionization rate is low. Judicial choices of layer thicknesses and doping concentrations can result in a substantial electron ionization rate for negligible hole ionization as will be discussed below.

We have modeled this device using a many particle, ensemble Monte Carlo technique which is particularly well adapted for high energy, high field transport. The full details of the GaAs conduction band structure derived from an empirical pseudopotential calculation [23], as well as the full details of both the GaAs and $Al_{0.45}Ga_{0.55}As$ valence band structures derived using a k*p calculation, are included in the analysis. At present, the $Al_{0.45}Ga_{0.55}As$ conduction band structure is not available to us. The AlGaAs conduction band can be modeled using the GaAs band structure with a modified energy gap and ionization energy. Substitution of GaAs in place of AlGaAs may not be fully justified since both Γ and L are degenerate in $Al_{0.45}Ga_{0.55}As$ while they are separated by 0.30 eV in GaAs. However, it is expected that the band structures are reasonably similar at high electron energies where impact ionization occurs. Inclusion of the full details of the AlGaAs valence band structure is more crucial since optimal device performance requires a negligible hole ionization rate. Hole ionization within the high field AlGaAs region, as well as within the GaAs layer, must be avoided which places constraints on the doping levels and layer widths used in the structure. Recent work by Brennan and Hess [25] has shown that significant hole ionization does indeed occur within bulk $Al_{0.45}Ga_{0.55}As$ for applied electric fields at or above 300 kV/cm.

The electron and hole scattering mechanisms included in the calculation are polar optical scattering, deformation potential, carrier-carrier, impact

ionization, and alloy scattering [26,27] within the AlGaAs layers. Impact ionization is treated as a scattering mechanism in accordance with the Kelydsh formulation [28]. As a control for the calculations, first both the bulk GaAs and AlGaAs electron and hole impact ionization rates are calculated and compared to existing experimental data [29]. The effect of the device geometry on the ionization rates (doping, layer widths, etc.) is isolated since any difference between the calculated bulk and superlattice ionization rates must be due solely to the presence of the superlattice structure.

The built-in field profile within the p-i-n region is calculated from the one-dimensional Poisson equation and is shown in Figure 1. From Gauss' Law, when the net charge in the n and p regions is the same, the high field region is completely confined to the p-i-n layers. The applied reverse bias must be sufficiently large to fully deplete the p and n layers. Additional reverse bias will only add a constant electric field perpendicular to the layers which acts to accelerate the carriers through the structure. Upon encountering the GaAs/AlGaAs heterointerface, the electrons and holes gain a kinetic energy boost equal to the conduction and valence band edge discontinuities, respectively. The band edge offsets are chosen in accordance with the best existing estimates to date, the 60/40 rule [12,13].

For small GaAs well widths, < 200 Å, spatial quantization effects become important. As is well known, spatial quantization introduces subbands within the quantum well that lie above the conduction band minimum [29]. The carriers can thermalize no lower in energy than the first subband rather than to the conduction band minimum. The subbands are calculated from a solution of the Schrödinger Equation for a finite square well. Since the barrier region (separation distance between adjacent walls) is very large, tunneling

effects between wells is neglected. For simplicity, only the effect of the first subband is considered. Spatial quantization has two important effects on the electron and hole transport in the device modeled here. The effective barrier height is reduced when subbands are present so the carriers gain less energy from the heterobarrier. In addition, the effective threshold energy for impact ionization is larger than in the bulk since the effective band gap is increased. Both of these effects are included in the calculations presented below.

IV. RESULTS OF THE CALCULATIONS

As discussed above, an ideal, noiseless, solid-state photodetector should have a negligible hole ionization rate while P, the fraction of impact ionizations per electron per stage (only those which ionize within the GaAs layer are important), should be as close to one as possible. Table 1 illustrates how α, β, and P vary with doping levels in a doped quantum well structure at fixed layer widths. (We have hypothetically selected doping levels which in practice may be difficult to achieve within the GaAs/AlGaAs material system in order to illustrate the underlying physics of this device.) As the built-in field within the p-i-n layer increases, at fixed applied field throughout, P increases dramatically. The distance the electrons travel from the heterointerface on average before impact ionizing decreases as well. The increase in P is due to the increase in the number of lucky-drift electrons within the GaAs layer. The electrons are "superheated" by the electric field in the p-i-n layer such that the distribution is greatly shifted in energy. Immediately thereafter, the electrons are injected into the GaAs well. Upon crossing the heterobarrier, the electrons overshoot their steady state energy

(gain more energy from the field than is lost to the phonons) and are accelerated semiballistically to energies at or above the ionization threshold energy. In this way, the electron ionization rate within the GaAs layer is greatly increased from its bulk value. As P increases, through the action of the built-in field, the hole ionization rate also increases as can be seen in Table 1. Consequently, a tradeoff exists between the hole ionization rate and P. The favorable increase in P is offset by the unfavorable increase in β.

From the above discussion, it is apparent that there is an optimal device design which maximizes P and minimizes β (hole ionization vanishes). Each device parameter can be isolated and its effect upon the device performance assessed independently. We present below detailed calculations which illustrate how P, α, and β depend upon the AlGaAs high field region width, the GaAs well width, the AlGaAs low field layer width, and the overall applied electric field.

Figure 2 shows the dependence of P upon the intrinsic AlGaAs high field layer width. All other parameters including electric field are held constant at the values listed in the figure. P clearly shows a maximum at a layer width of 200 Å which can be explained as follows. The "superheating" of the electron distribution depends upon the width of the built-in region (p-i-n layer). When the p-i-n layer width is small, the net energy gain from the field per electron, $eF\Delta x$, is insufficient such that most of the electrons do not ionize upon injection into the adjacent GaAs layer. As the layer width increases, more electrons are hot enough that upon injection they ionize. If the p-i-n layer width becomes too large, then electron ionization occurs within the high field AlGaAs layer. The number of electrons which ionize within the GaAs well then decreases, resulting in a smaller P.

Figure 3 illustrates how α and β depend upon the high field layer width. The holes are heated within the high field region as well, resulting in a substantial increase in the hole ionization rate as the layer width increases. Most of the hole ionization events occur within the GaAs well initially. Even though the holes are not immediately injected into the GaAs well from the high field region, cooling within the low field AlGaAs region is insufficient to totally reduce the ionization rate. A subsequent increase in the high field layer width results in hole ionization within the AlGaAs layers.

The dependence of P upon the GaAs well width is presented in Figure 4. For small well widths, P is small, < 0.10. The electron ionization rate is also less in very narrow width GaAs layer devices as seen in Figure 5. The effect of spatial quantization acts to reduce the electron ionization rate through the combined increase in the ionization threshold energy and the decrease in the effective barrier height as discussed above. Consequently, peak values of both P and α occur when the GaAs well width is sufficiently large that quantization effects are less important, ~ 200 Å. As the GaAs layer width increases further, P and α both decrease since the electrons are cooled more effectively by drifting within a now larger total low field region. As can be seen in Figure 5, the hole ionization rate is effectively zero for all values of the GaAs layer width. The small ionization rate calculated for a 400 Å well is statistically insignificant.

As the low field layer width increases, either through lengthening the GaAs well or the low field $Al_{0.45}Ga_{0.55}As$ layer (Table 2), the electron and hole ionization rates decrease. The low field regions serve to cool both distributions. As can be seen from Table 2, the hole ionization rate decreases more drastically with increasing low field region width. The hole-

energy relaxation rate is much larger than the energy relaxation rate [30]. Consequently, the holes relax faster to the corresponding low field steady state distribution.

In summary, it is apparent that several design trade-offs exist in the doped quantum well device. It is desirable to highly dope the p-i-n layers to produce an extremely large electric field. However, too high of a field results in significant hole ionization. Likewise, there exists an optimal length for the high field intrinsic region such that hole ionization does not occur, yet significant electron heating does, resulting in a substantial increase in P. Spatial quantization effects should be avoided in the GaAs well. However, as the GaAs and low field AlGaAs layer widths increase, the electron ionization rate decreases owing to the cooling effects within the low field regions.

In Figures 6 through 11, the effect on α, β, and P of the applied electric field is examined for three different device configurations. In all three devices as the electric field increases, P increases dramatically. Simultaneously, both the electron and hole ionization rates increase as well. At a field of 500.0 kV/cm, a P greater than 0.8 is attained as seen in Figure 10. However, the hole ionization rate approaches that of the electrons (Figure 11) counteracting the advantage of a large value of P. The results presented in Figures 6 through 11 clearly illustrate that a simultaneous large value of P, approaching fully deterministic electron ionization, is inconsistent with a negligible hole ionization rate in the GaAs/AlGaAs material system. It is evident that ideal, photomultiplier-like behavior cannot be produced in a doped quantum well APD made from GaAs/AlGaAs. This is because the conduction band edge discontinuity at the GaAs/AlGaAs heterointerface is

not a sufficiently large enough fraction of the band gap energy. Upon injection into the GaAs well, the electrons are not sufficiently heated such that impact ionization can occur. Attempts to further heat the electron distribution through use of the high-field p-i-n layer result in a substantial increase in β as well. It is expected then that a material system in which ΔE_c is a greater fraction of E_g in the narrow band gap layer will provide a better medium for an ideal, photomultiplier-like device.

Figures 12 and 13 illustrate the electron and hole energy distribution functions in the GaAs layer, low field AlGaAs layer, and within the high field AlGaAs layer for the device described in Figures 10 and 11 at an applied field of 150.0 kV/cm. As can be seen from Figure 12, the electron distribution within the GaAs quantum well has two peaks, one at very low energy and another ~ 0.60 eV. The low energy peak is due to the electrons which have impact ionized after transferring into the GaAs layer. The impact ionization process acts to greatly cool the superheated distribution resulting in many low energy electrons in the well. (It is quite possible that through impact ionization, carrier confinement within quantum wells may be improved.) The long tail in the distribution is due to the exceptionally hot carriers injected into the well. Notice that the tail extends well beyond the ionization threshold energy of 1.55 eV since we assume a "soft" threshold. Recent work by Tang and Hess [31] has determined that the ionization threshold must be "soft" in order to fully account for the injection of hot electrons from silicon into silicon dioxide in MOSFETs. If the threshold is "hard," each carrier that reaches the ionization threshold energy ionizes, then insufficient high energy carriers survive to account for the transfer of electrons into the silicon dioxide. As expected, the electron distribution is cooled considerably within the low

field AlGaAs region. The action of the high electric field within the p-i-n layers heats the electrons but the distribution is still cooler than that in the corresponding GaAs layer. The difference being due to the additional kinetic energy boost from the heterointerface upon entering the GaAs.

The hole energy distribution is presented in Figure 13. Contrary to the case for the electrons, the holes are hottest within the high field AlGaAs layer. The hole distribution is much cooler within the GaAs well since the holes are injected from the low field AlGaAs region. Even though the tail of the distribution crosses the ionization threshold, the hole ionization rate is negligible since the threshold is "soft" as discussed above. It is important to notice that the ionization events do not necessarily occur when the distribution tail exceeds the threshold energy. The likelihood of an ionization event also depends upon how long a carrier remains at or near the threshold which is a function of the scattering rate.

V. COMPARISON WITH OTHER SUPERLATTICE APDs

As mentioned above, Capasso et al. [18] have previously proposed a graded-gap staircase APD which, under the right conditions (ratio of conduction band edge discontinuity to band gap), mimics photomultiplier-like performance. For purposes of comparison, we have calculated the corresponding values of P, α, and β within both the graded-gap staircase and superlattice quantum well devices using the GaAs/AlGaAs material system. The results are summarized in Table 3. In previous work [16], it was determined that the maximum ratio of the electron to hole ionization coefficients occurs in both the quantum well and staircase APDs when the well width or stage length is 150 Å. Consequently, devices of these dimensions are selected for the

calculations. It is expected that these calculations will provide the most optimistic estimate of the APD device performance. Both the electron and hole ionization coefficients are calculated assuming the 60/40 rule for the conduction/valence band offsets [12,13]. At an applied electric field of 250.0 kV/cm P is small, < .1, in both devices. However, in the staircase APD, the electron to hole ionization rate ratio is much larger, three orders of magnitude, than in the quantum well device. In order to enhance P, it is necessary to increase the applied electric field in both devices. As can be seen from Table 3, at very high electric fields, 500 kV/cm, P increases significantly but at the expense of a dramatic increase in the hole ionization rate. Therefore, the same tradeoff exists between β and P in both the quantum well and staircase APDs as in the doped quantum well APD, but to an even greater extent. Comparison of the three devices indicates that the doped quantum well device most nearly approximates ideal, noiseless behavior at least as applied to GaAs/AlGaAs. It is, therefore, expected that the doped quantum well device will have the best noise figure of the superlattice APDs invented to date, the quantum well, staircase, and channeling APDs.

VI. CONCLUSIONS

In a uniform APD, the electrons and holes generated within the depletion region are produced by independent, randomly occurring impact ionization events. The statistical variation of the ionization rate from the average gain results in increased noise in the device. The excess noise factor in a uniform APD is given by [1],

$$Fe = M_N\left[1 - (1 - k)\left[(M_N - 1)/M_N\right]^2\right] \qquad (6)$$

where M_N is the electron multiplication rate and k is the hole to electron ionization rates ratio. When k = 0, no hole ionization, the excess noise factor reduces to two. From comparison to Eq. (5), it is clear that the excess noise of an ideal uniform APD, one in which the hole ionization rate vanishes, is twice as large as the excess noise of an ideal, photomultiplier-like device. Therefore, the highest sensitivity photodetectors should behave as close to a photomultiplier as possible.

A new solid-state device, the doped quantum well APD, has been analyzed above. It is found that this device more nearly mimics a photomultiplier as compared to other superlattice APDs, the quantum well and staircase APDs, when applied to the GaAs/AlGaAs material system. The use of doping interface dipoles, recently proposed by Capasso et al. [32] (a variation of the doped quantum well device) within the appropriate material system may also produce photomultiplier-like performance. However, it is found that in the doped quantum well device, and presumably through use of doped interface dipoles, that ideal performance is not possible to attain in any of the previously invented superlattice APDs in devices made from GaAs and AlGaAs. The explanation being that the conduction band edge offset is not a sufficiently large enough fraction of the energy band gap in the GaAs layer. By judicial choice of both the material system and the device parameters, doping and layer widths, well width, and applied electric field, it is expected that a true solid-state photomultiplier can be attained. It is suggested herein that the doped quantum well APD is the most promising existing structure in which photomultiplier-like performance can be exhibited.

ACKNOWLEDGEMENTS

The author would like to thank Dr. C. J. Summers, Dr. F. Capasso, and Prof. K. Hess for their comments on this work. The author would also like to thank Prof. M. Teich, Prof. B. K. Ridley, and Dr. S. Adachi for making their work available to him prior to publication. The technical assistance of Peggy Knight and Mary Ann Tripp at the Georgia Institute of Technology is gratefully appreciated. This work was supported by the Polaroid Corporation under contract B-10-635.

REFERENCES

[1] G. E. Stillman, V. M. Robbins, and N. Tabatabaie, "III-V compound semiconductor devices: optical detectors," IEEE Trans. Electron Dev., Vol. ED-31, pp. 1643-1655, 1984.

[2] R. J. McIntyre, "Multiplication noise in uniform avalanche diodes," IEEE Trans. Electron Dev., Vol. ED-13, pp. 164-168, 1966.

[3] G. E. Stillman and C. M. Wolfe, "Avalanche photodiodes," Semiconductors and Semimetals (R. K. Willardson and A. C. Beers, eds.), Vol. 12, pp. 291-393, Academic Press, New York, 1977.

[4] V. M. Robbins, T. Wang, K. F. Brennan, K. Hess, and G. E. Stillman, "Impact ionization coefficients in (100) and (111) silicon," to be published in Journal of Applied Physics.

[5] W. N. Grant, "Electron and hole ionization rates in epitaxial silicon at high electric fields," Solid-State Electron., Vol. 16, pp. 1189-1203, 1973.

[6] R. Chin, N. Holonyak, G. E. Stillman, J. Y. Tang, and K. Hess, "Impact ionization in multilayered heterojunction structures," Electron. Lett., Vol. 16, pp. 467-469, 1980.

[7] K. Brennan, T. Wang, and K. Hess, "Theory of electron impact ionization including a potential step: application to GaAs-AlGaAs," IEEE Electron. Dev. Lett., Vol. EDL-6, pp. 199-201, 1985.

[8] F. Capasso, W. T. Tsang, A. L. Hutchinson, and G. F. Williams, "Enhancement of electron impact ionization in superlattice: a new avalanche photodiode with large ionization rates ratio," Appl. Phys. Lett., Vol. 40, pp. 38-40, 1982.

[9] F.-Y. Juang, Y. Nashimoto, P. K. Bhattacharys, and S. Dhar, "Performance characteristics of high-quality GaAs/$Al_xGa_{1-x}As$ superlattice avalanche photodiodes," presented at the 43rd Annual Device Research Conference, Boulder, Colorado, June 1985.

[10] K. Brennan, "Generalized theory of impact ionization in modulated semiconductor structures," to be published in Surface Science.

[11] K. Hess, F. Capasso, private communication.

[12] R. C. Miller, D. A. Kleinman, and A. C. Gossard, "Energy-gap discontinuities and effective masses for GaAs-AlGaAs quantum wells," Phys. Rev. B., Vol. 29, pp. 7085-7087, 1984.

[13] R. C. Miller, A. C. Gossard, D. A. Kleinman, and O. Munteanu, "Parabolic quantum wells with the GaAs-$Al_xGa_{1-x}As$ system," Phys. Rev. B., Vol. 29, pp. 3740-3743, 1984.

[14] H. Shichijo and K. Hess, "Band-structure-dependent transport and impact ionization in GaAs," Phys. Rev. B., Vol. 23, pp. 4197-4207, 1981.

[15] B. K. Ridley, "Lucky-drift mechanism for impact ionization in semiconductors," J. Phys. C.: Solid State Phys., Vol. 16, pp. 3373-3388, 1983.

[16] K. Brennan, "Theory of electron and hole impact ionization in quantum well and staircase superlattice avalanche photodiode structures," to be published in IEEE Trans. Electron Dev., November 1985.

[17] B. K. Ridley, "Factors affecting impact ionization in multilayer avalanche photodiodes," IEE Proceedings, Vol. 132, pp. 177-183, 1985.

[18] F. Capasso, W. T. Tsang, and G. F. Williams, "Staircase solid state photomultipliers and avalanche photodiodes with enhanced ionization rate ratio," IEEE Trans. Electron Dev., Vol. ED-30, pp. 381-390, 1983.

[19] F. Capasso, "The channeling avalanche photodiode: a novel ultra-low-noise interdigitated p-n junction detector," IEEE Trans. Electron Dev., Vol. ED-29, pp. 1388-1395, 1982.

[20] H. Blauvelt, S. Margalit, and A. Yariv, "Single-carrier-type dominated impact ionization in multilayer structures," Electron. Lett., Vol. 18, pp. 375-376, 1982.

[21] K. Brennan, "Theory of the channeling avalanche photodiode," to be published in IEEE Trans. Electron Dev., November 1985.

[22] K. Matsuo, M. C. Teich, and B. E. A. Saleh, "Noise properties and time response of the staircase avalanche photodiode," to be published in IEEE Trans. Electron Dev., December 1985.

[23] M. L. Cohen and T. K. Bergstresser, "Band structures and pseudopotential form factors for fourteen semiconductors of the diamond and zinc-blende structures," Phys. Rev., Vol. 141, pp. 789-796, 1966.

[24] F. H. Pollak, C. W. Higginbotham, and M. Cardona, "Band structure of GaAs, GaP, InP, and AlSb: the k*p method," Proceedings of the International Conference on the Physics of Semiconductors, Kyoto, 1966, J. of the Phys. Soc. of Japan, Vol. 21, pp. 20-26, 1966.

[25] K. Brennan and K. Hess, "Theory of high field transport of holes in $Al_{0.45}Ga_{0.55}As$," submitted to J. Appl. Phys.

[26] J. W. Harrison and J. R. Hauser, "Alloy scattering in ternary III-V compounds," Phys. Rev. B., Vol. 13, pp. 5347-5350, 1976.

[27] J. W. Harrison and J. R. Hauser, "Theoretical calculations of electron mobility in ternary III-V compounds," J. Appl. Phys., Vol. 47, pp. 292-300, 1976.

[28] L. V. Keldysh, "Concerning the theory of impact ionization in semiconductors," Zh. Eksp. Teor. Fiz., Vol. 48, pp. 1692-1707, [Sov. Phys.-JETP, Vol. 21, pp. 1135-1144, 1965].

[29] R. Dingle, "Confined carrier quantum states in ultrathin semiconductor heterostructures," in Festkorperprobleme (H. J. Queisser, ed.), Advances in Solid State Physics, Vol. 15 (Pergamon/Vieweg, Braunshweig, 1975), pp. 21-48.

[30] K. Brennan and K. Hess, "Theory of high-field transport of holes in GaAs and InP," Phys. Rev. B., Vol. 29, pp. 5581-5590, 1984.

[31] J. Y. Tang and K. Hess, "Impact ionization of electrons in silicon (steady state)," J. Appl. Phys., Vol. 54, pp. 5139-5144, 1983.

[32] F. Capasso, K. Mohammed, and A. Y. Cho, "Tunable barrier heights and band discontinuities via doping interface dipoles: An interface engineering technique and its device applications," J. Vac. Sci. Technol. B, Vol. 3, pp. 1245-1251, 1985.

FIGURE CAPTIONS

FIGURE 1: Unit cell of the doped quantum well APD and the corresponding electric field profile.

FIGURE 2: Fraction of impact ionizations per electron per stage of the device, P, plotted versus intrinsic high field AlGaAs layer width at an applied electric field of 200.0 kV/cm for the device geometry listed. The resulting built-in electric field within the p-i-n region is 600.0 kV/cm.

FIGURE 3: Electron and hole impact ionization rates plotted as a function of intrinsic high field AlGaAs layer width at an applied electric field of 200.0 kV/cm for the device geometry listed. The resulting built-in electric field within the p-i-n region is 600.0 kV/cm.

FIGURE 4: Fraction of impact ionizations per electron per stage of the device, P, plotted versus GaAs well width at an applied electric field of 150.0 kV/cm for the device geometry listed.

FIGURE 5: Electron and hole impact ionization rate plotted versus GaAs well width at an applied electric field of 150.0 kV/cm. The hole impact ionization rates determined for GaAs well widths of 25, 75, and 200 Å are all calculated to be zero. The small value calculated for 400 Å wide layer is statistically negligible.

FIGURE 6: Fraction of impact ionizations per electron per stage of the device, P, plotted versus the applied electric field (the overall field after the p-i-n layers are fully depleted) for the device geometry shown.

FIGURE 7: Electron and hole impact ionization rates as a function of inverse electric field for the same device geometry as in Figure 6.

FIGURE 8: Fraction of impact ionizations per electron per stage of the device, P, plotted versus the applied electric field (the overall field after the p-i-n layers are fully depleted) for the device geometry shown.

FIGURE 9: Electron and hole impact ionization rates as a function of inverse electric field for the same device geometry as in Figure 8.

FIGURE 10: Fraction of impact ionizations per electron per stage of the device, P, plotted versus the applied electric field (the overall field after the p-i-n layers are fully depleted) for the device geometry shown.

FIGURE 11: Electron and hole impact ionization rates as a function of inverse electric field for the same device geometry as in Figure 10.

FIGURE 12: Electron energy distribution function plotted as a function of energy for the device geometry of Figures 10-11 at an applied electric field of 150.0 kV/cm. The three curves correspond to the distribution function within the high field AlGaAs, GaAs, and low field AlGaAs layers.

FIGURE 13: Hole energy distribution function plotted as a function of hole energy for the device of Figures 10-11 at an applied electric field of 150.0 kV/cm. The three curves correspond to the distribution function within the high field AlGaAs, GaAs, and low field AlGaAs layers.

TABLE 1

EFFECT OF DOPING LEVELS ON α, β, AND P

A.

Layer		Width (Å)	Doping ($1/cm^3$)
AlGaAs	p^+	50	6.42×10^{18}
	i	50	---
	N^+	50	6.42×10^{18}
GaAs		200	---
$Al_{0.45}Ga_{0.55}As$		350	---

Built-in field in p-i-n region = 450 kV/cm.

Carrier	Field (kV/cm)	% Impact Ion. in GaAs	P	Dist. Traveled From Interface Before Ionizing (Å)	α or β (1/cm)
Electrons	200.	100.	.154	44.8	2.4×10^4
Holes	200.	100.	--	--	3.0×10^2

B.

Layer		Width (Å)	Doping ($1/cm^3$)
AlGaAs	p^+	50	8.56×10^{18}
	i	50	---
	N^+	50	8.56×10^{18}
GaAs		200	---
$Al_{0.45}Ga_{0.55}As$		350	---

Built-in field in p-i-n region = 600 kV/cm.

Carrier	Field (kV/cm)	% Impact Ion. in GaAs	P	Dist. Traveled From Interface Before Ionizing (Å)	α or β (1/cm)
Electrons	200.	100.	.28	37.3	4.35×10^4
Holes	200.	100.	--	--	2.7×10^2

TABLE 1 (Continued)

C.

Layer		Width	Doping ($1/cm^3$)
AlGaAs	p^+	50	1.04×10^{19}
	i	50	---
	N^+	50	1.04×10^{19}
GaAs		200	---
$Al_{0.45}Ga_{0.55}As$		350	---

Built-in field in p-i-n region = 800 kV/cm.

Carrier	Field (kV/cm)	% Impact Ion. in GaAs	P	Dist. Traveled From Interface Before Ionizing (Å)	α or β (1/cm)
Electrons	200.	100.	.415	31.98	6.31×10^4
Holes	200.	97.2	--	---	6.64×10^2

TABLE 2

DEPENDENCE OF α, β, AND P ON THE LOW FIELD $Al_{0.45}Ga_{0.55}As$ LAYER WIDTH

Layer	Width (Å)	Doping ($1/cm^3$)
p^+	50	8.56×10^{18}
i	50	---
N^+	50	8.56×10^{18}
GaAs	200	---
$Al_{0.45}Ga_{0.55}As$	variable	---

Carrier	AlGaAs Layer Width (Å)	α or β (1/cm)	P
Electrons	100	2.92×10^4	.153
Electrons	350	2.4×10^4	.157
Electrons	700	1.6×10^4	.156
Holes	100	5.25×10^2	--
Holes	350	0.0	--
Holes	700*	3.8×10^1	--

*Only two ionization events occurred amongst 1500 carriers simulated for 8.0 psec. Consequently, the counting statistics are such that small fluctuations, a few unlikely "lucky" holes, can be observed.

TABLE 3

CALCULATIONS OF α AND β IN THE QUANTUM WELL SUPERLATTICE AND STAIRCASE APDs

A. Quantum Well Device

ΔE_c = .347 eV; ΔE_v = .214 eV

	Field (kV/cm)	L (Å)	α or β (1/cm)	P
Electrons	500	150	1.01×10^5	.288
	250	150	4.94×10^3	.014
Holes	500	150	4.097×10^4	--
	250	150	1.089×10^3	--

B. Staircase APD

ΔE_c = .347 eV; ΔE_v = .214 eV.

	Field (kV/cm)	L (Å)	α or β (1/cm)	P
Electrons	500	150	1.75×10^5	.261
	250	150	4.66×10^4	.067
Holes*	589.3	150	1.86×10^4	--
	339.3	150	2.717×10^1	--

*Effect of the quasi-field due to the graded band structure is included in accordance with Ref. [16].

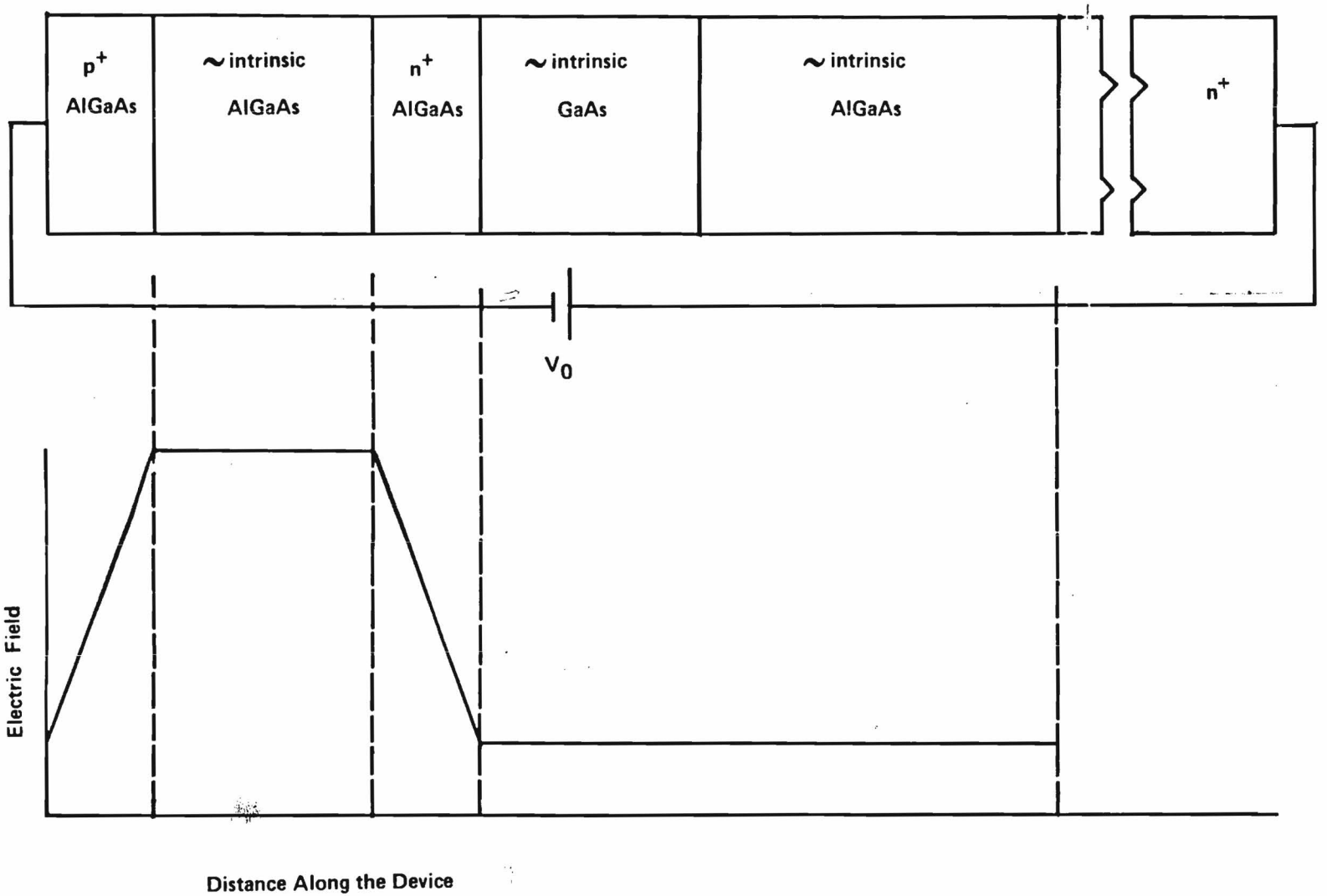

Fig. 1
Brennan

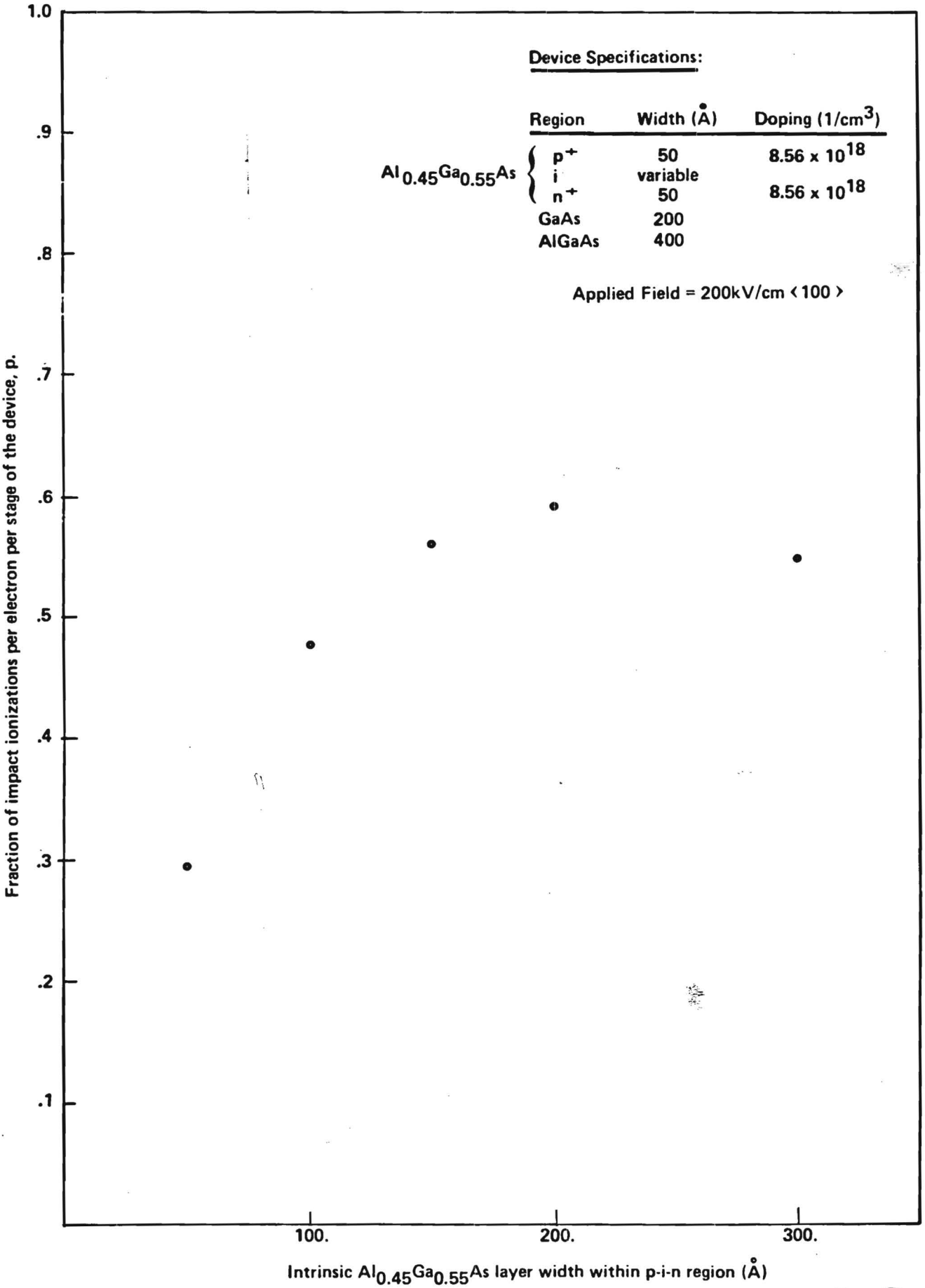

Fig. 2
Brennan

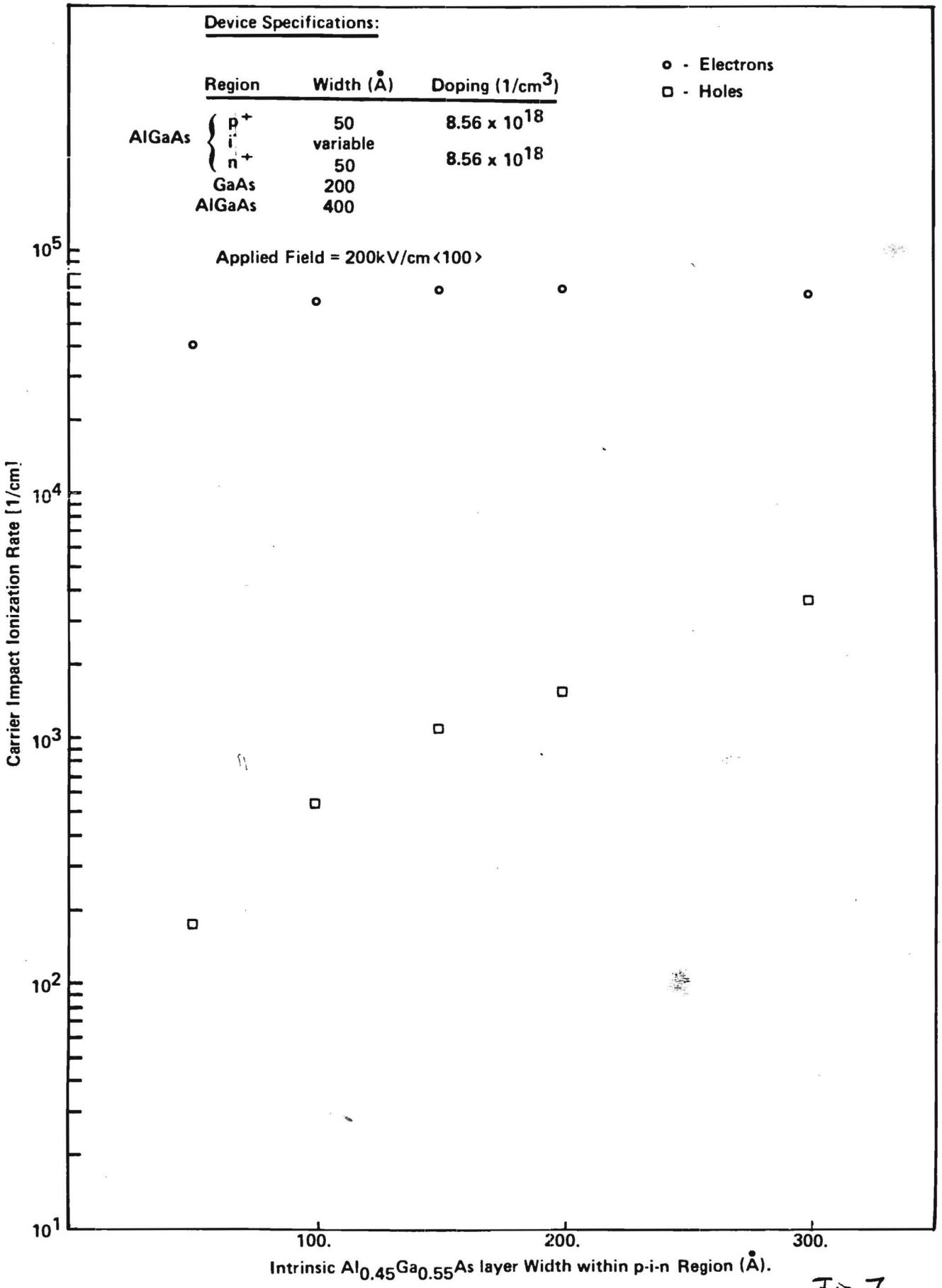

Fig. 3
Brennan

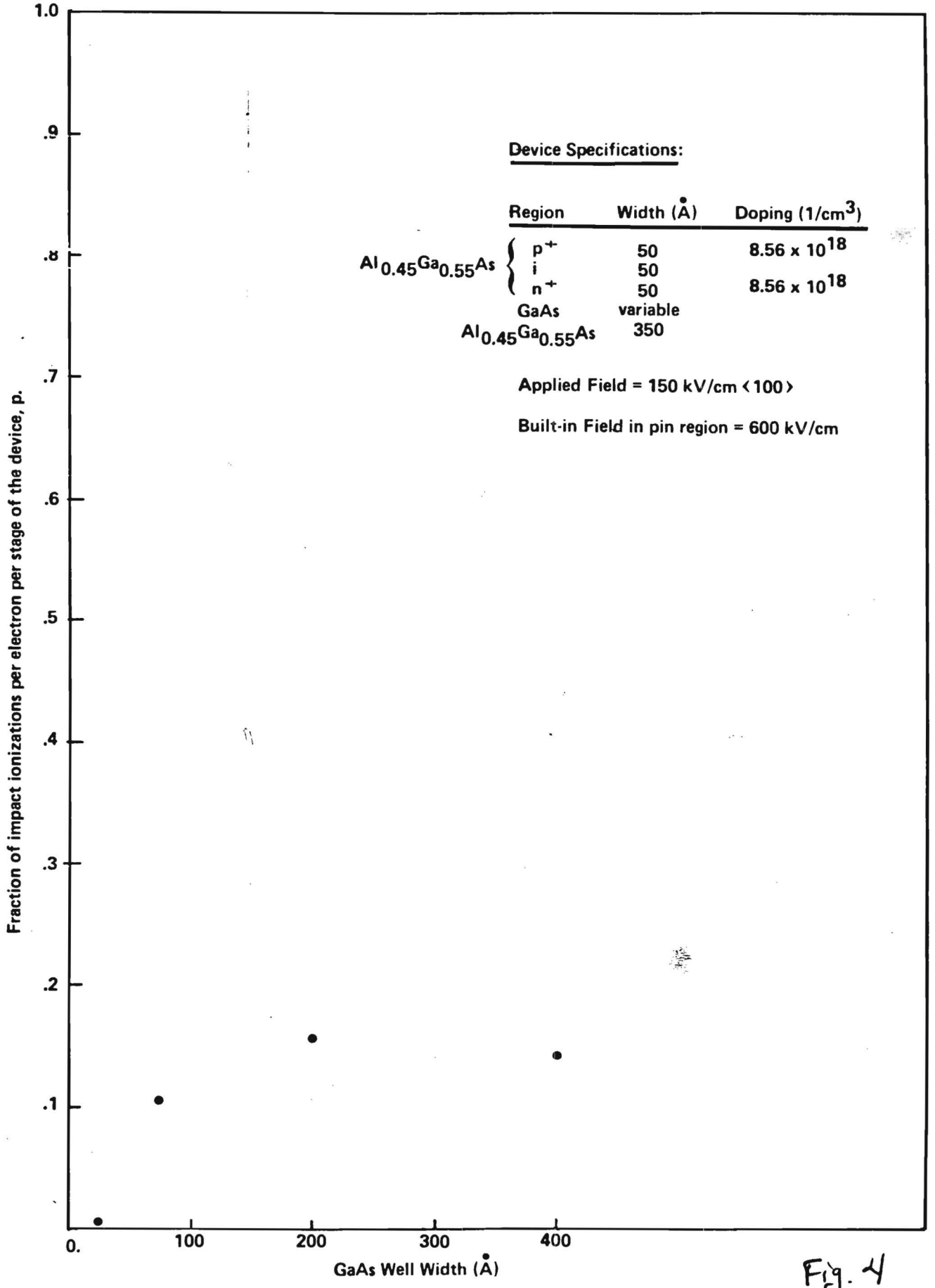

Fig. 4
Brennan

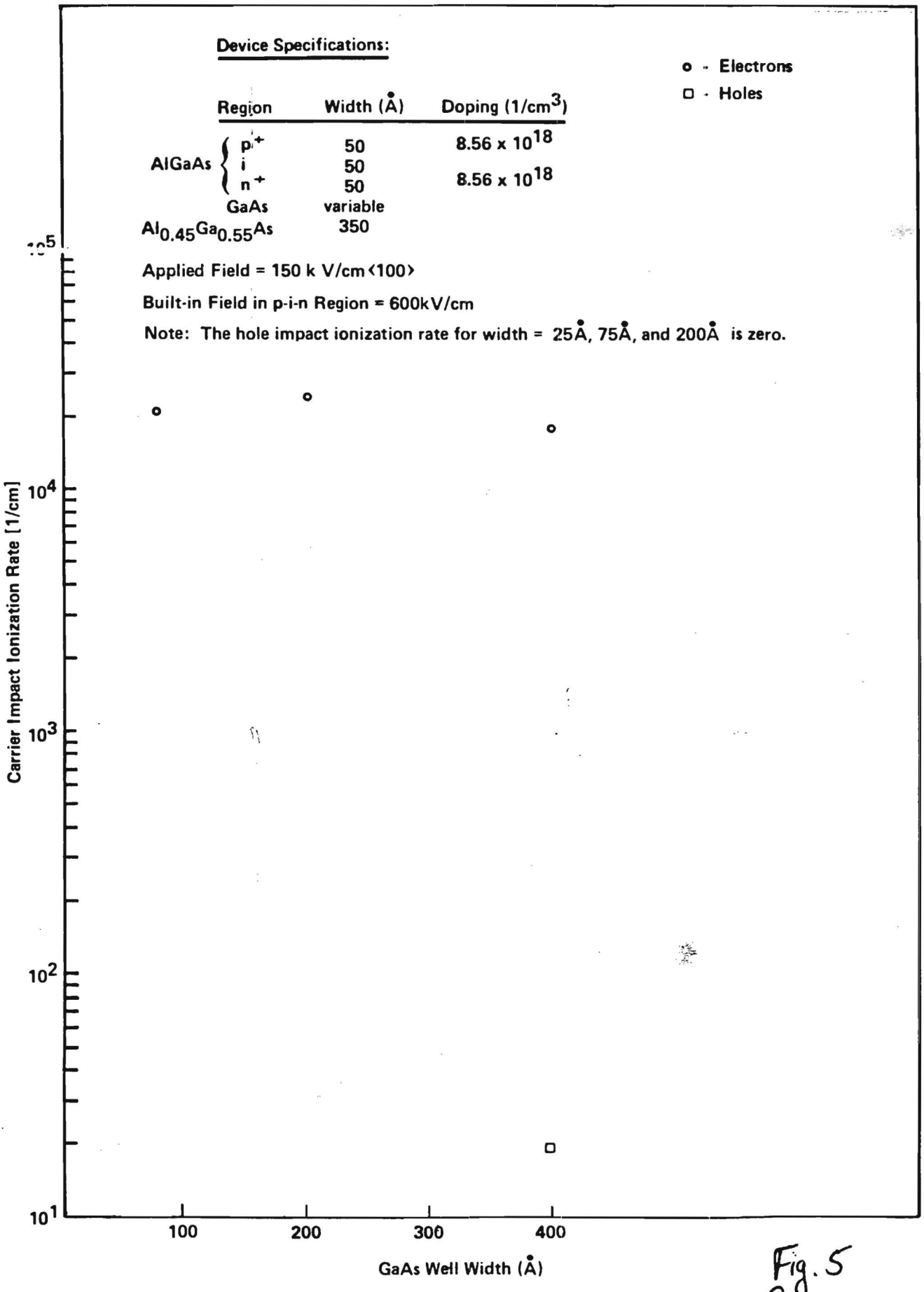

Fig. 5
Brennan

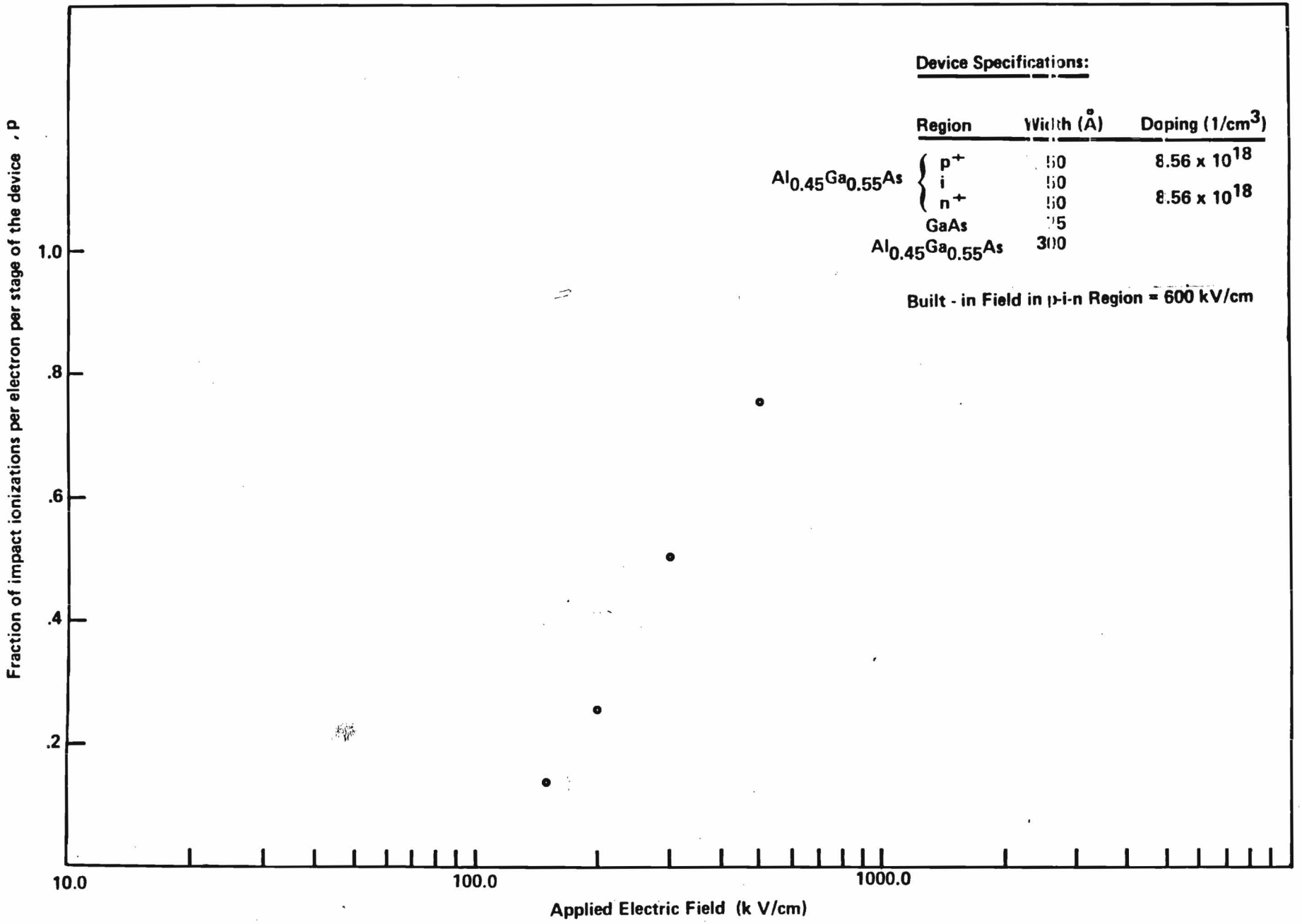

Fig. 6
Brennan

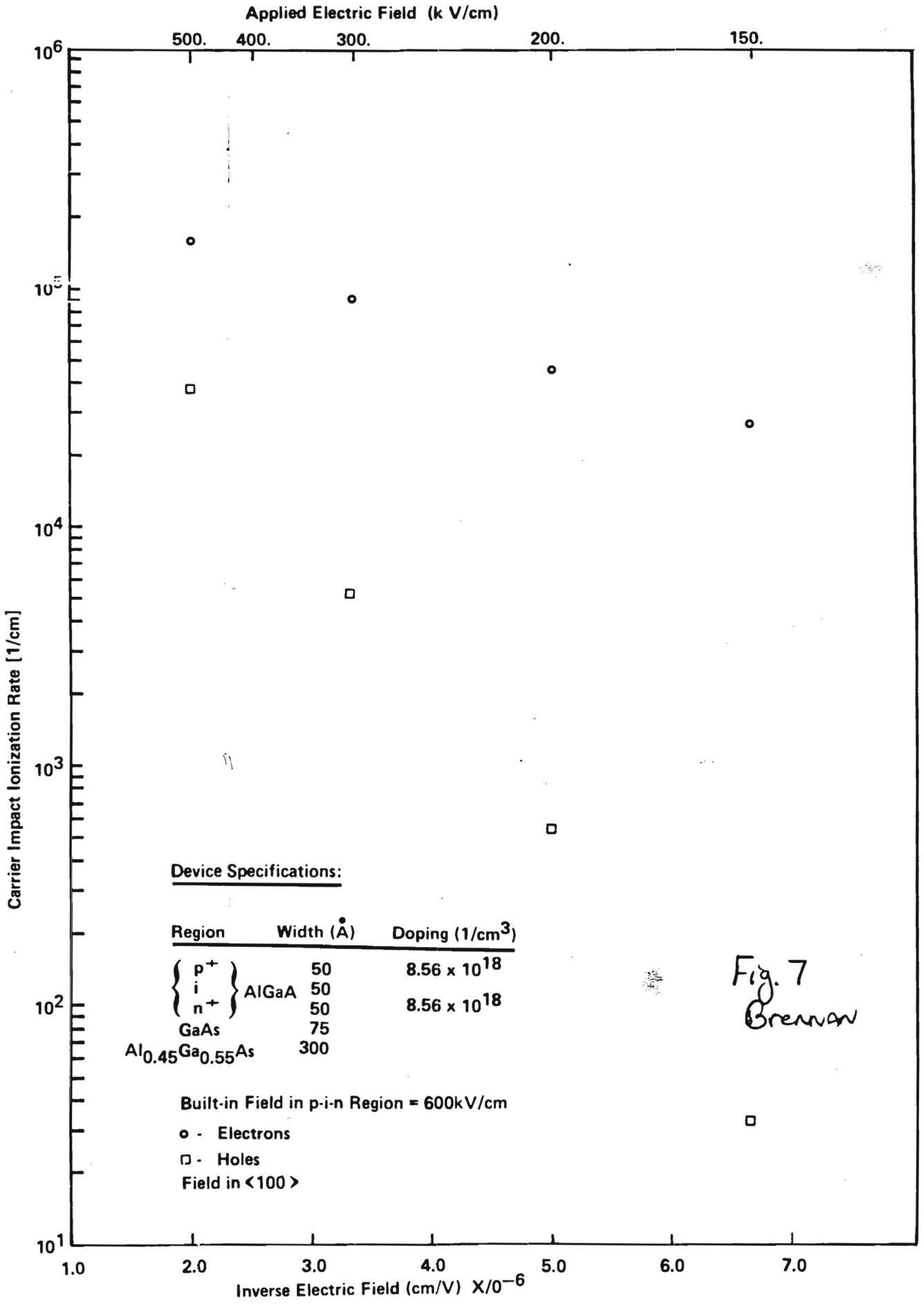

Fig. 7
Brennan

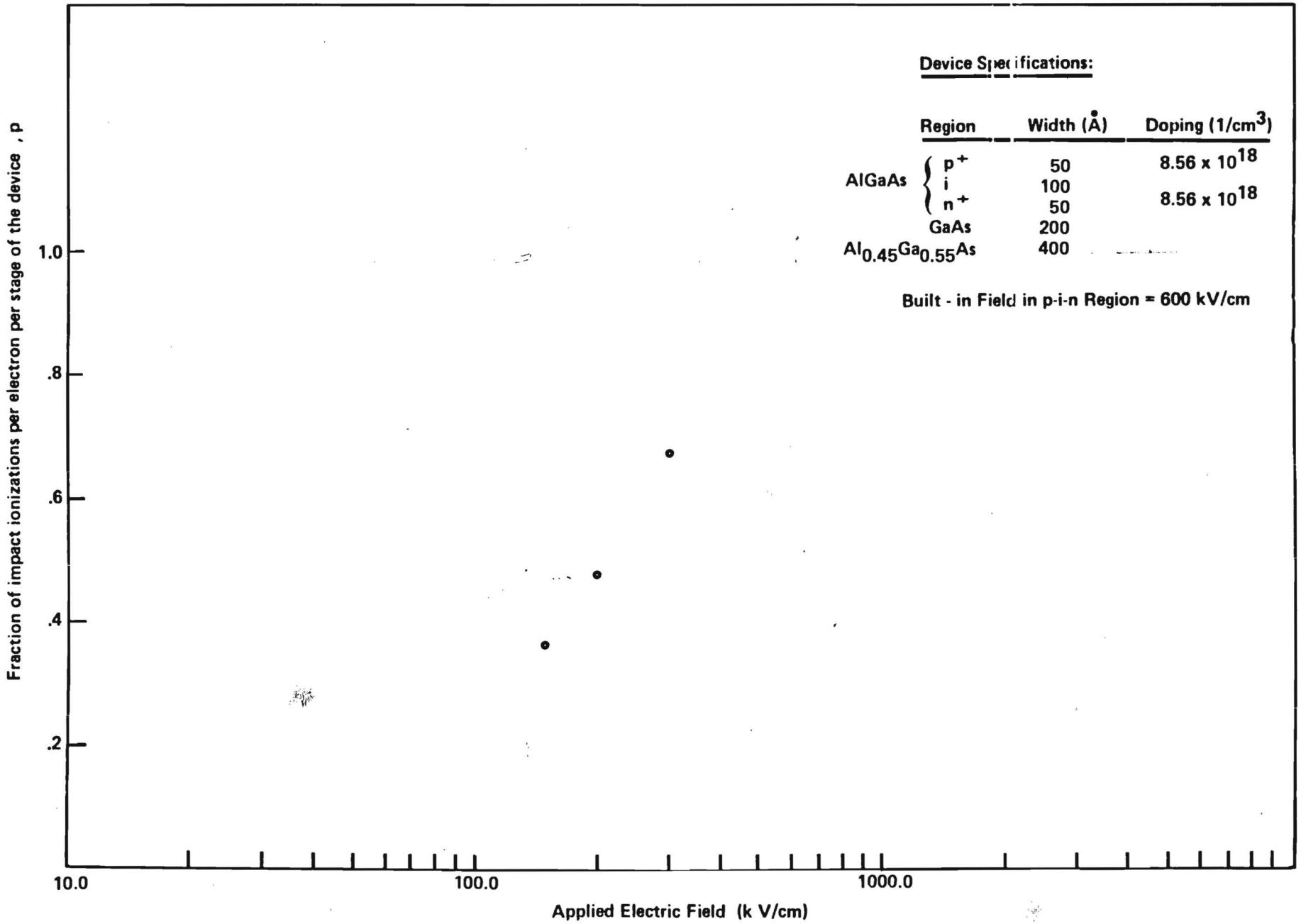

Fig. 8
Brennan

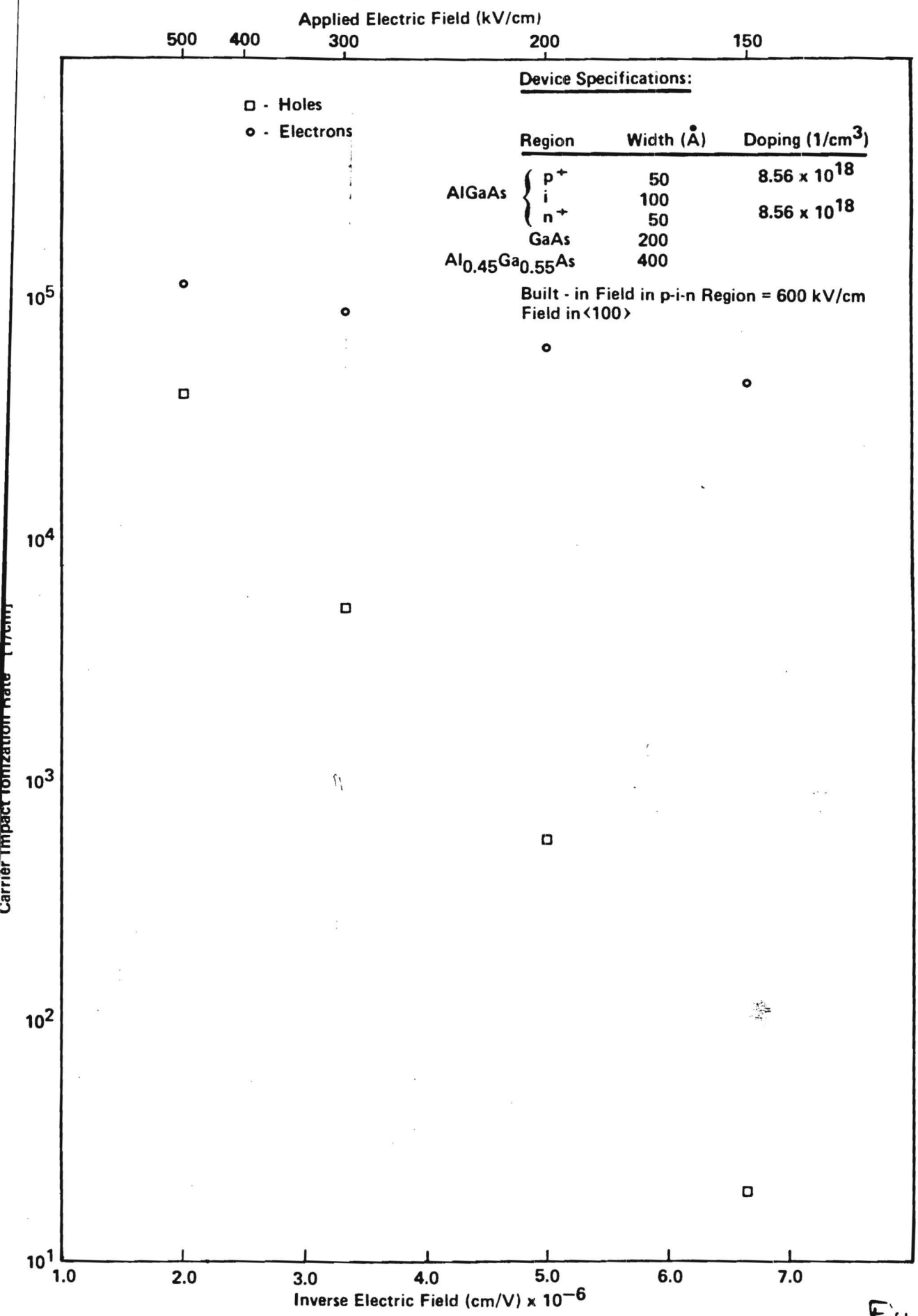

Fig-9
Brennan

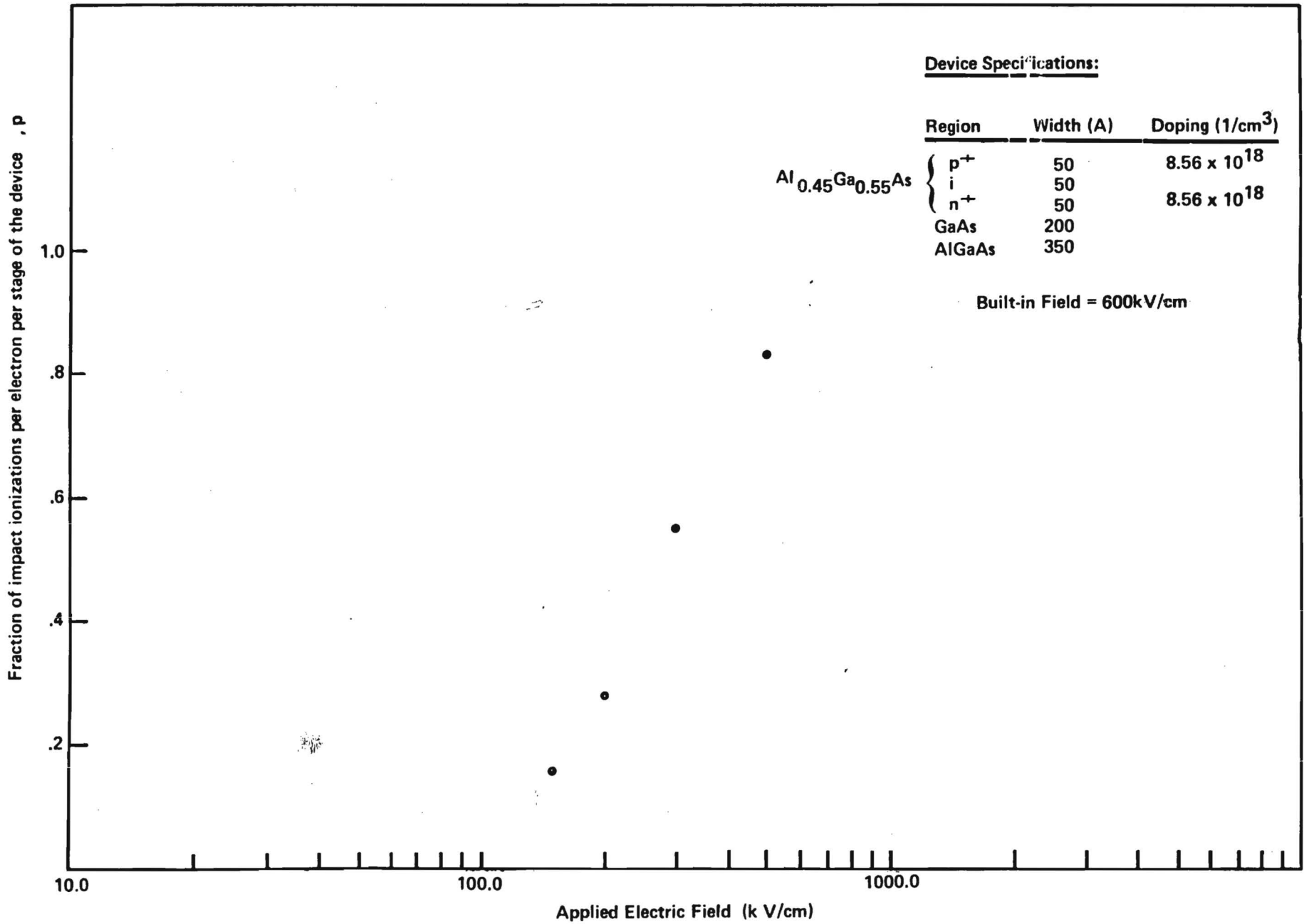

Fig. 10
Brennan

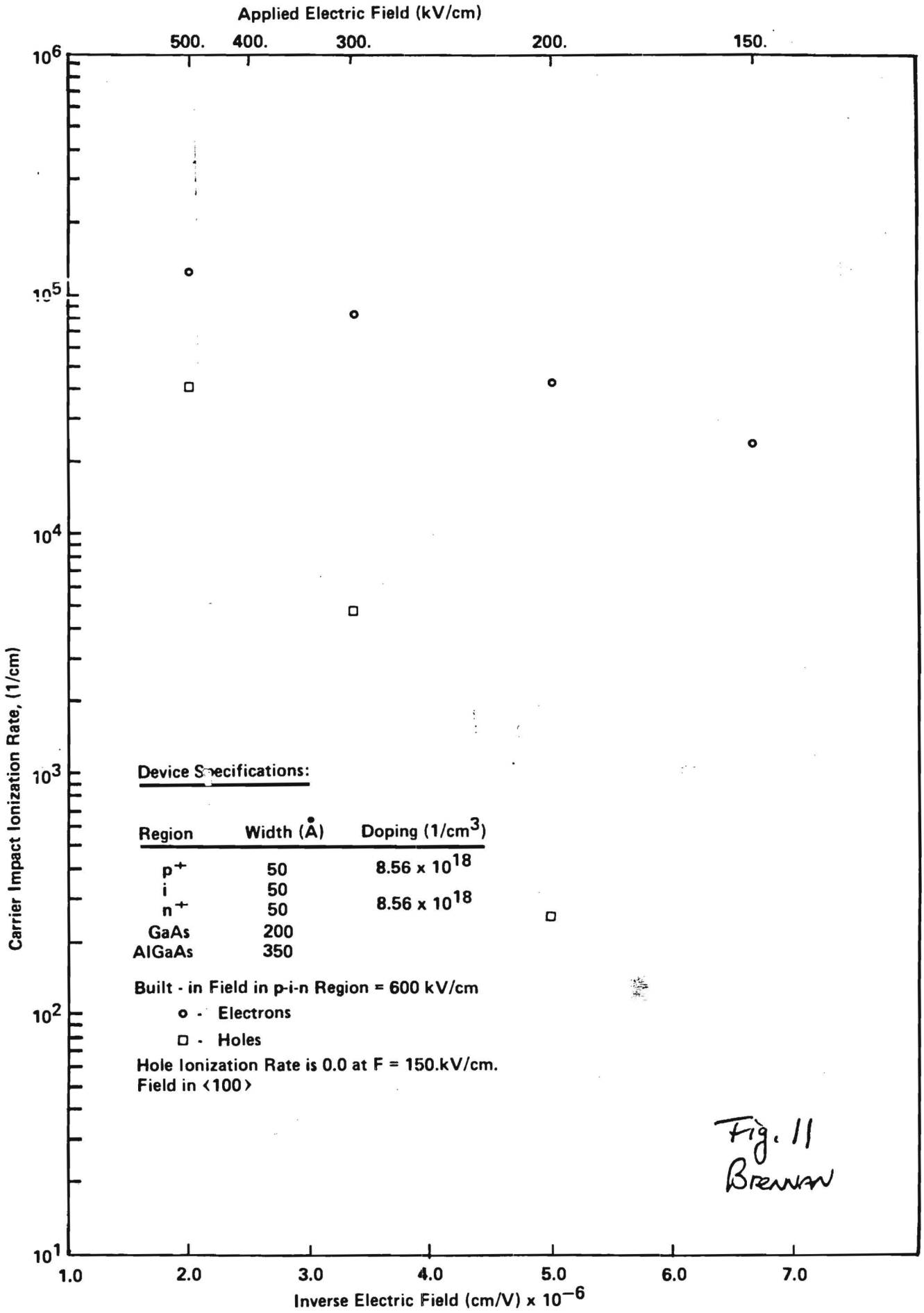

Device Specifications:

Region	Width (Å)	Doping ($1/cm^3$)
p^+	50	8.56×10^{18}
i	50	
n^+	50	8.56×10^{18}
GaAs	200	
AlGaAs	350	

Built - in Field in p-i-n Region = 600 kV/cm

o - Electrons

□ - Holes

Hole Ionization Rate is 0.0 at F = 150.kV/cm.
Field in ⟨100⟩

Fig. 11
Brennan

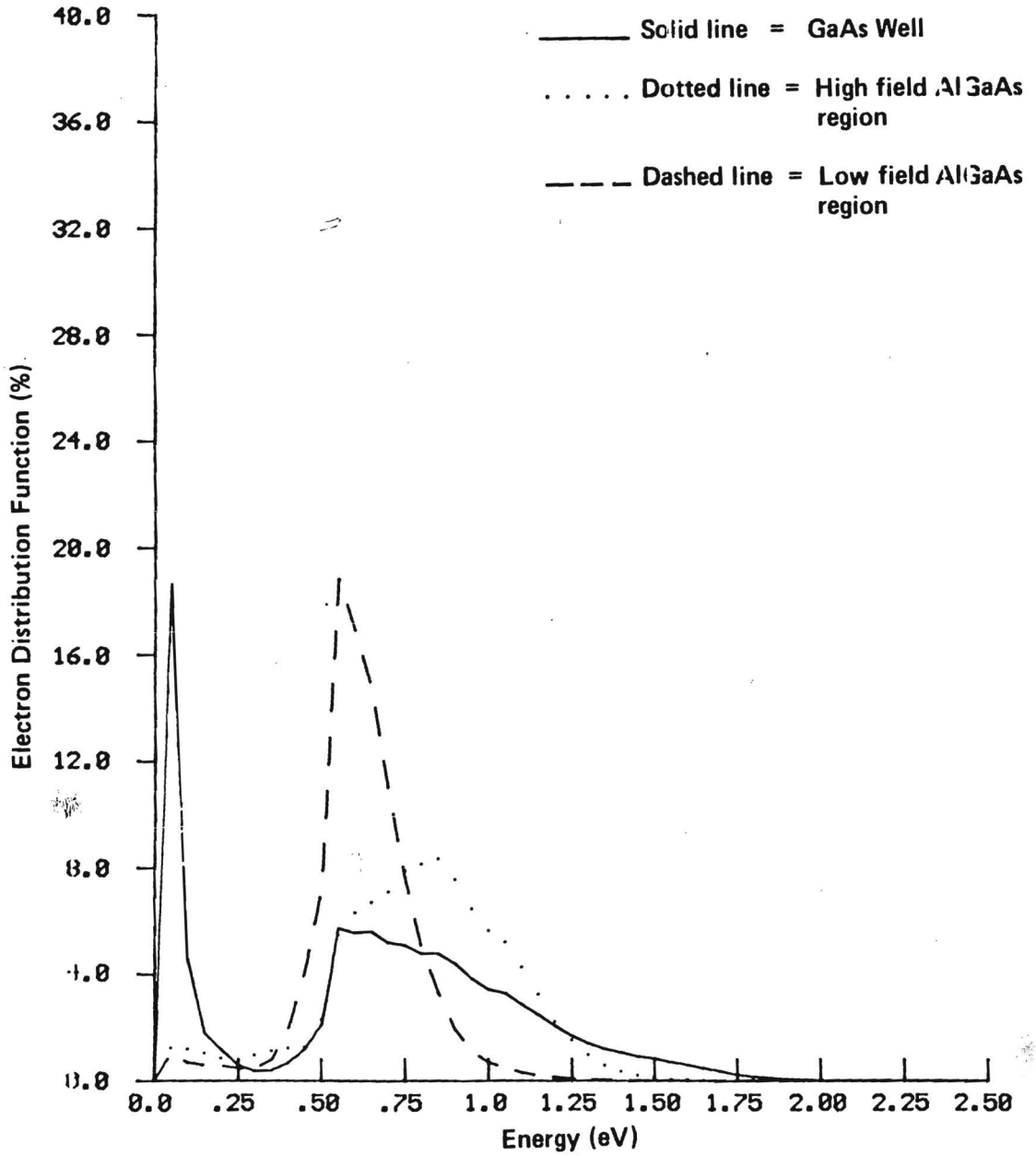
Solid line = GaAs Well
Dotted line = High field AlGaAs region
Dashed line = Low field AlGaAs region
Electron Distribution Function (%)
40.0
36.0
32.0
28.0
24.0
20.0
16.0
12.0
8.0
4.0
0.0
0.0 .25 .50 .75 1.0 1.25 1.50 1.75 2.00 2.25 2.50
Energy (eV)

Fig. 12

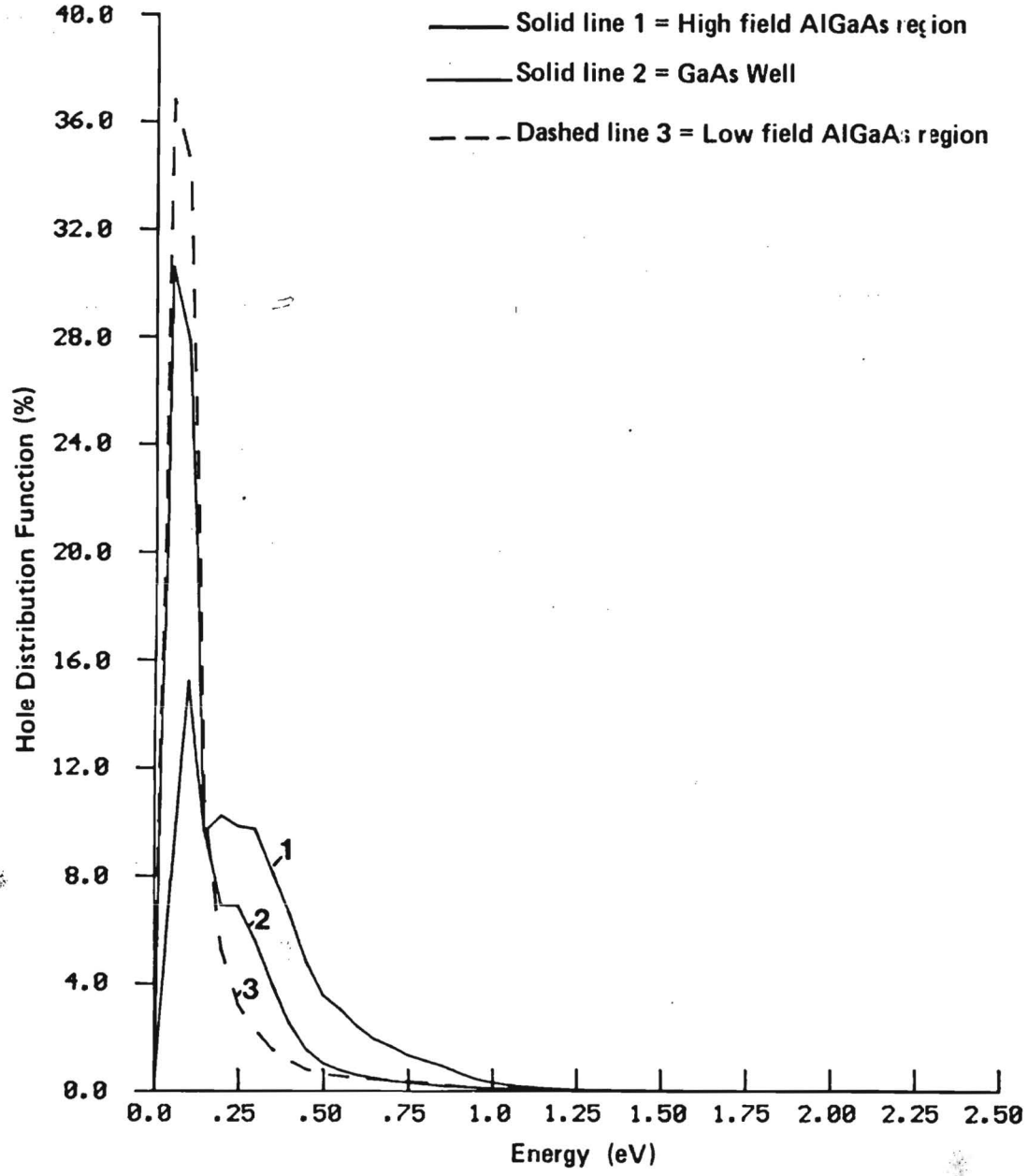

Fig. 13
BRENNAN

B-10-635
(A-4233)

~~IN CONFIDENCE~~

3

IN CONFIDENCE

HIGH PERFORMANCE PHOTODIODES

Quarterly Report No. 3
Report Period: 1 October 1985 - 31 December 1985

Project No. A-4233

Prepared for:

Dr. Kenneth A. Maloney
Polaroid Corporation
Microelectronics/Materials Center
21 Osborn Street, Dept. 775
Cambridge, MA 02139

Prepared by:

Dr. C. J. Summers and Dr. K. F. Brennan
Georgia Institute of Technology
Atlanta, GA 30332

CONTENTS

1. INTRODUCTION

During this report period investigations have continued on the theoretical studies of advanced superlattice AlGaAs avalanche photodiode devices and also on the calibration of the Georgia Tech Varian Gen II AlGaAs MBE system. The latter investigations have been supported by in-house Georgia Tech funds and are briefly described in Section 3.

2. THEORETICAL STUDIES OF AlGaAs SL-APD DEVICES

Recent activities in this area have been devoted to developing a greater understanding of the noise characteristics of new SL-APD devices and the preparation of a patent application on a "Superlattice Avalanche Photodetector."

Briefly, in the noise area, the work of Teich and collaborators on the noise performance characteristics of conventional APDs, single-carrier multiplication devices, single-carrier ionization and single-carrier multiplication (SCISCM) devices, superlattice APDs and the photomultiplier tube have been reviewed in detail. From this survey, it appears that by using Teich's formalisms accurate and meaningful noise figures can be obtained by using the electron and hole ionization probabilities per stage as calculated from hot electron transport theory. This is a very promising result and will be described in detail in the next report.

The major theoretical activity has been the generation of the patent application which for completeness is enclosed overleaf.

SUPERLATTICE AVALANCHE PHOTODETECTOR

Background of the Invention

The present invention pertains to a superlattice avalanche photodetector (APD).

Optical detectors used in lightwave communications systems must provide high gain at low noise for optimal system performance. The noise from a solid state junction optical detector primarily arises from two sources, the thermal noise of the load resistor, also known as Johnson noise, and the shot noise of the junction detector itself. Although Johnson noise can be reduced by making the load resistance very large, this limits the frequency response of the detector. Alternatively, for wide band applications, the use of an internal gain mechanism--such as an avalanche-multiplication-by-impact-ionization process which amplifies the signal without further increase in thermal noise--can substantially reduce the Johnson noise. Unfortunately, such an avalanche process introduces additional noise into the device.

As shown in an article entitled "Multiplication Noise In Uniform Avalanche Diodes," by R. J. McIntyre, IEEE Trans. Electron Dev., Vol. ED-13, 1966, pp. 164-168, the noise performance of a uniform avalanche photodiode depends upon the ratio of the electron and hole ionization rates. This is so because the predominant component of the noise in such a device is the shot noise which arises from the spatially random ionization events which occur within the active region. Such spatially random ionization events cause fluctuations in the carrier multiplication rate from the average and is thereby responsible for the increased noise. The above-cited article shows that if the electron ionization rate "α" and the hole ionization rate "β" are approximately equal, the excess noise factor is a maximum. Consequently, for a low noise APD, it is essential that "α" and "β" be as different as possible.

For wavelengths on the order of 1.06 um, low noise APDs can be made from silicon because the ratio of electron and hole

ionization rates is large, being at least as large as 20. However, APDs which are sensitive over a large range of wavelengths are necessarily made from many different material systems, in particular from III-V semiconductor compounds and their related alloys. Unfortunately, in most of these materials the bulk ionization rates for electrons and holes are roughly equal. As a consequence, low noise, high gain photodetectors for use in long wavelength operation require devices to include structural features which serve as a means by which the ratio of the electron and hole ionization rates can be increased over that naturally occurring in the materials from which the devices are fabricated.

One such structural feature for increasing the ratio of electron and hole ionization rates, a superlattice consisting of alternating thin layers of GaAs and $Al_xGa_{1-x}As$ which form part of a quantum well APD, has been disclosed in an article entitled "Impact Ionization In Multilayered Heterojunction Structures," by R. Chin, N. Holonyak, G. E. Stillman, J. Y. Tang, and K. Hess, Electronics Letters, Vol. 16, 1980, pp. 467-469. The article suggested that the superlattice could be used to selectively heat the electron distribution more than the hole distribution because of the relatively large difference between the conduction and valence band edge discontinuities, as well as the difference in the electron and hole ionization mean free paths. Because of the fact (1) that the superlattice is equivalent to a periodic electric field, (2) that there is a strong nonlinear, exponential, dependence of "α", and "β" on the field, and (3) that there is a threshold energy in the impact ionization process, both the electron and hole ionization rates are enhanced above their respective values in the absence of a superlattice structure. However, the enhancement of the hole ionization rate is much less than that of the electron ionization rate for two reasons. First, because the conduction band edge discontinuity in the material system disclosed in the article is significantly larger than the valence band discontinuity, electrons gain a larger kinetic energy boost from the heterointerface than the

holes. Second, and more important, because the hole energy relaxation rate is much larger than the electron relaxation rate for the average carrier energies involved in the devices, the holes relax faster to their steady state energy after crossing the heterointerface between the GaAs and $Al_xGa_{1-x}As$ layers. this results in fewer holes that "lucky-drift" to energies high enough to cause impact ionization.

Another structural feature for increasing the ratio of electron and hole ionization rates, a doped quantum well APD which includes an alternative superlattice, has been disclosed in an article entitled "Single-Carrier-Type Dominated Impact Ionization In Multilayer Structures," by H. Blauvelt, S. Margalit, and A. Yariv, Electronics Letters, Vol. 18, 1982, pp. 375-376. This structure attempts to spatially restrict the region wherein impact ionization occurs and thereby to obtain the benefit of a photomultiplier in this regard, namely, the benefit owing to the fact that the variability of the number of electrons generated per detected photon is minimized because electron multiplication occurs only at fixed grids therewithin. The doped quantum well APD more nearly approximates photomultiplier-like behavior in regard to the localization of carrier multiplication than two other structures disclosed in the art, namely, a channeling APD disclosed in an article entitled "The Channeling Avalanche Photodiode: A Novel Ultra-Low-Noise Interdigitated p-n Junction Detector," by F. Capasso, IEEE Trans. Electron Dev., Vol. ED-29, 1982, pp. 1388-1395 and a graded gap staircase APD disclosed in an article entitled "Staircase Solid State Photomultipliers And Avalanche Photodiodes With Enhanced Ionization Rate Ratio," by F. Capasso, W. T. Tsang and G. F. Williams, IEEE Trans. Electron Dev., Vol. ED-30 1983, pp. 381-390.

The disclosed channeling APD consists of a superlattice of alternating layers of n-GaAs and $p\text{-}Al_{0.45}Ga_{0.55}As$. In addition, the device is configured so that the application of a reverse bias produces both transverse and longitudinal electric field components. The transverse field sweeps holes out of the GaAs

layers and into adjacent $Al_{0.45}Ga_{0.55}As$ layers while confining the electrons within the GaAs layers. The disclosed graded gap staircase APD consists of a superlattice whose layers have a graded energy band gap. In a graded gap staircase APD the impact ionization events occur at specific and localized areas within the device, whereas, in a channeling APD the ionization events occur at random throughout a layer. Because of the localization of the impact ionization in a graded gap staircase APD, the variability and, hence, the gain fluctuation of the number of electrons generated per photon is reduced and the excess noise in this device will be lower than that in a conventional uniform APD and a channeling APD. Nevertheless, a graded gap staircase APD fabricated from a GaAs/AlGaAs material system will not behave like a photomultiplier since the conduction band edge offset between GaAs and AlGaAs is not a sufficiently large fraction of the energy bandgap in GaAs.

An example of a doped quantum well APD suggested in the above-referenced article by Blauvelt et al. is shown in Fig. 1. The APD comprises electrodes 31 and 32 contacted to p^+ region 34 and n^+ region 20, respectively, and a repeating superlattice unit. Each superlattice unit comprises p^+ AlGaAs layer 10 intrinsic AlGaAs layer 11, n^+ AlGaAs layer 12, intrinsic GaAs layer 13, and intrinsic AlGaAs layer 14, where each AlGaAs layer consists of the alloy $Al_{0.45}Ga_{0.55}As$. Voltage V_0 from voltage source 33 is applied to electrodes 31 and 32 to reverse-bias the device. The electric field profile in the superlattice unit 10-14 is shown in Fig. 2 to be asymmetric.

When the APD is reverse biased, electron are injected into GaAs layer 13, where avalanche multiplication occurs, after passing through the high field of layers 10-12, i.e., from the left of layer 13 in Fig. 1, and holes are injected after passing through the low field of layer 14, i.e., from the right of layer 13 in Fig. 1. As a result, the electrons are accelerated by a much greater field than the holes before arriving at GaAs layer 13. The combined action of the high field and the subsequent injection over the heterointerface between layers 12 and 13

produces such hot electrons within narrow band gap GaAs layer 13 that electron impact ionization events will occur. Conversely, holes undergo little heating within low field $Al_{0.45}Ga_{0.55}As$ layer 14 before being injected into narrow bandgap layer 13. Thus, few, if any, hole impact ionization events will occur. Even though holes also drift through high field P^+-i-n^+ layers 10-12, before being injected into GaAs layer 13, they cool off in low field GaAs layer 14 where the bandgap is much larger than in the GaAs layer. As a result, the hole ionization rate in layer 13 is low.

Unfortunately, Blauvelt et al. did not completely analyze the disclosed doped quantum well APD. The article did not consider a most important aspect of the noise component which is crucial in properly determining appropriate designs of practical APDs.

For example, the excess noise factor of a APD, the standard measure of avalanche noise, can be expressed as:

$$Fe = \langle N_m^2 \rangle / \langle N_m \rangle^2 \qquad (1)$$

where N_m is the gain random variable for a single event at the input to an m-stage device, i.e., the total number of carriers generated at the output stage of the m-stage device which result from a single primary event at the input; $\langle N_m^2 \rangle$ is the second moment of the gain random variable; and $\langle N_m \rangle^2$ is the square of the mean gain. The excess noise factor can be expressed in terms of the mean and the variance of N_m as:

$$Fe = 1 + Var(N_m)/\langle N_m \rangle^2. \qquad (2)$$

If there is no spatial fluctuation in the physical multiplication mechanism, then the variance of N_m, $Var(N_m)$, will be zero and Fe

= 1, i.e., the minimum noise factor possible. Thus, in order to make a completely noiseless APD, it is necessary that there be no fluctuation in the carrier multiplication; i.e., the multiplication must be completely deterministic.

The mean carrier gain in a "photomultiplier-like" APD, i.e., one in which carrier gain occurs at a specific spatial location in each stage of the APD, can be expressed as:

$$\langle N_m \rangle = (1 + p)^m \text{ for } m > = 1 \qquad (3)$$

where p is the probability that an incident carrier impact ionizes at the output of each stage in an m-stage APD. For an ideal, noiseless APD, p = 1. This means that there is a unity probability that each carrier incident upon each stage of the APD will ionize and that as a result $\langle N_m \rangle = 2^m$. Fe can be written in terms of p as:

$$Fe = 1 + [(1 - p)/(1 + p)] [1 - (1+p)^{-m}] \qquad (4)$$

From Equation 4, when p = 1, Fe = 1 and the APD is completely noiseless. For p > 0 Fe is always less than 2.

In the limit as the number stages, m, approaches infinity, Equation 4 becomes:

$$Fe = 2./(1 + p) \qquad (5)$$

Clearly, if p = 1, then Fe = 1. When p is equal to zero, the limit as $m \to \infty$ does not exist in Equation 4 but Equation 4 then reduces to Fe = 1. At either of these two extremes, the APD is completely deterministic--no random fluctuations exist--and the

excess noise vanishes. The case p = 0 is uninteresting since there is no gain and the APD is bandwidth limited. The most desirable APD is therefore one which optimizes p, i.e., one in which p = 1. As a consequence of the above, to produce a noiseless solid state APD, it is necessary to fulfill two conditions: (1) the hole ionization rate in the APD should be essentially zero, and (2) the gain per stage of the APD should be 2, i.e., p = 1. If these two conditions are met or reasonably met, an extremely low noise factor can be produced.

In analyzing the suggested doped quantum well APD, Blauvelt et al. recognized that is desirable to have a detector in which the multiplication process is dominated by one carrier type but they did not consider the effect of p. In addition, they recognized that the superlattice structure proposed by Chin et al. would enhance the ratio of ionization rates "α"/"β", the increase being primarily due to the fact that the discontinuity of the conduction band is larger than the discontinuity of the valence band in the GaAs/AlGaAs material system. As a result of the difference in band discontinuities, electrons would enter the GaAs multiplication region with more kinetic energy than would the holes, and the electrons would therefore be more likely to produce a secondary pair than the holes. Blauvelt et al. then proposed a device structure similar to that shown in Fig. 1 to further increase "α"/"β". They suggested applying a sufficiently large voltage to fully deplete the "multiplication" region, like GaAs layer 13 in Fig. 1, and the "acceleration" regions, like p^+ AlGaAs layer 10 and n^+ AlGaAs layer 12 in Fig. 1. Since the electric field in a depleted layer is proportional to the doping, the electric field changes abruptly in thin, heavily doped layers 10 and 12. In contrast, the field is nearly constant in lightly doped layers 11, 13 and 14. Thus, by doping the layers as suggested by Blauvelt et al., and shown in Fig. 1., the electric field on one side of GaAs layer 13 can be made larger than the electric field on the other. If electrons are injected into GaAs layer 13 from the high field side and holes are injected into GaAs layer 13 from the low field side, the fraction of electrons

that are injected with energies above the ionization threshold can be significantly larger than the fraction of holes that are injected with energies above the ionization threshold.

Further, Blauvelt et al. recognized that the suggested APD would operate most successfully if the two materials which formed the superlattice unit had "sufficiently" different ionization thresholds. Since the ionization thresholds of semiconductors are generally proportional to the bandgap, any two semiconductors with sufficiently different bandgaps could be used for the two materials. For the specific case of the ternary materials $Al_xGa_{1-x}As$, the bandgap increases as x increases. Since GaAs/AlGaAs superlattices have been fabricated using molecular beam epitaxy (MBE), Blauvelt et al. proposed GaAs, having a bandgap energy = 1.43 eV, and $Al_{0.45}Ga_{055}As$, having bandgap energy = 2.0 eV, to be suitable choices for the two materials.

Blauvelt et al. used a simple model of impact ionization to analyze the device. As a result of their calculations they determined that GaAs layer 13 should be 400 angstroms thick, that high field AlGaAs layers 10-12 should be 700 angstroms thick, and that low field AlGaAs layer 14 should be 900 angstroms thick.

Recognizing that their analysis was incomplete, Blauvelt et al. stated that optimized design of the proposed detector would necessitate calculation of the electron and hole distributions at each position as the carriers move through the layers of the detector. They did, however, point out several qualitative features of the detector design: (1) that n^+ AlGaAs layer 12 should be as thin as possible in order that the hot electrons do not lose much energy therein; (2) that high field AlGaAs layers 10-12 should have their thicknesses and electric fields adjusted so that a significant fraction of the electrons passing there through are injected into GaAs layer 13 with enough energy to produce secondary pairs; (3) that it is undesirable for the electric field to be so high that multiplication in the AlGaAs layers becomes significant; (4) that, in order to minimize secondary ionization by holes, low field layers 13-14 should be sufficiently thick to allow holes to lose, by phonon collision,

the kinetic energy they gained in the preceding high field layers; (5) that the difference between the electric fields in the high and low field regions should be as large as is practical, for example, a 50 angstrom thick n^+ layer 12 with a doping of 2×10^{18} cm^{-3} will result in a change in the electric field of approximately 1.6×10^5 V/cm; (6) that it is desirable to have the total number of donors in a superlattice unit nearly equal to the total number of acceptors so that the electric field pattern will repeat itself in each unit.

As discussed above, there are two conditions which need to be satisfied in order to determine the optimal design parameters for a practical APD fabricated as shown in Fig. 1. These being to maximize the ionization rate ratio "α"/"β" as well as to maximize p. Unfortunately, Blauvelt et al. did not consider the appropriate model for determining the parameters for their proposed device and thereby completely mischaracterized the optimal, or even the appropriate parameters for a working device.

Summary of the Invention

The preset invention pertains to a low noise superlattice avalanche photodetector (APD) comprising repeated superlattice units formed from a p^+-i-n^+ $Al_{0.45}Ga_{0.55}As$ region immediately followed by near intrinsic layers of GaAs and $Al_{.45}Ga_{0.55}As$. The inventive APD causes one type of charge carrier to ionize at a faster rate than the other type of charge carrier and the avalanche mechanism is initiated by the charge carrier having the larger ionization rate. By doping the layers of the superlattice unit as described above, i.e. p^+-i-n^+ $Al_{0.45}Ga_{0.55}As$ layers followed by near intrinsic GaAs and $Al_{0.45}Ga_{0.55}As$ layers, the electric field profile in the unit can be made asymmetric. When the APD is reverse biased, electrons are accelerated in a high electric field region before being injected into the GaAs layer, whereas holes are accelerated in a low electric field region before being injected into the GaAs layer. The combined action of being accelerated in a high electric field and subsequently being injected over the AlGaAs/GaAs heterointerface between the

n^+ AlGaAs layer and the GaAs layer produces very hot electrons within the narrow bandgap GaAs layer. The electrons are sufficiently hot that substantial impact ionization occurs. Conversely, the holes undergo little heating within the low field intrinsic $Al_{0.45}Ga_{0.55}As$ layer before being injected into the narrow bandgap GaAs layer and few, if any, impact ionization events occur. The holes, do, of course, also drift in the high field p^+-i-n^+ region. However, after that, they enter the low field intrinsic AlGaAs layer where the bandgap is much larger than in the GaAs layer, and in which layer they lose energy before being injected into the narrow bandgap GaAs layer. As a result, the hole ionization rate in the GaAs layer is low.

The present invention teaches the critical values of various parameters which are necessary in fabricating an optimal low noise doped quantum well APD:

(1) Doping Levels of the p^+ and n^+ Layers:
The doping level should be in the range of 7×10^{18} cm^{-3} to 1×10^{19} cm^{-3}.

(2) AlGaAs High Field Layer Widths (the layers comprising the p^+-i-n^+ region):
The width of the intrinsic layer is the most critical. The p^+ and the n^+ layers should be as small as possible but they should also be large enough to enclose a large amount of charge. Thus, the p^+ and the n^+ layers should be about 50 angstroms wide each and the intrinsic region width should be in the range between 50 and 100 angstroms.

(3) GaAs Layer Width:
Very small GaAs layer widths result in quantum mechanical spatial quantization effects which are deleterious to device performance. Thus, the GaAs layer width should be in the range between 180 and

300 angstroms.

(4) AlGaAs Low Field Layer Width:
It is important to have a sufficiently long region so that the holes can cool after drifting through the high field p^+-i-n^+ region. Thus, the intrinsic AlGaAs low field layer width should be in the range between 200 and 500 angstroms.

(5) Percentage of Al in the Ternary AlGaAs Composition:
It is desirable to use direct bandgap materials since no appreciable advantage can be attained from the use of an indirect bandgap material. In addition, in order to obtain the largest change in the conduction band between GaAs and AlGaAs, x should be in the range between .4 to .45, or wherever the transition occurs between the direct and indirect materials.

(6) Applied Electric Field:
The electric field should be in the range between 100 and 200 kV/cm.

Brief Description of the Drawing

A complete understanding of the present invention may be gained by considering the following detailed description in conjunction with the accompanying drawing, in which:

Fig. 1 shows, in pictoria form, a unit cell of a doped quantum well APD fabricated in accordance with the present invention;

Fig. 2 shows, in graphical form, the electric field profile of the unit cell in Fig. 1;

Fig. 3 shows, in graphical form, the fraction of impact ionizations per electron per stage of a doped quantum well APD,

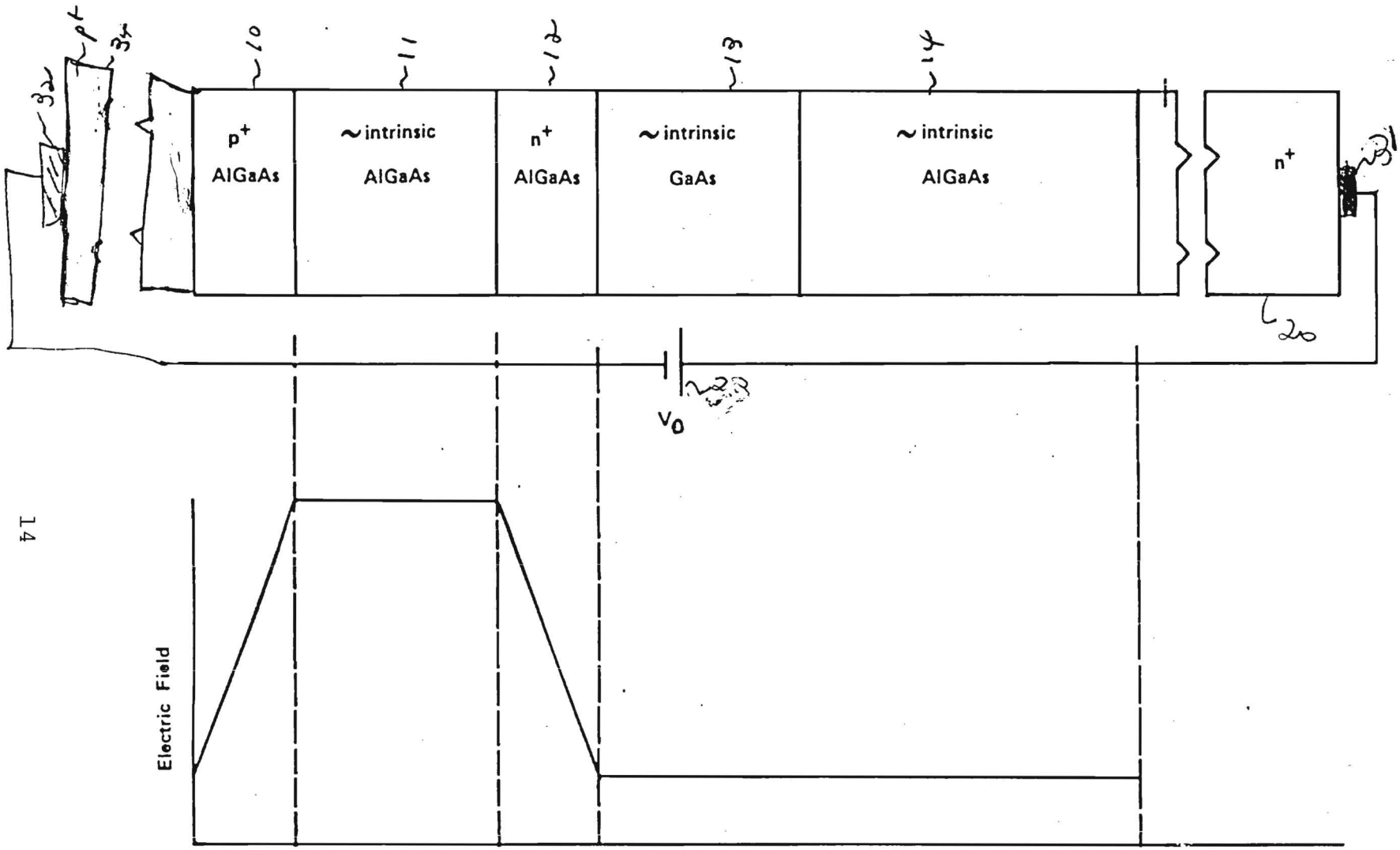
p+
AlGaAs
~intrinsic
AlGaAs
n+
AlGaAs
~intrinsic
GaAs
~intrinsic
AlGaAs
n+
V_0
Electric Field
Distance Along the Device

FIG. 1

FIG. 2

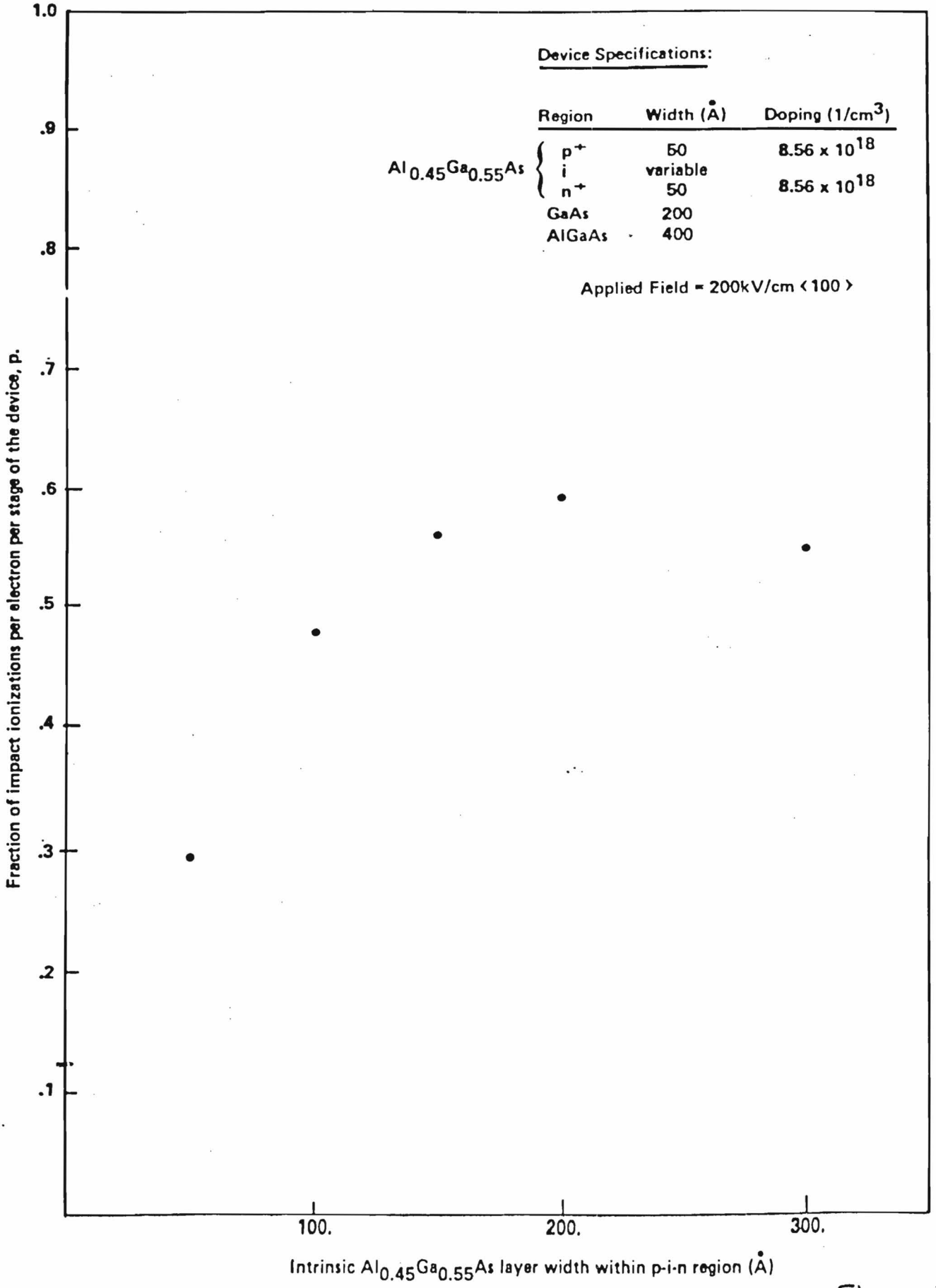
Device Specifications:
Region
Width (Å)
Doping (1/cm3)
Al0.45Ga0.55As
p+
50
8.56 x 10^18
i
variable
n+
50
8.56 x 10^18
GaAs
200
AlGaAs
400
Applied Field = 200kV/cm ‹100›
Fraction of impact ionizations per electron per stage of the device, p.
1.0
.9
.8
.7
.6
.5
.4
.3
.2
.1
100.
200.
300.
Intrinsic Al0.45Ga0.55As layer width within p-i-n region (Å)

Fig. 3

p, plotted against the width of intrinsic high field AlGaAs layer 11 at an applied electric field of 200.00 kV/cm and a resulting built-in electric field within p^+-i-n^+ layers 10-12 of 600.0 kV/cm;

Fig. 4 shows, in graphical form, the electron and hole impact ionization rates of a doped quantum well APD plotted as a function of the width of intrinsic high field AlGaAs layer 11 at an applied electric field of 200.0 kV/cm and a resulting built-in electric field within p^+-i-n^+ layers 10-12 of 600.0 kV/cm;

Fig. 5 shows, in graphical form, the fraction of impact ionizations per electron per stage of a doped quantum well APD, p, plotted against the width of GaAs well layer 13 at an applied electric field of 150.0 kV/cm;

Fig. 6 shows, in graphical form, the electron and hole impact ionization rate of a doped quantum well APD plotted as a function of the width of GaAs well layer 13 at an applied electric field of 150.0 kV/cm;

Fig. 7 shows, in graphical form, the fraction of impact ionizations per electron per stage of a doped quantum well APD, p, 1 against the applied electric field, the built-in electric field after p^+-i-n^+ layers 10-12 are fully depleted being equal to 600.0 kV/cm;

Fig. 8 shows, in graphical form, the electron and hole impact ionization rates of a doped quantum well APD as a function of inverse electric field;

Fig. 9 shows, in graphical form, the fraction of impact ionizations per electron per stage of a doped quantum well APD, p, plotted against the applied electrical field, the built-in electric field after p^+-i-n^+ layers 10-12 are fully depleted being equal to 600.0 kV/cm;

Fig. 10 shows, in graphical form, the electron and hole impact ionization rates of a doped quantum well APD as a function of inverse electric field;

Fig. 11 shows, in graphical form, fraction of impact ionizations per electron per stage of a doped quantum well APD, p, plotted versus the applied electric field, the built-in

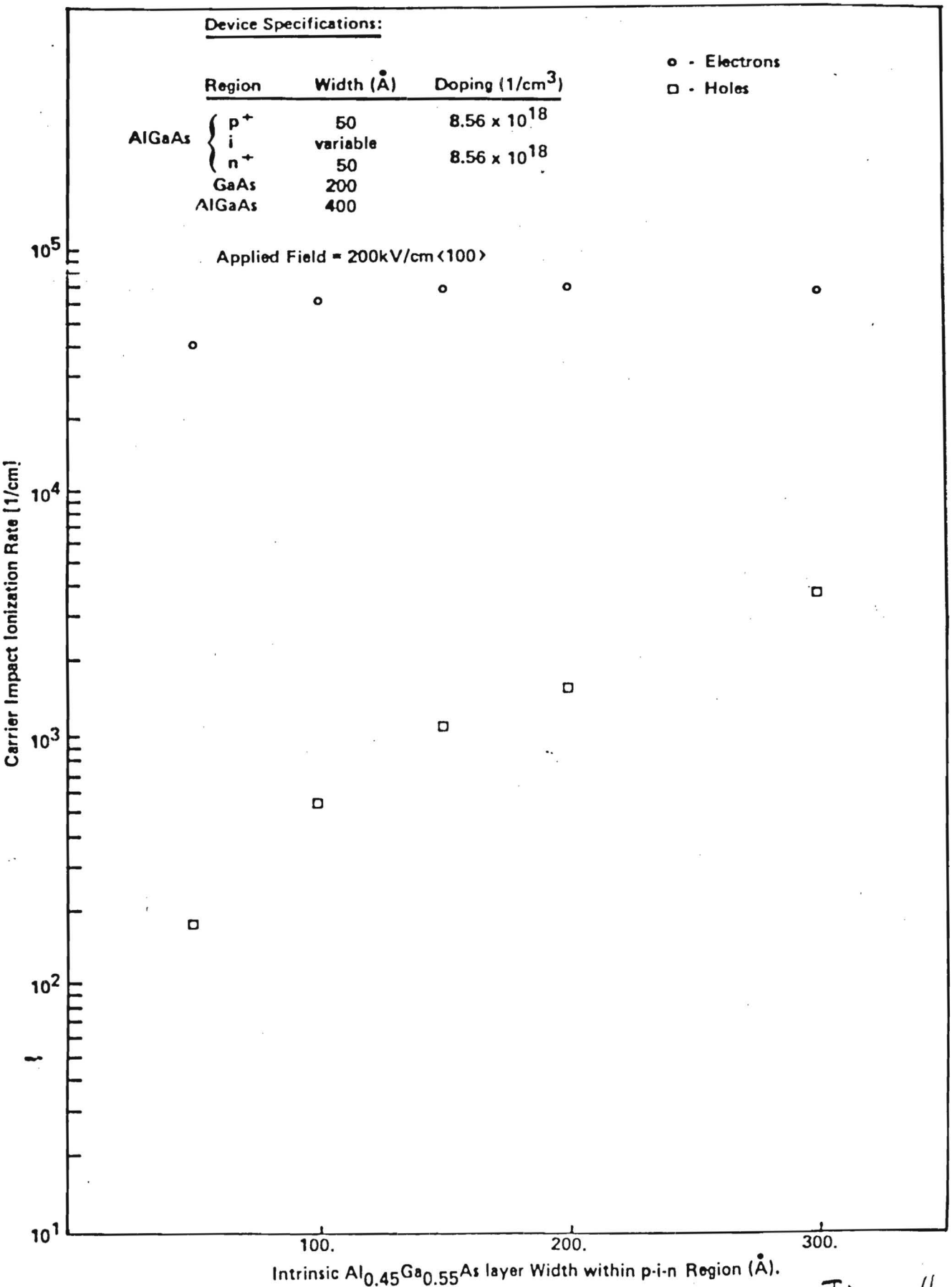
Device Specifications:
Region
Width (Å)
Doping (1/cm3)
AlGaAs
p+
50
8.56 x 10^18
i
variable
n+
50
8.56 x 10^18
GaAs
200
AlGaAs
400
o - Electrons
□ - Holes
Applied Field = 200kV/cm <100>
Carrier Impact Ionization Rate (1/cm)
10^5
10^4
10^3
10^2
10^1
100.
200.
300.
Intrinsic Al0.45Ga0.55As layer Width within p-i-n Region (Å).

Fig. 4

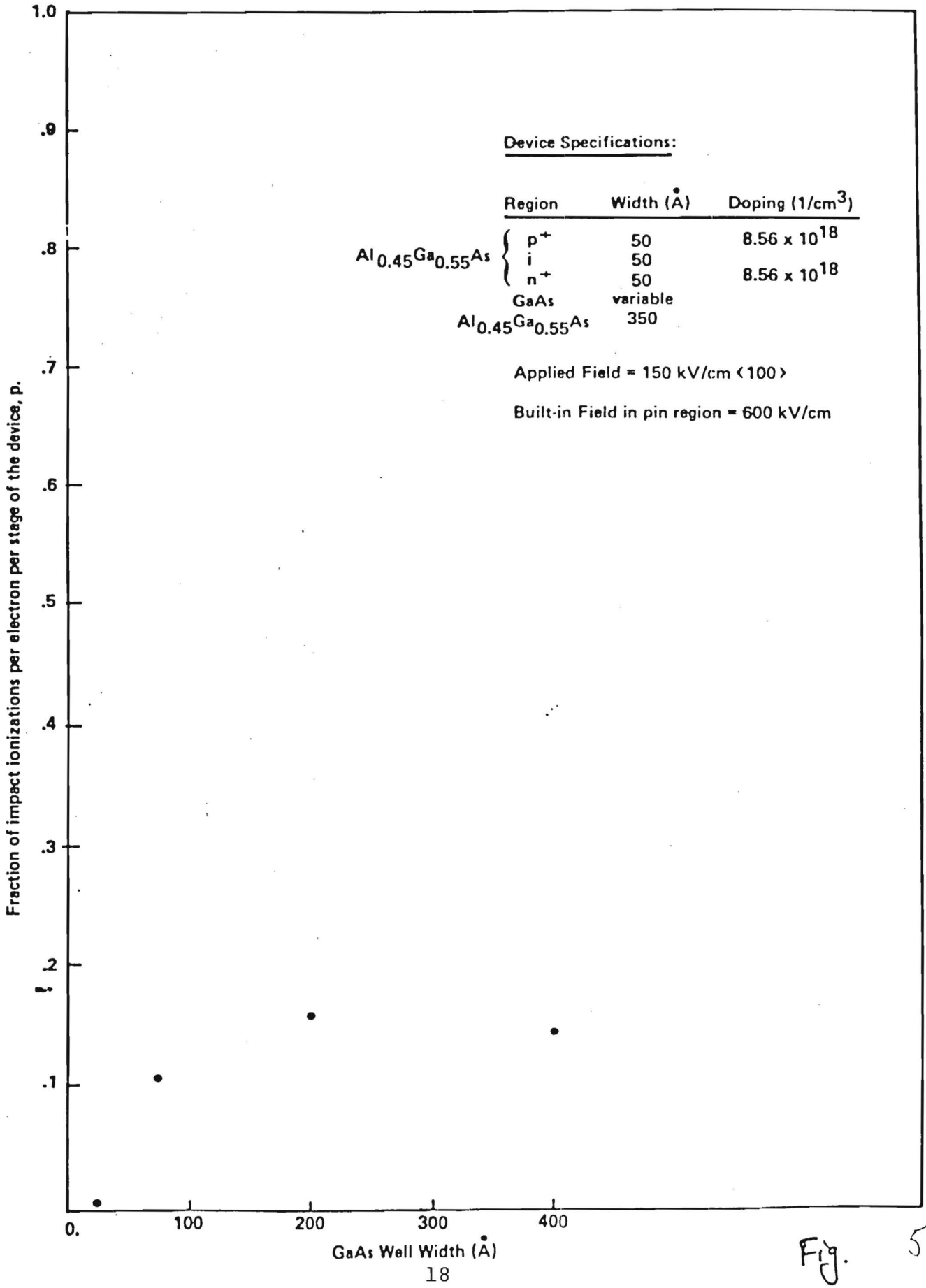
Device Specifications:
Region
Width (Å)
Doping (1/cm3)
Al0.45Ga0.55As
p+
50
8.56 x 10^18
i
50
n+
50
8.56 x 10^18
GaAs
variable
Al0.45Ga0.55As
350
Applied Field = 150 kV/cm ‹100›
Built-in Field in pin region = 600 kV/cm
Fraction of impact ionizations per electron per stage of the device, p.
1.0
.9
.8
.7
.6
.5
.4
.3
.2
.1
0.
100
200
300
400
GaAs Well Width (Å)

Fig. 5

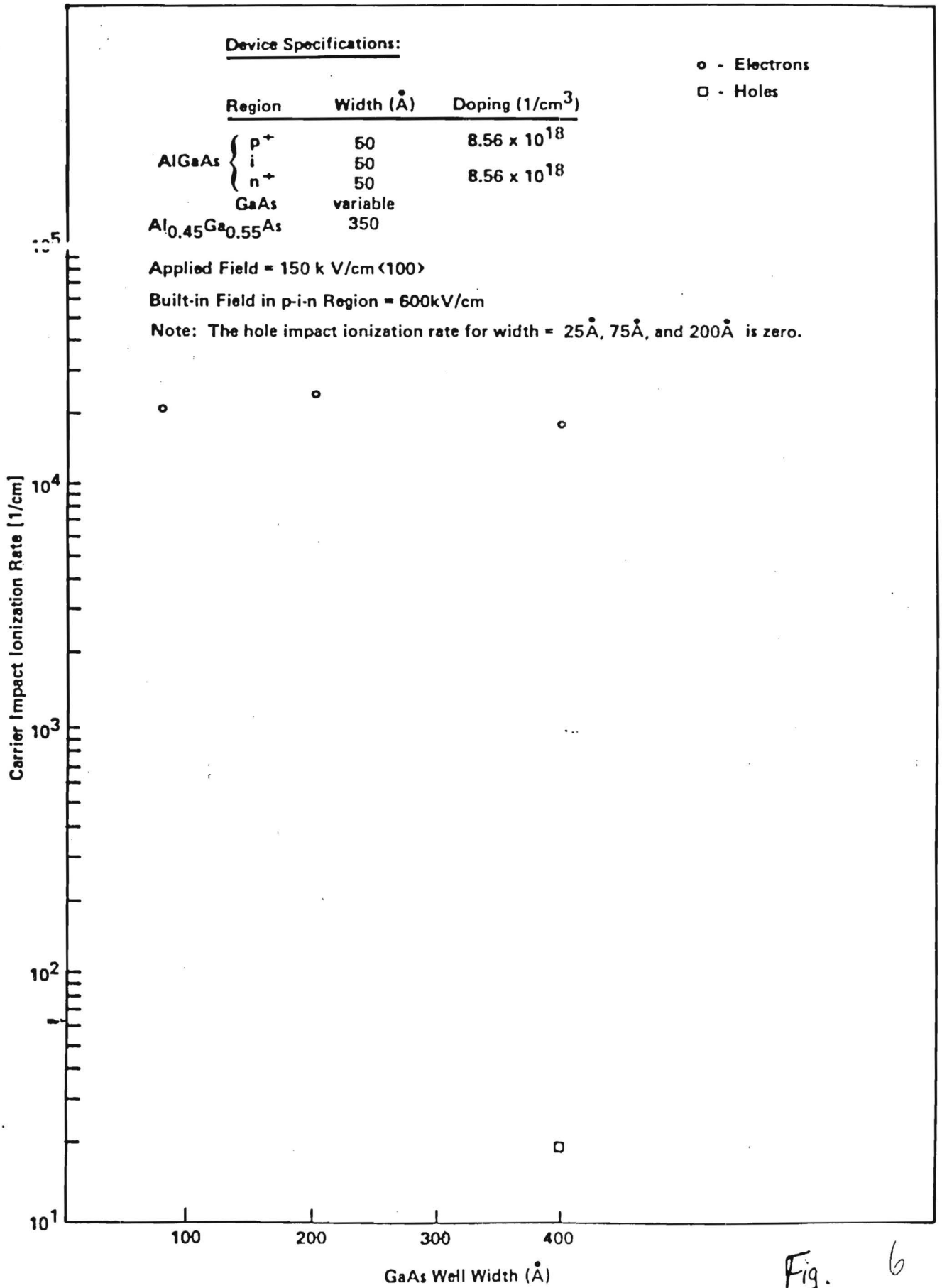
Device Specifications:
o - Electrons
□ - Holes
Region | Width (Å) | Doping (1/cm3)
AlGaAs p+ | 50 | 8.56 x 10^18
AlGaAs i | 50
AlGaAs n+ | 50 | 8.56 x 10^18
GaAs | variable
Al0.45Ga0.55As | 350
Applied Field = 150 k V/cm ⟨100⟩
Built-in Field in p-i-n Region = 600kV/cm
Note: The hole impact ionization rate for width = 25Å, 75Å, and 200Å is zero.
Carrier Impact Ionization Rate [1/cm]
10^5
10^4
10^3
10^2
10^1
100
200
300
400
GaAs Well Width (Å)

Fig. 6

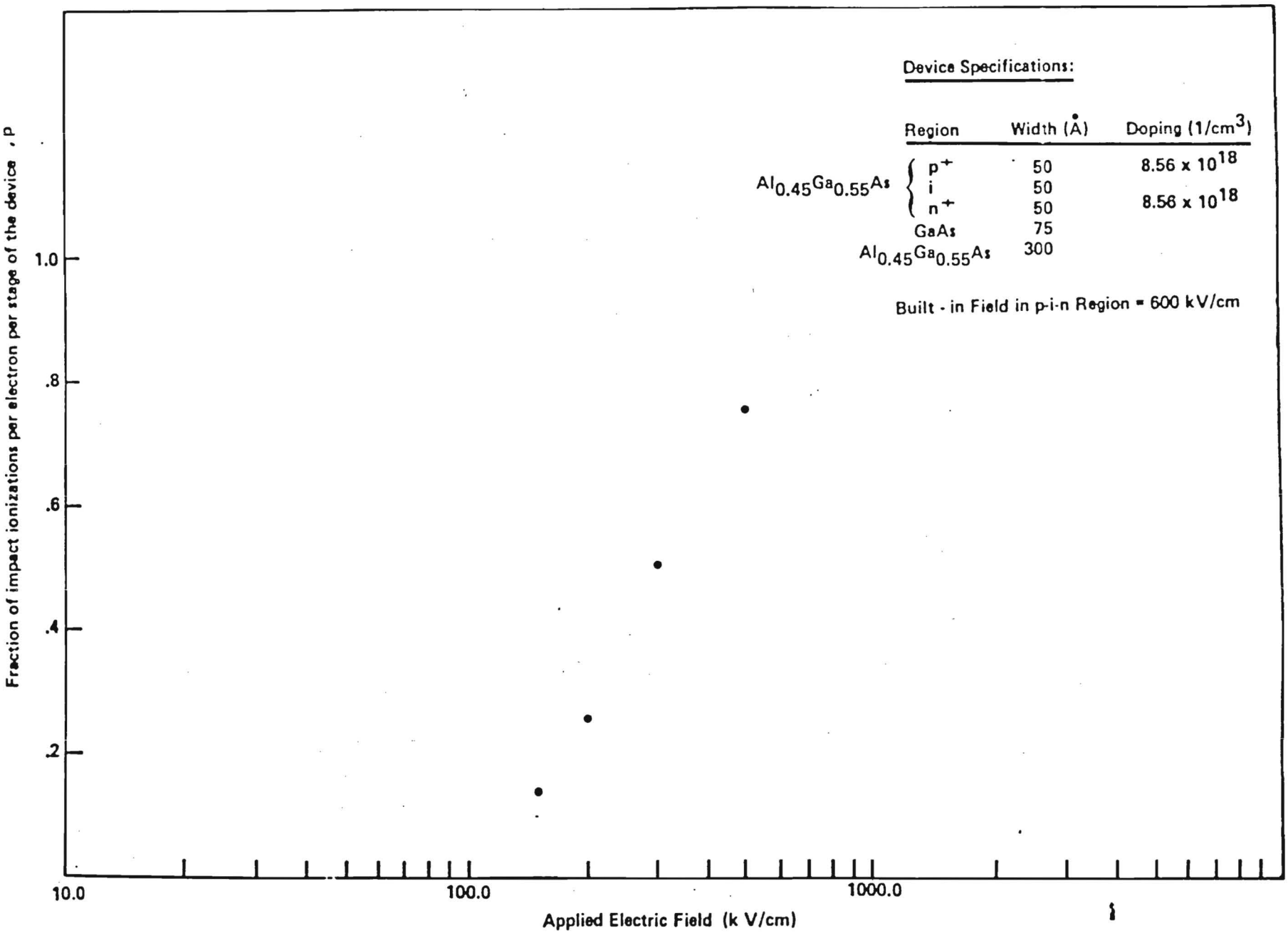
Device Specifications:
Region
Width (Å)
Doping (1/cm3)
Al0.45Ga0.55As
p+
50
8.56 x 10^18
i
50
n+
50
8.56 x 10^18
GaAs
75
Al0.45Ga0.55As
300
Built - in Field in p-i-n Region = 600 kV/cm
Fraction of impact ionizations per electron per stage of the device , P
1.0
.8
.6
.4
.2
10.0
100.0
1000.0
Applied Electric Field (k V/cm)

Fig. 7

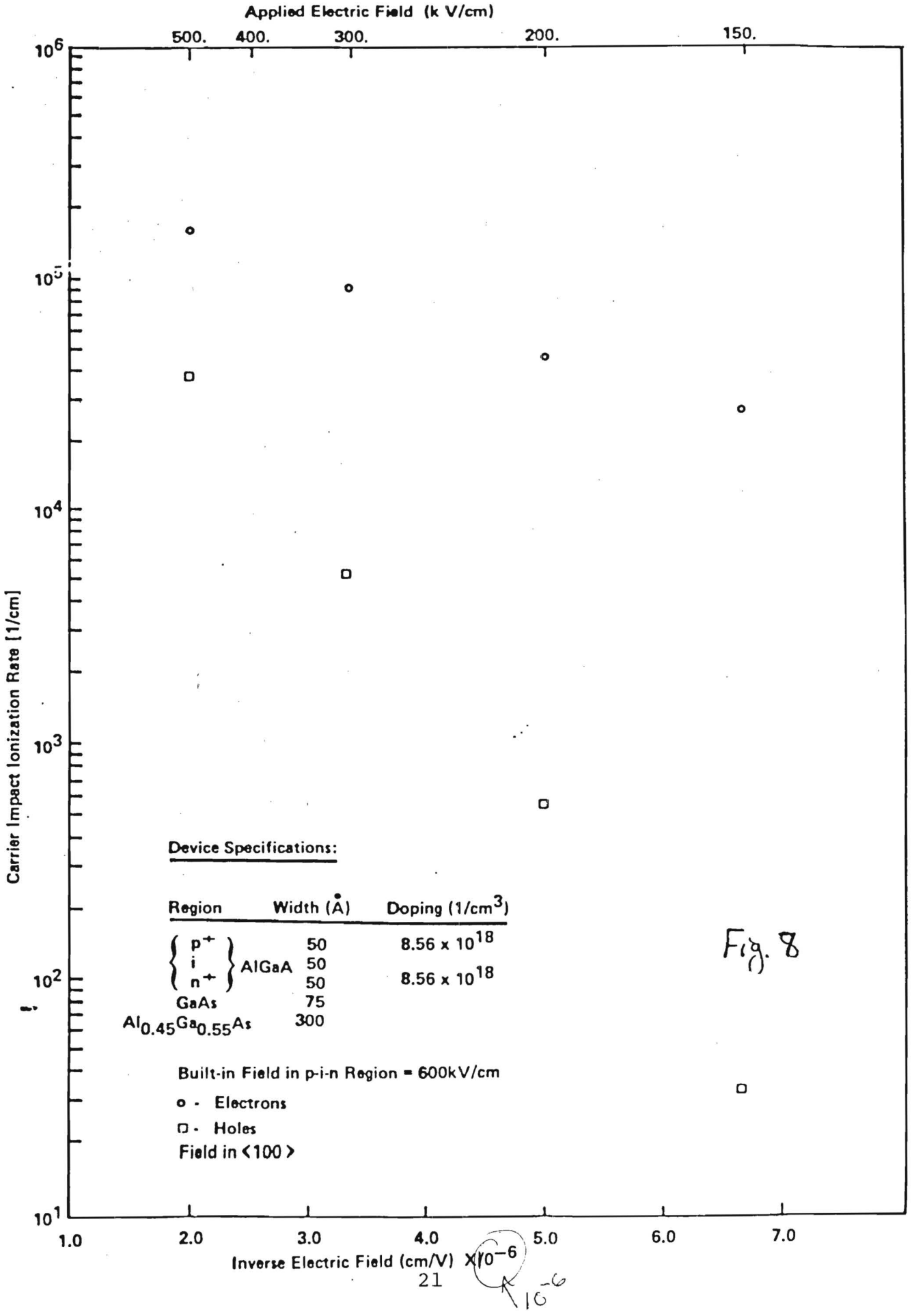
Applied Electric Field (k V/cm)
500.
400.
300.
200.
150.
10^6
10^5
10^4
10^3
10^2
10^1
Carrier Impact Ionization Rate [1/cm]
Device Specifications:
Region
Width (Å)
Doping (1/cm^3)
p+
i
n+
AlGaA
50
50
50
8.56 x 10^{18}
8.56 x 10^{18}
GaAs
75
$Al_{0.45}Ga_{0.55}As$
300
Built-in Field in p-i-n Region = 600kV/cm
o - Electrons
□ - Holes
Field in <100>
1.0
2.0
3.0
4.0
5.0
6.0
7.0
Inverse Electric Field (cm/V) X10^{-6}
10^{-6}

Fig. 8

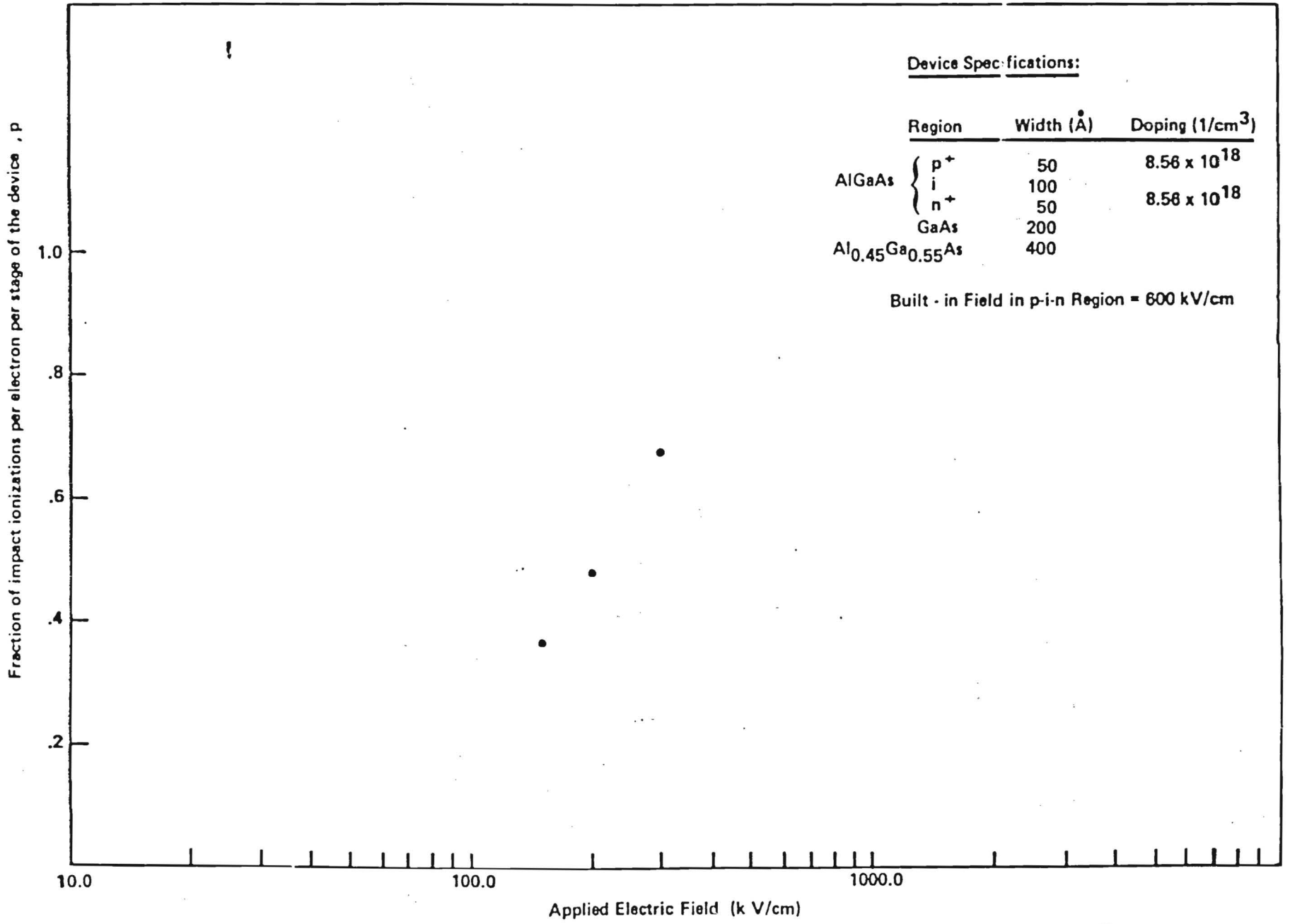
Device Specifications:
Region
Width (Å)
Doping (1/cm3)
AlGaAs
p+
50
8.56 x 10^18
i
100
n+
50
8.56 x 10^18
GaAs
200
Al0.45Ga0.55As
400
Built - in Field in p-i-n Region = 600 kV/cm
Fraction of impact ionizations per electron per stage of the device , p
1.0
.8
.6
.4
.2
10.0
100.0
1000.0
Applied Electric Field (k V/cm)

Fig. 9

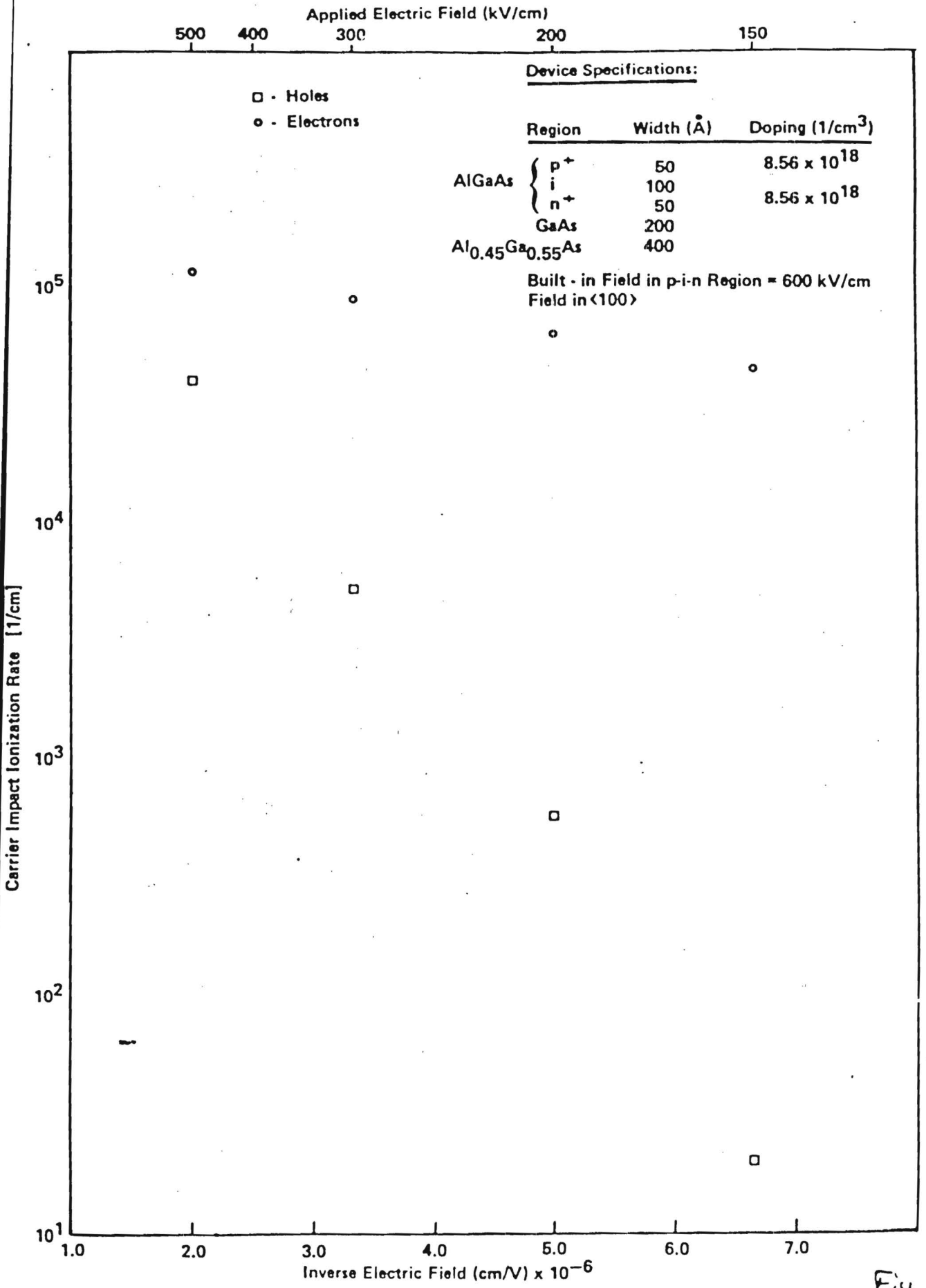
Applied Electric Field (kV/cm)
500
400
300
200
150
□ - Holes
o - Electrons
Device Specifications:
Region
Width (Å)
Doping (1/cm3)
AlGaAs p+ 50 8.56 x 10^18
i 100
n+ 50 8.56 x 10^18
GaAs 200
Al0.45Ga0.55As 400
Built - in Field in p-i-n Region = 600 kV/cm
Field in <100>
Carrier Impact Ionization Rate [1/cm]
10^5
10^4
10^3
10^2
10^1
1.0
2.0
3.0
4.0
5.0
6.0
7.0
Inverse Electric Field (cm/V) x 10^-6

Fig. 10

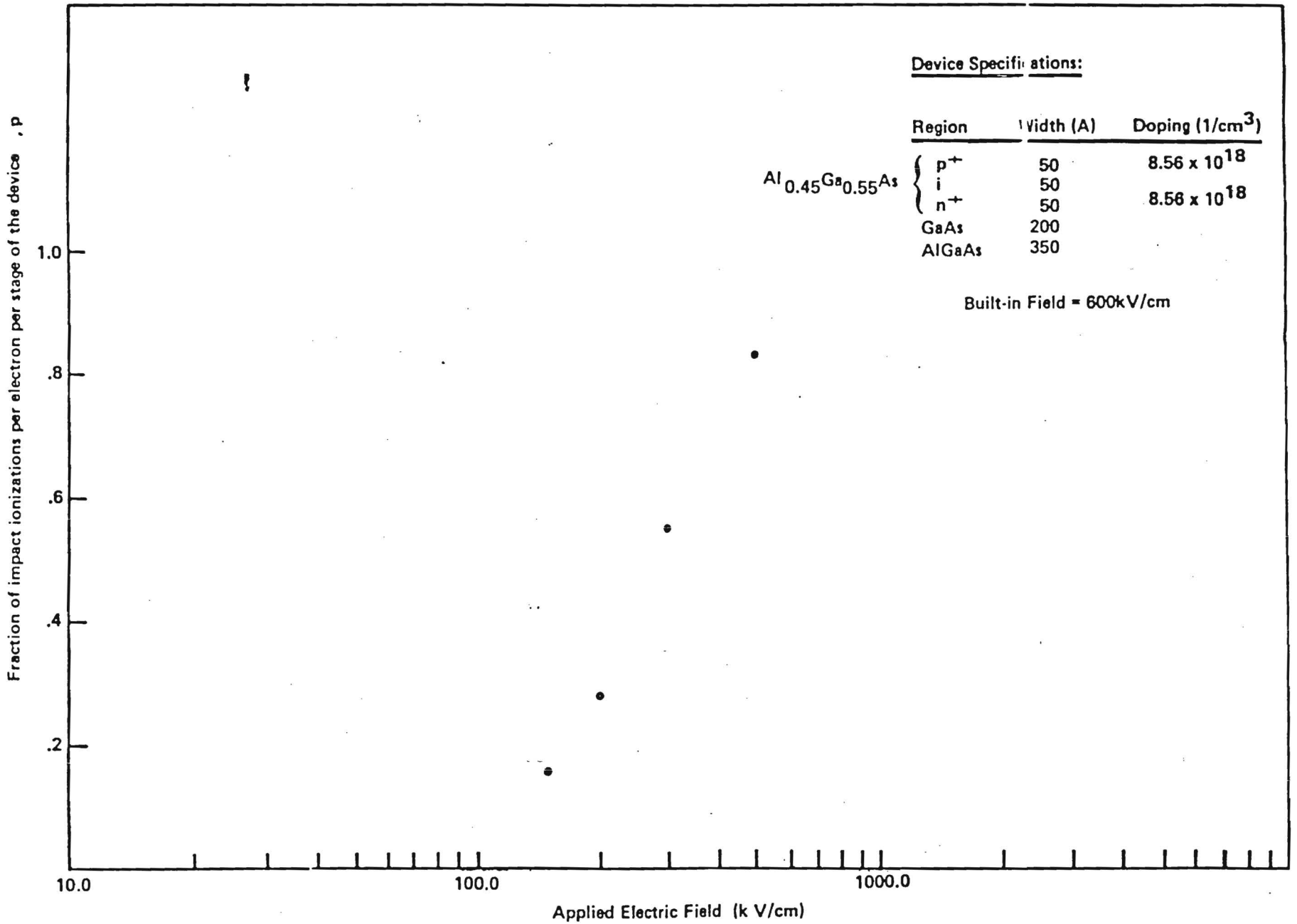
Device Specifi ations:
Region
Width (A)
Doping (1/cm3)
Al0.45Ga0.55As
p+
50
8.56 x 10^18
i
50
n+
50
8.56 x 10^18
GaAs
200
AlGaAs
350
Built-in Field = 600kV/cm
Fraction of impact ionizations per electron per stage of the device , p
1.0
.8
.6
.4
.2
10.0
100.0
1000.0
Applied Electric Field (k V/cm)

Fig. 11

electric field after p^+-i-n^+ layers 10-12 are fully depleted being equal to 600.0 kV/cm;

Fig. 12 shows, in graphical form, the electron and hole impact ionization rates of a doped quantum well APD as a function of inverse electric field;

Fig. 13 shows, in graphical form, the electron energy distribution plotted as function of energy in a doped quantum well APD at an applied electric field of 150.0 kV/cm, the three curves corresponding to the distribution function within high field AlGaAs layer 11, GaAs well layer 13, and low field AlGaAs layer 14;

Fig. 14 shows, in graphical form, the hole energy distribution plotted as function of energy in a doped quantum well APD at an applied electric field of 150.0 kV/cm, the three curves corresponding to the distribution function within high field AlGaAs layer 11, GaAs well layer 13, and low field AlGaAs layer 14;

Fig. 15 and 16 show, in pictorial form, two APDs fabricated in accordance with the present invention; and

Fig. 17 shows, in pictorial form, a flow chart of the Monte Carlo analysis performed to determine the optimal range of parameters for embodiments of the present invention.

To facilitate understanding, identical reference numerals are used to designate elements common to the figures.

Detailed Description

The present invention pertains to a low noise superlattice avalanche photodetector (APD) comprising repeated superlattice units formed from a p^+-i-n^+ $Al_{0.45}Ga_{0.55}As$ region immediately followed by near intrinsic layers of GaAs and $Al_{0.45}Ga_{0.55}As$. By doping the layers as described, i.e., p^+-i-n^+ $Al_{0.45}Ga_{0.55}As$ layers followed by ear intrinsic layers on GaAs and $Al_{0.45}Ga_{0.55}As$, the electric field is made asymmetric in the unit cell. When the APD is reverse biased, electrons are accelerated in a high electric field region before being injected into the GaAs layer, whereas holes are accelerated in a low electric field

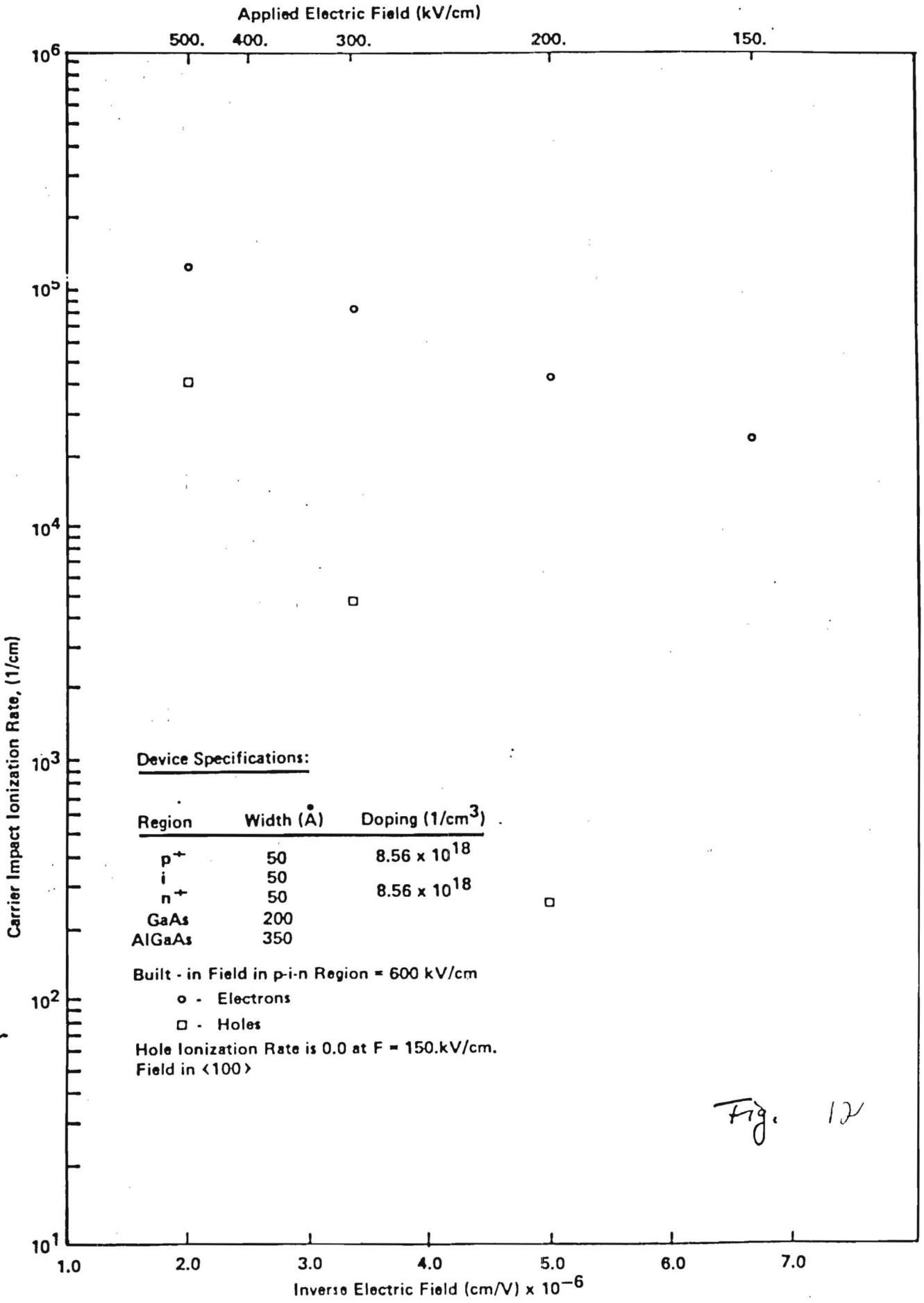

Device Specifications:

Region	Width (Å)	Doping ($1/cm^3$)
p^+	50	8.56×10^{18}
i	50	
n^+	50	8.56×10^{18}
GaAs	200	
AlGaAs	350	

Built - in Field in p-i-n Region = 600 kV/cm

o - Electrons

□ - Holes

Hole Ionization Rate is 0.0 at F = 150.kV/cm.
Field in ⟨100⟩

Fig. 12

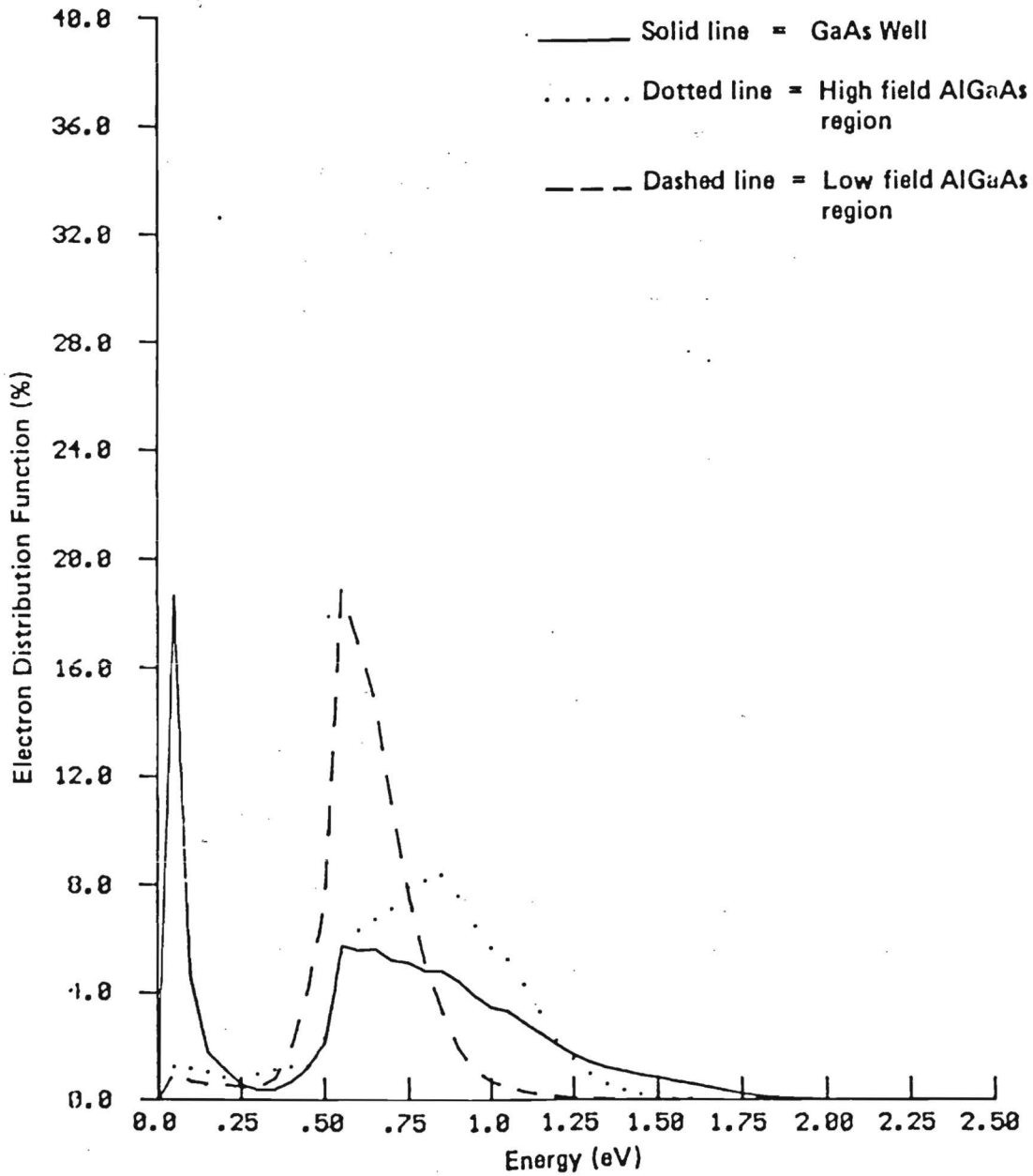
Solid line = GaAs Well
Dotted line = High field AlGaAs region
Dashed line = Low field AlGaAs region
Electron Distribution Function (%)
40.0
36.0
32.0
28.0
24.0
20.0
16.0
12.0
8.0
4.0
0.0
0.0
.25
.50
.75
1.0
1.25
1.50
1.75
2.00
2.25
2.50
Energy (eV)

Fig. 13

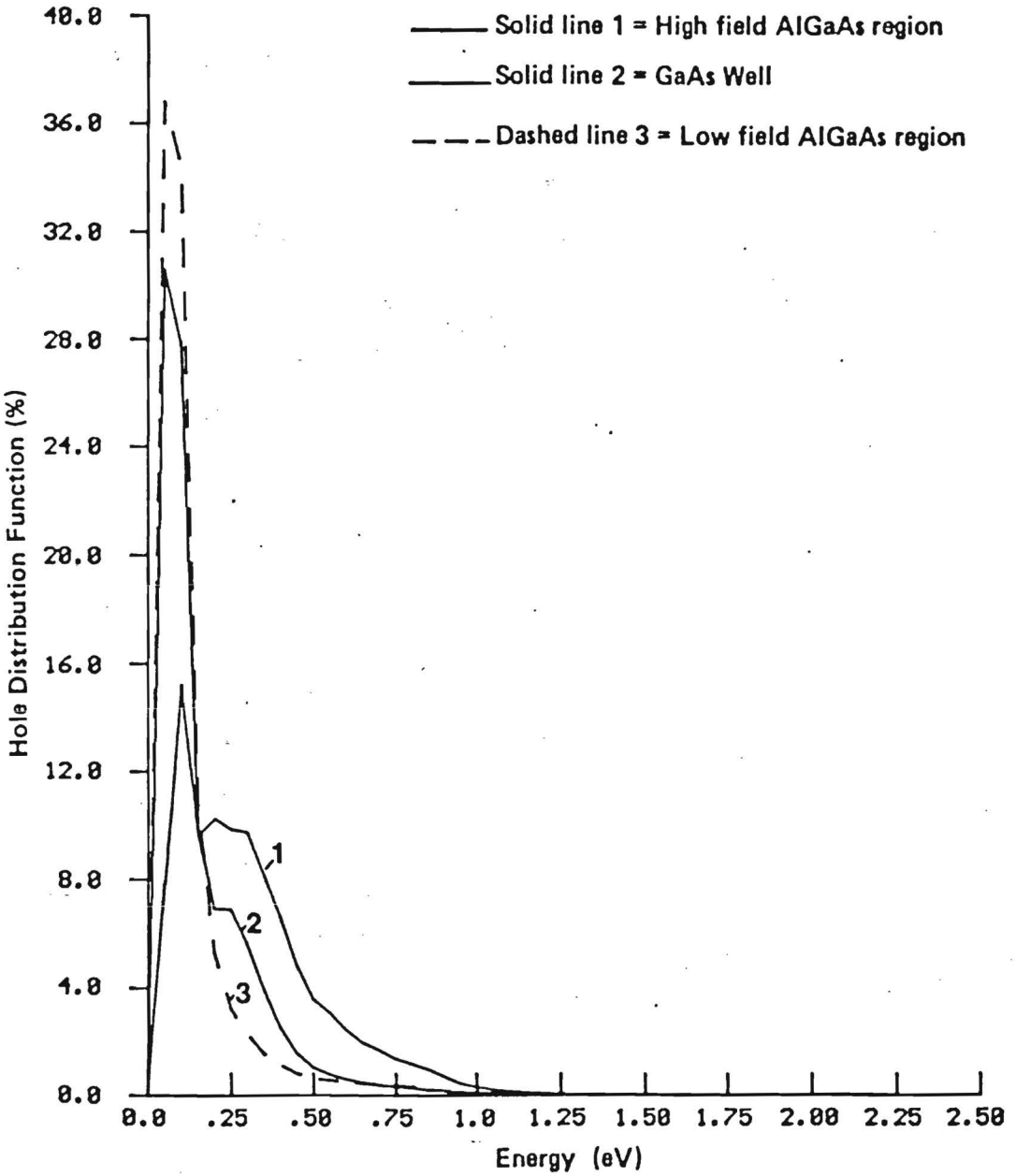
Solid line 1 = High field AlGaAs region
Solid line 2 = GaAs Well
Dashed line 3 = Low field AlGaAs region
Hole Distribution Function (%)
40.0
36.0
32.0
28.0
24.0
20.0
16.0
12.0
8.0
4.0
0.0
0.0
.25
.50
.75
1.0
1.25
1.50
1.75
2.00
2.25
2.50
Energy (eV)
1
2
3

Fig. 14

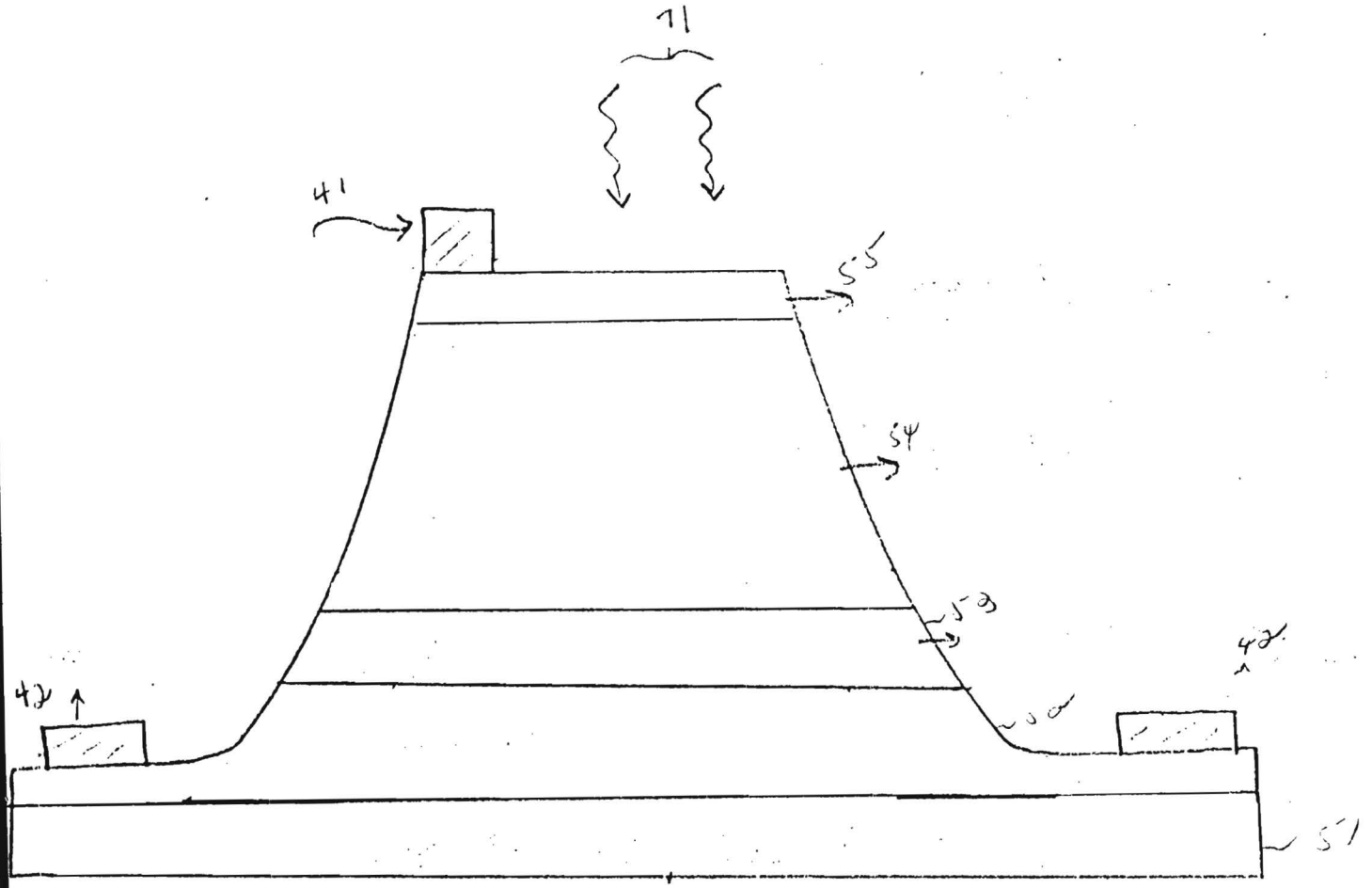

Fig. 15

87

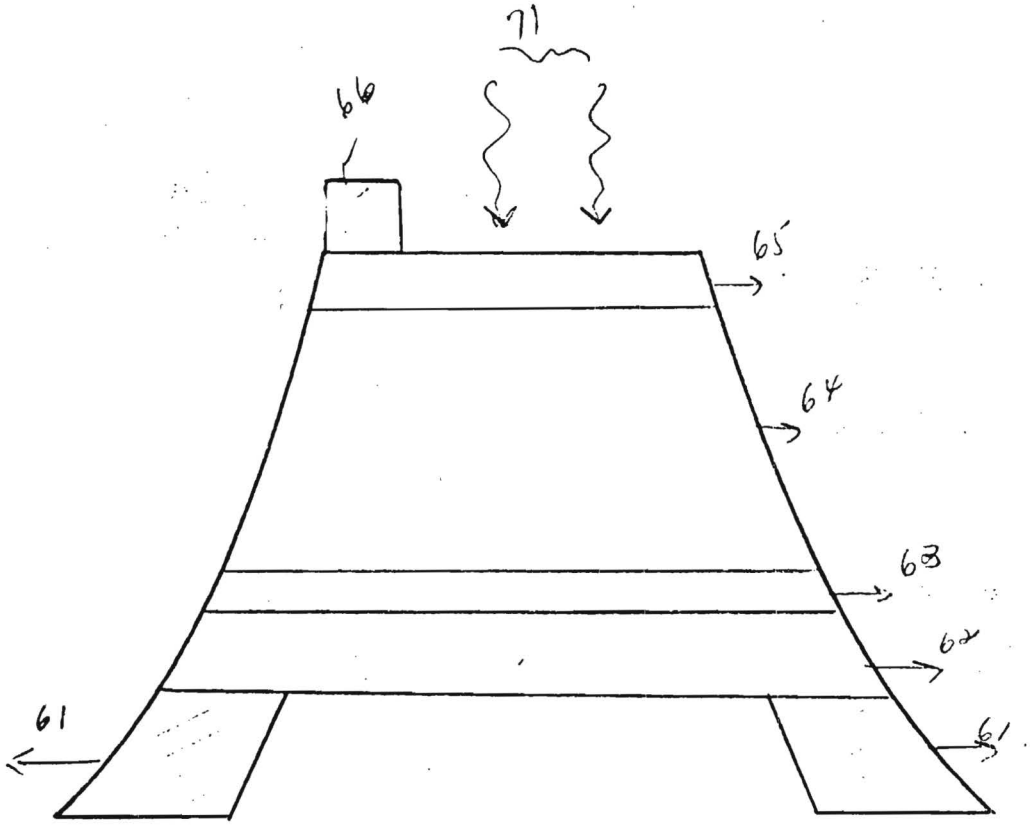

Fig. 16

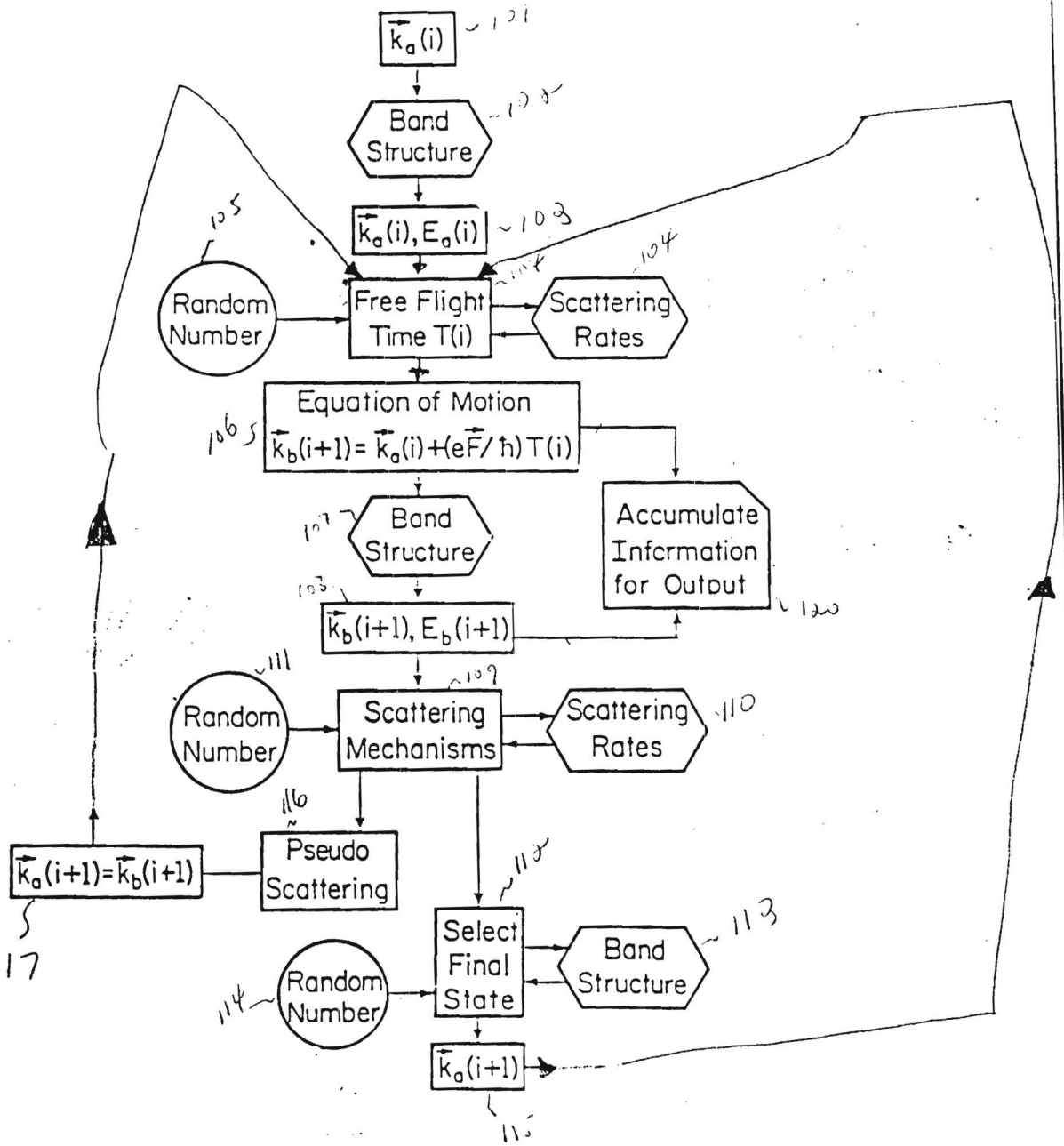
$\vec{k}_a(i)$
Band Structure
$\vec{k}_a(i), E_a(i)$
Random Number
Free Flight Time T(i)
Scattering Rates
Equation of Motion
$\vec{k}_b(i+1) = \vec{k}_a(i) + (e\vec{F}/\hbar)T(i)$
Band Structure
Accumulate Information for Output
$\vec{k}_b(i+1), E_b(i+1)$
Random Number
Scattering Mechanisms
Scattering Rates
Pseudo Scattering
$\vec{k}_a(i+1) = \vec{k}_b(i+1)$
17
Select Final State
Band Structure
Random Number
$\vec{k}_a(i+1)$

FIG. 17

region before being injected into the GaAs layer. The combined action of being accelerated in a high electric field and subsequently being injected over the heterointerface between the AlGaAs and GaAs layers produces very hot electrons within the narrow bandgap GaAs layer. The electrons are sufficiently hot that substantial impact ionization occurs. Conversely, the holes undergo little heating within the low field intrinsic $Al_{0.45}Ga_{0.55}As$ layer before being injected into the narrow bandgap GaAs region and few, if any, impact ionization events occur. The holes do, of course, also drift in the high field p^+-i-n^+ region. However, after that, they enter the low field intrinsic AlGaAs layer where the bandgap is much larger than in the GaAs layer, and in which layer they lose energy before being injected into the narrow bandgap GaAs layer. As a result, the hole ionization rate in the GaAs layer is low. Judicial choices of layer thicknesses and doping concentrations can result in a substantial electron ionization rate and for a negligible hole ionization rate.

I have modeled the doped quantum well APD using a many particle, ensemble Monte Carlo technique which is particularly well adapted for high energy, high field transport. The full details of the GaAs conduction band structure derived from an empirical pseudopotential calculation disclosed in an article entitled "Band Structures and Pseudopotential Form Factors for Fourteen Semiconductors of the Diamond and Zinc-Blende Structures," by M. L. Cohen and T. K. Bergstresser, Phys. Rev., Vol. 141, 1966, pp. 789-796, as well as the full details of both the GaAs and $Al_{0.45}Ga_{0.55}As$ valence band structures derived using a k*p calculation are included in the analysis. Although I did not have the full details of the AlGaAs conduction band structure, it can be modeled from the GaAs and structure by using a modified energy gap and ionization energy. Although the substitution of GaAs in place of AlGaAs may introduce some error both Gamma and L are degenerate in $Al_{0.45}Ga_{0.55}As$ while they are separated by 0.30 eV in GaAs, I expect that the band structures are reasonably similar at the high electron energies where impact

ionization occurs. Nevertheless, the inclusion of the full details of the AlGaAs valence band structure is more crucial to the model analysis since optimal APD performance requires a negligible hole ionization rate. Hole ionization within the high field AlGaAs region, as well as within the GaAs layer, must be avoided. This places constraints on the doping levels and layer widths used in the structure. For example, I have discovered that significant hole ionization occurs within bulk $Al_{0.45}Ga_{0.55}As$ for applied electric fields at or above 300 kV/cm.

I have included the following electron and hole scattering mechanisms in the model calculations: polar scattering, deformation potential, carrier-carrier, impact ionization, and alloy scattering within the AlGaAs. I treated impact ionization as a scattering mechanism in accordance with an article entitled "Concerning the Theory of Impact Ionization in Semiconductors," by L. V. Keldysh, Zh. Eksp. Teor. Fiz., 1965, Vol. 48, pp. 1692-1707, Soviet Physics. - JETP, 1965, Vol. 21, pp. 1135-1144. As a control for the calculations, I first calculated both the bulk GaAs and AlGaAs electron and hole impact ionization rates and compared them to existing data from an article entitled "Experimental Determination of Impact Ionization Coefficients in (100) GaAs," by G. E. Bulman, V. M. Robbins, K. F. Brennan, K. Hess, and G. E. Stillman, IEEE Electron Dev. Lett., Vol. EDL-4, pp. 181-185, 1983. My model is able to isolate the effect of the APD geometry on the ionization rates, doping, layer widths, and so forth, because any difference between the calculated bulk and superlattice ionization rates must be due solely to the presence of the superlattice structure.

The built-in field profile within the p^+-i-n^+ region of layers 10-12 shown in Fig. 2 is calculated from the one-dimensional Poisson equation. From Gauss' law, when the net charge in n^+ layer 12 and p^+ layer 10 is the same, the high field region is completely confined to p^+-i-n^+ layers 10-12. The reverse bias applied by voltage source 33 must be sufficiently large to fully deplete n^+ layer 12 and p^+ layer 10. Additional reverse bias will only add a constant electric field

perpendicular to the layers which acts to accelerate the carriers through the structure. Upon encountering the GaAs/AlGaAs heterointerface between layers 12 and 13 for electrons and between layers 13 and 14 for holes, the electrons and holes gain a kinetic energy boost equal to the conduction and valence band edge discontinuities, respectively. The band edge offsets are chosen in accordance with the 60/40 rule disclosed in an article entitled "Energy-Gap Discontinuities and Effective Masses for GaAs-AlGaAs Quantum Wells," by R. C. Miller, D. A. Kleinman, ad A. C. Gossard, Phys. Rev. B., Vol. 29, 1984, pp. 7085-7087 and an article entitled "Parabolic Quantum Wells with the GaAs-$Al_xGa_{1-x}As$ System," Phys. Rev. B Vol. 29, 1984, pp. 3740-3743.

For the GaAs/$Al_xGa_{1-x}As$ material system the energy bandgaps are 1.42 eV and 1.99 eV, respectively. Using the 60/40 rule, the conduction band energy difference at the heterointerface is .347 eV, whereas the valence band energy difference at the heterointerface is .213 eV. The large energy difference at the valence band shows why it is so important to cool the holes before they impinge upon the GaAs ionization layer.

For small GaAs well widths, i.e., widths of GaAs layer 13 that are less than 200 angstroms, spatial quantization effects become important. As is well known, spatial quantization introduces subbands within a quantum well that lie above the conduction band minimum [reference Dingle]. The carriers can thermalize no lower in energy than the first subband rather than at the conduction band minimum. The subbands are calculated from a solution of the Schrodinger Equation for a finite square well. Since the barrier region--the separation distance between adjacent wells, i.e., the distance between layer 13 in adjacent superlattice units--, is very large, I neglected tunneling effects between wells. For simplicity, I only considered the effect of the first subband. Spatial quantization has two important effects on electron and hole transport in the APD. First, the effective barrier height is reduced when subbands are present, thus, carriers gain less energy from the heterointerface. Second, the effective threshold energy for

impact ionization is larger than in the bulk since the effective bandgap is increased. I included both of these effects in my calculations.

The principal equation governing transport phenomena in a solid is the Boltzmann Transport Equation. However, in a complicated system like a solid, the Boltzmann equation is exceedingly difficult to solve while at the same time retaining the essential physics of the process. Thus, its general solution requires a numerical approach such as the Monte Carlo method. I have developed a Monte Carlo analysis that simulates the flight of electrons in semiconductor materials and devices and which includes a realistic band structure for the semiconductor, i.e., I used the full details of the band structure derived from a pseudopotential calculation.

Fig. 17 shows, in pictorial form, a flow chart of the Monte Carlo analysis I performed to determine the optimal range of parameters for embodiments of the present invention. An initial momentum and position is chosen at box 101. Since I am looking at a steady state solution, the method I used to choose the initial state is irrelevant, for example in this case I used a Maxwell-Boltzmann distribution. However, if one were to compute a transient response for the APD, a more appropriate choice for an initial state might entail use of the Fermi-Dirac distribution.

The corresponding energy is then computed from the band structure at box 102 and shown at box 103. The detailed band structure is numerically used to provide an accurate conversion from momentum to energy. A free flight time T(i) is computed at box 104 by utilizing a random number and a representative scattering rate determined from a composite of the scattering rates for all the competing physical scattering mechanisms. The free flight time T(i) is used to compute a new momentum in box 106 from the following semiclassical equation of motion:

$$k_f = k_1 + (eF_{ext}/\hbar)T(i) \qquad (7)$$

where E_{ext} is the effective external force on a carrier, including the electric field. The electric field includes the applied electric field and the force due to the doping and is shown in Fig. 2.

The energy is computed from the band structure, as before, in boxes 107 and 108. The results produced in boxes 106 and 108 are accumulated for output.

In box 109, a determination is made as to whether the carrier scatters by considering the scattering rates for the various scattering mechanisms from box 110 along with a random number from box 111. If the carrier does not scatter, it is assumed to continue to drift under the action of the electric field. In the flow chart this is indicated by branching to boxes 116 and 117 and then returning back to box 104. If the carrier is predicted to scatter at box 109, control transfers to box 112. There, the scattering mechanism is chosen stochastically by using a random number from box 114 and the comparative strength of the scattering process. Box 112 determines the final state momentum from the physics of the scattering mechanism itself and the band structure input from box 113. The momentum of the scattered carrier is transmitted to box 115 and control returns to box 104 for iteration.

The Monte Carlo simulation then proceeds to accumulate such information in box 120 as average energy, velocity and impact ionization rate until a steady state is achieved. Steady state, in the context of these calculations, occurs when the accumulators all average to constant values. For most of the calculations performed, many carriers, for example 1000-1500, are simulated simultaneously for up to 10 psec of travel time and yield excellent convergence to a steady state.

As discussed above, an ideal, noiseless, solid-state photodetector should have a negligible hole ionization rate while, P, the fraction of impact ionizations per electron per stage, only those which ionize within the GaAs layer are

important, should be as close to one as possible.

Table 1 shows how "α", "β", and p vary with doping levels in a doped quantum well structure at fixed layer widths.

Table 1 - EFFECT OF DOPING LEVELS ON "α", "β" and p

A. Layer	Width (angstroms)	Doping (cm^{-3})
p^+	50	6.42×10^{18}
AlGaAs i	50	---
n^+	50	6.42×10^{18}
GaAs	200	---
$Al_{0.45}Ga_{0.55}As$	350	---

built-in field p-i-n layers 10-12 = 450 kV/cm

Carrier	Field (kV/cm)	% Imp. Ion. in GaAs	p	Dist. Traveled From Interface before Ionizing (ang.)	(cm^{-3})
Electrons	200.	100.	.154	44.8	2.4×10^4
Holes	200.	100.	---	---	3.0×10^2

B. Layer	Width (angstroms)	Doping (cm^{-3})
p^+	50	8.56×10^{18}
AlGaAs i	50	---
n^+	50	8.56×10^{18}
GaAs	200	---
$Al_{0.45}Ga_{0.55}As$	350	---

built-in field p-i-n layers 10-12 = 800 kV/cm

Carrier	Field (kV/cm)	% Imp. Ion. in GaAs	p	Dist. Traveled From Interface before Ionizing (ang.)	(cm^{-3})
Electrons	200.	100.	.28	44.8	4.35×10^4
Holes	200.	100.	---	---	2.7×10^2

C.

Layer		Width (angstroms)	Doping (cm^{-3})
	p^+	50	1.04×10^{19}
AlGaAs	i	50	---
	n^+	50	1.04×10^{19}
GaAs		200	---
$Al_{0.45}Ga_{0.55}As$		350	---

built-in field p-i-n layers 10-12 = 800 kV/cm

Carrier	Field (kV/cm)	% Imp. Ion. in GaAs	p	Dist. Traveled From Interface before Ionizing (ang.)	(cm^{-3})
Electrons	200.	100.	.415	31.98	6.31×10^4
Holes	200.	97.2	---	---	6.64×10^2

As the built-in field within p^+-i-n^+ layers 10-12 increases, at fixed applied field throughout, p increases dramatically. In addition, the average distance the electrons travel from the heterointerface before impact ionizing decreases The increase in p is due to the increase in the number of lucky-drift electrons within GaAs layer 13. The electrons are "superheated" by the electric field in p^+-i-n^+ layers 10-12 such that their distribution is greatly shifted in energy. Immediately thereafter, the electrons are injected into GaAs well layer 13. Upon crossing the heterointerface, the electrons overshoot their

steady state energy, i.e., they gain more energy from the field than is lost to phonons, and they are accelerated semiballistically to energies at or above the ionization threshold energy. In this way, the electron ionization rate within GaAs layer 13 is greatly increased from its bulk value. However, As can be seen in Table 1, as p increases through the action of the built-in field, so does the hole ionization rate also increase. Consequently, a tradeoff exists between the hole ionization rate and p, i.e., the favorable increase in p is offset by the unfavorable increase in "β". This shows that an optimal device design exists, i.e., one which maximizes p and minimizes "β".

The following shows how p, "α", and "β" depend upon the width of AlGaAs high field region layer 11, the width of GaAs well layer 13, and the overall applied electric field.

Fig. 3 shows the dependence of p upon the width of high field intrinsic AlGaAs layer 11. All the other parameters, including the electric field are held constant at the values listed in Fig. 3. p clearly shows a maximum at a layer width of 200 angstroms. This can be understood on a physical basis as follows: The "superheating" of the electron distribution depends upon the width of the p^+-i-n^+ layers 10-12. When the width of p^+-i-n^+ layers 10-12 is small, the net energy gain from the electric field per electron is not large. As a result, most electrons do not impact ionize upon being injected into adjacent GaAs layer 13. As the width of layer 11 increases, however, more electrons become hot enough so that upon being injected into GaAs layer 13, they impact ionize. However, if the width of p^+-i-n^+ layers 10-13 becomes too large, the electron impact ionization will occur within high electric field AlGaAs layer 11. Then the number of electrons which impact ionize within GaAs well layer 13 decreases, resulting in a lower value of p.

Fig. 4 illustrates how "α" and "β" depend upon the width of high field AlGaAs layer 11. Holes are heated in high field layer 11, along with electrons. As a result, there is a substantial increase in the hole impact ionization rate as the width of layer

11 increases. In addition, most hole impact ionization events occur within GaAs layer 13. This is so even though the holes are not immediately injected into GaAs layer 13 from the high field region of layers 10-12. Even though holes have to pass through the cooling region of low field AlGaAs layer 14, the cooling within layer 14 is insufficient to totally reduce the hole ionization rate. Moreover, an increase in the width of high field layers 10-12, also results in hole ionization within AlGaAs layers 10 and 12.

Fig. 5 shows the dependence of p upon the width of GaAs well layer 13. For small widths of GaAs well layer 13, p is small, <0.10. The electron ionization rate is also less in very narrow width GaAs layer 13 devices as shown in Fig. 6. As discussed above, the effect of spatial quantization acts to reduce the electron ionization rate through the increase in the ionization threshold energy and the decrease in the effective heterointerface barrier height. Consequently, the peak values of both p and "α" occur when the width of GaAs well layer 13 is sufficiently large that quantization effects are less important, i.e., approximately 200 angstroms. As the width of GaAs layer 13 increases further, p and "α" both decrease since the electrons are cooled more effectively by drifting within a now larger total low electric field region. As can be seen in Fig. 6, the hole ionization rate is effectively zero for all values of the width of GaAs layer 13. The small ionization rate calculated for a 400 angstrom wide GaAs well layer 13 is statistically insignificant.

As the width of the low field region increases, either through increasing the width of GaAs well layer 13 or low field $Al_{0.45}Ga_{0.55}As$ layer 14, the electron and hole ionization rates decrease. The low field region of layers 13-14 cool both the electron and hole distributions. As can be seen in Table 2, the hole ionization rate decreases more with increasing width of the low field region than does that of the electrons. The hole energy relaxation rate is much larger than the electron relaxation rate. Consequently, the holes relax faster to the corresponding low field steady state distribution.

Table 2 - DEPENDENCE OF "α", "β", AND P ON THE WIDTH OF THE LOW FIELD AlGaAs LAYER

Layer	Width (angstroms)	Doping (cm^{-3})
p^+	50	8.56×10^{18}
AlGaAs i	50	---
n^+	50	8.56×10^{18}
GaAs	200	---
$Al_{0.45}Ga_{0.55}As$	variable	---

Carrier	AlGaAs Layer Width (ang.)	"α" or "β" (cm^{-3})	p
Electrons	100	2.92×10^4	.153
Electrons	350	2.4×10^4	.157
Electrons	100	1.6×10^4	.156
Holes	100.	5.25×10^2	---
Holes	350	0.0	---
Holes	700	3.8×10^1	---

In summary, several design trade-offs exist in the doped quantum well APD of the present invention. It is desirable to highly dope the p^+-i-n^+ layers 10-12 to produce an extremely large electric field. However, too large an electric field results in a large hole impact ionization. Likewise, there exists an optimal length for the high field intrinsic layer 11 such that hole ionization does not occur, yet significant electron heating does, resulting in a substantial increase in p. Spatial quantization effects should be avoided in GaAs well layer 13. However, as the widths of GaAs layer 13 and low field AlGaAs layer 14 increase, the electron impact ionization rate decreases, owing to the cooling effects within the low field region of layers 13-14.

In Figs. 7-12, the effect of the applied electric field upon

p, "α", and "β" is examined for three different APD configurations. In all three APDs, as the electric field increases, p increases dramatically. Simultaneously, "α" and "β" increase as well. Fig. 11 shows that p greater than 0.8 is attained at a field of 500.0 kV/cm. Figs. 7-12 show that a large value of p, approaching a fully deterministic electron ionization, is inconsistent with a simultaneously negligible hole ionization rate in the GaAs/AlGaAs material system. The conduction band edge discontinuity at the GaAs/AlGaAs heterointerface is not a large fraction of the band gap energy. As a result, the electrons are not sufficiently heated upon being injected into GaAs well layer 13 to cause impact ionization to occur. Attempts to further heat electrons through use of high field p^+-i-n^+ layers 10-12, result in substantial increase in "β" as well. I expect that a material system where the energy difference in the conduction band discontinuity is a greater fraction of the bandgap energy in the narrow bandgap layer, e.g., layer 13, will provide a better medium for an ideal, photomultiplier-like device. An example of such a material system is $Al_xIn_{1-x}As/Ga_yIn_{1-y}As$.

Figs. 13 and 14 show the electron and hole energy distribution functions in GaAs layer 13, low field AlGaAs layer 14, and within high field AlGaAs layer 11 for the APD described in Figs. 11 and 12 at an applied field of 150.0 kV/cm. As can be seen from Fig. 13, the electron distribution within GaAs quantum well layer 13 has two peaks, one at very low energy and another at approximately 0.60 eV. The low energy peak is due to the electrons which have impact ionized after transferring into GaAs layer 13. The impact ionization process acts to greatly cool the superheated distribution and results in many low energy electrons in the well of layer 13. The long tail in the electron distribution is due to exceptionally hot carriers being injected into the well of layer 13. Note that the tail of the distribution extends well beyond the ionization threshold energy of 1.55 eV since I assume a "soft" threshold. As shown in the figures, and as is expected, the electron distribution is cooled

considerably within low field AlGaAs layer 14. The high electric field with p^+-i-n^+ layers 10-12 heats the electrons but the distribution is still cooler than that in the corresponding GaAs layer 13. The difference being due to the additional kinetic energy boost from the GaAs/AlGaAs heterointerface upon entering GaAs layer 13.

The hole energy distribution is presented in Fig. 14. Contrary to the case for the electrons, the holes are hottest within high field AlGaAs layer 11. The hole distribution is much cooler within GaAs well layer 13 since the holes are injected thereinto from low field AlGaAs layer 14. Even though the tail of the hole distribution crosses the ionization threshold, the hole ionization rate is negligible since the threshold is "soft". It is important to notice that the ionization events do not necessarily occur when the distribution tail exceeds the threshold energy. The likelihood of an ionization event also depends upon how long a carrier remains at or near the threshold. This is a function of scattering rate.

As a result of the above-described analysis of the doped quantum well superlattice APD, I have determined the following to be an optimal set of parameters:

1. doping of p^+ layer 10 and n^+ layer 12

the optimal doping lies in the range between 7×10^{18} cm^{-3} and 1×10^{19} cm^{-3}.

2. width of layers in the high field p^+-i-n^+ region of layers 10-12

(a) the most important width is that of intrinsic AlGaAs layer 11, it should have a width in the range between 50 and 100 angstroms

(b) the widths of p^+ layer 10 and n^+ layer 12 should be as small as possible but should enclose a large amount of charge and should both be in the order of 50 angstroms

3. width of GaAs well layer 13

the optimal width lies in the range between 180 and 300 angstroms. Very small widths result in quantum mechanical spatial quantization effects which are deleterious to device performance by causing two effects, both of which effects act to reduce "α" and p:

(a) as the layer width decreases, spatial quantization levels lie at higher energies. Consequently, the effective barrier height decreases and the impact ionization threshold energy increases.

(b) too large a layer width acts to reduce "α" because fewer ionizations occur per unit length

4. width of low field AlGaAs layer 14

the optimal width lies in the range between 200 and 500 angstroms. It is important to have a sufficiently long region so that holes can cool after crossing from the p^+-i-n^+ layers 10-12 before entering GaAs layer 13. However, if layer 14 is too long, as described above, "α" will be reduced.

5. applied electric field

the optimal applied electric field lies in the range between 100 and 200 kV/cm

6. percentage of Al in the $Al_xGa_{1-x}As$ composition

the optimal percentage lies in the range between .40 to .45 or wherever the transition between the direct/indirect band energy transition occurs. This range will provide the largest difference between the conduction band edges of the GaAs and the AlGaAs.

Figs. 15 and 16 show, in pictorial form, two devices fabricated in accordance with the present invention.

Fig. 15 shows APD 87 being fabricated upon GaAs semi-insulating substrate 51, for example a Cr-doped (001) oriented semi-insulating GaAs substrate. Illustratively, APD has a mesa geometry. n^+ GaAs layer 52 is epitaxially grown upon substrate 51 by liquid phase epitaxy (LPE) or by molecular beam epitaxy

(MBE); typically n^+ layer 52 is doped with Si. Layer 52 is etched to permit the deposition of metal electrode 42 thereon and is highly doped to enable a low resistance connection to metal electrode 42 and a low voltage drop between the electrode and superlattice 54. Metal electrode 42 may comprise an Au-Ge alloy which is sintered onto layer 52. n-type GaAs layer 53 is epitaxially grown on layer 52. The widths of GaAs layers 52 and 53 depend only on the frequency response of the device. Otherwise, the widths can be taken to be whatever is necessary for proper doping, metallization and mechanical stress support.

Superlattice 54 is epitaxially grown by MBE on layer 53. Superlattice 54 comprises a multiplicity of units of p^+-i-n^+ AlGaAs layers 10-12, intrinsic GaAs layer 13 and intrinsic AlGaAs layer 14 shown in Fig. 1. The widths of the layers in each unit of superlattice 54 are taken from the optimal parameters set forth hereinabove. The number of units to be used in any particular device depend on the frequency response of the device--the higher the frequency response, the fewer the number of units--and the desired gain of the device. The gain can be simply estimated from:

$$G = (1+p)^N \tag{6}$$

where N = number of units.

Thus, if we want a gain of 1000 when p = .1, then N must be approximately 72. Because the p^+ and n^+ layers of p^+-i-n^+ layers 10-12 of the superlattice unit are heavily doped, almost all the voltage drop across the unit occurs across the intrinsic region. In addition, the voltage depletes the p^+-i-n^+ region and provides a uniform field in the intrinsic region.

p^+ $Al_{0.45}Ga_{0.55}As$ layer 55 is epitaxially grown by MBE on superlattice 54; typically, p^+ layer 55 is doped using magnesium, beryllium, or zinc. Metal contact 41 is deposited on layer 41 and has an aperture to permit incident radiation 71 to impinge

upon layer 55. Layer 55 is heavily doped to enable a low resistance connection to be made to metal electrode 41. The Al concentration in AlGaAs layer 55 depends upon the wavelength of the radiation one desires to detect. The maximum photon energy detectable using the GaAs/$Al_xGa_{1-x}As$ material system is 1.99 eV, corresponding to x = 0.45. The thickness of layer 55 depends upon the absorption coefficient of the material and the material quality, particularly the diffusion coefficient of electrons, and the surface state concentration. The higher the quality the material, the thicker the layer can be. Advantageously, the radiation should be absorbed within a diffusion length of the region where avalanche multiplication takes place; superlattice 54. In practice, the thickness of layer 55 should be approximately .1 to .5 um thick.

Fig. 16 shows another embodiment of the inventive APD. Here, APD 88 is fabricated upon n^+ GaAs substrate layer 62. Metal electrode 61 is deposited directly upon layer 62. Hereinafter, layers 62-65 and electrode 66 are directly analogous to layers 53-55 and electrode 41 of Fig. 15.

Clearly, those skilled in the art recognize that further embodiments of the present invention may be made without departing from its teachings. For example, the teachings could be expanded for use on the AlInAs/GaInAs material system. There, advantage accrues from the fact that the bandgap energies are 1.5 eV/0.7 eV. This produces the desired enhancement in electron kinetic energy as the electron traverses the heterointerface, said enhancement being even greater than that which occurs with the GaAs/AlGaAs material system.

3. MBE GROWTH OF GaAs AND AlGaAs

The Varian Gen II MBE system was received by Georgia Tech in July 1985 and after assembly and checking, accepted in late August. Since then, the system has been prepared for growth and calibrated for the Si-doping of GaAs and the growth of AlGaAs. These procedures are described briefly in the following sections.

3.1 Preparation of MBE Gen II System

The system was put together by factory representatives and after bake out, the pressure in the growth chamber without cooling was in high 10^{-11} Torr. The transition tube and the load lock system had low 10^{-9} Torr pressure. The eight furnaces were individually baked at 700°C in the load lock for 24 to 48 hours. PBN crucibles without cleaning were placed in the furnaces and baked individually at 700°C in the load lock for 24-48 hours. All eight crucibles and furnaces were then placed in the growth chamber and sequentially baked at 1600°C for one hour, 1400°C for two hours, 1200°C for two hours, and 1000°C for two hours. Two of the 40cc downward pointing furnaces were subsequently loaded with preformed, 7 N's purity As slugs obtained from United Mineral and Chemical Company, NY. A 16cc upward looking crucible was filled with 7 N's purity Ga (in frozen slug form) from Alueswisse (Ventran). In another 16cc crucible we placed a few small pieces of aluminum pellets of 5 N purity obtained from Electronic Space Technology, CA. These crucibles were then further baked out. The As at 350°C for one hour, Ga at 1400°C for one hour and Al at 1500°C for one hour.

Finally, the entire MBE and Auger spectroscopy system was baked out for a two week period. The final pressure in the growth chamber was in the 10^{-11} Torr range.

After 20 preliminary experimental runs, the system was loaded with Be of 4.5 N's purity, obtained from Electronic Space Technology, Inc., CA, (this was the highest purity that could be obtained) and with Si of >7 N's purity obtained from Dr. Heiblum of IBM. The Si and Be crucibles were then baked at 1700°C for

one hour and the system was baked for a week before further experiments were performed.

3.2. System Calibration

The system was first calibrated to determine the dependence of the GaAs growth rate at a temperature of 600°C on the Ga flux. For these runs, the P_{AS4}/P_{Ga} ratio was maintained between 15 and 20. As observed from Figure 1, the growth rate increases linearly with Ga flux and a Ga flux of 7.8×10^{-7} Torr is required to establish a growth rate of 1 um/hr. These growth conditions were maintained for all future calibrations involving doping studies and the growth of AlGaAs. In this latter study considerable delays were experienced because the system was delivered without the As_2 crack source. This necessitated using the conventional As_4 sources. These are quite acceptable for GaAs, but their use requires that the AlGaAs alloys be grown at 700°C, approximately 100°C above the usual growth temperature for GaAs and the temperature that can be used for AlGaAs growth using a As_2 source. For temperature above 650°C, the Ga sticking coefficient decreases rapidly with increasing temperature. Thus the growth of AlGaAs with a As_4 source requires very accurate temperature control. Unfortunately, in the new Varian Gen II system the thermocouple used to measure and monitor the sample temperature is physical decoupled from the substrate ensemble in order to allow for sample rotation. As a consequence of this arrangement the growth surface temperature can differ by as much as 60°C from the thermocouple reading. This difference is also very dependent on the properties of the substrate holder and thus can differ appreciably from run to run. This means that because of the strong dependence of the Ga sticking coefficient on temperature above 650°C the Al:Ga ratio can vary significantly unless the substrate temperature is monitored directly. Because of this effect it was not possible to obtain reproducible data, i.e., targeted Al:Ga ratios, in the first set of runs as shown in Figure 2. However, the initial calibration runs taken on the same substrate showed very good agreement as demonstrated by Fig.

3. As a result of these problems a near infrared sensitive optical pyrometer has been installed in the MBE system in a position to directly observe the substrate surface temperature. Also the use of RHEED to monitor temperature related changes in the substrate surface conditions has been employed to obtain an accurate calibration of the surface temperature. These include measurement of the oxide desorbtion temperature at ~580°C and the point of congruent evaporation of GaAs at 640°C. With these procedures, the experimental accuracy and control over the Al:Ga ratio has increased significantly as shown in Figures 4 and 5.

Figure 4 shows the Al/(Al+Ga) ratio or X-value obtained from Auger measurements as a function of the beam equivalent pressure (BEP) of Al for twelve samples grown. The scatter in the data is believed to partly result from the difficulty experienced in obtaining reproducible Auger data in addition to some problems in obtaining stable growth conditions. Figure 5 shows the most recent data obtained for the systems calibration using photoluminescence data. In this figure the peak photoluminescence energy is plotted as a function of the beam equivalent pressure ratio [Al/(Al+Ga)] measured by the flux gauge in the system. For these last seven runs the correlation between sample properties and system parameters is excellent as shown.

In Figure 6, the dependence of the electron-concentration produced in GaAs by doping with Si is shown as a function of the reciprocal temperature of the silicon oven. As observed, the electron concentration has the expected dependence on temperature and demonstrates that we achieved doping levels between 4×10^{18} to $<1 \times 10^{15}$ cm^{-3} for silicon doping. This data was taken 2-3 months ago and indicates that for oven temperatures less than 1350K our background doping level was 7×10^{14} cm^{-3}.

It should be noted that these data were taken on 4-5 um thick layers which were grown on n-type GaAs substrates with a 0.5 um thick buffer layer between the doped layer and substrate. Recently, we have grown a large number of AlGaAs layers and thus expect the system to be cleaner because of the gettering action of Al. This and the use of new types of buffer layers such as

the growth of a series of very fine AlAs-GaAs superlattices within the GaAs buffer layer has produced a significant reduction in the background doping level. GaAs samples grown without Si doping have very high resistivities which makes precise measurement of their electrical properties very difficult. However, the indications are that these samples can be slightly n or p-type. This is a significant result and suggests that the system is very clean. For example, the background conditions for typical MBE systems normally show p-type doping in the 10^{14} cm^{-3} range because of the presence of carbon.

The electrical data obtained so far are listed in Table 1 and show several samples with 77K mobility values exceeding 60,000 cm^2/Vs.

Table 1. Electrical Properties of MBE Grown GaAs:Si at 77K.

Sample	N(cm^{-3})	u(cm^2/Vs)
B86-16	9.9×10^{14}	67,202
B86-14	1.27×10^{15}	61,415
B86-15	2.92×10^{15}	40,328
B86-18	6.43×10^{15}	27,620
B86-11 (undoped)	slightly n-type	$<10^{12}$ cm^{-3}
B86-19 (undoped)	slightly p-type	

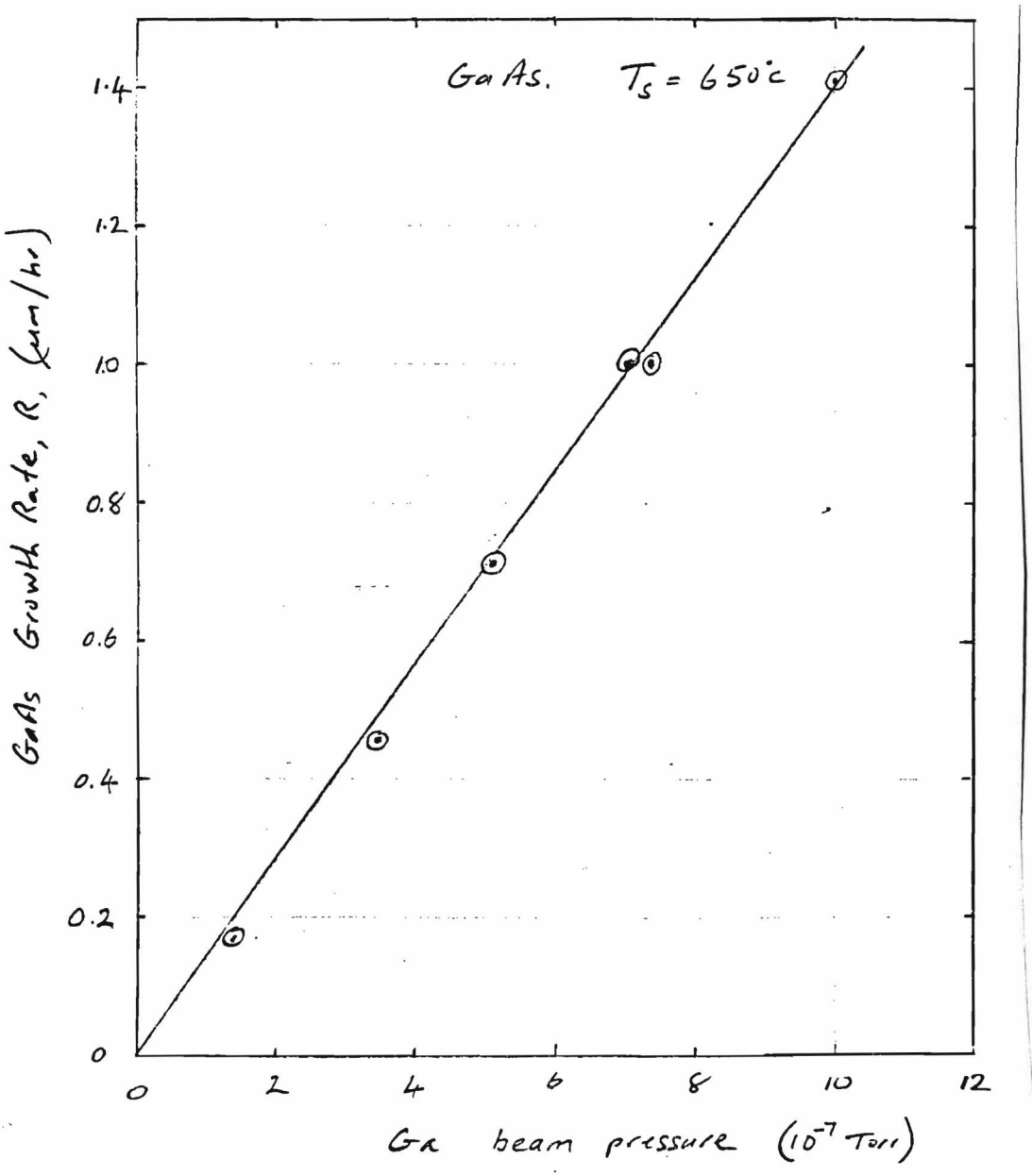
GaAs. T_s = 650°c
GaAs Growth Rate, R, (μm/hr)
1.4
1.2
1.0
0.8
0.6
0.4
0.2
0
0
2
4
6
8
10
12
Ga beam pressure (10^{-7} Torr)

Fig. 1.

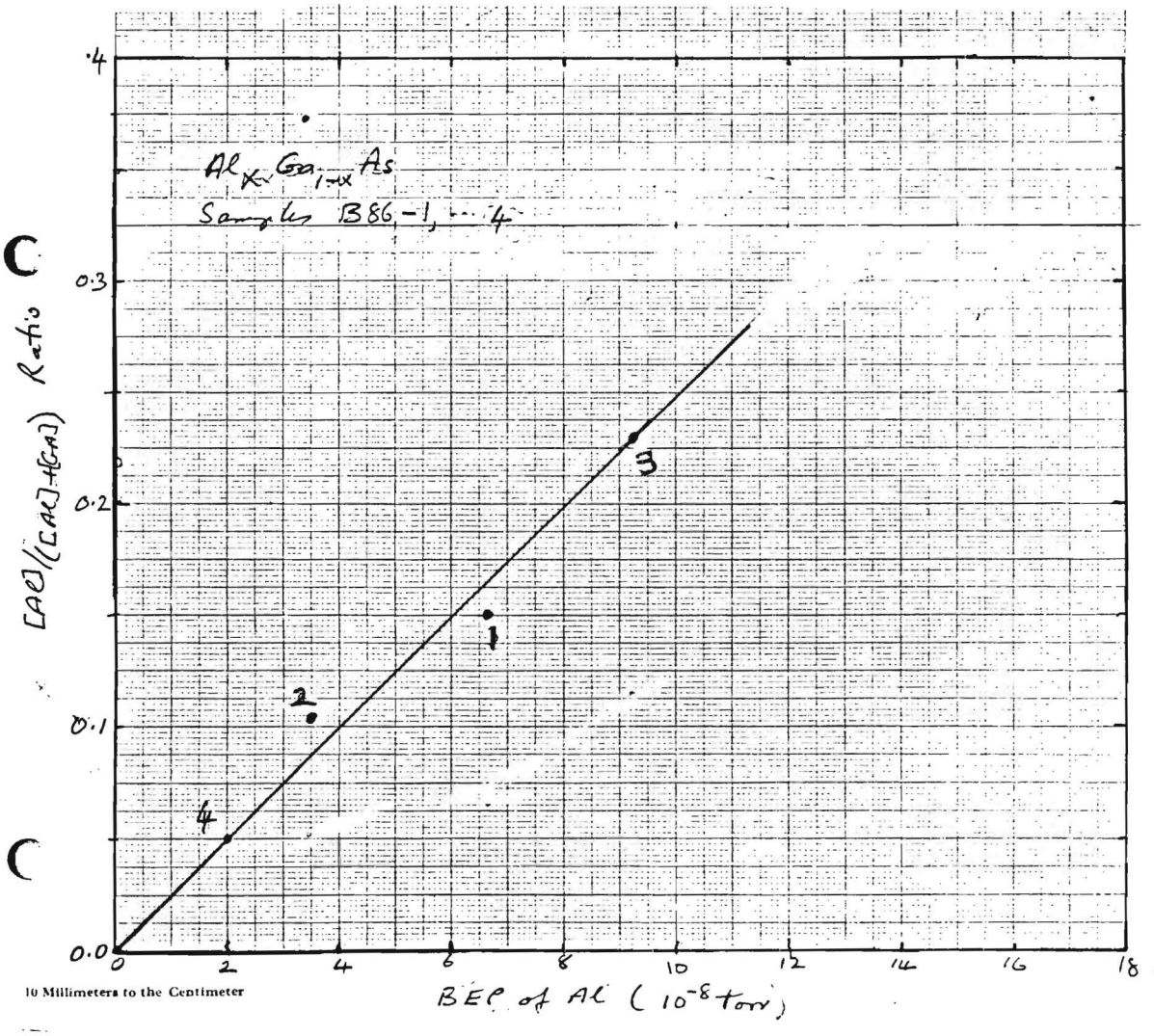
$Al_xGa_{1-x}As$
Samples B86-1, ... 4
[Al]/([Al]+[Ga]) Ratio
0.0
0.1
0.2
0.3
.4
0
2
4
6
8
10
12
14
16
18
BEP of Al (10^{-8} torr)
1
2
3
4
10 Millimeters to the Centimeter

Fig. 2.

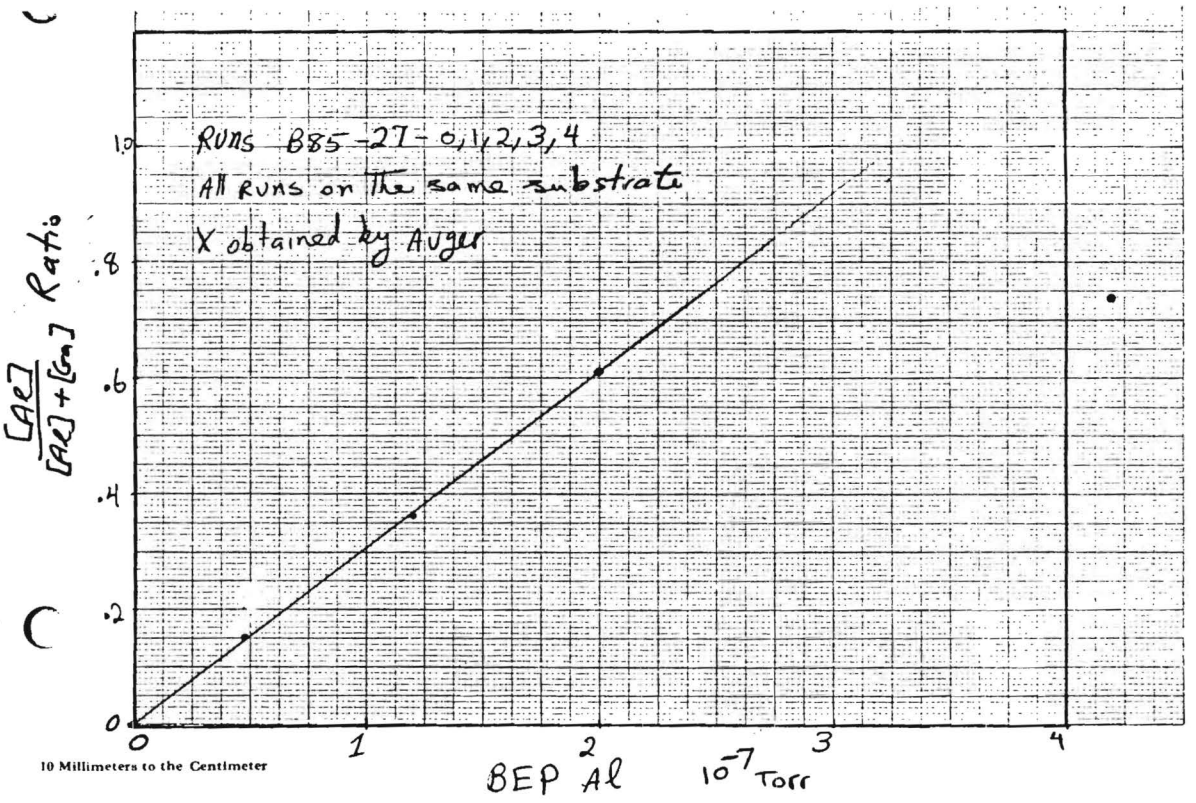
Runs B85-27-0,1,2,3,4
All runs on the same substrate
X obtained by Auger
[Ae] / [Ae] + [Ga] Ratio
1.0
.8
.6
.4
.2
0
0
1
2
3
4
BEP Al 10⁻⁷ Torr
10 Millimeters to the Centimeter

Fig. 3.

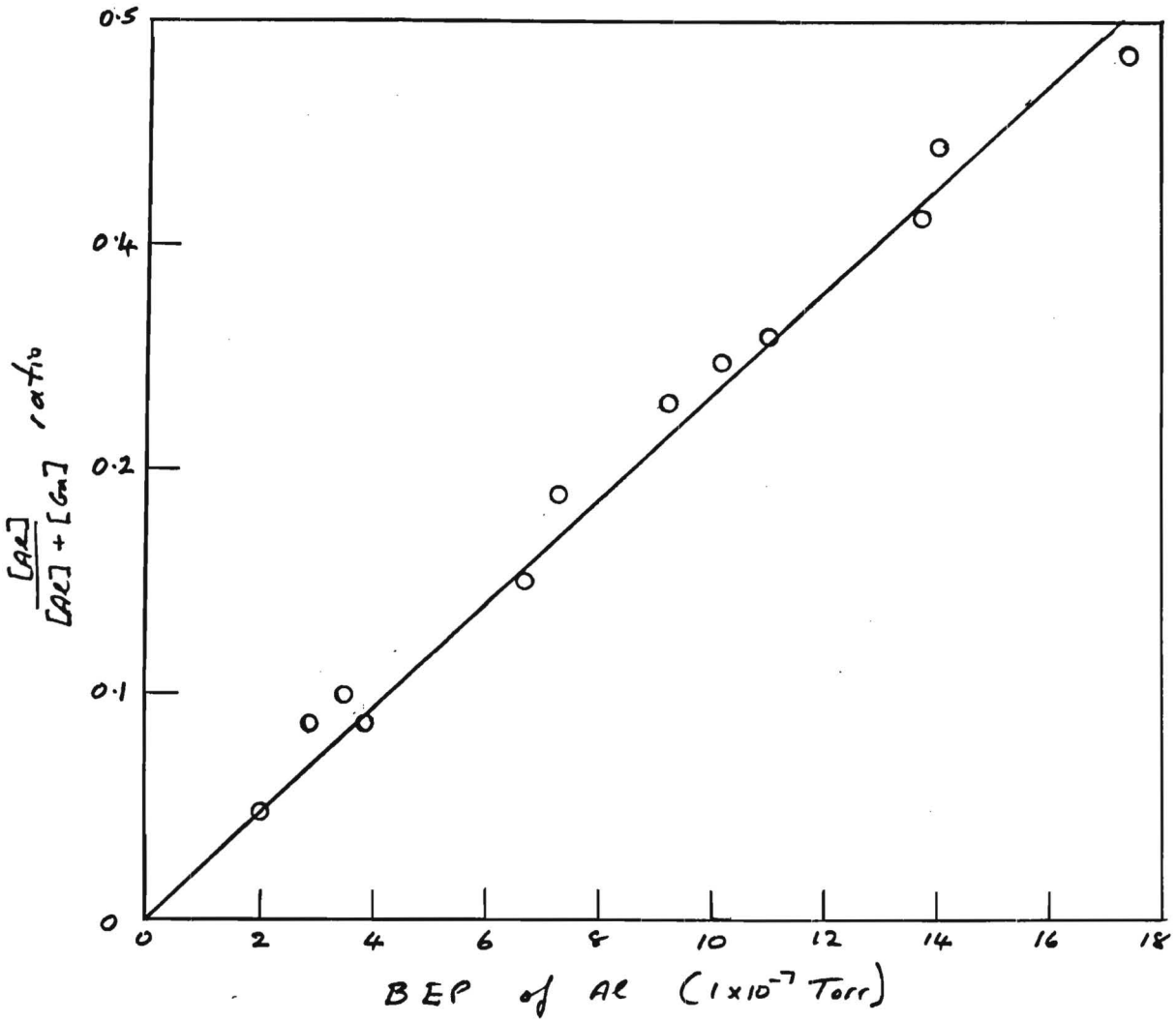
0·5
0·4
0·2
0·1
0
0
2
4
6
8
10
12
14
16
18
[Al] / [Al] + [Ga] ratio
BEP of Al (1 x 10⁻⁷ Torr)

Fig. 4.

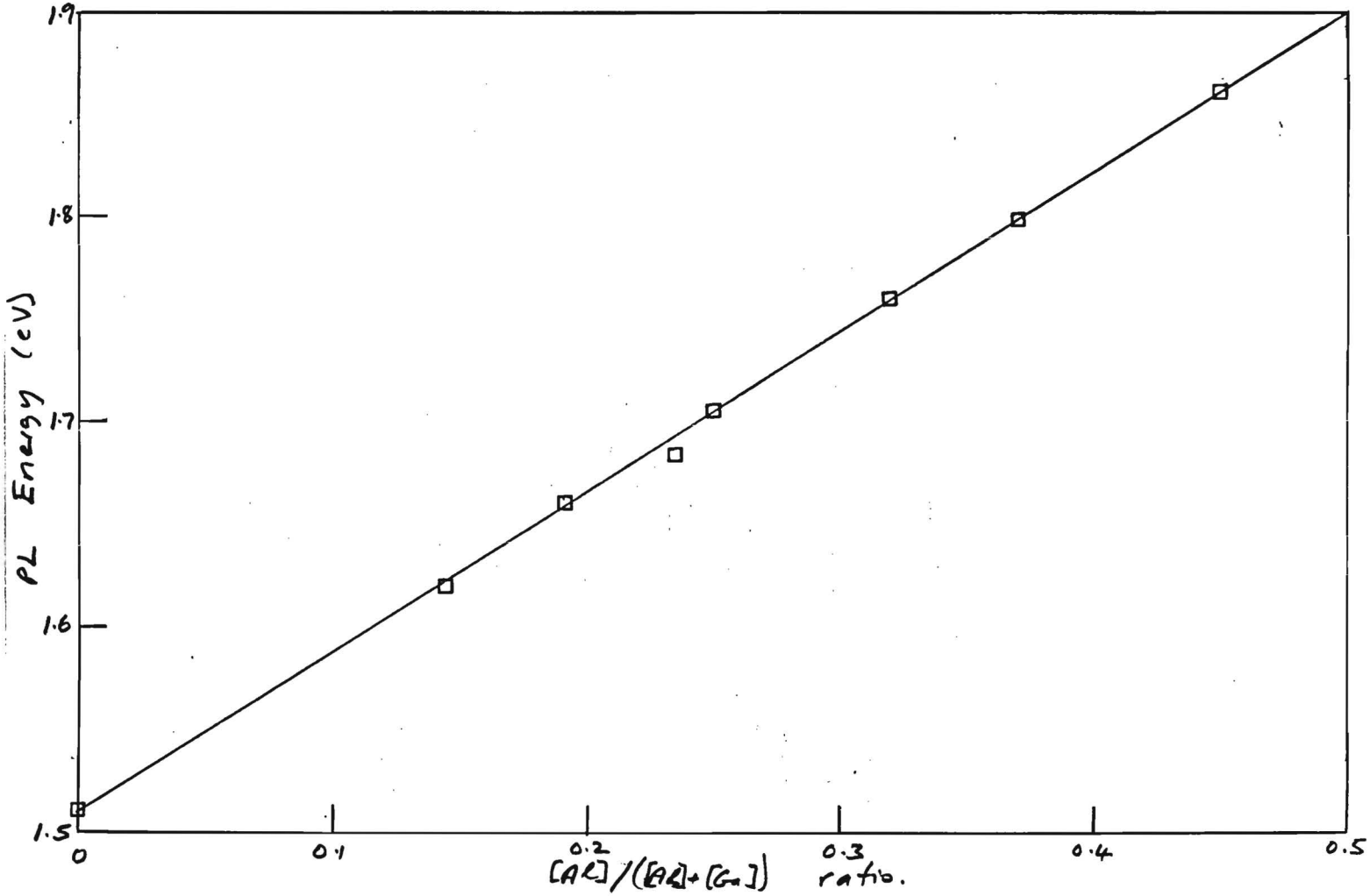

Fig. 5.

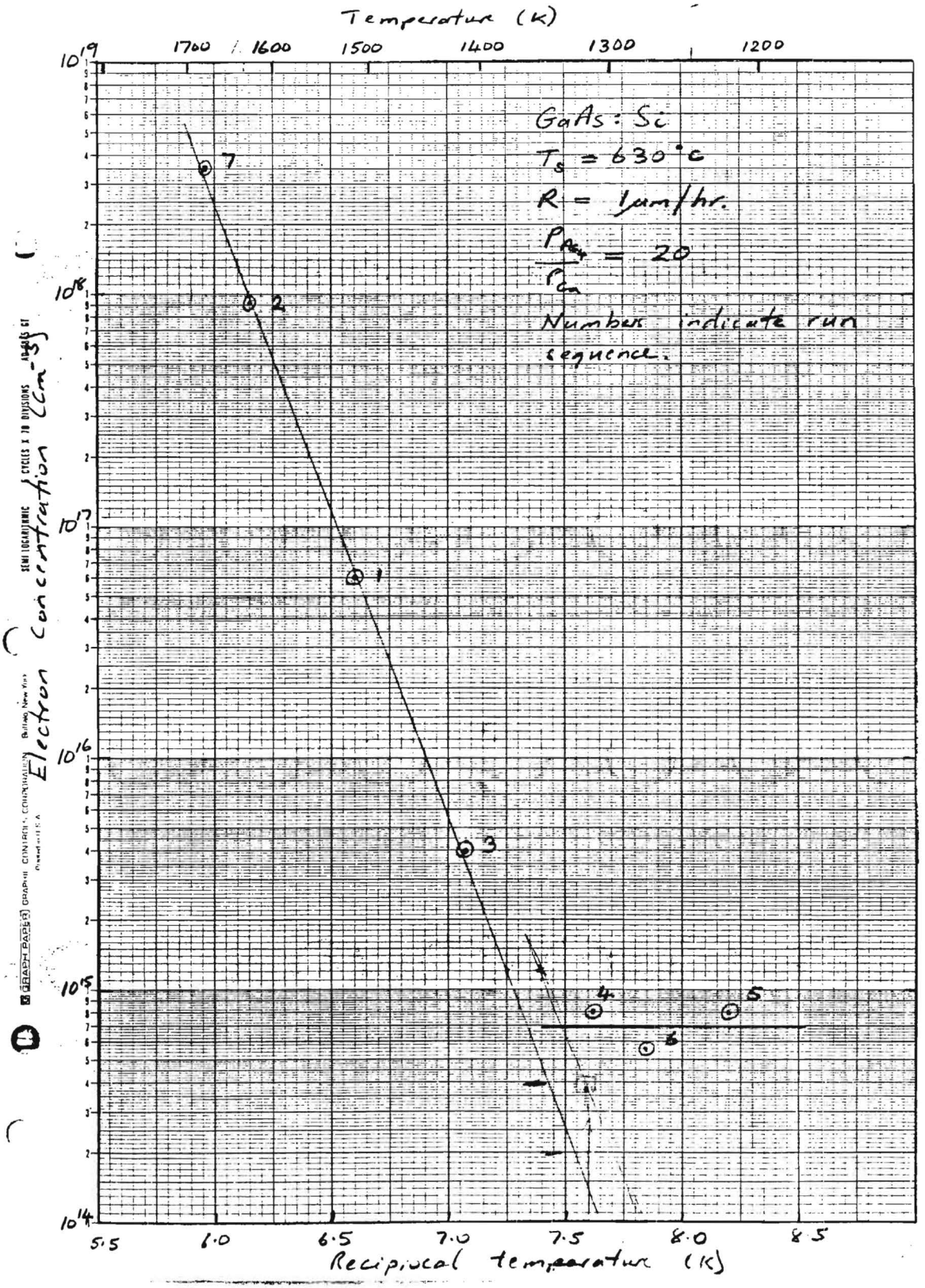
Temperature (K)
1700
1600
1500
1400
1300
1200
10^{19}
10^{18}
10^{17}
10^{16}
10^{15}
10^{14}
GaAs : Si
$T_s = 630°C$
$R = 1 \mu m/hr.$
$P_{As_4}/P_{Ga} = 20$
Numbers indicate run sequence.
1
2
3
4
5
6
7
Electron Concentration (cm^{-3})
5.5
6.0
6.5
7.0
7.5
8.0
8.5
Reciprocal temperature (K)

Fig. 6.

IN CONFIDENCE

HIGH PERFORMANCE PHOTODIODES

Quarterly Reports No. 4, 5, 6
Report Period: 1 January 1986 - 30 September 1986

Project No. A-4233

Prepared for:

Dr. Kenneth A. Maloney
Polaroid Corporation
Microelectronics/Materials Center
21 Osborn Street, Dept. 775
Cambridge, MA 02139

Prepared by:

Dr. C. J. Summers and Dr. K. F. Brennan
Georgia Institute of Technology
Atlanta, GA 30332

1. SUMMARY

This report describes research on the theoretically modeling and growth of new material structures in the AlGaAs system for fabricating "High Performance Photodiodes."

In the first phase of this work, theoretical studies were performed to realistically describe the mechanisms controlling the operation of the new superlattice avalanche photodiodes, proposed as offering significant improvements in performance, i.e., high-gain with ultra-low excess-noise contribution. This formalism was successfully accomplished and led to the invention of two new doped superlattice avalanche photodiode structures which, from the modeling studies, should result in still further enhancements in photodetector performance. Patents for these inventions have recently been filed by Polaroid.

In the second phase of this program, an MBE facility for growing high quality AlGaAs and GaAs epitaxial layers, both with high purity, and with heavy controlled n- and p-type doping concentrations was developed. Additionally, this capability was applied to the growth of $Al_xGa_{1-x}As/GaAs$ superlattices and conventional and superlattice PIN avalanche photodiode structures. These latter structures were fabricated into test devices and preliminary electrical and optical characterizations performed. Reasonable current-voltage characteristics were obtained on these early device structures and photodetection was demonstrated. Work is continuing as rapidly as possible in this area. The highlights of this program are described in Section 3, which for completeness is preceded by a discussion on new photodiode device structures.

2. BACKGROUND AND TECHNICAL DISCUSSION

One of the most effective structures for realizing the requirements for fast infrared detectors is a shallow junction n-i-p device in which the space-charge depletion width is greater than $2/\alpha$, where α is the absorption coefficient of the detector material at the signal wavelength.[1,2] For this design criteria 90% of the signal raditation is absorbed within the depletion region and creates an electron-hole distribution that is immediately separated and sensed by the junction. The frequency response of the device is then given by the transit time for carriers to drift across the junction and/or the RC time constant resulting from the capacitance and resistance of the space-charge region and external circuitry. By constructing p-i-n structures in which the signal radiation is absorbed in the depletion width and using small devices to limit the RC product, operation to 10 GHz is possible with high signal-to-noise ratios.

Avalanche Photodiode (APD)

As is well known, the performance of a p-i-n device can be significantly enhanced by reverse biasing to the avalanche condition so as to provide internal gain. In this process the photo-excited free carriers are accelerated by the electric field and gain sufficient energy such that a collision with a valence electron excites the electron to the conduction band leaving a free hole in the valance band. This process, called impact ionization, is repeated for the newly generated electron and hole which in turn impact ionize and produce more carriers. Thus the avalanche process can provide very large amplification of the original signal. It should be noted that the avalanche mechanism also produces more noise, but for typical near-infrared detector applications where the thermal noise of the external circuitry dominates the total device noise, the current gain produced by avalanche multiplication results in a corresponding increase in the total systems signal-to-noise ratio.[3]

Thus to optimize the performance of an APD it is necessary to maximize the current gain and to minimize the excess noise

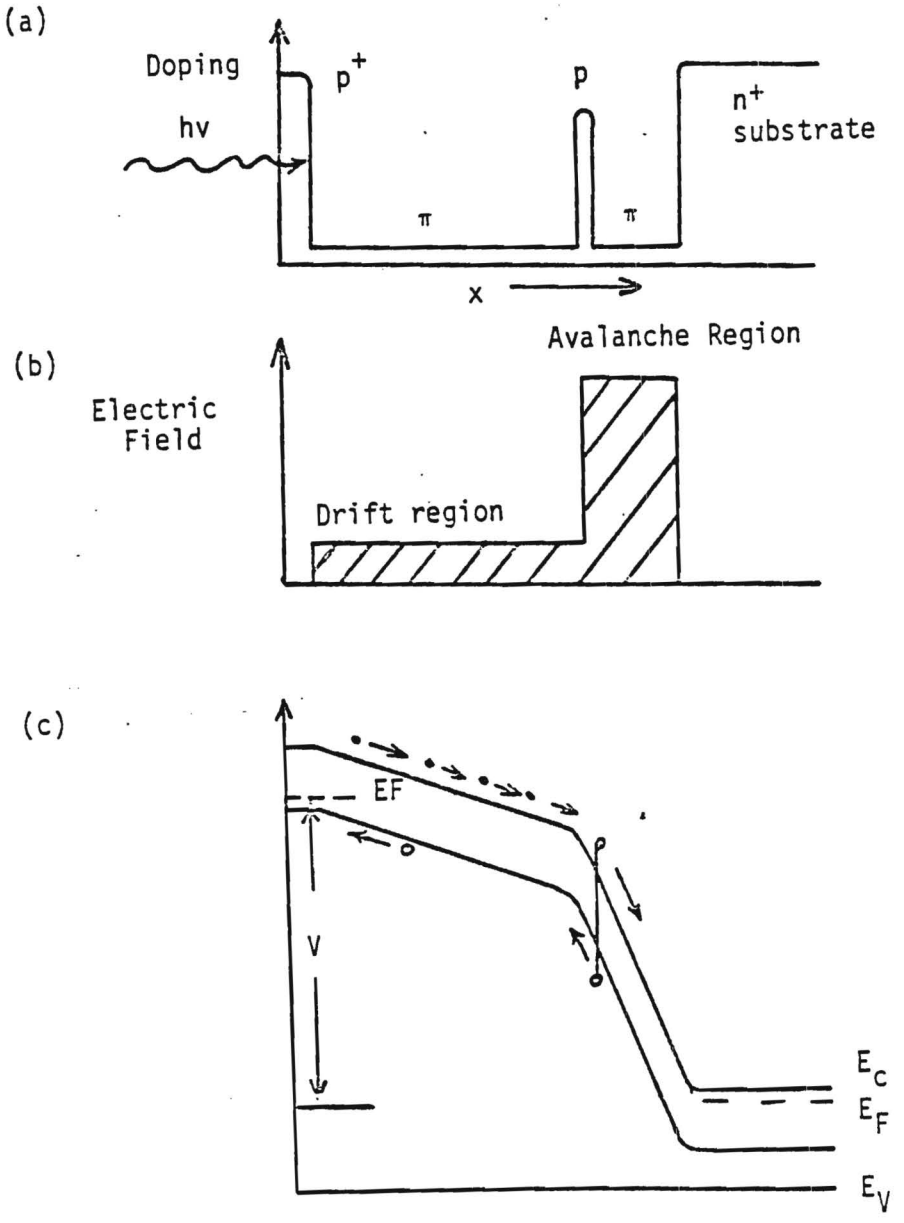

Figure 1. Reach - through APD, (a) Doping profile (b) Electric field distribution (c) Energy band diagram under bias conditions.

contribution from the avalanche process and its effect on the bandwidth of the diode. Theoretical considerations show that these conditions can be realized when there is a large difference between the carrier ionization rates and the avalanche is initiated by the carrier with the higher ionization coefficient.[5] It is also found that this situation makes the multiplication rate of charge carriers less strongly dependent on field strength enabling better control to be obtained over the gain processes.

The material requirements for avalanche photodiodes are therefore a high absorption coefficient to absorb the radiation in the depletion width, high drift velocities to minimize carrier transit times, and a large difference between the electron and hole ionization rates. To simultaneously realize all of these conditions in a simple p-n junction device is impossible and thus to avoid compromising performance new device structures have been developed.

A significant advance in APD design was made with the introduction of the reach-through structure shown in Figure 1.[5] In this structure the function of the p+-π-p region is to absorb the photon flux and provide a high electric field to separate the electron-hole pairs produced by photo—annihilation. Holes are immediately swept to the p+ junciton and out of the device; concurrently electrons are accelerated to their maximum drift velocity. When the electrons reach the p-type layer they are accelerated further by the high field across the narrow p-n+ region to produce charge multiplication and current gain. Thus, the processes of electron-hole pair generation and charge multiplicaton are spatially separated making it possible to optimize each process and the total performance of the device by the correct choice of doping profiles, structure length and applied voltage. The quantum efficiency and speed of response of the device are determined by the p+-π-p region. Near unity quantum efficiencies can be obtained by making the length of this region equal to $2/\alpha$. The speed-of-response is limited by the limiting carrier velocity in the p+-π-p region divided by its length. Thus for carier velocities of approximately 2 x 10^7 cm/s

and $\alpha > 10^4$, bandwidths greater than 100 GHz are possible.

The most successful APD devices to date have used Si because the electron ionization rate is much greater than the hole ionization rate in this material. Germanium APD's whose spectral response extends out to 1.8 um have been developed but are very noisy because the electron and hole ionization rates are nearly equal.

At present, the major thrust in APDs is to use alloys based on III-V semiconductor systems such as AlGaSb, GaInAs, and InGaAsP, because these semiconductors allow the wavelength response of the diode to be varied by adjusting the alloy composition. These material systems can also be lattice matched over an appreciable range of alloy compositions thus enabling the fabrication of heterojunction devices that can result in a significant improvement in device performance. It should be emphasized that exact lattice matching is essential for these structures because a mis-match between layers will produce interface states and stress gradients that will degrade device performance and result in failure at high electric fields.

Besides improving device characteristics it has recently been realized that new device structures can be fabricated by molecular beam epitaxy that enable the ionization ratio between electrons and holes to be artificially enhanced. This is very significant because for most III-V semiconductors the electron and hole ionization rates are nearly equal.[3] Several schemes being investigated for enhancing the performance of APDs are described below.

Heterojunction APD (HAPD)

This device is the simplest of the new heterojunction structures currently being investigated and has principally been fabricated in GaInAs and GaInAsP alloys grown on InP.[6,7] These alloys are used because they can be perfectly lattice matched to InP and have a spectral response extending to 1.6 um as required for optical fiber communication links. The actual structures used are n-GaInAs/n-InP/p^+-InP, n-GaInAsP/n-InP/p^+-InP or n-

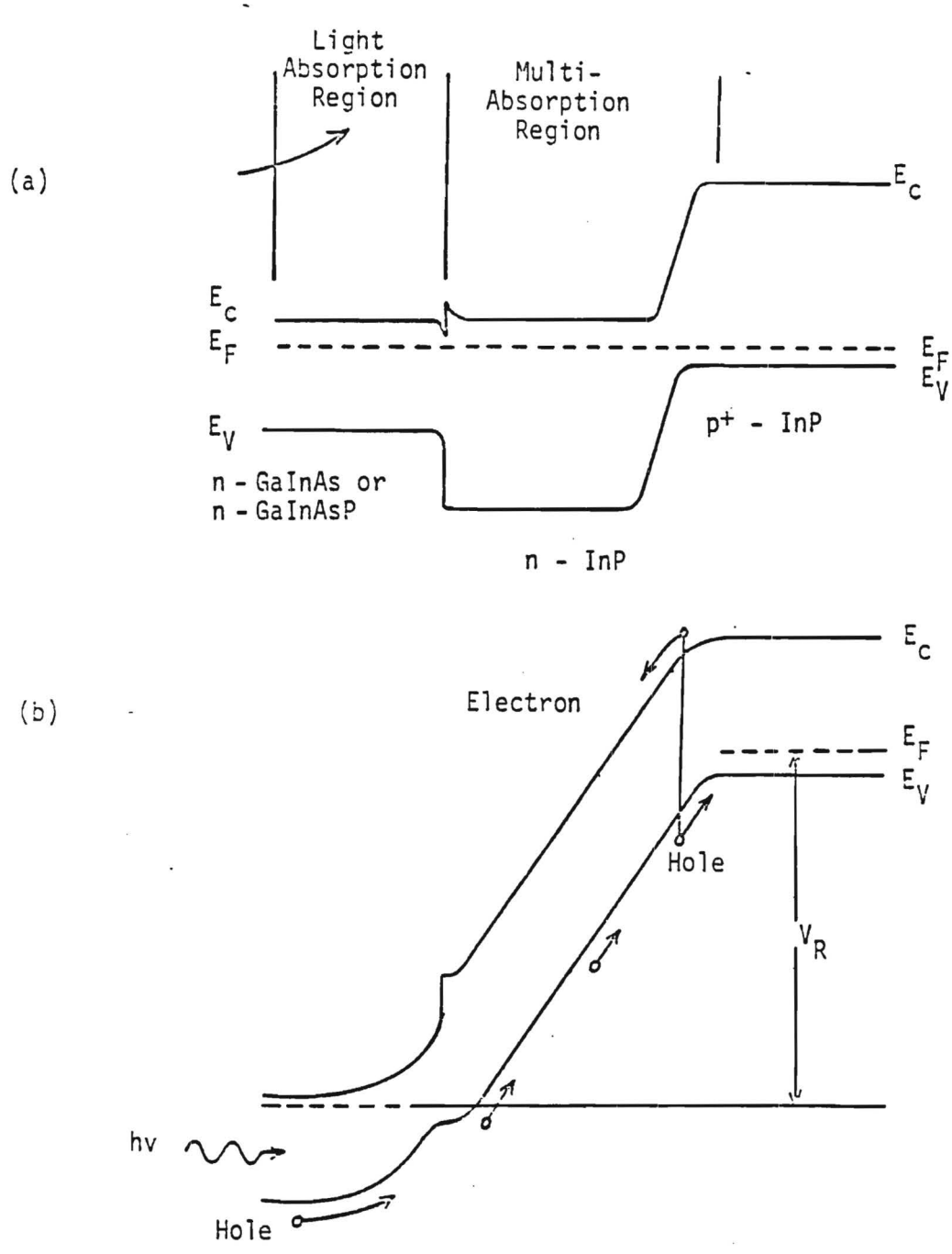

Figure 2. (a) Energy-band diagram of a InP-GaInAs hetero-junction at equilibrium. (b) Energy-band diagram at avalanche breakdown.

InP/n-GaInAsP/n-InP/p+-InP where the extra InP layer in the last device is used as a window. As shown in Figure 2, light is absorbed by the ternary or quarternary layer, and the avalanche process is optimized to achieve hole injection by adjusting the doping and layer thicknesses so that under reverse bias the n-InP depletion layer reaches through into the GaInAs or GaInAsP layer. The heterojunction is used to reduce the dark current leakage in the device thus enabling higher voltages to be applied to increase the gain. The performance of these devices is significantly better than achieved with Ge APDs, but because the hole to electron ionization ratio is small, it is far from that possible with a more optimized material or device structure.

Superlattice APD

A third type of APD structure recently proposed and demonstrated by Capasso et al.[8] makes use of the dependence of the ionization rate on bandgap energy and the conduction band edge discontinuity between undoped GaAs and AlGaAs layers to produce an enhancement of the effective ionization ratio. The band structure of the device under reverse bias is shown in Figure 3. The device consists of a p+-type photo-collection electrode, a superlattice avalanche region consisting of 50 alternating GaAs and AlGaAs layers and an n+-type collection electrode. The composition of the AlGaAs is adjusted to give a 0.5 eV discontinuity between the conduction band edges of AlGaAs and GaAs. The photo-excited electrons are accelerated into the superlattice region and gain an energy several tenths of an electron volt above the conduction band energy of AlGaAs. When the hot electron enters the GaAs well, it experiences a reduction of the ionization threshold enery equal to the energy discontinuity between the AlGaAs and GaAs layers. Because the ionization rate increases rapidly for decreasing ionization threshold energy, the electron ionization rate is increased by this structure. As the electron re-enters the next AlGaAs layer, the reverse situation occurs and the electron ionization rate decreases. However, because the ionization rate is larger in

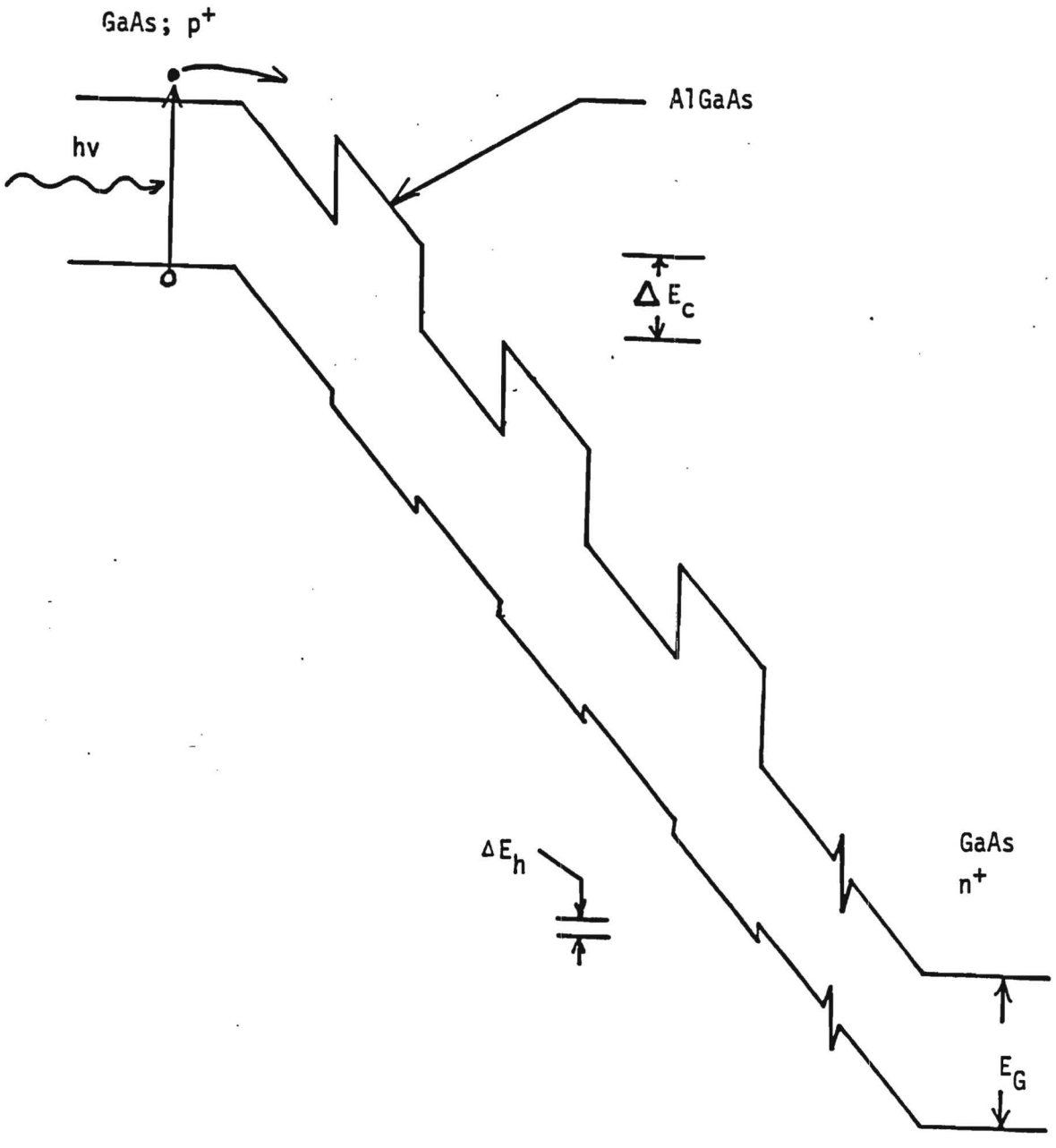

Figure 3. Energy Band diagram of superlattice APD.

GaAs than in AlGaAs and the GaAs layer can be made thicker than the AlGaAs layer, a net increase in the ionization rate is observed. The small discontinuity in the valence band has little impact on the ionization rate for holes which essentially remains unaltered. Thus this structure produces an enhancement of the electron to hole ionization ratio. This device has been fabricated and shown to have a electron to hole ionization ratio of 10. It should be noted that the magnitude of the enhancement of the electron to hole ionization ratio is strongly dependent on the size of the conduction and valence band-edge discontinuities between the AlGaAs and GaAs layers. Conventionally, the energy difference in the vacuum potentials between the GaAs and AlGaAs layers is assumed to be shared in the ratio 85:15 between the conduction and valence band edge discontinuities. But recent optical data suggest the ratio should be closer to 57:43[10]. This difference will have a large effect on the optimum attainable electron to hole ionization ratio and thus investigations need to be performed to establish its precise value. The influence of the conduction band effective mass on this ratio also needs to be measured.

Graded Bandgap Multilayer APD

The purpose of this structure is to cause only electrons to be ionized thus producing high signal gains with very low noise.[11,12] (Fig. 4). The structure consists of a graded-bandgap multilayer structure, each stage of which is linearly graded in alloy composition from a low bandgap energy (E_{G1}) to a high bandgap energy (E_{G2}) followed by an abrupt step back to the low bandgap energy. The materials of the structure are chosen such that the largest bandgap difference produces an energy discontinuity greater than the electron ionization energy, E_1, in the low bandgap material. The operating conditions of the structure are shown in Figure 4b. A photon-excited electron in the p^+ region experiences the combined field of the electrical bias and bandgap grading which accelerates it toward the first step. The field is small enough so that the electron does not

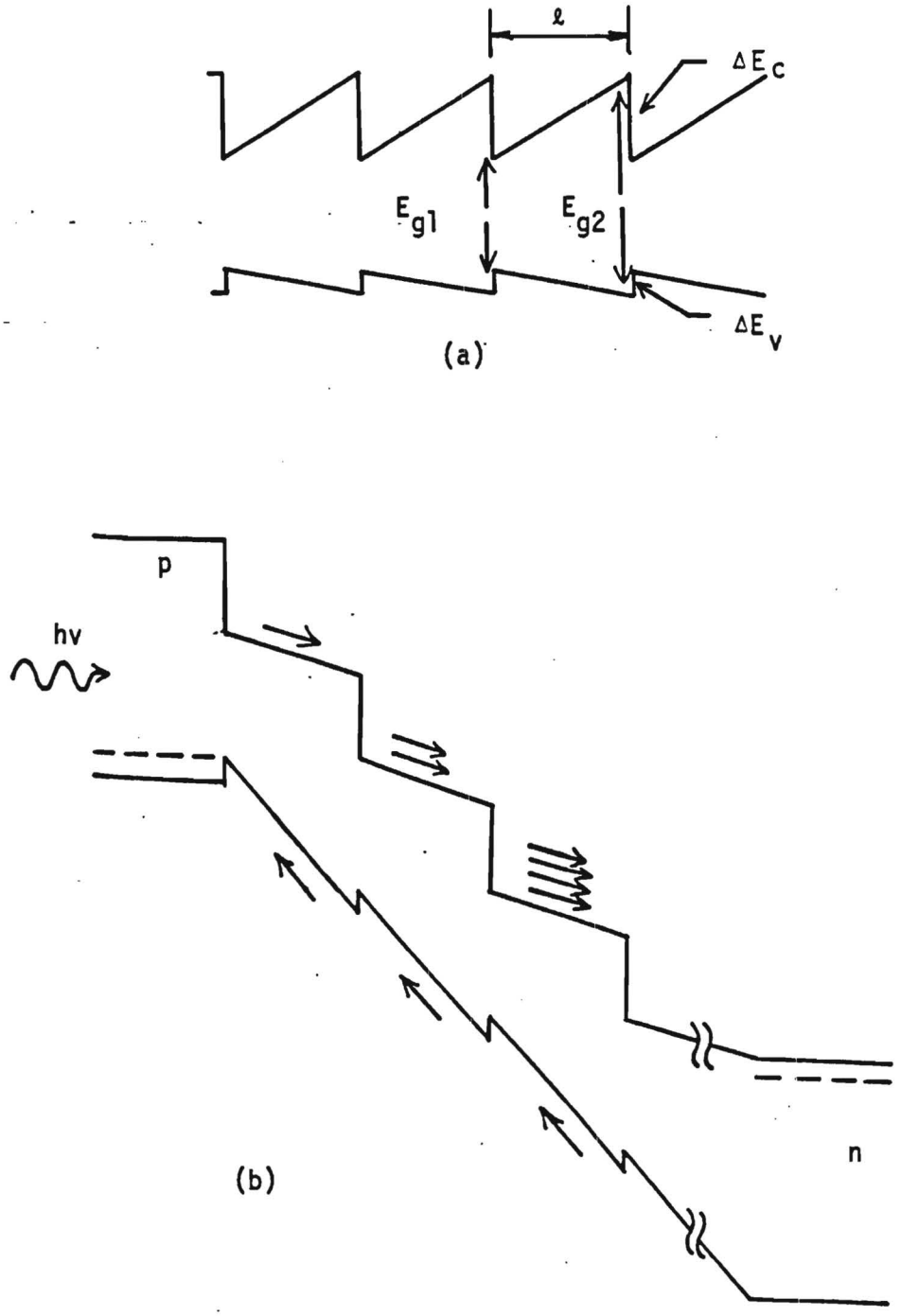

Figure 4. Band diagrams for (a) the unbiased graded multilayer region and (b) the complete detector under bias.

impact ionize before it reaches the step. At the step, impact ionization occurs because the energy discontinuity is greater than E_1. This process is repeated for each step as shown in the figure. At each step the maximum theoretical gain is two, giving a theoretical gain for the structure of $(2-\delta)^N$ where N is the number of graded layers and δ is the loss at each stage. For a perfect structure the major loss mechanism is expected to be from optical phonon emission. However, this is predicted to be small because it must be involved in a multi-phonon process to lose all of the ionization energy of the electron and because the electron-phonon interaction can be minimized by making the interface region between the high and low bandgaps smaller than the mean free path for phonon scattering, <100A.

Because the energy steps provide most of the energy for ionization the operating voltages are very low (<5V) which also minimizes the device leakage current. A single graded layer device has recently been tested in the AlGaAs system and shown to produce a significant enhancement in the electron-to-hole ionization ratio.

3. REVIEW OF PROGRESS

3.1 Highlights of Theoretical Work in the 1st Contract Year

We have developed a rigorous analysis of multi-quantum well and superlattice avalanche photodiode structures based on the numerical solution of the Boltzman Transport Equation. The analysis uniquely includes the most important aspects of high field, high energy transport, i.e., the complete details of both the conduction and valence bands as well as all of the relevant phonon scattering mechanisms calculated from the full order electron self-energy equation. A built-in control on the calculations is provided by first calculating the bulk GaAs electron and hole impact ionization rates and comparing them to existing experimental data. The effects of the device geometry are then completely isolated since any difference between the calculated bulk and superlattice ionization rates must be due solely to the presence of the superlattice structure. Variations in the device geometry, layer widths, doping concentrations, and applied electric field are then examined as to their effect upon the calculated electron and hole ionization coefficients. Knowledge of the electron and hole ionization rates, or equivalently the ionization probabilities, P and Q, can be used to predict the most important device figures of merit, the gain and excess noise factor. The gain can be expressed as a function of the number of stages, m, P and Q as,

$$\langle M\rangle = \frac{(1+P)^m\,(1-k_s)}{[(1+k_sP)^{m+1} - k_s(1+P)^{m+1}]} \qquad (1)$$

where k_s is the ratio of Q to P. The excess noise factor, Fe, can also be calculated from P, Q, m, and K_s as,

$$Fe = 1 + \frac{(1-1/\langle m\rangle)(1-k_s)}{2+P(1+k_s)}\left[-P + \frac{2(1-k_sP^2)}{(1+k_sP)}\left(\frac{\langle m\rangle k_s(1+P)}{(1-k_s)} + \frac{1}{(1+P)}\right)\right] \qquad (2)$$

Therefore, a numerical optimization scheme is used to determine the best possible device geometry, in terms of the maximum gain at the lowest excess noise factor. The procedure, though time consuming, is extremely accurate since its predictions are based on a first principles assessment of the device performance.

The optimal device structure, in terms of gain to excess noise performance, is one in which the hole ionization rate effectively vanishes, Q=0, and the electron ionization probability is as close to one as possible, P=1. We have examined five different multiquantum well/superlattice structures using the above mentioned procedure, the simple multiquantum well device (composed of alternating GaAs/AlGaAs layers), the channeling avalanche photodiode (a interdigitated p-n junction device), the staircase APD, the doped quantum well device, and the p-n junction quantum well APD. Of these devices, it is found that both the doped quantum well and p-n junction quantum well devices provide optimal performance; these structures can be designed to produce high gain at low excess noise by enhancing the value of P well over that of Q.

3.2 Highlights of Experimental Program

Under our original agreement, the initial phase of this program was supported by Georgia Tech and included the calibration of the Varian Gen II System to grow high quality low doped n-type GaAs and also AlGaAs epitaxial layers. Following this work heavy n- and p-typing doping of GaAs and AlGaAs was performed and also PIN and SL-APD material structures were grown and fabricated into test devices. The details of each stage of this investigation is given below

High Quality GaAs Layers

To obtain high quality pure GaAs layers which could be back doped with Si to the low $10^{14}cm^{-3}$ range, a special procedure for substrate cleaning and growing a fine GaAs/AlGaAs superlattice structure was developed. This structure inhibits flaws and

dislocation lines from propagating from the substrate into the growing layers, thereby increasing crystal perfection and purity. These techniques are listed in Fig. 5 and will be discussed in detail in the Final Report. A list of the samples grown, their doping conditions, and their electrical properties at 300 and 77K as measured from Hall effect and resistivity measurements, is given in Table 1. Examination of these results showed that electron mobilities greater than 100,000 cm^2/Vs were obtained for most samples doped under $10^{15}cm^{-3}$, with the highest mobility being 117,219 cm^2/Vs for a doping of $3.2 \times 10^{14}cm^{-3}$. The full impact of these results is shown by Fig. 6 in which the electron mobility is plotted as a function of the electron concentration. As shown at 300K, the data is well-behaved and extrapolates to the theoretical limit at very low electron concentrations, $<10^{13}cm^{-3}$. At 77K the data falls very close, or above, the line calculated by Stillman and Wolfe[13] for samples with a compensation ratio, δ , of 2. These data indicate that the compensating acceptor concentrations in our samples are very low $< 10^{14}cm^{-3}$ and this result has indeed been confirmed by photoluminescence data. It should be emphasized that the data shown in Fig. 6 compares very favorably with published data.

Doping Studies of GaAs and AlGaAs

The data obtained for heavy n-type Si doping of GaAs and AlGaAs are depicted in Figure 7 which shows the measured electron concentration plotted as a function of the reciprocal of the Si-oven temperature. As observed the data is well behaved for both GaAs and AlGaAs and emprical equations were determined for the dependence of the electron concentration on Si-oven temperature. Electron concentrations of $> 4 \times 10^{18}cm^{-3}$ were obtained, as shown, but for these samples a loss in surface quality was observed. Thus, for Si-doping we presently believe that a concentration of $3.5 \times 10^{18}cm^{-3}$ is the maximum attainable under the current growth conditions of 1 um/hr at either 600°C or 700°C for GaAs or AlGaAs, respectively. These conclusions were also supported by the photoluminescence data taken on these samples.

Fig. 8 depicts a similar plot for the Be-doping of GaAs and

GROWTH PROCEDURE FOR GaAs

GROWTH STRUCTURE

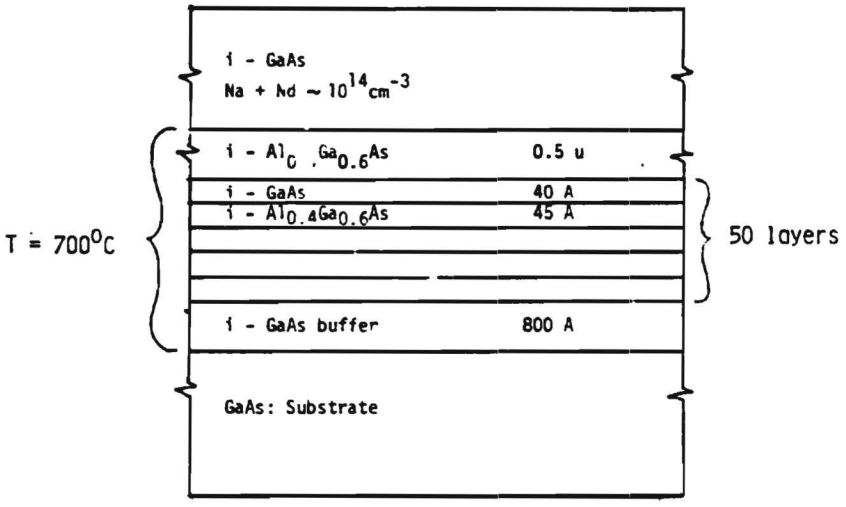

GROWTH PROCEDURE

1. CLEAN GaAs SUBSTRATES, ETCH IN 5:1:1
2. MOUNT SUBSTRATES ON MO HOLDERS USING IN
3. PLACE IN LOAD-LOCK AND HEAT TO 380°C FOR 24 H.
4. HEAT IN GROWTH CHAMBER AT 600°C UNDER AS_4 FLUX FOR 60 MIN.
5. GROW GaAs BUFFER LAYER FOR 5 MIN. AT 700°C
6. GROW GaAs/$Al_{0.4}Ga_{0.6}As$ SL, 25-50 LAYERS AT 700°C
7. LOWER SUBTEMPERATURE TO 600°C, INITIATE GaAs GROWTH
8. TURN OFF RHEED, QMS, AND ION-GAUGES

Figure 5. Growth structure and procedure developed for growing high-quality GaAs epitaxial layers.

Table 1.

ELECTRICAL PROPERTIES OF MBE GROWN GaAs;Si
(from Hall Effect Measurements)

Sample No.	Si-Oven Temp. ^{o}C	Electron Concentration (cm^{-3})		Electron Mobility (cm^2/Vs)	
		300K	77K	300K	77K
11	undoped	slightly n-type $<10^{12}cm^{-3}$			
14	1080	$1.17x10^{15}$	$1.27x10^{15}$	6,922.2	61,415.1
15	1060	$2.75x10^{15}$	$2.92x10^{15}$	6,781.9	40,327.7
16	1040	$9.59x10^{16}$	$4.94x10^{14}$	3,730.2	103,342.3
17	1100	$7.05x10^{15}$	$5.50x10^{13}$	6,378.0	38,871.5
18	1125	$1.57x10^{16}$	$6.43x10^{15}$	5,396.8	27,620.3
19	undoped	slightly p-type			
21	1025				
22	1000	$2.98x10^{16}$	$6.43x10^{15}$	1,662.6	17,394.9
23	980				
24					
26					
27	1000	$5.61x10^{14}$ $6.00x10^{14}$ (C-V)	$6.18x10^{14}$	7,718.3	105.088.2
28	960	$7.80x10^{14}$ (C-V)			
30	960	$7.05x10^{14}$	$6.66x10^{14}$	7,987.6	103,353.8
31	940	$3.90x10^{16}$	$3.83x10^{16}$	6,567.5	44,019.6
32	0				
33	9600	$7.00x10^{14}$ (C-V)			
34	980				
35	940	$9.50x10^{14}$ (C-V)			

ELECTRICAL PROPERTIES OF MBE GROWN GaAs:Si (Continued)

Sample No.	Si-Oven Temp. °C	Electron Concentration (cm^{-3})		Electron Mobility (cm^2/Vs)	
		300K	77K	300K	77K
37	922	3.22×10^{14}	3.45×10^{14}		117,219.2
39	910				

Ohmic Contacts formed by:

1. Au:Ge (12%); 500 Å
2. Ni; 200 Å
3. Au; 1500 Å
4. Alloyed at 375 °C, 4 min.

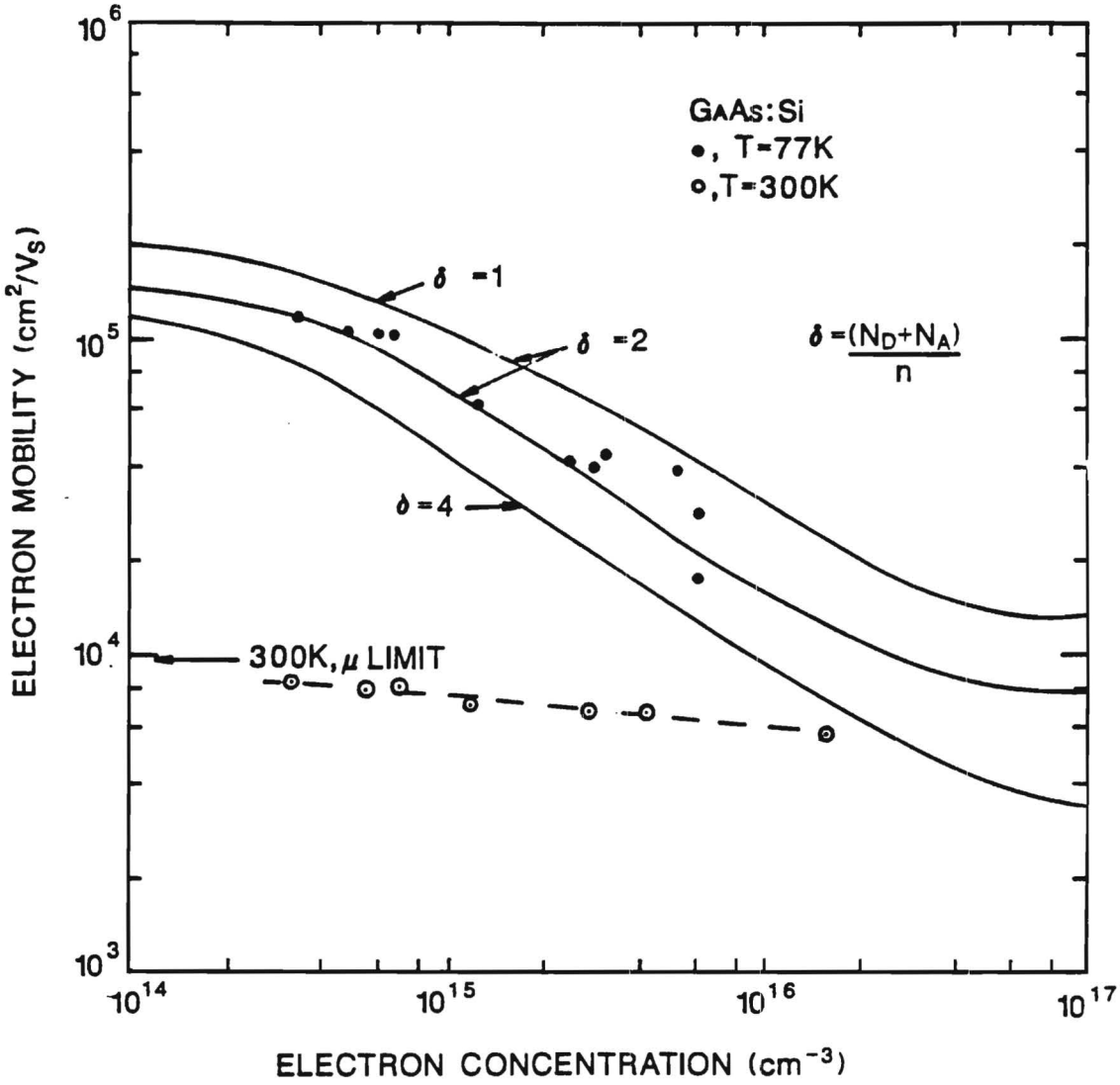

Figure 6. Experimental and theoretical dependence of the electron mobility on electron concentration for Si-doped GaAs at 77 and 300K.

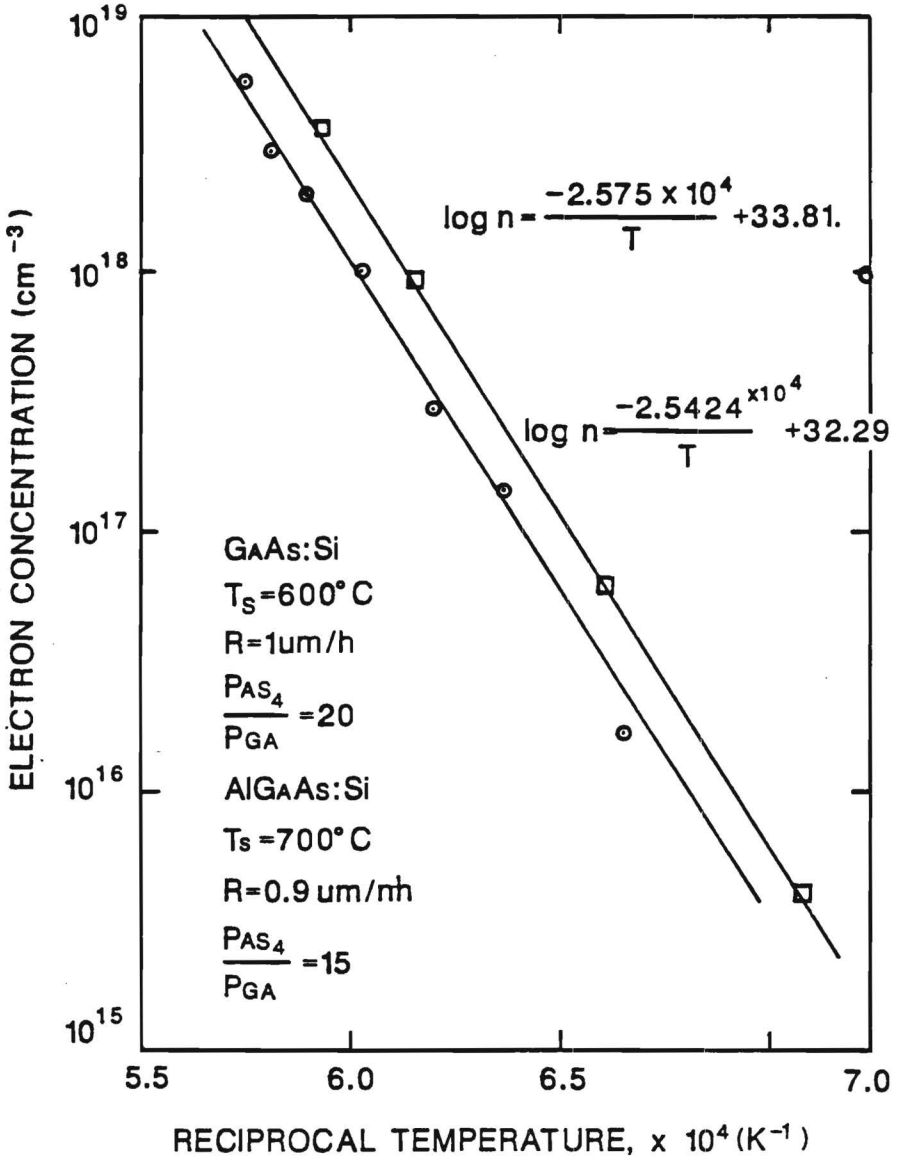

Figure 7. Dependence of electron concentration on Si-oven temperature for Si-doping of GaAs and $Al_xGa_{1-x}As$.

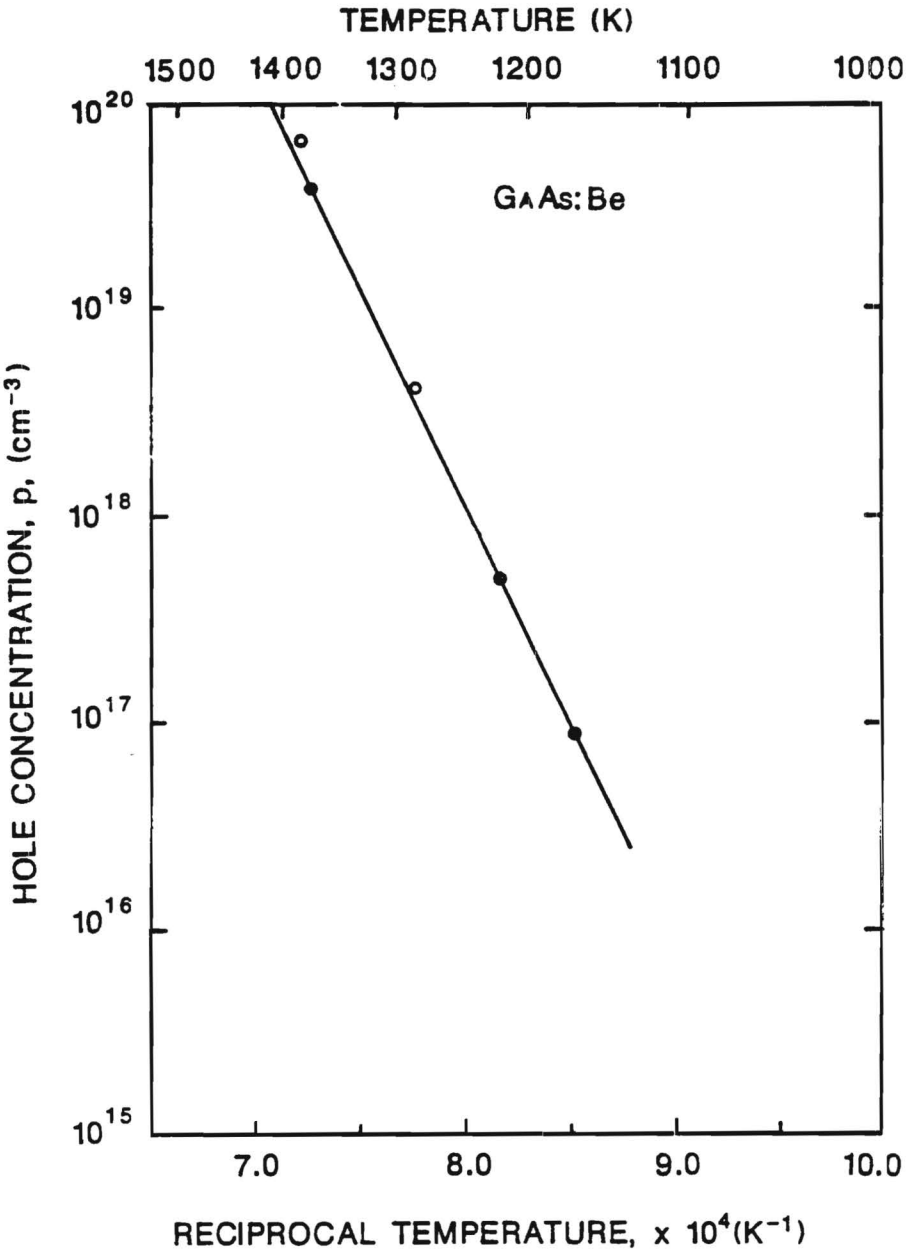

Figure 8. Dependence of hole concentration on Be-oven temperature for Be-doped GaAs.

shows that hole concentrations of 8×10^{19} cm^{-3} can be obtained before a loss in surface quality is observed. Identical runs have been performed for AlGaAs, but problems with making good ohmic contacts to these samples has prevented their evaluation.

Growth of Superlattice Structures

Superlattices of AlGaAs/GaAs were also grown and characterized by photoluminescence to determine the confined energy states in these structure. Figure 9 shows the dependence of the emission energy on the width of the GaAs quantum wells in the superlattice. The expected dependence was obtained and the width of the emission peaks was also analyzed and shown to correspond to a well definition width of 2-3 monolayers of GaAs. SIMS data was also taken on these SL structures. The interpretation of this data is presently being developed and will be explained in greater detail in the Final Report.

Device Fabrication

Figure 10 shows a cross-sectional drawing of the APD design being developed for this program. For this part of the contract, both PIN and SL-APD material structures were grown using the techniques previously developed. Four masking levels consisting of p+ contact, mesa, n+ contact and passivation are required for this design. Three effective diode diameters were selected for the initial investigation. These diameters are 75, 150, and 300 microns, and their respective areas are defined by the region inside the p+ contact ring as shown in Figure 10. Mesa etching is used to electrically isolate the diodes, and contact to the cathode is made by ohmic contact metallization deposited close to the mesa. An outline of the procedure used for fabricating these APDs is given in Table 2. Figures 11, 12 and 13 show typical SEM photomicrographs of the resulting structures. As can be seen, the devices show good edge acuity and the metallizations are well-confined to their respective doping layers. The I-V characteristics of these devices is shown in Fig. 14 and clearly demonstrates the electrical integrity of these structures. These device characteristics have been observed to be sensitive to light, but at present no quantitative optical characterizations

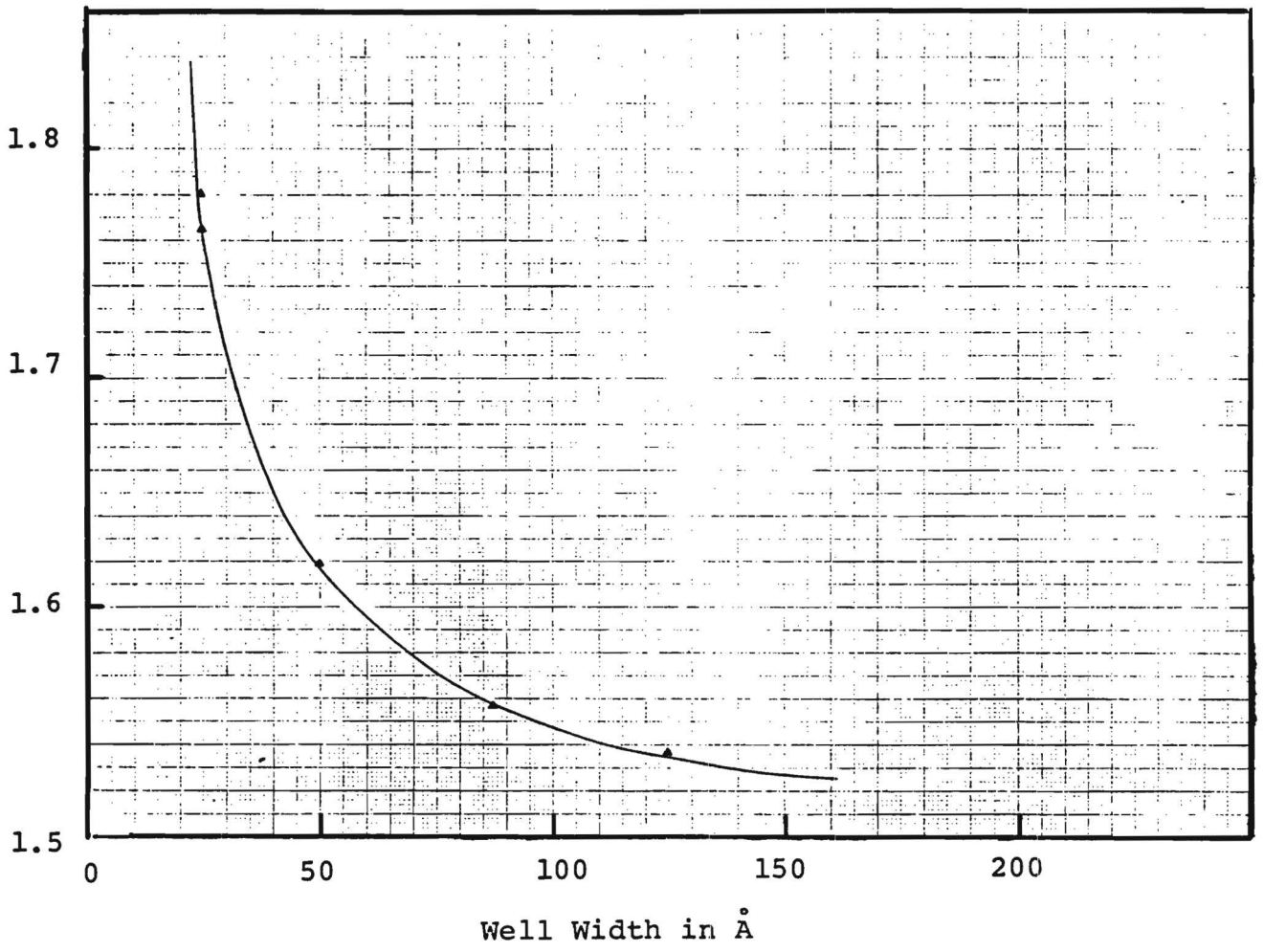

Figure 9. Photoluminescence energy vs. well width. The wells are decoupled by 150A of $Al_xGa_{1-x}As$.

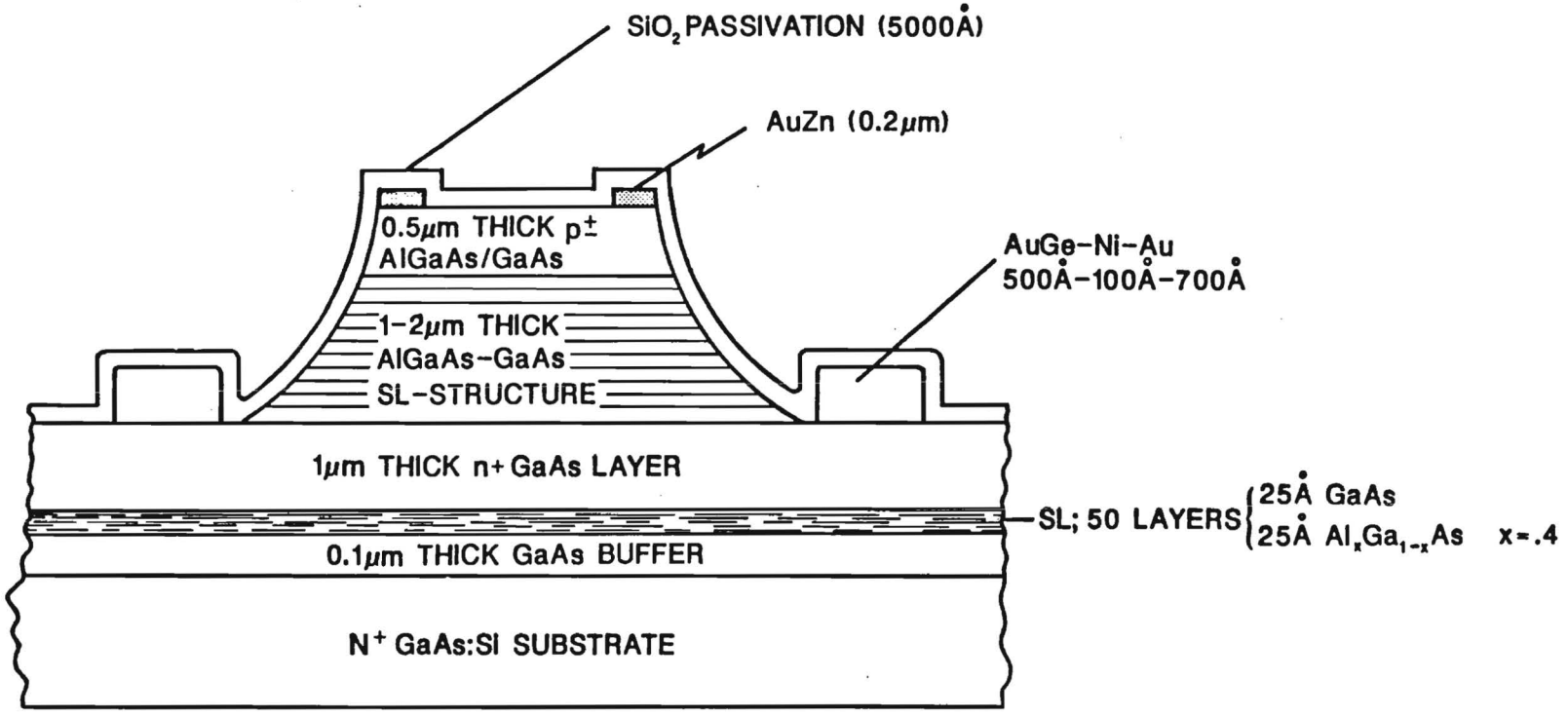

Figure 10. Cross Section of an APD.

Table 2.

APD Fabrication Process

1. Remove indium from backside
2. Lap backside of wafer
3. Clean
4. Apply AZ 1350J photoresist (3:1)
   Bake
   Expose
   Chlorobenzene soak
   Bake
   Develop
5. Inspect
6. Deposit AuZn [95% - 5%]
   1000-2000 Å thick
7. Lift-off excess metal
8. Alloy
   400°C (ramp at 800°C/min.)
   4 min.
9. Apply mesa photoresist AZ 1350J (3:1)
   Bake
   Expose
   Develop
10. Inspect
11. Post bake
    110°C
    10 min.
12. Etch GaAs
    Clorox or 3:1:50 solution of H_3PO_4:H_2O_2:H_2O
13. Clean
    HCl
    DI
    N_2 dry
14. Remove resist
15. Apply N+ contact photoresist
    (see Step 4)
16. Deposit N+ contact metals
    AuGe - 500 Å
    Ni - 100 Å
    Au - 700 Å
17. Lift-off
18. Alloy
    375°C ramp 800°C/min.
    4 min.
19. Clean
    Solvent
    N_2 dry
20. Deposit SiO_2
    Plasma enhanced CVD
    175°C
    5000 Å
21. Apply passivation photoresist
    (see Step 9)
22. Inspect
23. Post bake
    110°C
    10 min.
24. Etch SiO_2
    60:10
    NH_3F:HF
    Etch rate ≈80 Å/sec.
25. Rinse
26. Electrical Probe
    (To ensure SiO_2 is removed)
27. Thin wafer
28. Saw
29. Mount
30. Wire bond
31. Electrical Test

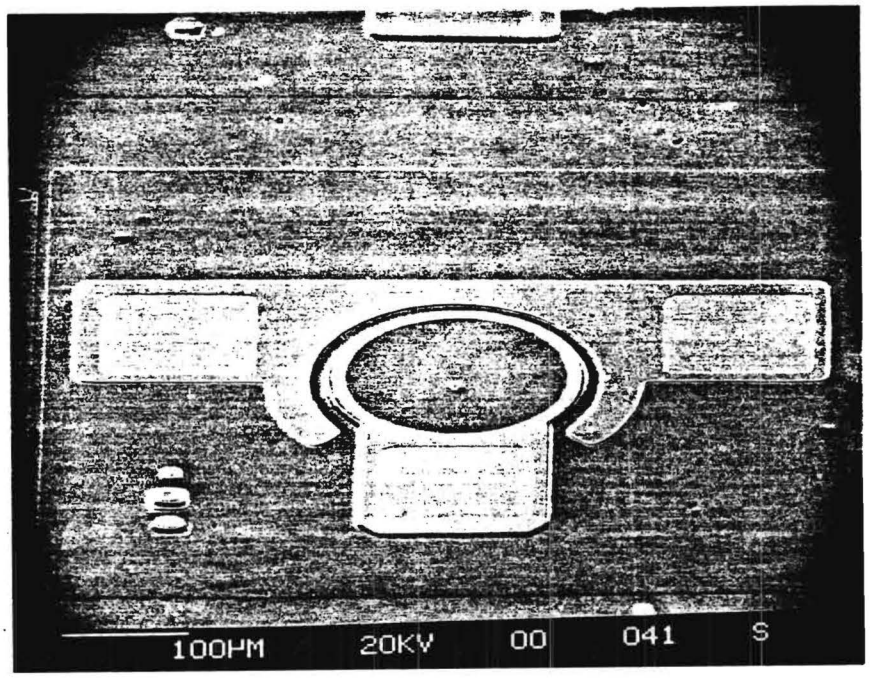

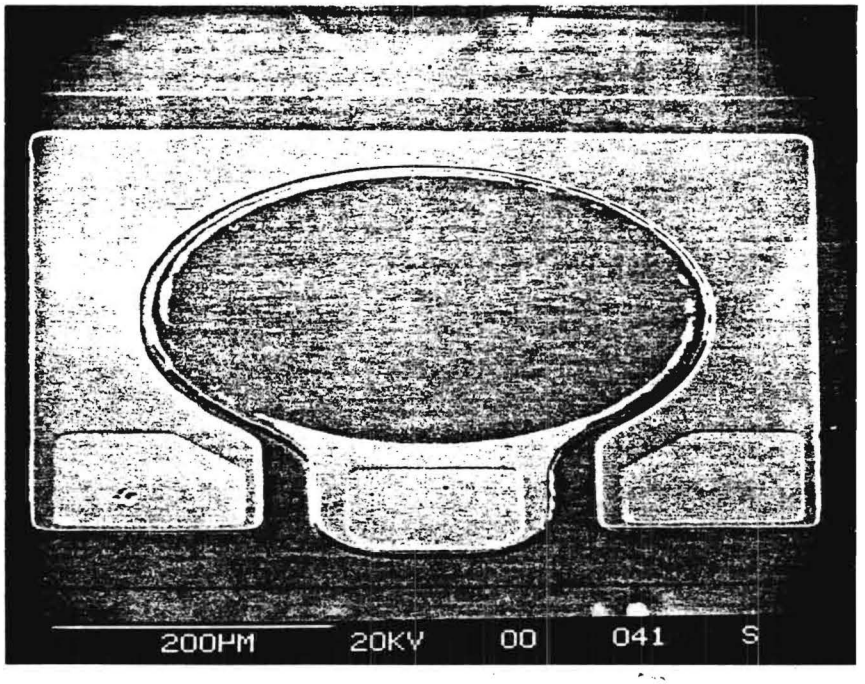

APD TEST STRUCTURES

Figure 11. First APD test structures fabricated in program.

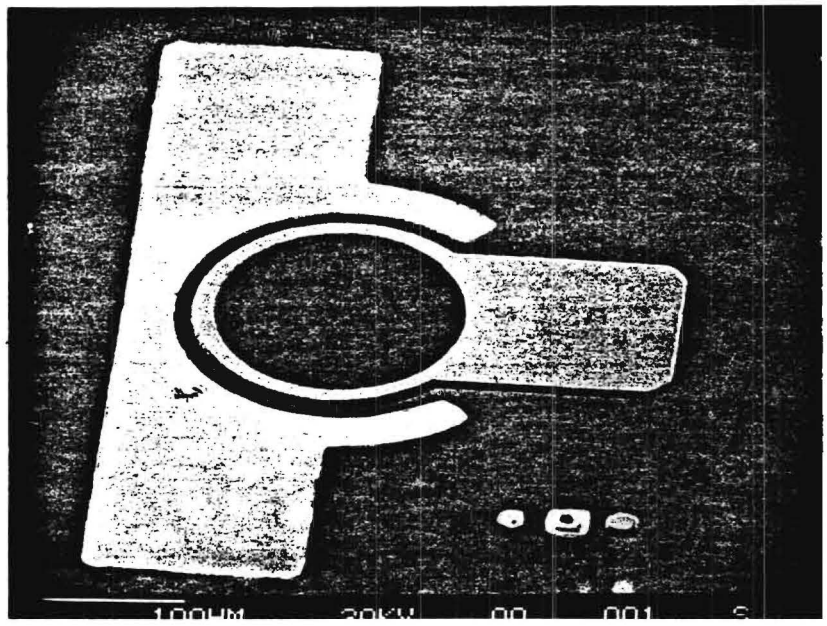

Figure 12. APD Structure Fabricated with Second Mask Set.

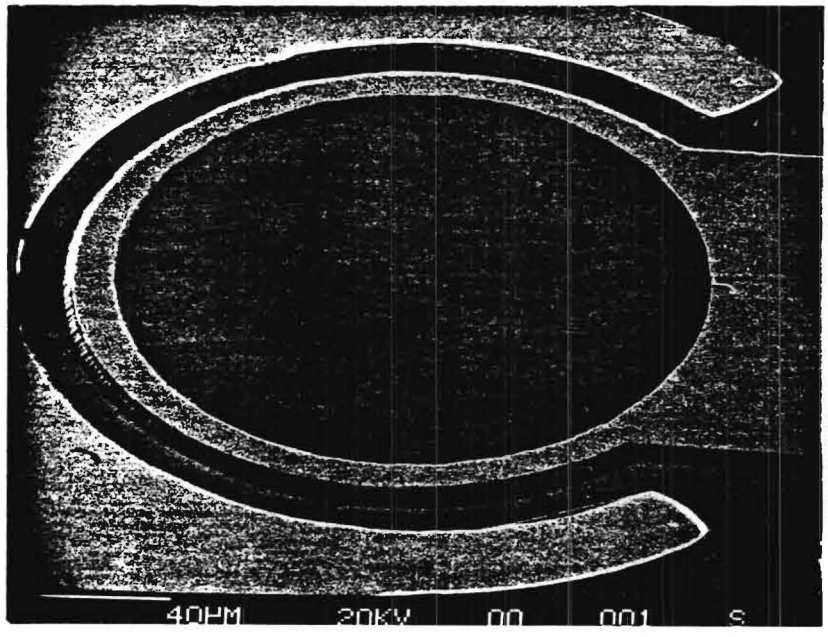

Figure 13. APD at High Magnification Showing No Mesa Overhang.

PIN PHOTODIDE I-V CHARACTERISTICS

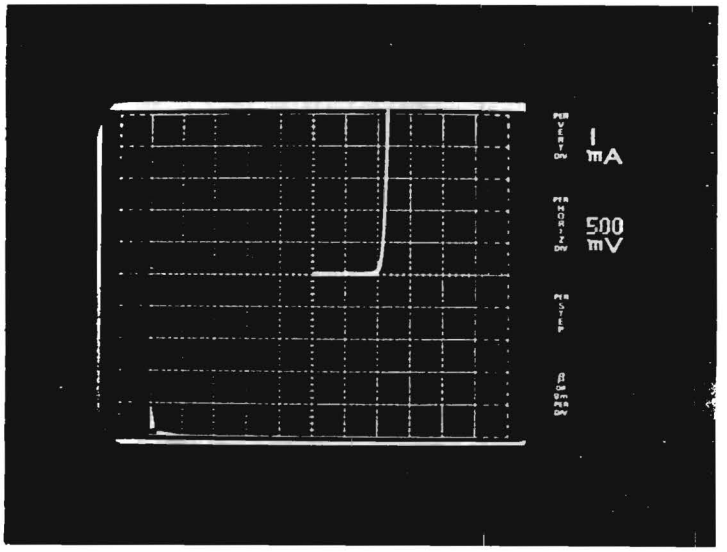

FORWARD

75 MICRON DIAMETER

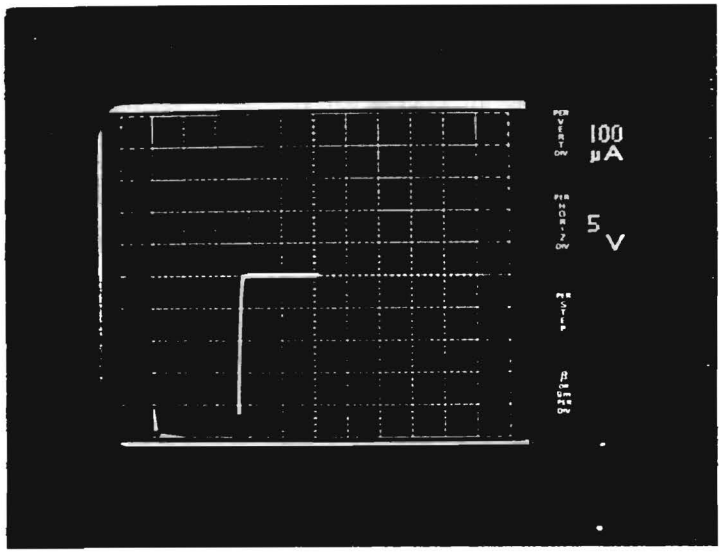

REVERSE

Figure 14. Room-temperature I-V characteristics measured for APD structure shown previously.

have been performed.

Summary

To summarize the achievements of the initial phase of this program we list on the following page the principal milestone achievements of the theoretical modeling, material growth, and device fabrication activities.

PRINCIPAL MILESTONES

1985	
April	Program initiated
April	Theoretical Program started
August	Model of SL-APD formulated
August	GaAs - MBE System delivered and accepted
August/Sept.	System prepared, sources loaded and baked out
September 11	First GaAs Sample grown
Oct/Nov/Dec	MBE System calibrated and high mobility samples grown
November	New Modulation doped PIN SL-APD modeled
1986	
February	Experimental Program started
Feb/Mar/April	N- and P-Type GaAs Samples grown and evaluated
May	Mew Modulation doped PN SL-APD conceived
May/June	N- and P-Type AlGaAs Sample grown and evaluated
June	AlGaAs/GaAs SL-structures grown
June	Masks for APDs designed and completed
July	Two patents for new device structures (PIN and PN SL-APD) submitted
August	PIN-APDs and SL-APDs grown and fabricated
September	Device structures evaluated

10. REFERENCES

1. S. Sze, Semiconductor Device Physics J. Wiley, 1965.

2. G. Lucovsky and R. B. Emmons, High Frequency Photodiodes, Appl. Optics 4, 697-702, (1965).

3. G. E. Stillman and C. N. Wolfe, Avalanche Photodiodes, Semiconductors and Semimetals Vol. 12, (Eds. R. K. Willardson and A. C. Beer, Academic Press, N. U. 1977). p. 291.

4. R. J. McIntyre, "Multiplication Noise in Uniform Avalanche Diodes, " IEEE Trans. Electron. Dev. ED-13, 164-168 (1966).

5. W. Ruegg, An Optimized Avalanche Photodiode, IEEE Trans. of Electron Devices, ED-14, 239-251 (1967).

6. Y. Matsushima, K. Sakai and Y. Noda, New Type InGaAs/InP Heterostructure Avalanche Photodiode with Buffer Layer, IEEE Electron Device letters, EDL-2, 179-181, p (1981).

7. K. Nishida, Taguchi, and Y. Matsumoto, InGaAsP Heterostructure Avalanche Photodiodes with High Avalanche Gain, Appl. Phys. Lett. 35, 251 (1979).

8. J. P. Gordon, R. E. Nahory, M. A. Pollack and J. M. Worlock, Low-noise Multistage Avalanche Photodetector, Electron. Lett. 15, 518-519, (1979).

9. F. Capasso, W. T. Tsang, A. L. Hutchison, and G. F. Williams, Enhancement of Electron Impact Ionization in a Superlattice: A New Avalanche Photodiode with a Large Ionization Rate Ratio, Appl. Phys. Lett. 40, 38-30 (1982).

10. R. C. Miller, D. A. Kirimman and A. C. Gossard "Energy Gap Discontinuities and Effective Masses for GaAs and $Al_xGa_{1-x}As$ Quantum Wells, Phys. Rev. B. 29 7085-7087 (1984).

11. F. Capasso, W. T. Tsang, A. L. Hutchinson and P. W. Foy, "The Graded Bandgap Avalanche Diode: A New Molecular Beam Epitaxial Structure with a Large Ionization Ratio," Proc. 1981 Symp. on GaAs and Related Compounds, 473-478 (1982).

12. G. F. Williams, F. Capasso and W. T. Tsang, The Graded Bandgap Multilayer Avalanche Photodiode: A New Low Noise Detector, IEEE Electron Dev. Lett. EDL-13, T1-73 (1982).

13. G. E. Stillman and C. M. Wolfe, Thin Solid Films 31, 69 (1976).

14. M. Heiblman, E. E. Mendez and L. Osterling, Growth by Molecular Beam Epitaxy and characterization of high purity GaAs and AlGaAs, J. Appl. Phys. 54, 6982-6988 (1983).

15. K. Ploog, Molecular Beam Epitaxy of III-V Compounds, Crystals, Vol. 3 Springer-Verlag, N.Y. (1980).

16. T. J. Drummond, W. T. Masselink and H. Morkoc, Modulation-doped GaAs/(Al,Ga)As heterojunction field-effect transistors: MODFETs. Proc. IEEE 74, 773-822 (1980).

17. H. Morkoc, L. C. Witkowski, T. J. Drummond, C. M. Stanchak, A. Y. Cho, and B. G. Streetman, "Growth Conditions to Achieve Mobility Enhancement in AlGaAs-GaAs heterojunctions by MBE," Electron. Lett., Vol. 16, pp. 753-754, 1980.

18. J. Singh and K. K. Bajai, "Theoretical Investigations or the Nature of the Normal and Inverted GaAs-AlGaAs Structure Grown by Molecular Beam Epitaxy," J. Vac. Sci. Technol. B, Vol. 2, pp. 576-591, 1984.

19. T. J. Drummond, S. L. Su, W. G. Lyons, R. Rischer, W. Kopp, H. Morkoc, K. Lee, and M. S. Shur, "Enhancement of Electron Velocity in Modulation Doped (AlGa)As/GaAs FETS at Cryogenic Temperatures," Electron. Lett., Vol. 28, pp. 794-796, 1982.

20. T. J. Drummond, R. Fisher, W. Kopp, H. Morkoc, K. Lee and M. S. Shur, "Bias Dependence and Light Sensitivity or (Al,Ga)As/GaAs MODFETs at 77K," IEEE Trans. Electron Devices, Vol. ED-30, pp. 1806-1811, 1983.

21. J. F. Rochette, P. Delescluse, M. Laviron, D. Delagebeaudeuf, F. Diamand, and J. Chevrier, "Low Temperature Photoconductivity in Two-Dimensional Electron Gain FETs," in Proc. 1982 GaAs Symp. (Inst. Phys. Conf. Ser.), Vol. 65, pp. 385-392, 1985.

22. D. V. Lang, R. A. Logan and M. Jaros, "Trapping characteristics and a donor complex (DX) model for the persistent photoconductivity trapping center in $Al_xGa_{1-x}As$," Phys. Rev. G, Vol. 19, pp. 1015-1030, 1979.

23. K. Hikosaka, T. Mimura, and S. Hiyamizu, "Deep Electron Traps in MBE Grown (Al,Ga)As Ternary Alloy for Heterojunction Devices," in Proc. 1980 GaAs Symp. (Inst. Phys. Conf. Ser.), Vol. 63, pp. 233-238, 1981.

24. P. Chen, J. Y. Kim, A. Madhukar and N. M. Cho, Optimal Surface and Growth Front of III-V Semiconductors in Molecular Beam Epitaxy, J. Vac. Sci. Technol. B 4, 890-895 (1986).

25. T. Sakamoto, H. Funabashi, K. Ohta, T. Nakagawa, N. J. Kawai, and T. Kojima, Phase-Locked Epitaxy Using RHEED Oscillation, Jap. J. Appl. Phys. 23, to be published (1984).

26. J. N. Neave, B. A. Joyce and P. J. Dobson, Dynamic RHEED Observations of the MBE Growth of GaAs, Appl. Phys. A 34, 179-184 (1984).

27. J. M. Van Hore, P. R. Pukite, and P. I. Cohen, The Dependence of RHEED Oscellations on MBE Growth Parameters, J. Vac. Sci. Technol. B 3, 563-567 (1984).

28. M. Hieblum, W. I. Wang, L. E. Osterling and V. Deline, J. Appl. Phys. 54, 6751 (1983).

29. M. Ogawa and T. Baba, Heavily Si-Doped GaAs and AlAs/n-GaAs Superlattices Grown by Molecular Beam Epitaxy, Jap. J. Appl. Phys. 24, 6572-6574 (1985).

30. E. F. Schubert, Y. Horikoshi and K. Ploog Radioactive electron-hole recombination in a new sawtooth semiconductor super lattice grown by molecular-beam epitaxy, Phys. Rev. B 32, 1085-1089 (1985).

31. S. Sasa, S. Muto, K. Kondo, H. Ishekawa and S. Hiyomizu, Si Atomic-Planar-Doping in GaAs Made by Molecular Beam Epitaxy, Jap. J. Applied Phys. 24, L602-L604 (1985).

32. A. Rockett, J. Klem, S. A. Barnett, J. E. Greene and H. Morkoc, Si Incorporation and Segregation in $Ga_{1-x}A_xAs$ (100) Films Grown by Molecular Beam Epitaxy, J. Vac. Sci. Technol. B4, 519-520 (1986).

33. S. A. Barnett and J. E. Greene, Surf. Sci. 151, 67 (1985).

B-10-635
7-9

IN CONFIDENCE

HIGH PERFORMANCE PHOTODIODES

Quarterly Report No. 7, 8, 9
Report Period: 1 October 1986 - 30 June 1987

Project No. A-4233

Prepared for:

Dr. Kenneth A. Maloney
Polaroid Corporation
Microelectronics/Materials Center
21 Osborn Street, Dept. 775
Cambridge, MA 02139

Prepared by:

Dr. C. J. Summers and Dr. K. F. Brennan
Georgia Institute of Technology
Atlanta, GA 30332

1. SUMMARY

In this phase of this program, substantial progress was made in both the theoretical understanding of these devices and the growth and fabrication technologies of advanced superlattice avalanche photodiode detectors (SL-APD).

In the theoretical area, studies continued into the basic physics of impact ionization and avalanching devices. It was demonstrated that the enhancement of the electron ionization rate in a SL is a special case for devices in a linear or spatially periodic electric field and the optimum geometry for a AlGaAs/GaAs SL was predicted. Also, new device geometries, the p-n homojunction and the p-n heterojunction SL-APD were investigated.

Significant progress was also made in developing new growth techniques to achieve very planar interfaces and high n- and p-type doping in thin GaAs and AlGaAs layers. A reflection-high energy electron diffraction RHEED system was set up in the Varian system and used to measure RHEED oscillations during growth. From these measurements the thickness of the layers can be controlled to one monolayer thickness of GaAs (2.83Å) and also the composition of AlGaAs determine to within 2%. Pulse and delta doping studies in GaAs also showed the limitation of the former technique and the potential of the latter method.

The highlights of this program are described in Section 3, which summarizes oral reports given to Polaroid in December 1987. The final report for the second phase of this program will be submitted to Polaroid in March 1988. Section 4 describes the work proposed for the next phase of this contract in theoretical modeling, materials growth, and device fabrication and evaluation, which for completeness if preceded by a discussion on new avalanche photodiode structures.

2. BACKGROUND AND TECHNICAL DISCUSSION

One of the most effective structures for realizing the requirements for fast infrared detectors is a shallow junction n-i-p device in which the space-charge depletion width is greater than $2/\alpha$, where α is the absorption coefficient of the detector material at the signal wavelength.[1,2] For this design criteria 90% of the signal radiation is absorbed within the depletion region and creates an electron-hole distribution that is immediately separated and sensed by the junction. The frequency response of the device is then given by the transit time for carriers to drift across the junction and/or the RC time constant resulting from the capacitance and resistance of the space-charge region and external circuitry. By constructing p-i-n structures in which the signal radiation is absorbed in the depletion width and using small devices to limit the RC product, operation to 10 GHz is possible with high signal-to-noise ratios.

Avalanche Photodiode (APD)

As is well known, the performance of a p-i-n device can be significantly enhanced by reverse biasing to the avalanche condition so as to provide internal gain. In this process the photo-excited free carriers are accelerated by the electric field and gain sufficient energy such that a collision with a valence electron excites the electron to the conduction band, leaving a free hole in the valence band. This process, called impact ionization, is repeated for the newly generated electron and hole which in turn impact ionize and produce more carriers. Thus, the avalanche process can provide very large amplification of the original signal. It should be noted that the avalanche mechanism also produces more noise, but for typical detector applications where the thermal noise of the external circuitry dominates the total device noise, the current gain produced by avalanche multiplication results in a corresponding increase in the total system signal-to-noise ratio.[3]

Thus, to optimize the performance of an APD it is necessary to maximize the current gain and to minimize the excess noise contribution from the avalanche process and its effect on the bandwidth of the diode. Theoretical considerations show that these conditions can be realized when there is a large difference between the carrier ionization rates and the avalanche is initiated by the carrier with the higher ionization coefficient.[5] It is also found that this situation makes the multiplication rate of charge carriers less strongly dependent on field strength, enabling better control to be obtained over the gain processes.

The material requirements for avalanche photodiodes are therefore a high absorption coefficient to absorb the radiation in the depletion width, high drift velocities to minimize carrier transit times, and a large difference between the electron and hole ionization rates. To simultaneously realize all of these conditions in a simple p-n junction device is impossible and thus, to avoid compromising performance, new device structures have been developed.

A significant advance in APD design was made with the introduction of the reach-through structure shown in Figure 1.[5] In this structure the function of the p^+-π-p region is to absorb the photon flux and provide a high electric field to separate the electron-hole pairs produced by photo-annihilation. Holes are immediately swept to the p^+ junction and out of the device; concurrently electrons are accelerated to their maximum drift velocity. When the electrons reach the p-type layer they are accelerated further by the high field across the narrow p-π-n^+ region to produce charge multiplication and current gain. Thus, the processes of electron-hole pair generation and charge multiplication are spatially separated, making it possible to optimize each process and the total performance of the device by the correct choice of doping profiles, structure length and applied voltage. The quantum efficiency and speed of response of the device are determined by the p^+-π-p region. Near unity quantum efficiencies can be obtained by making the length of this

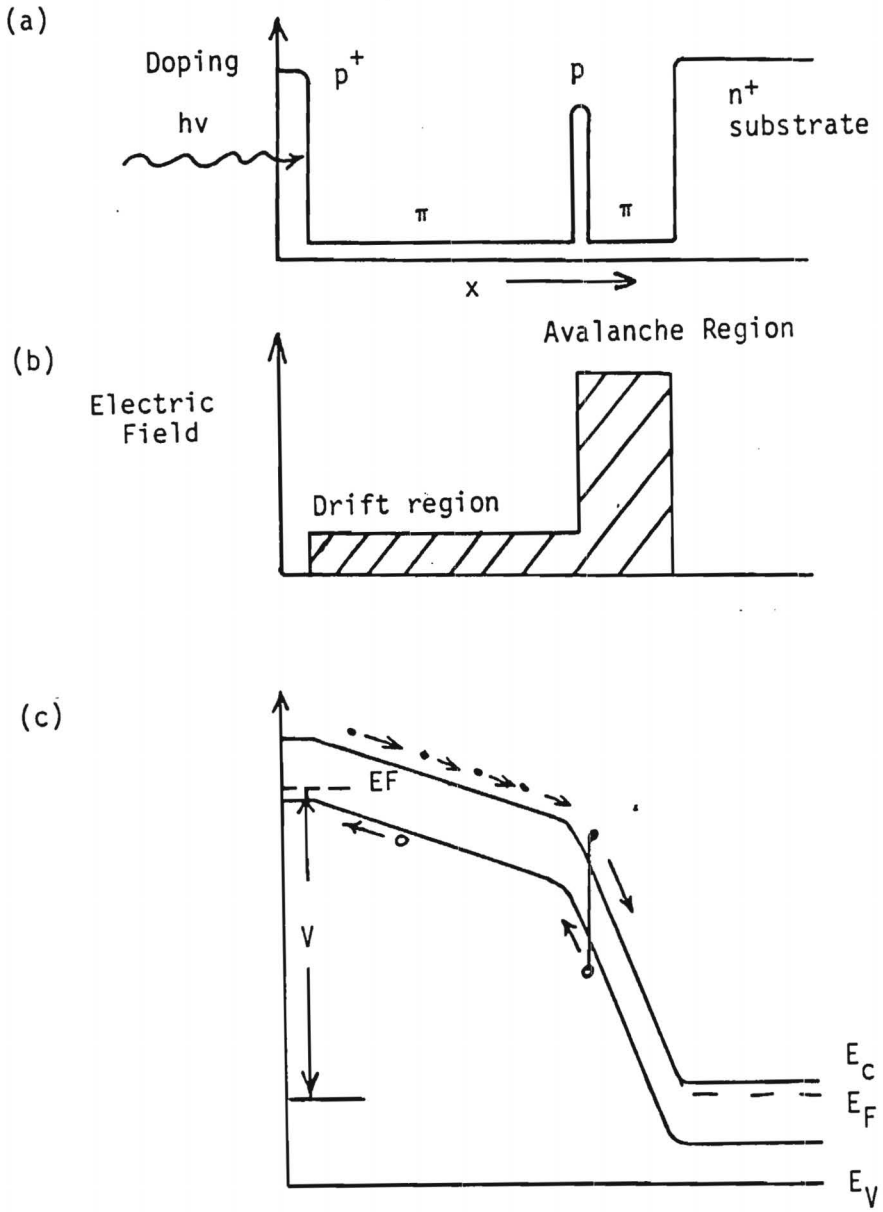

Figure 1. Reach - Through APD, (a) Doping Profile (b) Electric Field Distribution (c) Energy Band Diagram Under Bias Conditions.

region equal to $2/\alpha$. The speed-of-response is limited by the limiting carrier velocity in the $p^+-\pi-p$ region divided by its length. Thus, for carrier velocities of approximately $2x10^7$ cm/s and > 10^4, bandwidths greater than 100 GHz are possible.

The most successful APD devices to date have used Si because the electron ionization rate is much greater than the hole ionization rate in this material. Germanium APD's whose spectral response extends out to 1.8 um have been developed but are very noisy because the electron and hole ionization rates are nearly equal.

At present, the major thrust in APDs is to use alloys based on III-V semiconductor systems such as AlGaSb, GaInAs, and InGaAsP, because these semiconductors allow the wavelength response of the diode to be varied by adjusting the alloy composition. These material systems can also be lattice matched over an appreciable range of alloy compositions, thus enabling the fabrication of heterojunction devices that can result in a significant improvement in device performance. It should be emphasized that exact lattice matching is essential for these structures because a mismatch between layers will produce interface states and stress gradients that will degrade device performance and result in failure at high electric fields.

Besides improving device characteristics it has recently been realized that new device structures can be fabricated by molecular beam epitaxy that enables the ionization ratio between electrons and holes to be artificially enhanced. This is very significant because for most III-V semiconductors the electron and hole ionization rates are nearly equal.[3] Several schemes being investigated for enhancing the performance of APDs are described below.

Heterojunction APD (HAPD

This device is the simplest of the new heterojunction structures currently being investigated and has principally been fabricated in GaInAs and GaInAsP alloys grown on InP.[6,7] These alloys are used because they can be perfectly lattice matched to

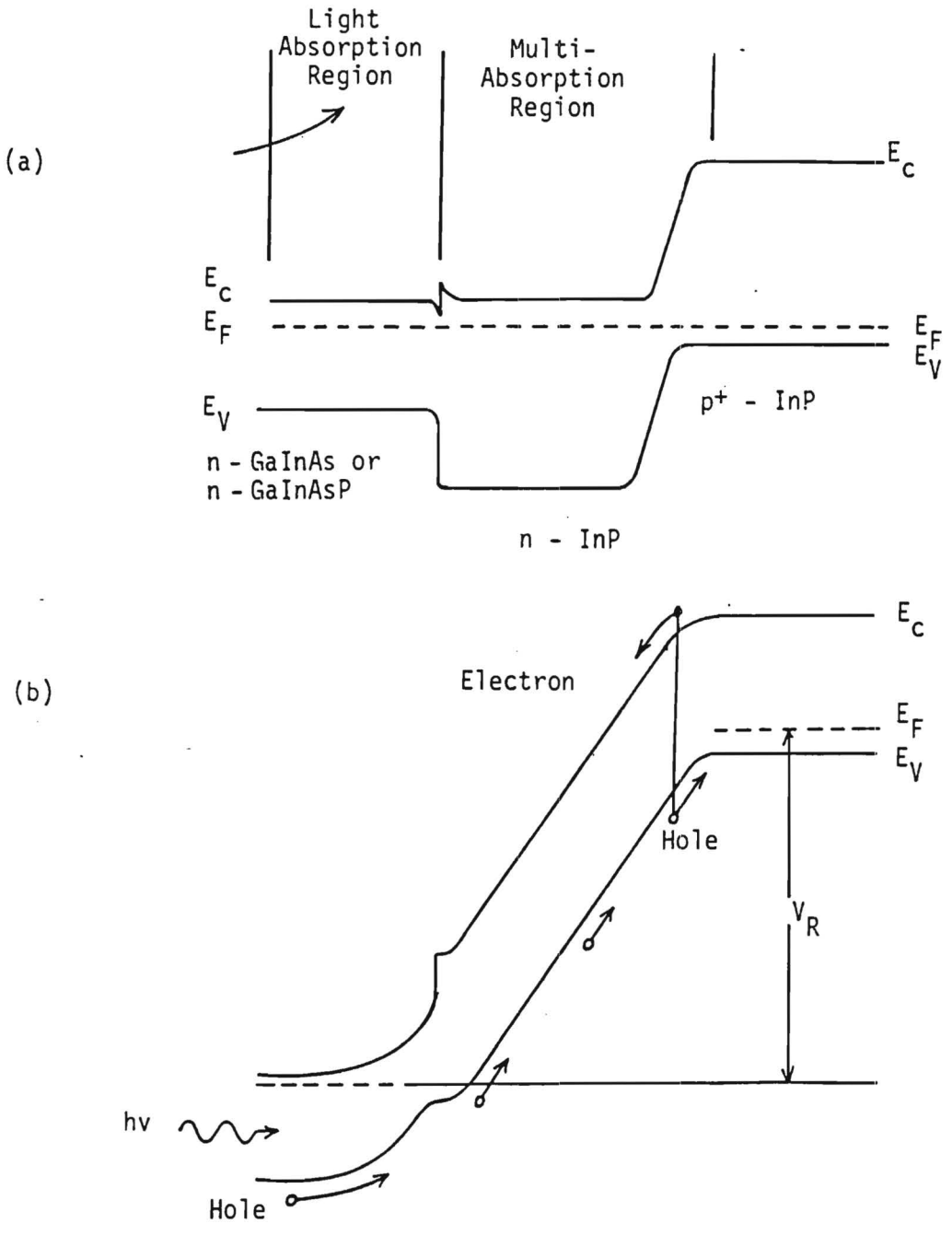

Figure 2. (a) Energy-band Diagram of a InP-GaInAs Heterojunction at Equilibrium. (b) Energy-band Diagram at Avalanche Breakdown.

InP and have a spectral response extending to 1.6 um as required for optical fiber communication links. The actual structures used are n-GaInAs/n-InP/p^+-InP, n-GaInAsP/n-InP/p^+-InP or n-InP/n-InP/p^+-InP, where the extra InP layer in the last device is used as a window. As shown in Figure 2, light is absorbed by the ternary or quarternary layer, and the avalanche process is optimized to achieve hole injection by adjusting the doping and layer thicknesses so that under reverse bias the n-InP depletion layer reaches through into the GaInAs or GaInAsP layer. The heterojunction is used to reduce the dark current leakage in the device, thus enabling higher voltages to be applied to increase the gain. The performance of these devices is significantly better than achieved with Ge APDs, but because the hole to electron ionization ratio is small, it is far from that possible with a more optimized material or device structure.

Superlattice APD

A third type of APD structure recently proposed and demonstrated by Capasso et al.[8] makes use of the dependence of the ionization rate on bandgap energy and the conduction band edge discontinuity between undoped GaAs and AlGaAs layers to produce an enhancement of the effective ionization ratio. The band structure of the device under reverse bias is shown in Figure 3. The device consists of a p^+-type photo-collection electrode, a superlattice avalanche region consisting of 50 alternating GaAs and AlGaAs layers and an n^+-type collection electrode. The composition of the AlGaAs is adjusted to give a 0.5 eV discontinuity between the conduction band edges of AlGaAs and GaAs. The photo-excited electrons are accelerated into the superlattice region and gain an energy several tenths of an electron volt above the conduction band energy of AlGaAs. When the hot electron enters the GaAs well, it experiences a reduction of the ionization threshold energy equal to the energy discontinuity between the AlGaAs and GaAs layers. Because the ionization rate increases rapidly for decreasing ionization threshold energy, the electron ionization rate is increased by

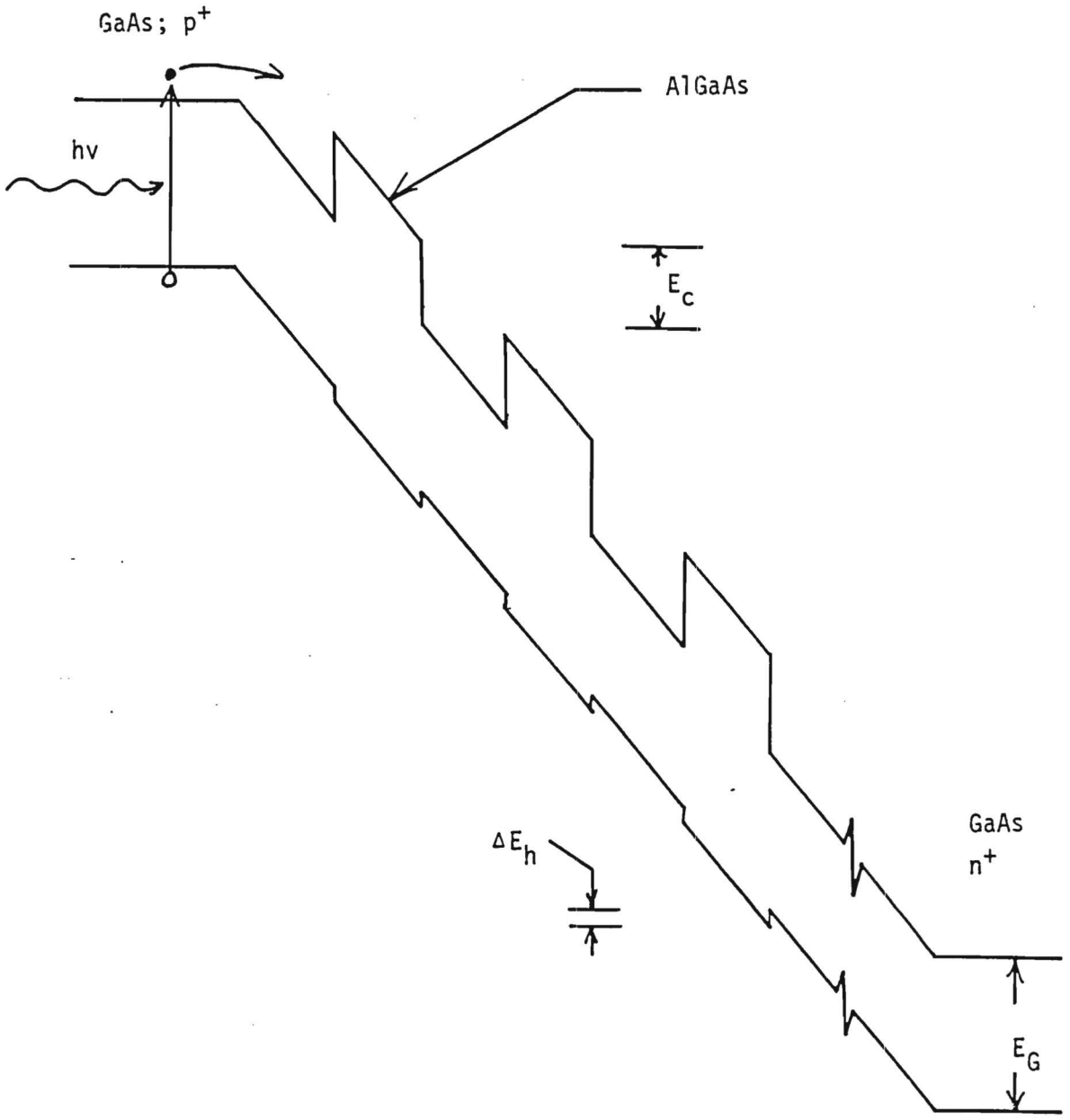

Figure 3. Energy Band Diagram of Superlattice APD.

this structure. As the electron re-enters the next AlGaAs layer, the reverse situation occurs and the electron ionization rate decreases. However, because the ionization rate is larger in GaAs than in AlGaAs and the GaAs layer can be made thicker than the AlGaAs layer, a net increase in the ionization rate is observed. The small discontinuity in the valence band has little impact on the ionization rate for holes which essentially remains unaltered. Thus, this structure produces an enhancement of the electron to hole ionization ratio. This device has been fabricated and shown to have an electron to hole ionization ratio of 10. It should be noted that the magnitude of the enhancement of the electron to hole ionization ratio is strongly dependent on the size of the conduction and valence band-edge discontinuities between the AlGaAs and GaAs layers. Conventionally, the energy difference in the vacuum potentials between the GaAs and AlGaAs layer is assumed to be shared in the ratio 85:15 between the conduction and valence band edge discontinuities. But recent optical data suggest the ratio should be closer to 57:43[10]. This difference will have a large effect on the optimum attainable electron to hole ionization ratio, and thus, investigations need to be performed to establish its precise value. The influence of the conduction band effective mass on this ratio also needs to be measured.

Graded Bandgap Multilayer APD

The purpose of this structure is to cause only electrons to be ionized, thus producing high signal gains with very low noise.[11,12] (Fig. 4). The structure consists of a graded-bandgap multilayer structure, each stage of which is linearly graded in alloy composition from a low bandgap energy (E_{G1}) to a high bandgap energy (E_{G2}) followed by an abrupt step back to the low bandgap energy. The materials of the structure are chosen such that the largest bandgap difference produces an energy discontinuity greater than the electron ionization energy, E_1, in the low bandgap material. The operating conditions of the structure are shown in Figure 4b. A photon-excited electron in

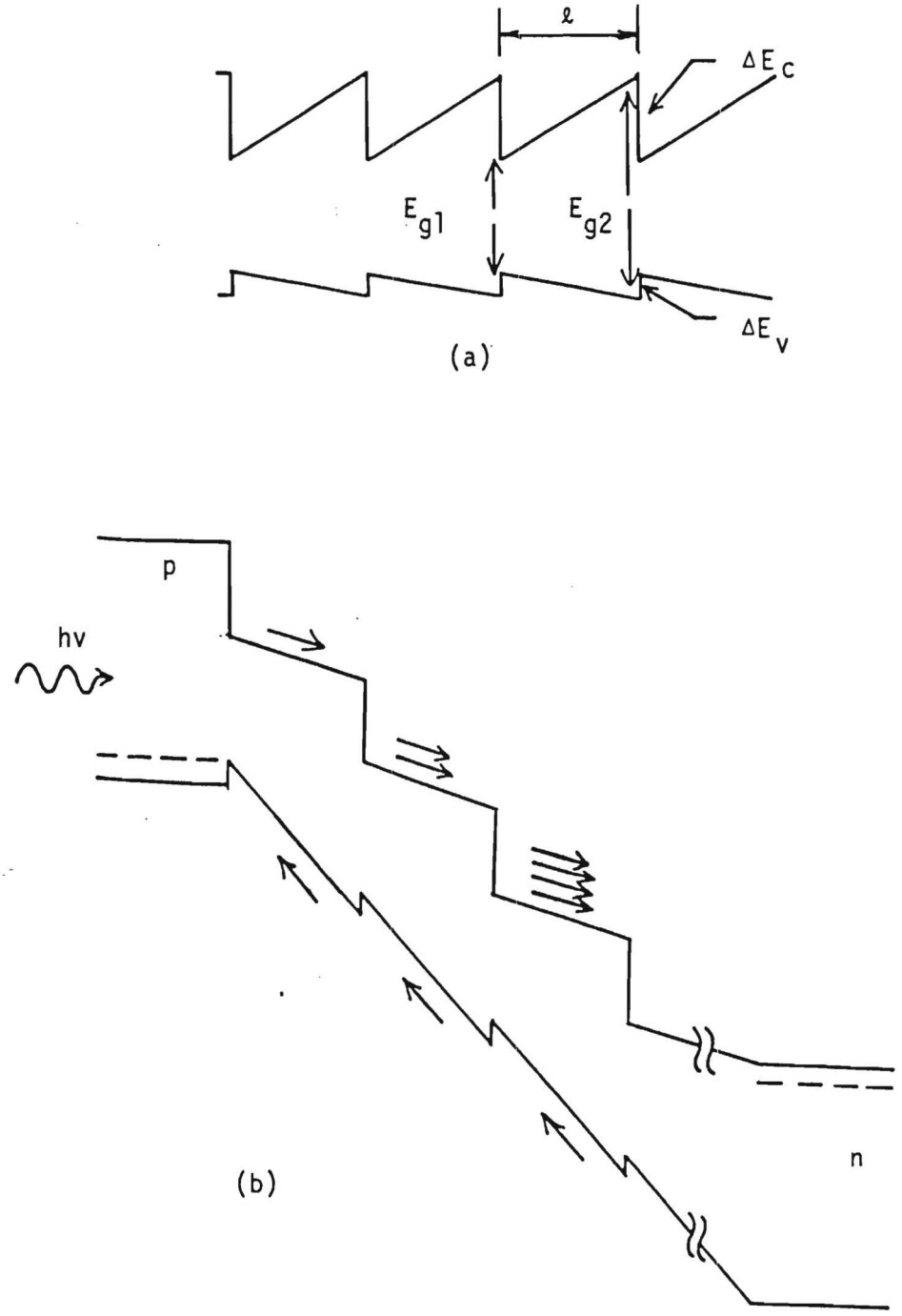

Figure 4. Band Diagrams for (a) the Unbiased Graded Multilayer Region and (b) the Complete Detector Under Bias.

the p^+ region experiences the combined field of the electrical bias and bandgap grading which accelerates it toward the first step. The field is small enough so that the electron does not impact ionize before it reaches the step. At the step, impact ionization occurs because the energy discontinuity is greater than E_1. This process is repeated for each step as shown in the figure. At each step the maximum theoretical gain is two, giving a theoretical gain for the structure of $(2-\delta)^N$, where N is the number of graded layers and δ is the loss at each stage. For a perfect structure the major loss mechanism is expected to be from optical phonon emission. However, this is predicted to be small because it must be involved in a multi-phonon process to lose all of the ionization energy of the electron and because the electron-phonon interaction can be minimized by making the interface region between the high and low bandgaps smaller than the mean free path for phonon scattering, <100A.

Because the energy steps provide most of the energy for ionization the operating voltages are very low (<5V) which also minimizes the device leakage current. A single graded layer device has recently been tested in the AlGaAs system and shown to produce a significant enhancement in the electron-to-hole ionization ratio.

3. REVIEW OF PROGRESS

3.1 Theoretical Program

Substantial progress was made throughout calendar year 1987 in the theoretical part of the program. The key problems addressed can be broken down into two main thrusts, the basic physics of impact ionization and avalanching devices, and new device structures and their performance. The former program addressed the issue of the physical origin of the electron ionization rate enhancement in a multiquantum well structure. We have developed an analytical proof of the enhancement effect based on a fundamental, first principles formulation of the problem using Shockley's lucky electron theory. It was found that due to the nonlinear aspects of impact ionization, that the ionization rate can be significantly enhanced by the super position of a uniform electric field and any spatially periodic electric field. The result is quite general, and therefore applies to all of the superlattice device structures considered in this program. This work was published in Applied Physics Letters.[13]

We further probed the underlying physics of the enhancement effect using our numerical, Monte Carlo formulation. Specifically, we determined the field and geometry dependence of the electron and hole ionization rate in a simple multiquantum well device. The net rate, the weighted average of the GaAs and AlGaAs layer rates, greatly depends upon both the layer widths and the magnitude of the applied electric field. Even though the electron ionization rate is enhanced over its corresponding bulk rate in the GaAs layer, the net superlattice rate may not exceed the comparable bulk GaAs rate. This is because the addition of the AlGaAs layer, though it acts to enhance the rate in the GaAs, acts as a dead layer in which no ionization occurs. Therefore, in order for the net rate, found from averaging over <u>both</u> layers, to exceed the bulk GaAs rate, the extent of the enhancement of the ionization rate in the GaAs must be large enough to offset the effect of the AlGaAs dead layer.

It was found that under certain conditions of applied field and layer widths, that the net superlattice electron ionization rate exceeds the corresponding weighted average of the bulk rates by an order of magnitude. This implies that the ionization rate in the GaAs layer in the superlattice is much greater than the corresponding bulk GaAs rate. The greatest enhancement in the electron ionization rate as well as the largest ratio of the electron to hole ionization rates occurs in a 500/500 A, GaAs/AlGaAs unit cell structure with an applied electric field of 250 kV/cm. At higher electric fields, the net superlattice rate approaches the weighted average of the bulk rates. This is not surprising since at high electric fields the effect of the potential discontinuity on the carrier temperature is less significant. Most of the carrier heating is due to the action of the electric field, resulting in bulk-like behavior of the ionization rates.

The second part of the theoretical program was focused on new superlattice avalanche photodiode structures and their performance characterization. We analyzed two variations of the doped quantum well device, the p-n homojunction and p-n heterojunction APDs. This work resulted in four publications[14-17]. It was found that the doped quantum well device outperforms the simple and graded barrier devices. In fact, the doped quantum well device offers four orders of magnitude enhancement of the electron ionization rate over the hole ionization rate as compared to roughly one order of magnitude improvement in either the simple or graded barrier devices. The dramatic enhancement of the electron ionization rate translates into improved gain to noise performance as well as larger bandwidth operation.

Of great importance was the finding that the p-n junction device offers comparable performance to the p-i-n doped quantum well device, but can be grown more easily by MBE. The p-n junction structure is more easily realized than the p-i-n device, since it places less stringent requirements on the doping concentrations necessary in the p and n layers of the unit cell. P-n devices doped to roughly one third the concentration in

corresponding p-i-n devices are predicted to yield comparable gain to noise ratios as well as bandwidths. Therefore, we have embarked on the experimental realization of these structures.

3.2 Material Growth Studies

The materials growth and device fabrication development also made significant advances in 1987. Both material quality and control over the layer thickness and heterojunction interface quality improved considerably. Further, our basic understanding of the growth dynamics was advanced to a level such that important contributions can be made to improve the quality of SL-APD materials and devices.

Over the year more than 20 samples were grown for SL-APD devices, with various parameters varied from one run to the next. These devices exhibit reverse biased breakdown voltages of 80-140 V with dark currents about ~10 pA. The success of these devices are heavily dependent on our current understanding of the process involved in photocurrent generation in SL-APDs and the optimization of various material parameters. Parameters of prime importance for these devices are: quantum well and barrier thickness, which should be known and controlled to high accuracy, the heterojunction interface smoothness, and the control of n- and p-type doping over very small dimensions.

A major accomplishment was the development of experimental tools and theoretical models to use RHEED intensity oscillations. Using RHEED oscillations we have been able to clarify many points about the material growth. By observing the specular reflection beam during crystal growth, it is possible to observe intensity oscillations which are indicative of layer by layer deposition of a thin film. Figure 5 shows the growth of (a) AlGaAs, (b) AlAs and (c) GaAs during the deposition of ~10 monolayers. These techniques make it possible to control the growth rate to less than 2% accuracy and to fabricate quantum wells with well widths predetermined to within a single atomic layer (2.83Å). Also, by using RHEED intensity oscillations the Al mole fraction can be determined to less than 1% prior to growth. Another advantage of

RHEED OSCILLATIONS DURING GROWTH OF GaAs, AlAs, and AlGaAs

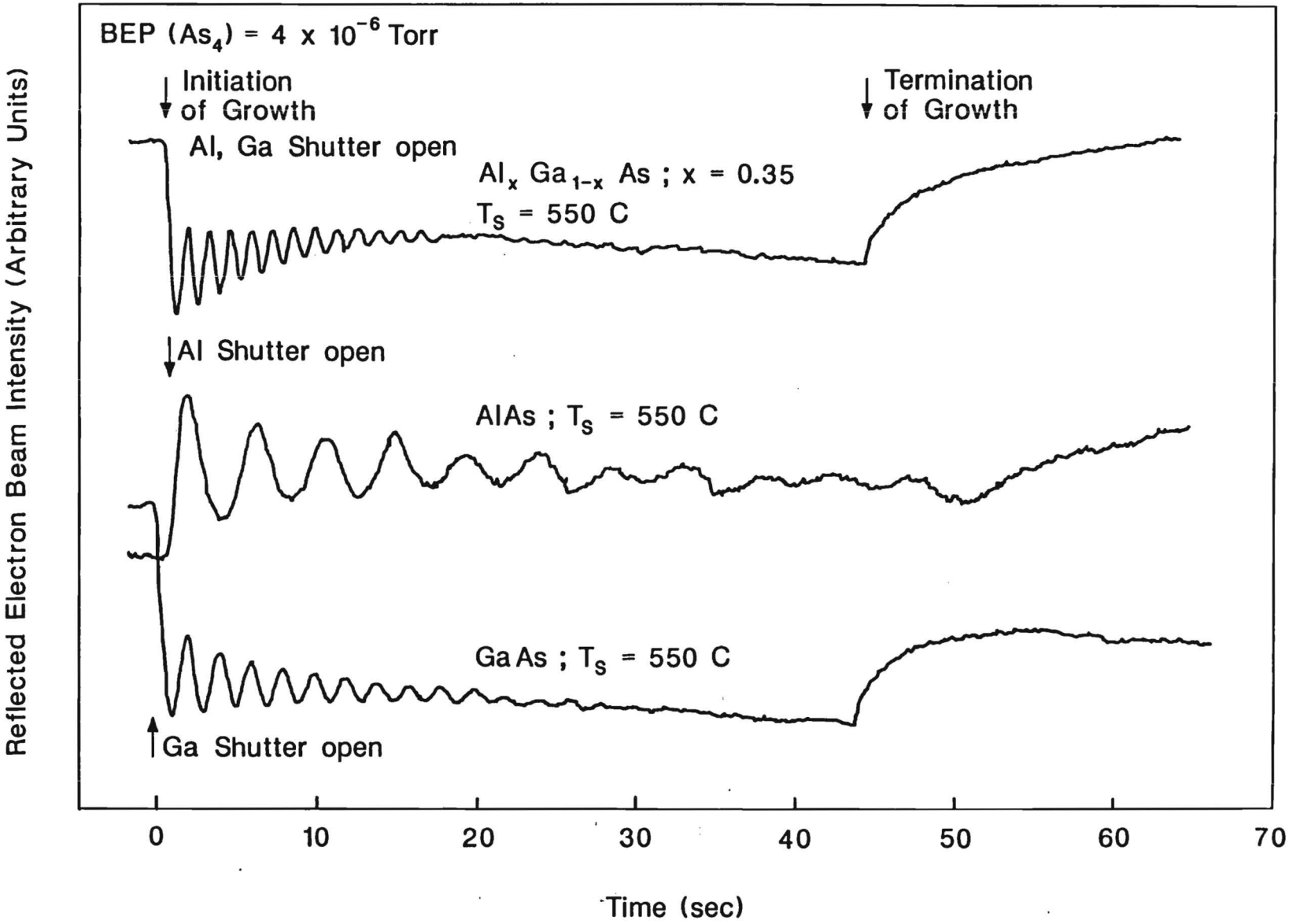

Figure 5. RHEED Oscillations Obtained During the Growth of AlGaAs, AlAs and GaAs.

the RHEED development has been the information it proves on enhancing the heterojunction interface smoothness and uniformity. RHEED intensity oscillation experiments have indicated the proper approach to interface smoothening, which is essential to the operation of high performance SL-APDs.

Characteristics of single quantum wells show that these can be fabricated with only one to two monolayer width differences and that it is possible to detect luminescence from each well.[18,19] The x-ray data shown in Fig. 6 also confirm the high quality of these superlattice structures by the measurement of 15-20 arc second diffraction width lines, which is indicative of the uniformity of the layers. Auger and SIMS analysis on these superlattices also gave excellent profile definition.

In other developments we have demonstrated controlled n- and p-type doping of GaAs and obtained precisely controlled doping profiles to within 20% doping level accuracy (Fig. 7). The p-type doping of AlGaAs also seems to be well controlled, but n-type doping of AlGaAs with Si has produced some difficulties in confining the high doping profile to thin regions. The diffusion of the dopant (Si) appears to be strongly concentration dependent. Work is in progress to circumvent this difficulty.

We have also investigated the delta doping of (Al, Ga)As in a set of recent experiments. In these experiments doping is performed in a very thin sheet on one atomic plane at very high concentrations. The net effect is that planar doped layers act similar to bulk doping with the added advantage of confining the dopants and avoiding dopant diffusion. The first set of experiments produced sheet doping of 7×10^{12} cm^{-2}, which is equivalent to $2 \times 10^{19} cm^{-3}$ bulk doping. Further, the C-V profile measured for this sample and shown in Fig. 8 indicates that the FWHM for this sample was ~100Å and that the doping varied by 4 orders of magnitude within 0.1 um. These results are very encouraging and we foresee considerable use of this technique.

In summary, because of the progress made in material growth and the improved understanding obtained of the basic physical processes involved, we are in an excellent position to fabricate

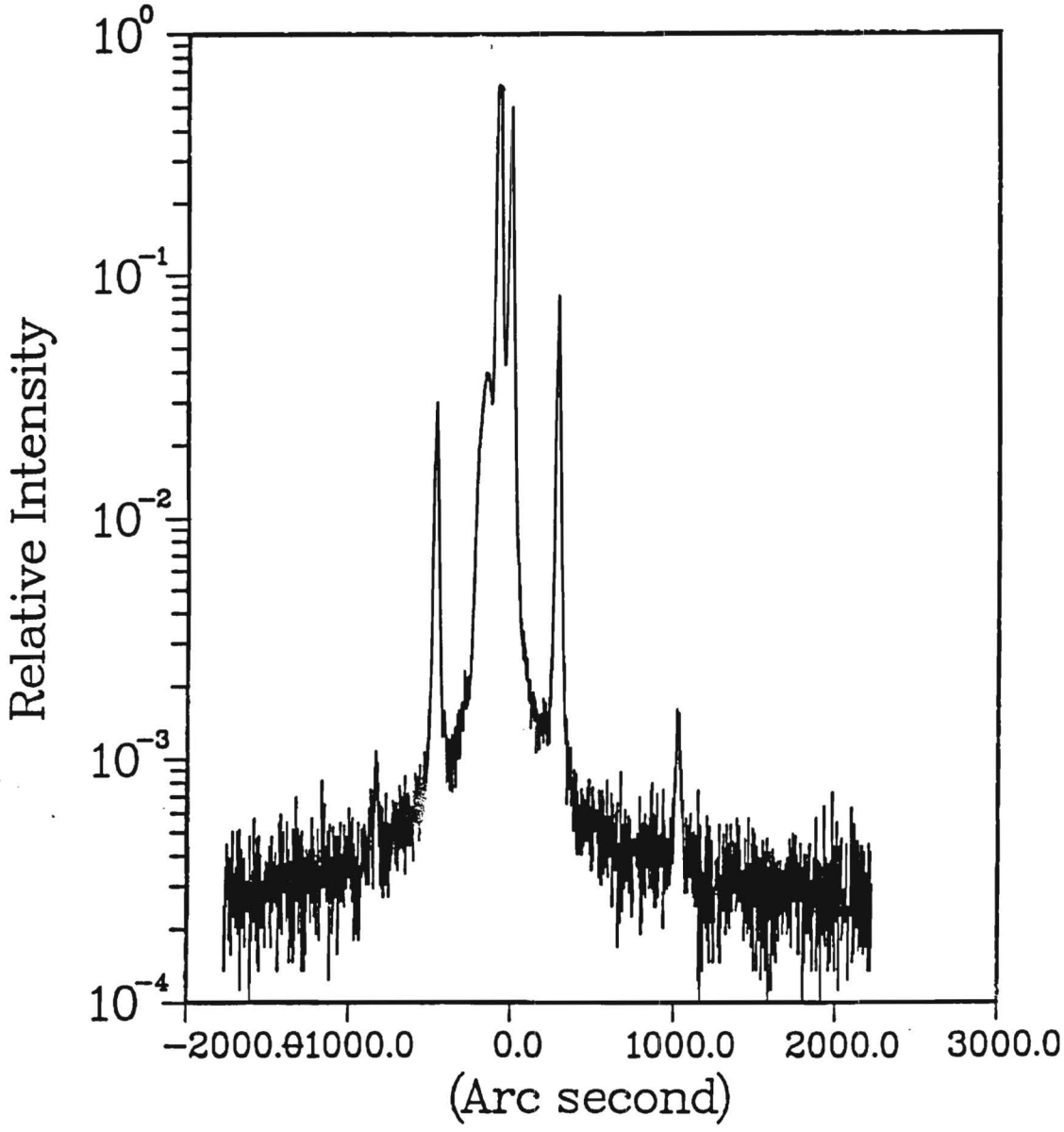

Figure 6. Double Crystal Rocking Curve Measured on a Superlattice Structure with Equal Barrier and Well Widths of 300Å.

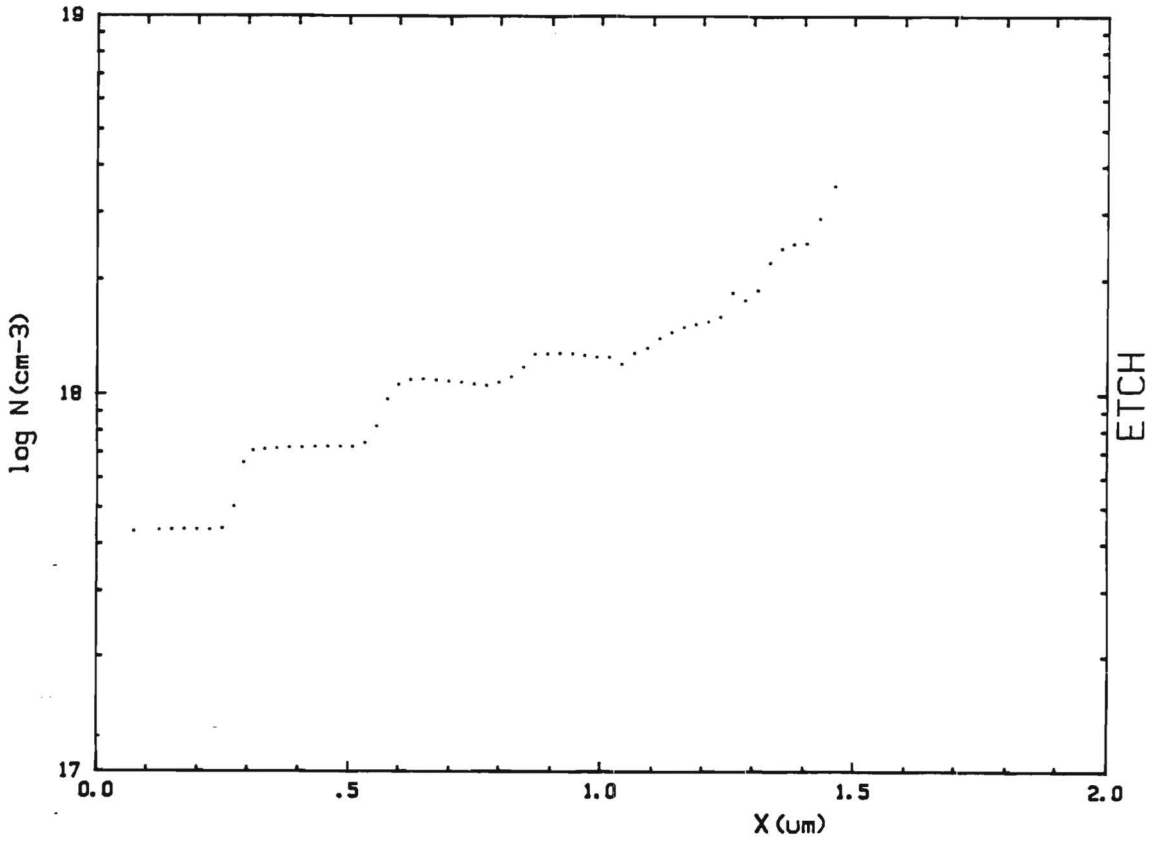

Figure 7. Polaron Plot of Electron Concentration Profiles Grown Into Si Doped GaAs.

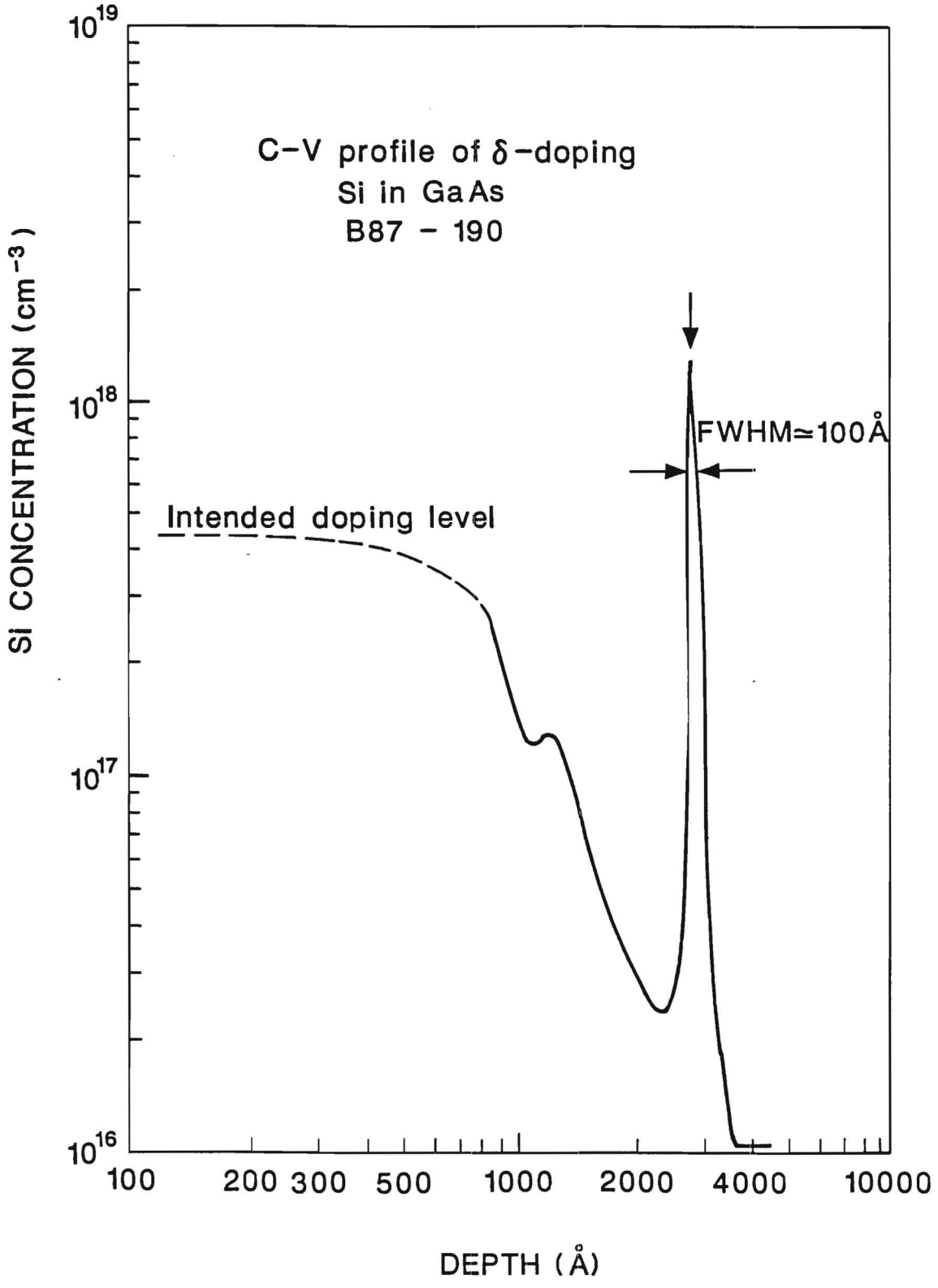

Figure 8. C-V Profile of Delta-Doped GaAs:Si Sample.

high performance SL-APDs. We have also explored new directions to improve various device parameters and thus, device performance.

3.3 APD Device Fabrication

Low leakage current avalanche photodiodes have been fabricated on MBE grown AlGaAs/GaAs heterostructures. Primary tasks which were addressed in this part of the research project are discussed in this section. These tasks include mask set design, fabrication processes, semiconductor etching, device fabrication, assembly and electrical characterization.

Mask Set Design

A quality mask set is required to fabricate high performance avalanche photodiodes. Features which Polaroid and Georgia Tech researchers considered important were top side contacts for the cathode and anode, multiple active areas to assess edge effects, provisions for back side illumination and diagnostic structures to monitor contact resistance. Four active area designs were developed and included 75, 100, 130 and 200 micron diameters. The p^+ contact pad was designed to be as small as possible since it is a part of the mesa structure. A novel flip chip diode structure was also included in the mask design. This device, which has no p^+ contact pad, is a high risk device with respect to packaging; however, it should be the highest performance due to minimum parasitic capacitance.

Five masking levels are included in the mask design. The p^+ level forms the anode contact to the device. Mesa definition is the second level and is used to isolate the devices and to provide a region for the n^+ contact. The n^+ contact is the third level and forms the cathode contact. Passivation is the fourth level in the set and is used to remove dielectric coatings in the bond pad and scribe regions. Via is the fifth level and is used to thin the device to permit back side illumination.

Semiconductor Etching

APD device fabrication, proposed in this research, requires both selective and nonselective etchants. Hydrogen peroxide, pH adjusted to 7.05, was found to be reasonably selective as an etchant for GaAs with respect to AlGaAs, even with Al fractions as low as 0.35. Hydrogen peroxide will react with AlGaAs; however, the reaction tends to be self limiting due to the formation of a surface oxide. Etch stop layers of AlGaAs on the order of 1000Å thick are adequate when using hydrogen peroxide.

Concentrated hydrofluoric acid at 60°C etches $Al_{0.4}Ga_{0.6}As$ at a rate of 0.1 micron per minute. When the Al fraction is increased to 0.6, the etch rate increases to approximately 0.15 microns per minute. GaAs layers were not affected by HF at this temperature.

Nonselective etches which were evaluated included Methanol:H_3PO_4:H_2O_2 in the ratio of 3:1:1 and H_3PO_4:H_2O_2:Di water in the ration 3:1:50. Both etchants appear to be nonselective and relatively isotropic. 3:1:1 etches GaAs/AlGaAs at approximately 2.5 microns per minute at 25°C. 3:1:50 is a much slower etch, having a rate of 0.1 micron per minute.

The methanol based etchant was predominantly used to etch the mesas. It was found that the mesa profile can vary considerably as function of time after mixing the etchant. Figure 9 shows mesas which were etched at different times after mixing the etchant. Best results were obtained when etching soon after mixing.

Fabrication Processes

Three fabrication processes have been developed to investigate APD performance. MBE layers grown on conducting substrates can be fabricated into devices using a simple one level mask process in which the p^+ contact mask also serves as the mesa etch mask. Cathode contact is made to the back side of the wafer. This process provides quick information on MBE growth runs; however, optical absorption is restricted to the mesa edge.

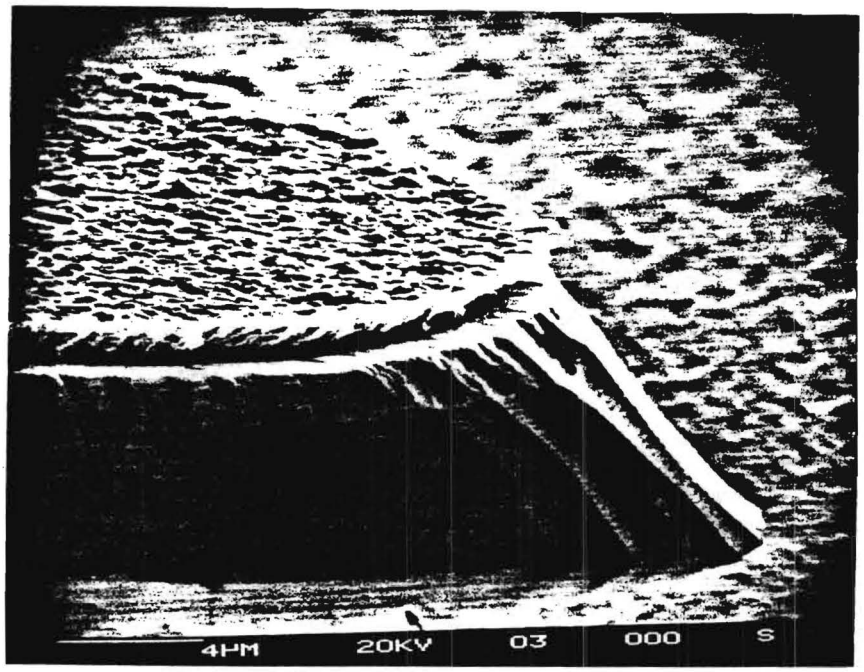

Figure 9a. Mesa Profile Obtained by Etching Soon After Mixing Etchant.

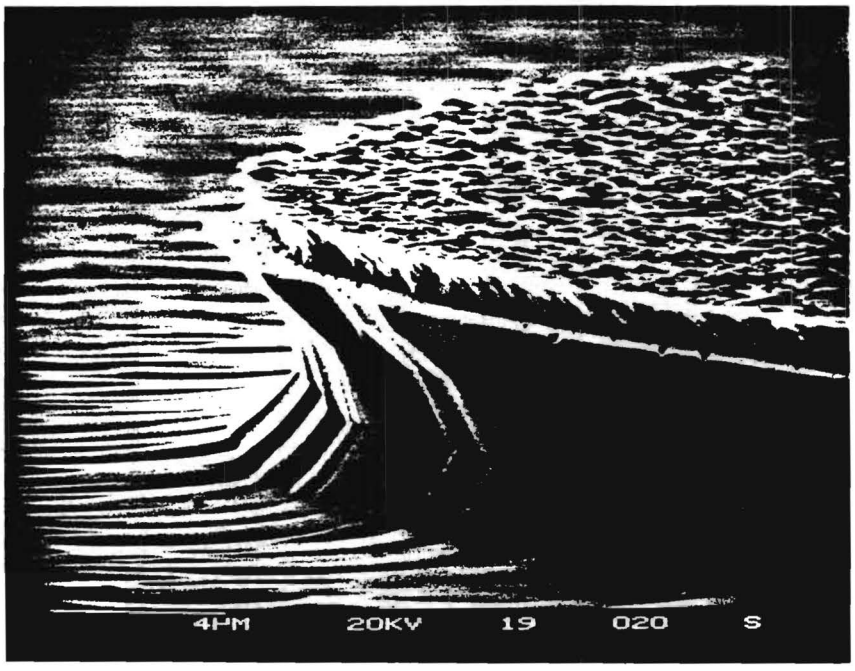

Figure 9b. Mesa Profile Obtained Using Old Etchant.

Fabrication process two utilizes 4 levels of the 5 level mask set. Both p^+ and n^+ contacts are on the top side of the wafer and passivation can be incorporated into the structure. Process three is identical to process two with respect to front side processing; however, provision for back side illumination is included in process three.

AuZn [95%-5%] is used for p^+ contacts. Best results have been obtained when substrates are heated to 140°C prior to deposition. AuGe-Ni-Au is used for the n^+ contact. This metallization scheme is a standard process providing contact resistance on the order of 0.2 ohm-mm on $2x10^{17}$ cm^{-3} doped layers.

Device Fabrication

Using the processes described above, over eleven MBE wafers have been processed. Figure 10 is an SEM micrograph of a device fabricated with process one. Wafers B87-80 and B87-84 have been processed with process two and a device typical of this process is shown in Figure 11.

Assembly

After wafer fabrication, the APD wafers are mounted on a silicon host wafer and the APD wafer is diced completely through using a Microautomation Model 1006 dicing saw. Separated chips are removed and cleaned and mounted in standard 161d dual-in-line integrated circuit packages using silver epoxy. Electrical connection to the anode contact is made using 0.7 mil gold wire with thermocompression bonding techniques.

Electrical Characterization

DC characteristics of the fabricated APDs have been evaluated at Georgia Tech using a curve tracer and an HP 4145A semiconductor parameter analyzer. Figure 12 is representative IV signatures. Figure 13 is a plot of the leakage current using the very sensitive parameter analyzer. As seen in the figure, pico ampere leakage currents have been observed on devices having

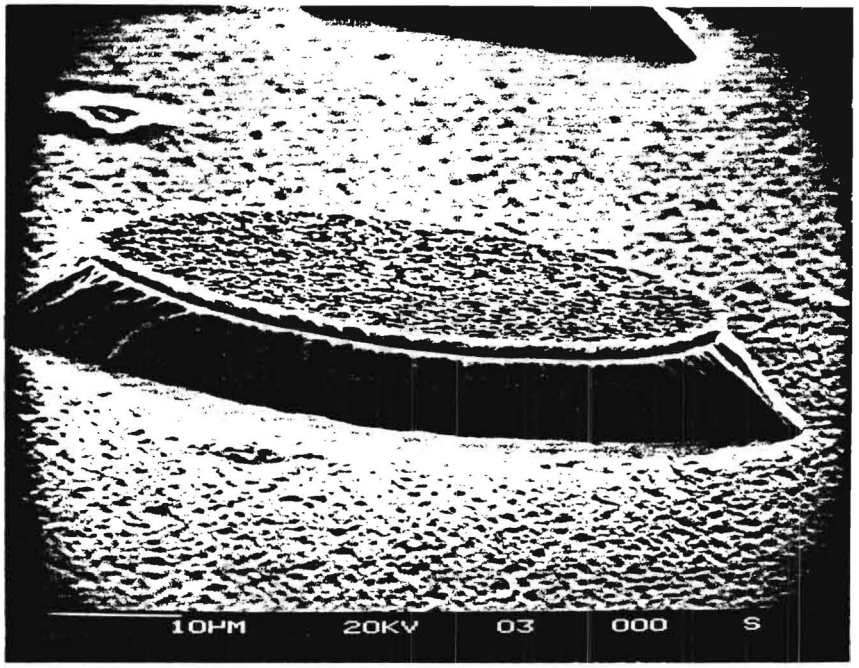

Figure 10. APD Fabricated with Process One.

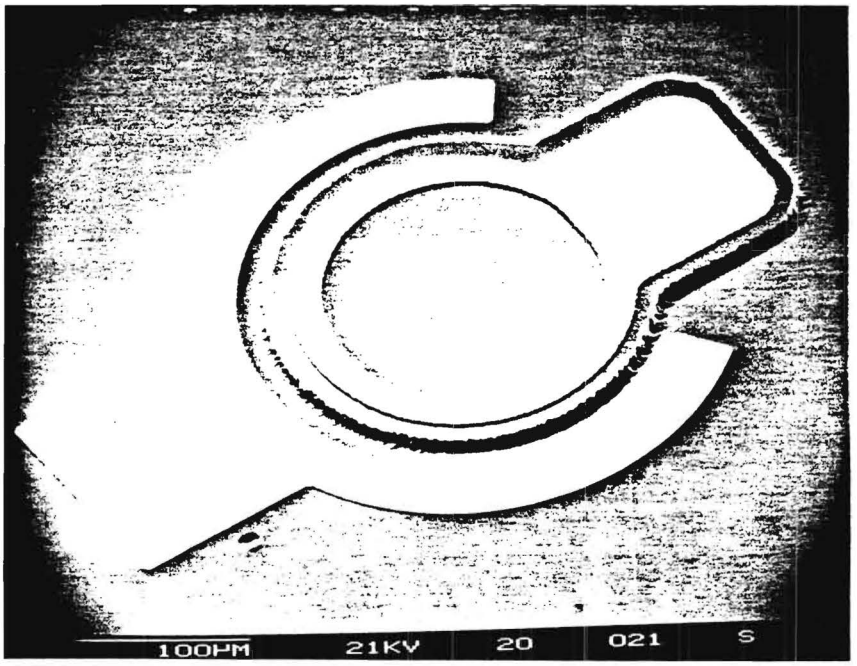

Figure 11. APD Fabricated with Process Two.

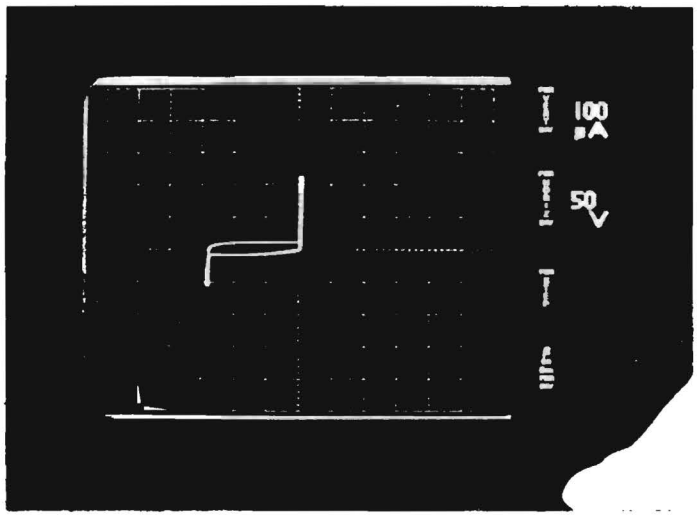

Figure 12. IV Characteristics of an APD Using a Standard Curve Tracer.

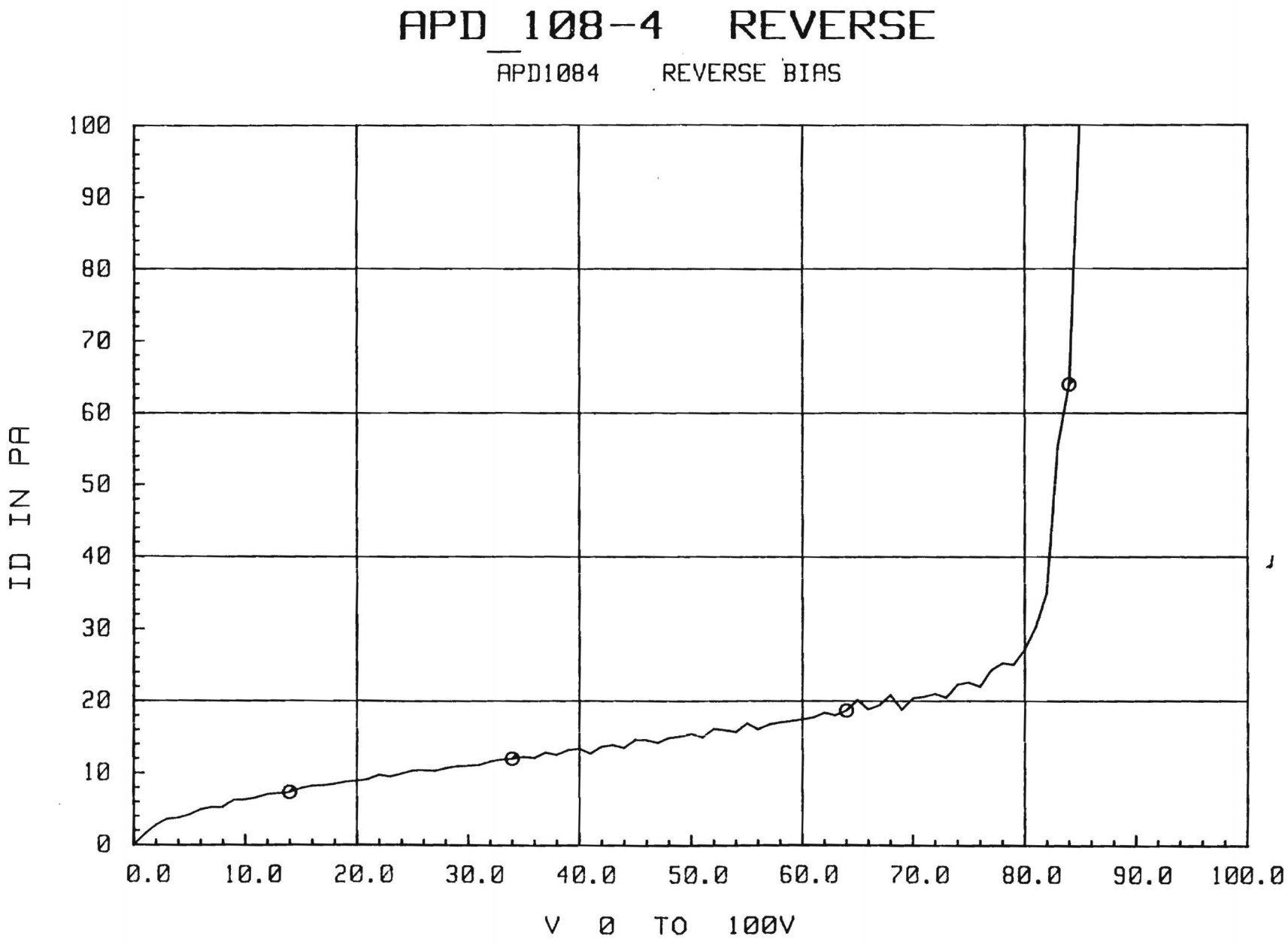

Figure 13. Reverse Current-Voltage Characteristics of an APD Using a Semiconductor Parameter Analyzer.

undoped barriers. Extremely sharp breakdown characteristics were noted on these devices. These results are very encouraging and indicate that high performance avalanche photodiodes can be made from MBE grown epitaxial layers.

9. REFERENCES

1. S. Sze, Semiconductor Device Physics J. Wiley, 1965.

2. G. Lucovsky and R.B. Emmons, High Frequency Photodiodes, Appl. Optics 4, 697-702, (1965).

3. G.E. Stillman and C.N. Wolfe, Avalanche Photodiodes, Semiconductors and Semimetals, Vol. 12, (Eds, R.K. Willardson and A.C. Beer, Academic Press, N.U. 1977). p. 291.

4. R.J. McIntyre, "Multiplication Noies in Uniform Avalanche Diodes, "IEEE Trans. Electron. Dev. ED-13, 164-168 (1966).

5. W. Ruegg, An Optimized Avalanche Photodiode, IEEE Trans. of Electron Devices, ED-14, 239-251 (1967).

6. Y. Matsushima, K. Sakai and Y. Noda, New Type InGaAs/InP Heterostructure Avalanche Photodiode with Buffer Layer, IEEE Electron Device Letters, EDL-2, 179-181, p (1981).

7. K. Nishida, Tagucki, and Y. Matsumoto, InGaAsP Heterostructure Avalanche Photodiodes with High Avalanche Gain, Appl. Phys. Lett. 35, 251 (1979).

8. J.P. Gordon, R.E. Nahory, M.A. Pollack and J.M. Worlock, Low-Noie Multistage Avalanche Photodetector, Electron. Lett. 15, 518-519, (1979).

9. F. Capasso, W.T. Tsang, A.L. Hutchison and G.F. Williams, Enhancement of Electron Impact Ionization in a Superlattice: A New Avalanche Photodiode with a Large Ionization Rate Ratio, Appl. Phys. Lett. 40, 30-38 (1982).

10. R.C. Miller, D.A. Kirlmman and A.C. Gossard, "Energy Gap Discontinuities and Effective Masses for GaAs and $Al_xGa_{1-x}As$ Quantum Wells, Phys. Rev. B., 29, 7085-7087 (1984).

11. F. Capasso, W.T. Tsang, A.L. Hutchinson and P.W. Foy, "The Graded Bandgap Avalanche Diode. A New Molecular Beam Epitaxial Structure with a Large Ionization Ratio," Proc. 1981 Symp. on GaAs and Related Compounds, 473-478 (1982.

12. G.F. Williams, F. Capasso and W.T. Tsang, The Graded Bandgap Multilayer Avalanche Photodiode. A New Low Noise Detector, IEEE Electron Dev. Lett. EDL-13, T1-73 (1982).

13. K.F. Brennan, K. Hess and F. Capasso, Physics of the Enhancement of Impact Ionization in Multiquantum Well Structures, Appl. Phys. Lett. 50, 1897 (1987).

14. K.F. Brennan, The p-n Heterojunction Quantum Well APD: A New High-Gain Low-Noise High-Speed Photodetector Suitable for Lightwave Communications and Digital Applications, IEEE Trans. Electron. Devices ED-34, 793-803 (1987).

15. K.F. Brennan, The p-n Junction Quantum Well APD: A New Solid State Photodetector for Lightwave Communications Systems and On-Chip Detector Applications, IEEE Trans. Quan. Electron., QE-23, 1273-1282 (1987).

16. K.F. Brennan, Optimization and Modeling of Avalanche Photodiode Structures: Application to a New Class of Superlattice Photodetectors, The p-i-n, p-n Homojunction, and p-n Heterojunction APDs, IEEE Trans. on Electron Devices, ED-34, 1658-1669 (1987).

17. K.F. Brennan, Comparison of Multiquantum Well, Graded Barrier, and Doped Quantum Well GaInAs/AlInAs Avalanche Photodiodes: A Theoretical Approach, IEEE Trans. on Electron Devices, ED-34, 782-792 (1987).

18. A. Torabi, K.F. Brennan and C.J. Summers, Photoluminescence Studies of Coupled Quantum Well Structures in the AlGaAs/GaAs System, SPIE 792, Quantum Well and Superlattice Physics 152-156 (1987).

19. Growth and Application of Superlattices and Quantum Wells, A. Torabi, K.F. Brennan and C.J. Summers, SPIE, Optoelectronics (to be published).

HIGH PERFORMANCE PHOTODIODES

Final Report for Project A-4233

Prepared for

Dr. William T. Vetterling
Microelectronics/Materials Center
Polaroid Corporation
21 Osborn Street, Dept. 775
Cambridge, MA 02139

Prepared by

Dr. Christopher J. Summers
Georgia Tech Microelectronics Research Center
Georgia Institute of Technology
Atlanta, Georgia 30332

April 1995

TABLE OF CONTENTS

1. INTRODUCTION

The objective of this program was to develop a very low noise solid state diode detector which could be applied to a broad range of Polaroid activities, including light metering, detection of fluorescent emission (biomedical applications), optical disk or card reading (or tracking), and high-sensitivity camera applications when incorporated into array structures.

In this program multiple quantum well structures were used to design high performance APDs because of their potential to minimize the excess noise in the avalanche process. Low noise is achieved if the ionization rates of the electrons and the holes, α and β respectively, are greatly different, equivalently α/β (or β/α) is high. Since the presentation of the original idea by Chin et al (1980) and the first experimental investigations by Capasso et al (1982A), several novel designs have been proposed: the doped multilayer APD (1982), the staircase APD (1982b), the channeling APD (1983), the pn-doped homojunction and heterojunction APD (1986) (or doped barrier APD) and the doped quantum well APD (1990). It is predicted that the last two designs could lead to the first solid state photomultiplier APD where the avalanche excess noise has been totally suppressed.

In this program quantitative experimental investigations of several AlGaAs/GaAs multiple-quantum-well avalanche photodiode (APD) structures, the superlattice APD, the doped barrier APD and the doped quantum well APD are reported. Only diodes exhibiting

self consistent C-V, I-V and breakdown voltage characteristics were investigated and showed strong agreement between electron- and hole-ionization rates, as determined from gain and noise measurements, respectively. This study provides new data on the performance of doped barrier and quantum well APDs and establishes a comparison with the electron- and hole-ionization rates for $Al_xGa_{1-x}As$/GaAs MQW-APDs. These devices exhibit gains of ~ 20 with excess-noise factors <5 at bias voltages <10V. Thus significant results were obtained on both conventional AlGaAs/GaAs superlattice APD's and barrier-doped superlattice APDs. Preliminary data was also obtained on some delta-doped quantum well devices. Additionally, it should be noted that this excess noise factor is within 18% of the value given for a Hamamatsu Si avalanche photodiode detector and demonstrates the high potential of these concepts. Progress was also made in developing better models and insight into device operation. However, further work remains to be done on resolving the differences between experiment and the theoretical predictions which ideally suggest that a further two orders of magnitude improvement is possible.

The success of this effort was based on developing a stable and reproducible material growth and device fabrication technology and the setting up of the equipment and a dedicated electromagnetic shielded room to perform very sensitive gain and noise measurements on advanced APD structures. Full details of the work on device fabrication, evaluation, and results are described in appendices I and II, respectively.

2. PROGRESS

This report presents detailed investigations on undoped MQW APDs having different geometries and aluminum compositions, doped barrier and doped well APDs. A comprehensive self-consistent methodology was used where current-voltage, capacitance-voltage, doping profile, and noise characteristics were extensively analyzed.

2. EXPERIMENTAL

The structures were grown by molecular beam epitaxy. Growth was initiated on an n^+ Si doped substrate followed by a short period superlattice to prevent propagation of dislocations and impurities. All the device structures were PINs where the I region was composed of the MQW structure with P and N contact layers of 1 μm and 1.5 μm doped to 1 x 10^{18} cm^{-3} with Be and Si, respectively. The MQW structures had 25 $Al_xGa_{1-x}As/GaAs$ multilayers with aluminum compositions of 0.30, 0.35 and 0.45. The aluminum composition, x, of the AlGaAs layers was calibrated using photoluminescence measurements. The samples showed high exciton recombination photoluminescence intensities with a half width of 5 mev. Growth interruption techniques were used to obtain well defined pn doped regions in the MQW structures. The dopant concentration was calibrated by Hall effect and was kept below 6 x 10^{18} cm^{-3} to limit dopant diffusion.

The devices were fabricated into 2 x 10^{-4} cm^{-2} area mesa

structures using standard photolithography techniques (Appendix I). The device configuration allows for electron or hole injection because both p^+ and n^+ layers can be illuminated. Precise control of the growth and fabrication procedures yields identical photodiode characteristics on the same wafer and from one run to another. A SiO_2 dielectric coating suppressed surface leakage currents and provided devices with very low dark currents. The photodiode characterization consisted of computer automated I-V, C-V and noise measurements. The dc I-V characteristics were measured in the dark and under illumination by a HeNe laser light with a 5 μm diameter spot. The photocurrent gain was calculated from the increase of the unmultiplied photocurrent and was verified to be independent of the light intensity. The C-V measurements were made on a LCZ meter between 80 Khz and 1 Mhz and at 300 K and 77 K. The apparent free carrier concentration profile was obtained from differentiation of the C-V data. Noise measurements consisted of measuring the variance of the photodiode output current for different gains. Absolute noise measurements were performed using a spectrum analyzer tuned to a frequency of 200 Khz. Several noise sources were used to calibrate the system and the noise measurements are accurate to within a few percent.

3. RESULTS

3.1 Undoped MQW APDs

Investigations were first performed on 2.5 μm thick MQW $Al_xGa_{1-x}As/GaAs$ structures with different well and barrier widths, L_B and L_Z respectively, and with a constant MQW period width of 1000 Å. The values of L_Z studied were: 200 Å, 350 Å, 500 Å, 650 Å and 800 Å. A 400 Å thick spacer layer was added prior to the first well on the P^+ contact side and also prior to the first barrier on the N^+ contact side to avoid trapped carriers at the first heterojunction for electric fields above 100 kV/cm. The MQW structures have an Al composition, x, of 0.3, 0.35 and 0.43. Typical dark I-V characteristics are shown in Figure 1 for electron injection. The dark current was below 10 nA at 80 % of the breakdown voltage for x = 0.30 and below 1 nA for x = 0.43. The dark current decreased with decreasing well width, and with increasing x.

The photocurrent increases slowly with the applied voltage, becomes constant between 25-35 V and finally increases exponentially above 50 V. As also shown in Figure 1, the breakdown voltage, V_B, increased from 70 to 85 V as the barrier width increased from 200 Å to 800 Å. For a given geometry and Al composition, V_B is constant within 2 % for all photodiodes tested, and increases as the Al composition increases. Similarly, I-V measurements were taken for hole injection. These results indicate that the dark current is due to the generation-recombination of

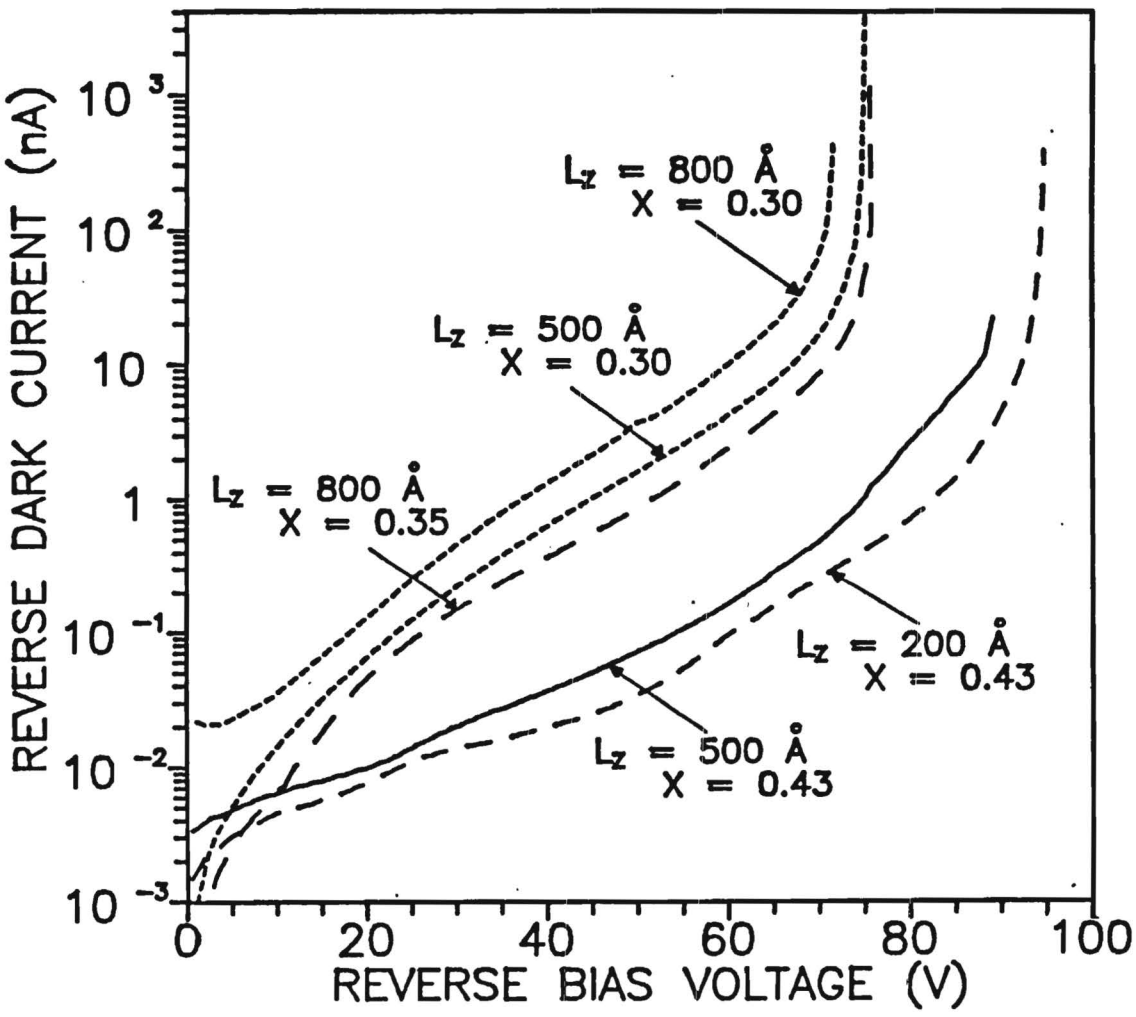

Figure 1. Typical Dark I-V Characteristics for Undoped $Al_xGa_{1-x}As/GaAs$ MQW APDs.

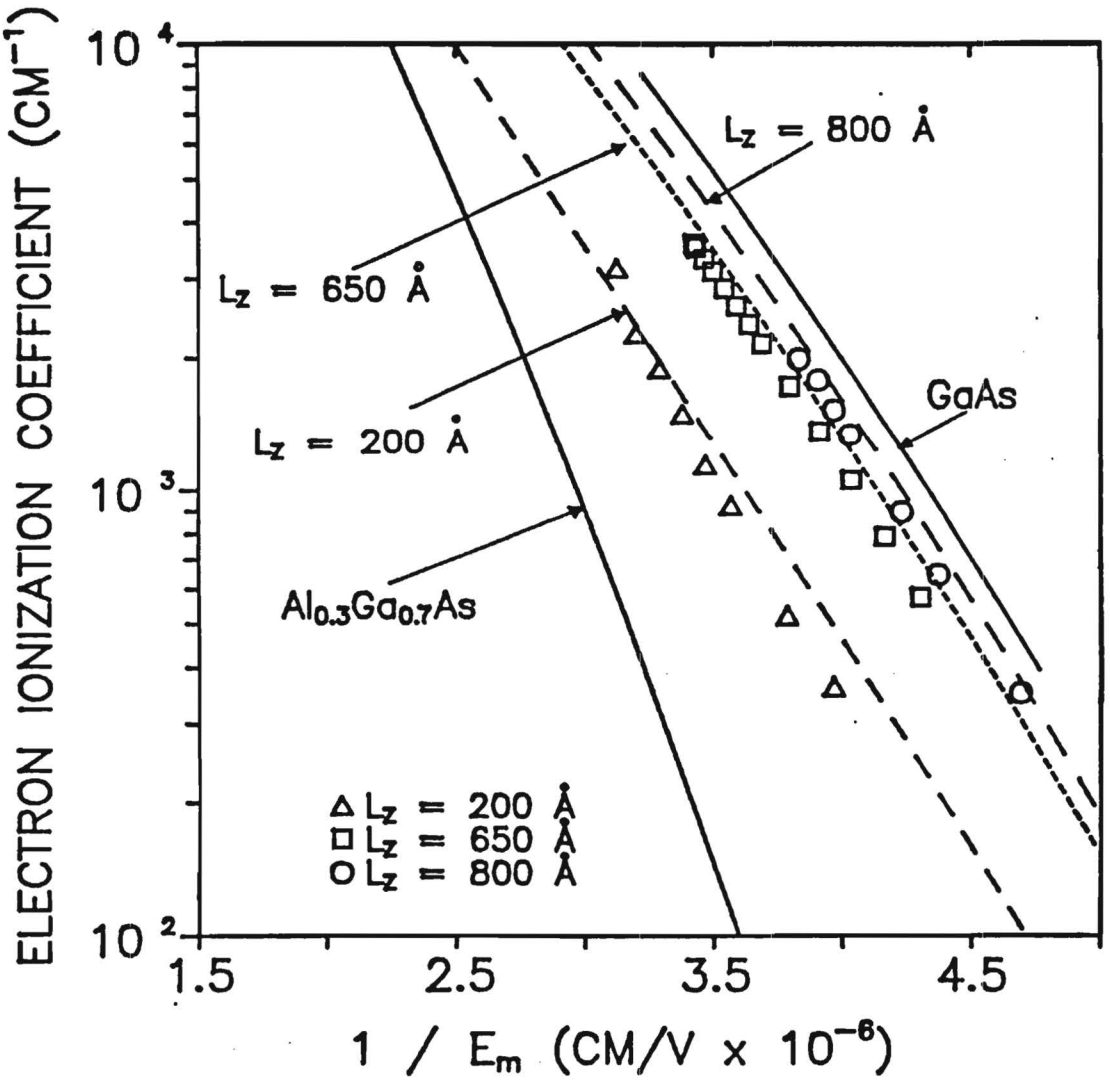

Figure 2. α_{MQW} for $Al_{0.3}Ga_{0.7}As$/GaAs MQW APDs.

conduction band edge discontinuity does not contribute to the enhancement of the electron ionization since α_{MQW} is not enhanced over its value in the bulk GaAs.

The results indicate also that for a higher Al composition, α_{MQW} stays in the same range [300-4000 cm^{-1}], but the corresponding range of electric fields is shifted to higher values. As x increases, the value of E_m at which multiplication starts is increased from 222 Kv/cm for x = 0.30 to 315 Kv/cm for x = 0.42. Consequently, as x increases, the breakdown voltage increases. This is indicated in Figure 3 by a translation of the data to higher electron field values. These results show that the AlGaAs layer of the MQW is "inactive" for x values of 0.30. However, for x = 0.43, the AlGaAs layer appears to reduce the average kinetic energy of the electrons which enter the GaAs layer since the device operates under higher applied electric fields. This energy loss is due to scattering in the X-band of the AlGaAs layer which increases exponentially with the Al composition.

The ratio $k_{MQW}(E_m) = \alpha_{MQW}(E_m)/\beta_{MQW}(E_m)$ increased from 1.72 to 2.5 when the electric field increased from 220 Kv/cm to 280 Kv/cm for the 5 geometries studied and x = 0.30. However $k_{MQW}(E_m)$ was reduced to a constant k = 2.5 for x = 0.43. The results agree with the predicted value using the relation $k_{MQW}(E_m) = \alpha_{AV}(E)/\beta_{AV}(E)$ for x = 0.30, but fail for x = 0.43 since the ratio obtained from the measurements is lower. These results indicate that both the electron and hole average energy are reduced due to the AlGaAs

layer. The hole average energy is reduced by a larger amount since MQW structures with x = 0.43 give a higher k value.

Noise measurements indicate a k value (McIntyre 1966) between 1.7 and 2.5 for the x = 0.30 MQW and between 2.5 and 3.3 for the x = 0.43 MQW. Results for F_e are plotted versus M_e in Figure 3 for the 200 Å well MQW APD having x = 0.30 and 0.43. The solid lines correspond to the theoretical curves of McIntyre. These results agree with the k_{MQW} obtained from the coefficients $\alpha_{MQW}(E_m)$ which were calculated separately using the electron and hole gain measurements and demonstrate that the characterization techniques are self-consistent.

3.2 Doped MQW APDs: the pn junction doped barrier and doped well APDs.

The doped barrier APD was designed with the same unit cell as the undoped MQW APD and consists of a 800 Å barrier, 200 Å well $Al_{0.35}Ga_{0.65}As/GaAs$ MQW structure where a p^+n^+ equally doped junction was built in the barrier prior to the GaAs well. The fully depleted 150 Å p^+/150 Å n^+ junction, doped at 3 x 10^{18} cm^{-3}, locally enhances the electric field of the MQW structure by superimposing 0.5 eV on the MQW band potential.

The I-V characteristics indicate a low dark current and a low breakdown voltage of about -10 V. C-V characteristics indicate that the photodiode capacitance is higher (15 Pf) than measured for the MQW APD (0.9 Pf) and decreases for increasing diode bias voltage as for a one sided abrupt pn^+ junction. The free carrier

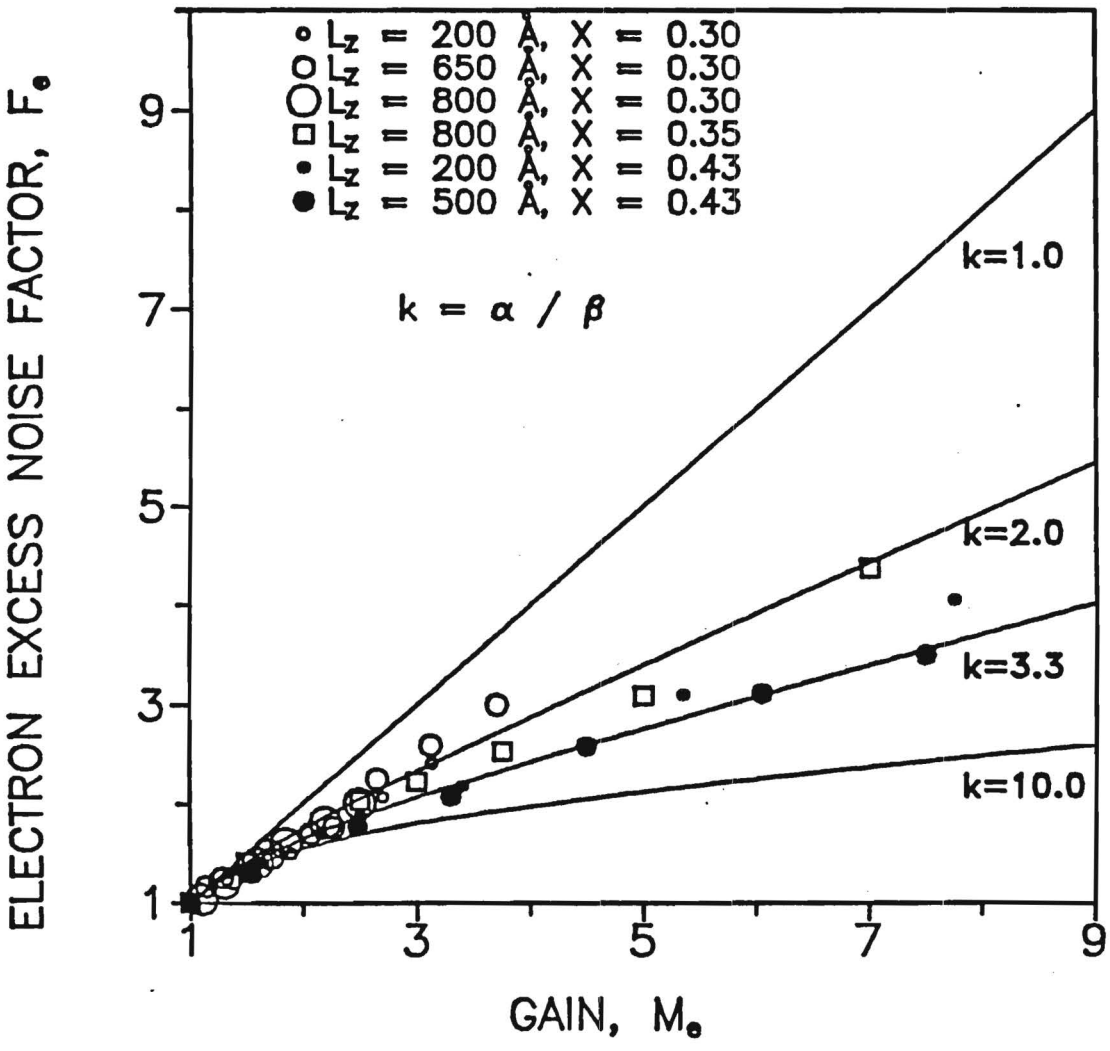

Figure 3. Electron Excess Noise Versus Gain for Undoped MQW APDs.

concentration profile obtained from the analysis of the C-V data is presented in Figure 4. This modeling shows that only one period of the MQW structure is fully depleted at zero bias due to unbalanced doping concentrations in the 300 Å thick junctions. As the field is increased, the depletion width punches through the highest doped side of the 300 Å thick junction to deplete the second period and pn junction of the MQW structure. The results confirm that the depletion region is located close to the P^+ contact thus indicating that $p^+ << n^+$ in the 300 Å thick pn junctions. This is due to the difficulty of achieving equal p- and n- type dopant concentrations in the AlGaAs layer by using solid dopant sources. Although a qualitative variation of the electric field E is predicted, precise calculations of E are not available at present. This α and β can not be obtained separately from the gain measurements. Noise measurement results are presented in Figure 5 were F_e is plotted versus M_e and show that F_e is low for gains up to 5 with a corresponding k between 12.5 and 50. As M_e increases, F_e also increases with a corresponding K between 5 and 10.

The results indicate that k is reduced at low applied electric fields. Since the peak of the electric field is located prior to the well, the injected electrons are more likely to ionize in the well. However, holes generated from ionizations in the well travel in the opposite direction and enter the AlGaAs layer where their ionization probability is smaller compared to the ionization probability of the electrons in GaAs. consequently, α is greatly different from β and a noise reduction is observed. However, K

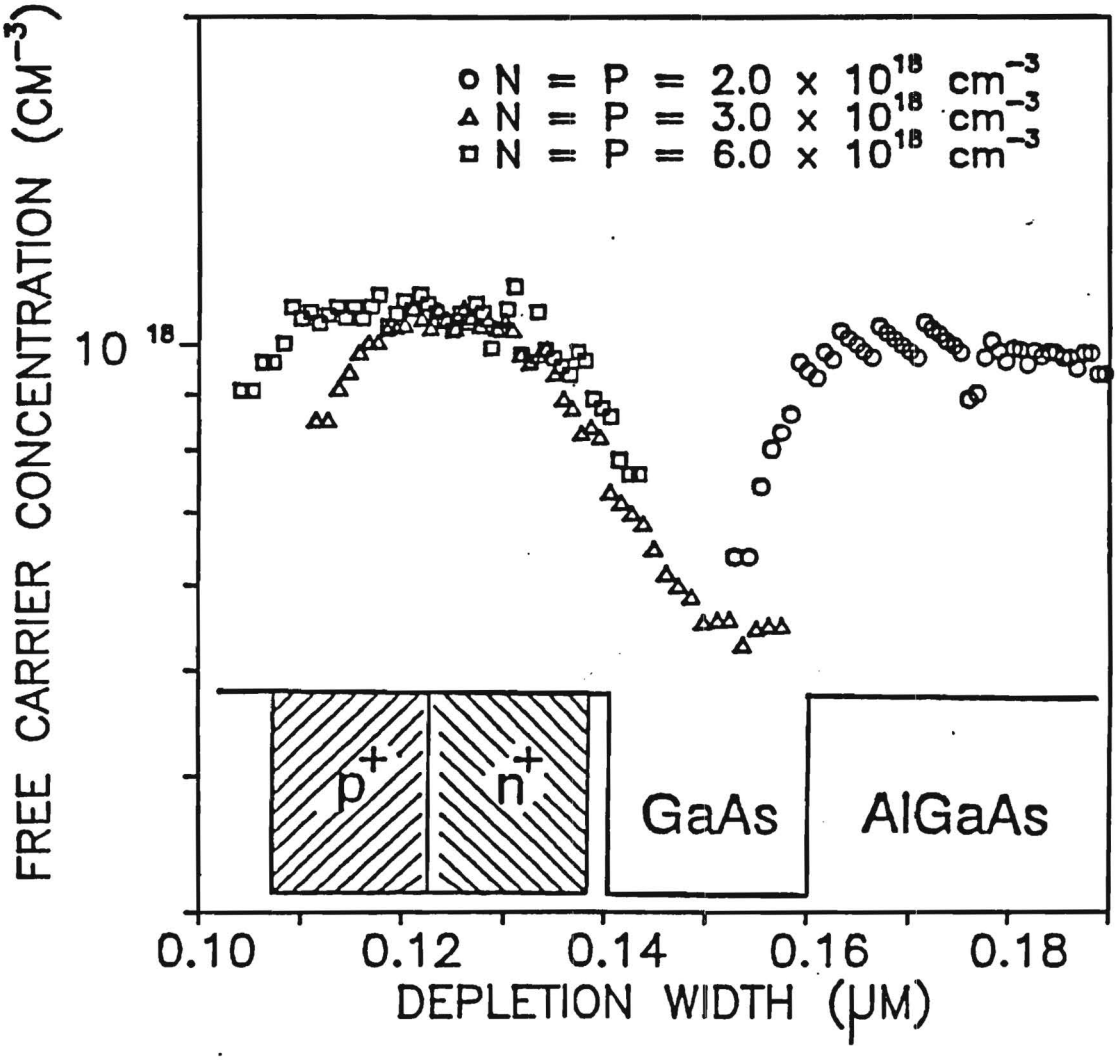

Figure 4. Apparent Free Carrier Concentration of Doped Barrier APDs.

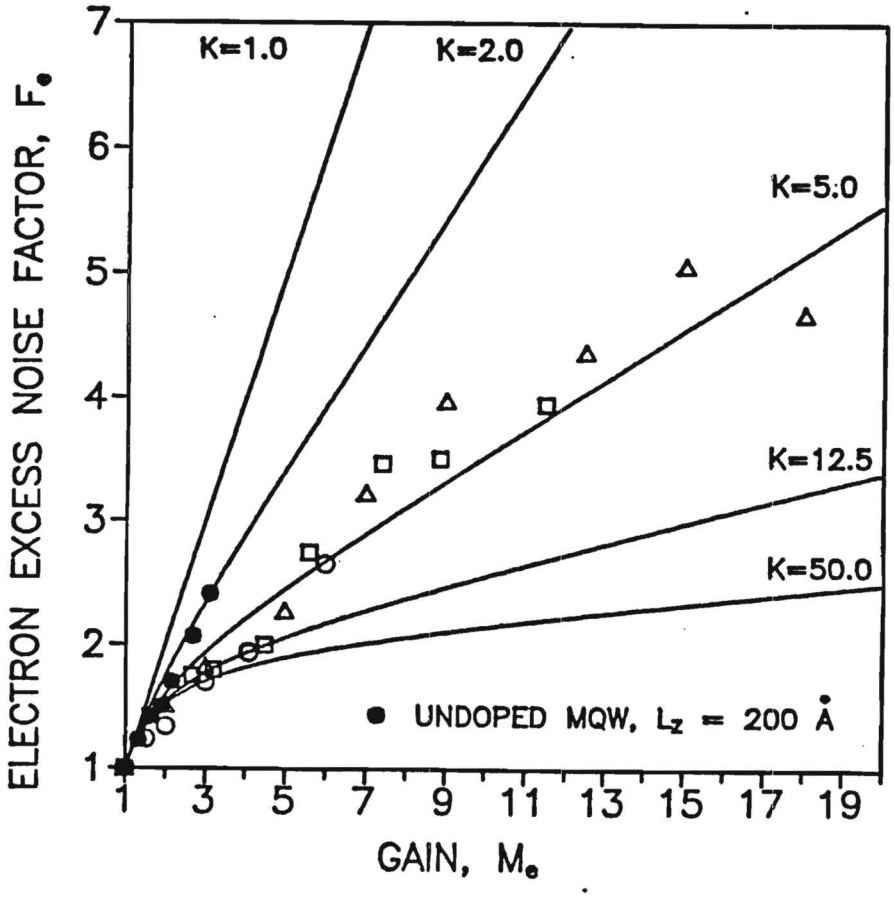

Figure 5. Electron Excess Noise Factor vs Gain, the Solid Circles are for the MQW APD, L_z = 200 Å, and the Open Symbols for the Doped Barrier APD.

increases at higher gain indicating that the hole ionization probability is no longer small compared to the electrons and the applied electric field is high enough to supply kinetic energy to the holes to impact ionize in the following well.

Similar results were obtained for a doped 500 Å well/500 Å barrier $Al_{0.43}Ga_{0.57}As$/GaAs MQW structure where a 300 Å thick pn junction was grown into the well immediately following the barrier. I-V and C-V measurements show that 2 to 3 periods were depleted when the bias voltage was increased from 0 to -12 V at the avalanche breakdown, for these structures high gains up to 400 were obtained. Noise measurements give a similarly low k value as reported for the doped barrier APDs. These results indicate that α/β is enhanced, consequently the noise is reduced, but no information was obtained on the separate magnitude of α and β. The comparable noise performance of both designs suggests that the location of the pn junctions, either in AlGaAs or GaAs material, has little consequence as long as the other parameters of the MQW remain constant (L_2 = 200 Å, L_B = 500 Å). However, the two designs have some differences in their characteristics since the gain is 10 times greater for the doped well than for the doped barrier APD. Further studies are needed to explain this difference.

4. CONCLUSION

The investigations of undoped $Al_xGa_{1-x}Ga/GaAs$ MQW APDs show that α_{MQW} is not enhanced over its value in the bulk materials. Since $\alpha_{GaAs} >> \alpha_{AlGaAs}$, α_{MQW} in the MQW is obtained from an average calculation of the bulk values of low x values, x = 0.3. This, $K_{MQW} = \alpha_{MQW}(E)/\beta_{MQW}(E)$ is between 1.72 and 2.5 which is higher than for GaAs in the same electric field range (k = 1.6). For higher Al composition, x = 0.43, higher electric fields are required for impact ionization. This indicates that both the electron and hole average kinetic energy is reduced due to the AlGaAs layer. However, low k values indicate a noise reduction. Even though the ratio α_{MQW}/β_{MQW} is enhanced, α_{MQW} is not enhanced over its value in the bulk GaAs material. These results have been demonstrated using self-consistent measurement and analysis techniques since similar values of α/β were obtained from gain and noise measurements.

Results on doped barrier and doped well MQW APDs show that the noise of the doped structures is always lower than for the undoped structure having the same geometry. The noise reduction is due to a local enhancement of the built-in potential which confines the electron ionization in the GaAs well. High k values between 12.5 and 50 were obtained for gains up to 5, and values between 5 and 10 for gains above 5. These new designs provide low noise, low breakdown voltage and high gain as required for optoelectronic applications.

5. REFERENCES

1. Blauvelt H., Margalit S. and Yariv A., 1982, Electron. Lett. **18** 375.
2. Brennan K., 1986 IEEE Trans. Electron Dev. **ED-33** 1683.
3. Brennan K. and Vetterling, W.T., 1990 IEEE Trans. Electron Dev. **37** 536.
4. Bulman, G.E., Robbins, V.M., Brennan, K., Hess, K. and Stillman, G.E., 1983, IEEE Trans. Electron Dev. **EDL-4** 181.
5. Capasso, F., Tsang, W.T., Hutchinson, A.L. and Williams, G., 1982a Appl. Phys. Lett. **40** 38.
6. Capasso F., Tsang, W.T., Hutchinson, A.L. and Foy, P., 1982b, Conf. Ser.-Inst. Phys. **63** 473.
7. Capasso, F., Tsang, W.T. and Williams, G.P., 1983, IEEE Trans. Electron Dev. **ED-30** 381.
8. Capasso, F., 1985 Semiconductors and Semimetals - ed R.K. Willardson and A.C. Beer (New York:Wiley) p. 121.
9. Chin, R., Holoniak, N., Stillman, G.E., Tsang, J. and Hess, K., 1982, Appl. Phys. Lett. **16** 467.
10. McIntyre, R.J., 1966, IEEE Trans. Electron Dev. **ED-13** 164.
11. Robbins, V.M., Smith, S.C. and Stillman, G.E., 1988, Appl. Phys. Lett. **52** 296.

APPENDIX I

FABRICATION PROCEDURES FOR SL AVALANCHE PHOTODIODES

New processing techniques have been developed to yield repeatable results and high performance devices. A reliable processing is necessary to insure that materials characteristics are being measured and not artifacts of the processing.

A six level mask is used to fabricate devices having mesa sizes of 75, 100, 130, 200 micron. These different steps include

1. P^+ Contact,
2. Contact Gold Plating,
3. Mesa Fabrication,
4. N^+ Contact,
5. Passivation,
6. Via Hole Fabrication

The ohmic contact and mesa fabrication have been reworked because it has been observed that the details of these processes significantly influence the device performance. The last step, the via hole formation has been developed during the last year. This feature permits the backside illumination of the photodiode and, thus, the characterization of both electron and hole injection modes.

1. Ohmic Contact Fabrication

The emphasis in the ohmic contact work has been to avoid metal diffusion in the window area of the photodiode and to improve the

contact resistance values. Both the p^+- and n^+- contacts were, deposited using a chlorobenzene assisted lift-off process. Since the metal was not deposited on the top window, the metal diffusion was limited to underneath the contact areas only. Thus, the contact area was well defined and the top window material had a better morphology. The p^+ contact was made using 400Å of AuZn and 1000Å of Au. Alloy time and alloy temperature have been optimized to achieve a low contact resistance, R_c. With a p-layer doping level between 10^{17} and 10^{18} cm^{-3}, an average contact resistance of 0.2 ohm·mm was obtained. The alloy was made in a diffusion oven at 400° for 4 minutes in a forming gas environment. The n^+ contact was made using 500Å of AuGe, 100Å of Ni, and 800Å of Au and was alloyed at 375° for 3 minutes. With an n- layer doping level of 10^{18} cm^{-3}, an average contact resistance of 0.07 ohm·mm was obtained.

2. Mesa Fabrication

The mesa etch is a critical step in the device fabrication because it impacts how well the device is defined and also strongly influences the electrical and optical properties of the photodiode. The mesa etch has to preserve the surface morphology of the GaAs to insure success in the N ohmic contact fabrication which is the following step in the processing of the photodiode. In addition, the mesa wall profile has to be smooth to insure a low leakage current.

Etching GaAs is very delicate because of the crystalline

nature of the GaAs lattice. Many GaAs etchants lead to anisotropic etching, because the etch rate depends on the crystal orientation. The etchant currently used is a phosphoric acid based etchant composed of phosphoric acid, hydrogen peroxide as oxidant and methanol as solvent in the ration 1:1:3. Several parameters had to be optimized to have the mesa shape required. These parameters include the temperature of the solution and the agitation motion to insure an etch rate of 2 micron per minute, a minimum undercut, and a repeatable process. The present etching technique yields a leakage current of 1 nA at 90% of the breakdown voltage for most of the SL structures.

3. Via Hole Fabrication

The backside fabrication was composed of two steps: the backside preparation and the via hole etch. In the first step, the wafer was thinned from 250 micron to 75 micron using lapping and polishing techniques. In the second step, the via hole pattern was aligned with the top side of the device using an infrared mask aligner model MJB3 from Karl Suss. The via hole was etched using wet etching techniques. The etching solution was sprayed on the wafer to uniformly etch all the holes on the wafer. The bottom of the via hole is defined by an etch stop layer of AlGaAs ($x>0.5$). Unfortunately, the selective etching of GaAs is a slow process, incompatible with removing 70 micron of material in a short period of time. To solve this problem, 60 micron of GaAs was first removed using a phosphoric acid based etchant which etches GaAs

uniformly at a rate of 4 micron per minute. Then, a selective etchant was used to removed the remaining few microns to stop uniformly at the AlGaAs layer. The solution used was composed of hydrogen peroxide neutralized to a pH of 7 with a few drops of ammonium hydroxide.

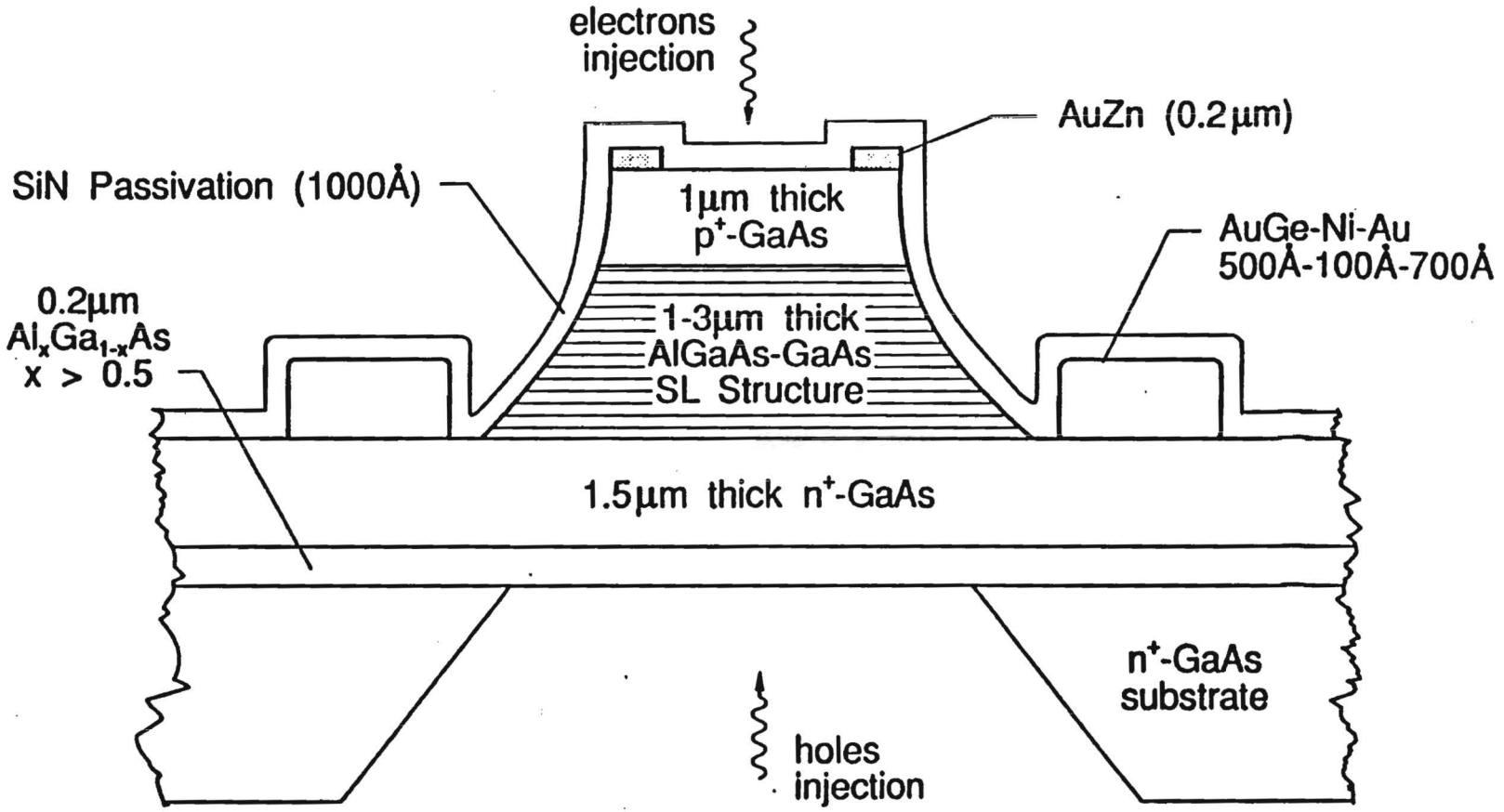

Superlattice Avalanche Photodiode Structure.

APPENDIX II

CHARACTERIZATION OF THE SL APDs

I. Introduction

To evaluate the performance of the APDs, it was necessary to measure the avalanche gain, the excess noise factor and the quantum efficiency of the devices. The current gain, as a function of reverse bias voltage, was found from the I-V curves of the diodes measured both in the dark and under illumination by a He-Ne laser. The excess noise factor, as a function of the avalanche gain, was calculated by measuring the noise power of the device for different values of the diode bias voltage. The quantum efficiency is determined by measuring the photogenerated current by an illuminating beam of known intensity under low bias voltage condition.

A. Description of the Optical Apparatus

The apparatus for the optical characterization has been configured to provide flexibility and reproducibility in the measurements. The optical source and accessories were mounted on an optical table and the power level of the laser beam was adjusted with an attenuator and neutral density filters. Figure 1 shows the complete optical system. The laser beam was split into two beams with a beam splitter and both beams were focused to the same point on the top of the microscope on either side of the diode box. The diode box contains the photodiode and the accompanying

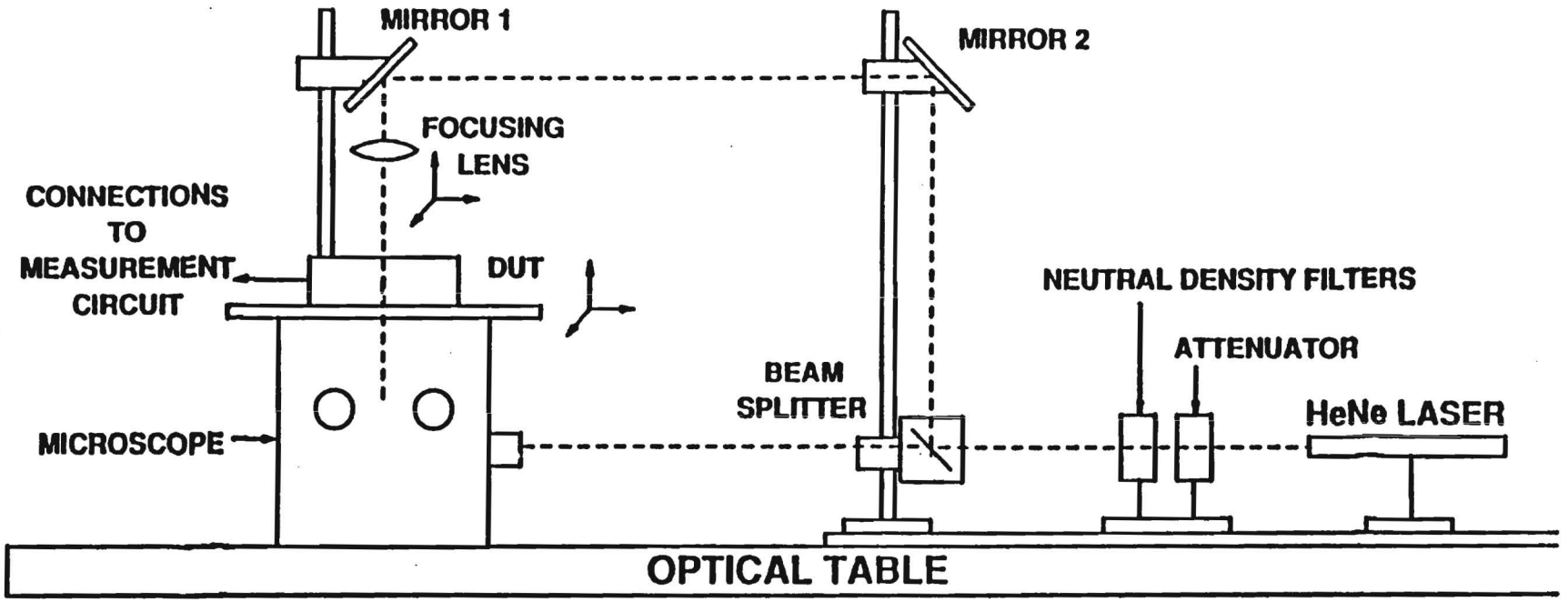

Figure 1. Optical Apparatus.

electrical circuit. The box has a hole on the top for illuminating the top side of the photodiode, and another hole on the bottom for illuminating the back side of the photodiode. The XYZ stage of the microscope was used for positioning the photodiode in the illuminating beam. A tungsten light placed in the microscope optical path instead of the laser was used for this purpose. The laser beam that goes through the microscope was focused with a 40X long focal length objective onto the photodiode with a 5 μm beam spot diameter. This small spot size was used to scan the active area of the photodiode to detect any non-uniformity in the light injection.

B. Description of the Electrical Circuit

The photodiode was mounted in a 8 pin dual-in-line package and inserted into the circuit showed in Figure 2. To permit the back side illumination, a hole of 20 mil diameter was laser drilled in the center of the package. The electrical circuit of the photodiode was divided into two parts to perform the following dc and ac measurements:

1. Current-voltage measurements were performed with the dc part of the circuit. The diode was connected in series with a precision resistor which provides a high input impedance to the ac circuit. The diode and the resistor were reverse biased with a battery that supplied a voltage selectable to within 2mV. The diode voltage bias then was the voltage dropped measured across the precision resistor. The selectivity of the system provides an

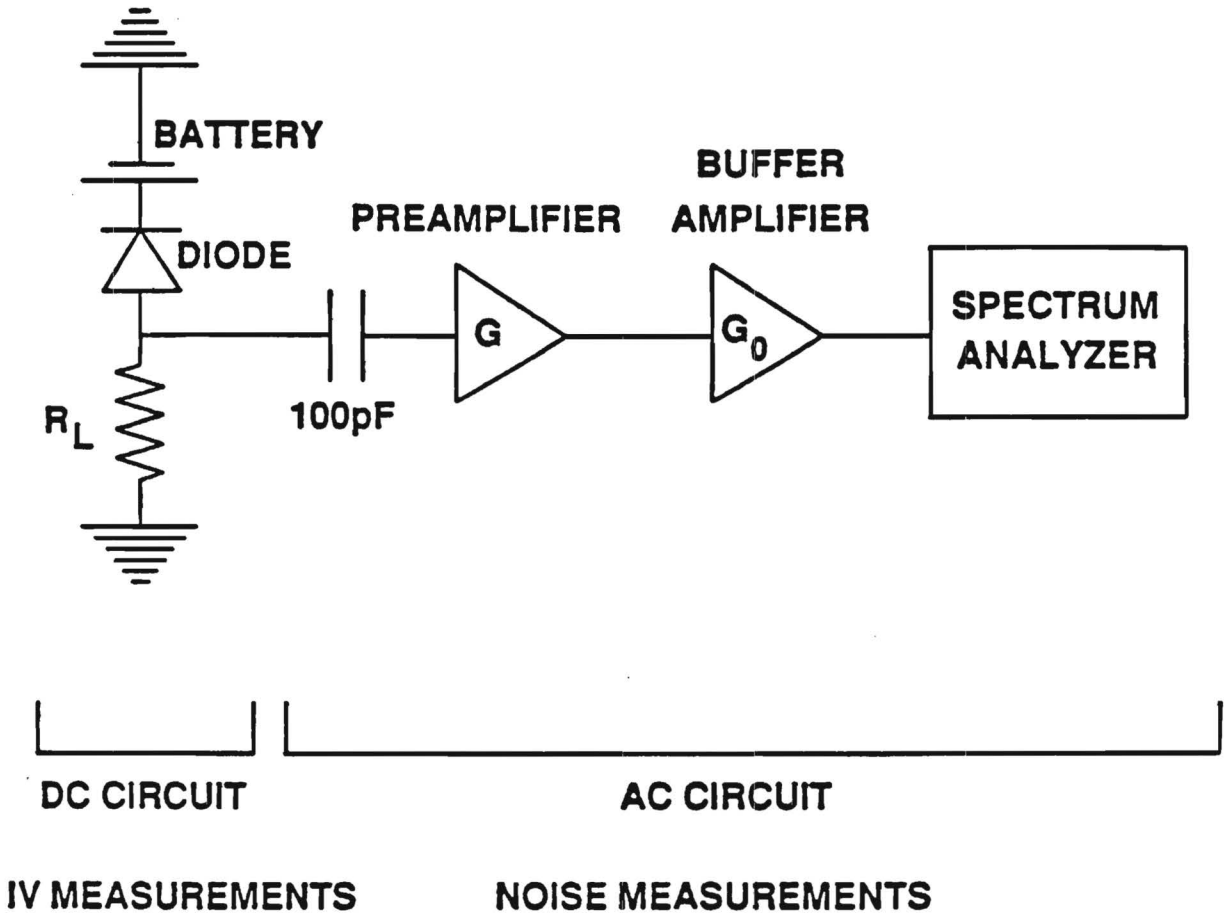

Figure 2. Diode Characterization Circuit

accuracy of 2pA in the bias current.

2. Absolute noise measurements were performed using the ac part of the circuit. The photodiode noise signal was coupled through a 100pF capacitor to a low noise preamplifier and the power of the amplified signal was measured on a spectrum analyzer at a fixed center frequency within a selected bandwidth. This frequency was chosen between 200 kHz and 300 kHz to avoid interferences with the 1/f noise of the photodiode. The measured power is the total output noise power of the circuit which includes the avalanche noise of the diode, the thermal noise of the diode series resistance and the load resistor, and the noise of the preamplifier. The preamplifier was chosen to provide a low noise with a medium input impedance (1 Kohms - 1 Mohms) in the frequency range of the measurements. A buffer amplifier was also added to the circuit in order to match the low output impedance of the preamplifier (1 Kohm) to the low input impedance of the spectrum analyzer. The equivalent electrical circuit is presented in Figure 3, where i^2 is the noise current source of the photodiode,

C_D is the photodiode capacitance,

R_D is the photodiode series resistance with $10 < R_D < 10^3$

e^2_D is the thermal noise of the diode resistance,

e^2_L is the thermal noise of the load resistor,

C_A is the input capacitance of the preamplifier,

R_A is the input resistance of the preamplifier and,

e^2_A and i^2_A are respectively the noise voltage and noise

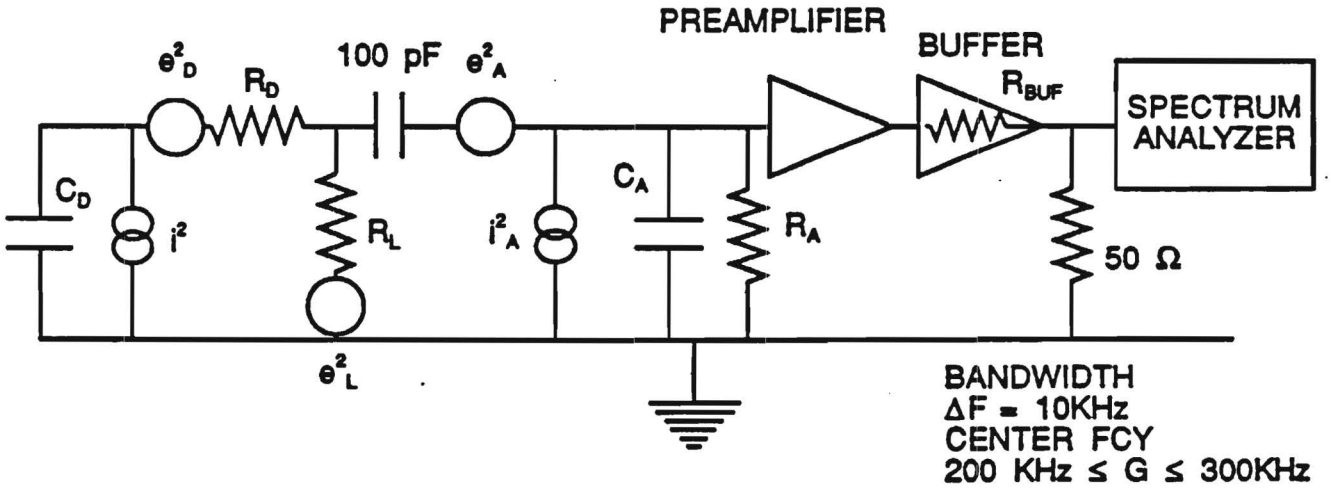

Figure 3. Equivalent Electrical Circuit

current source of the preamplifier.

C. Description of the Instruments

All the instruments used in the measurements were chosen based on noise considerations. The bias voltage supply, the voltmeter and the picoameter were battery powered in order to avoid the difficulty of rectifying noisy line voltages (120 V). From the previous description, the most critical instruments of the circuit were the low noise preamplifier and the spectrum analyzer. The Princeton Applied Research (PAR) preamplifier model 5004 was chosen for its low noise characteristics and compatible bandwidth of 0.5Hz - 1MHz. The spectrum analyzer had to meet the following requirements in order to obtain accurate noise measurements: a synthesized source stabilized to the center frequency of the measurements with a resolution bandwidth of <10 Khz, and a noise power accuracy of plus or minus 0.1 dBm. The Hewlett Packard model 8568B meets these specifications and was, therefore, used for these measurements.

II. Calibration of the Measurement Circuit.

To insure proper operation of the measurements system, it was necessary to obtain a precise and complete calibration of the circuit. The calibration includes three parts. The first part was related to the accurate determination of the parameters of the circuit presented previously in Figure 3. The second part was related to the measurement of the noise power of the circuit (without the photodiode) for a series of load resistors. The plot of the noise power as a function of the resistor value was compared with the plot obtained from the known contour figure of the preamplifier. From the plots, the parameters of the circuit were verified and any additional anomalies detected. The third part was to measure the noise of a well known device. A Si PIN photodiode was chosen for this purpose.

Part 1. I-V Measurements and Multiplication Gain Calculation

The following parameters were measured:

1. Total gain of the combination preamplifier-buffer amplifier
2. Noise equivalent bandwidth of the spectrum analyzer
3. The buffer amplifier output resistance.
4. The input capacitance of the preamplifier.

Part 2. Calibration of Entire Measurement Circuit

The noise power was measured for various load resistors, between 10 ohms and 1.5 Mohms, at the input of the ac circuit. The

equivalent electrical circuit is presented in Figure 4. The theoretical equation of the noise power measured on the spectrum analyzer is

$$\text{PowerMeasured} = (G+G_o)^2 \frac{e^2_A + R^2 i^2_A + e^2_R}{(1 + 4\ R^2_E C_A^2 \pi^2 F^2)^2} * \frac{50}{(50 + R_{buf})^2} * B$$

where $G+G_0$ is the total gain of the circuit,

e^2_A and i^2_A are respectively the noise voltage and noise current sources of the preamplifier,

R_E is the parallel combination of the amplifier input resistor R_A and the load resistor R_L,

e^2_R is the noise voltage source of the precision resistor,

C_A is the input capacitance of the preamplifier,

R_{buf} is the output resistance of the buffer,

F is the center frequency of the measurements and,

B is the equivalent noise bandwidth of the measurements.

The measured values of the output circuit noise power were compared with the theoretical values calculated with the above equation. The values of the parameters determined in part A were, in addition to the factory noise contour figure of the preamplifier. As shown in Figure 5, the theoretical predictions are in agreement with our experimental results.

A. Calibration Circuit

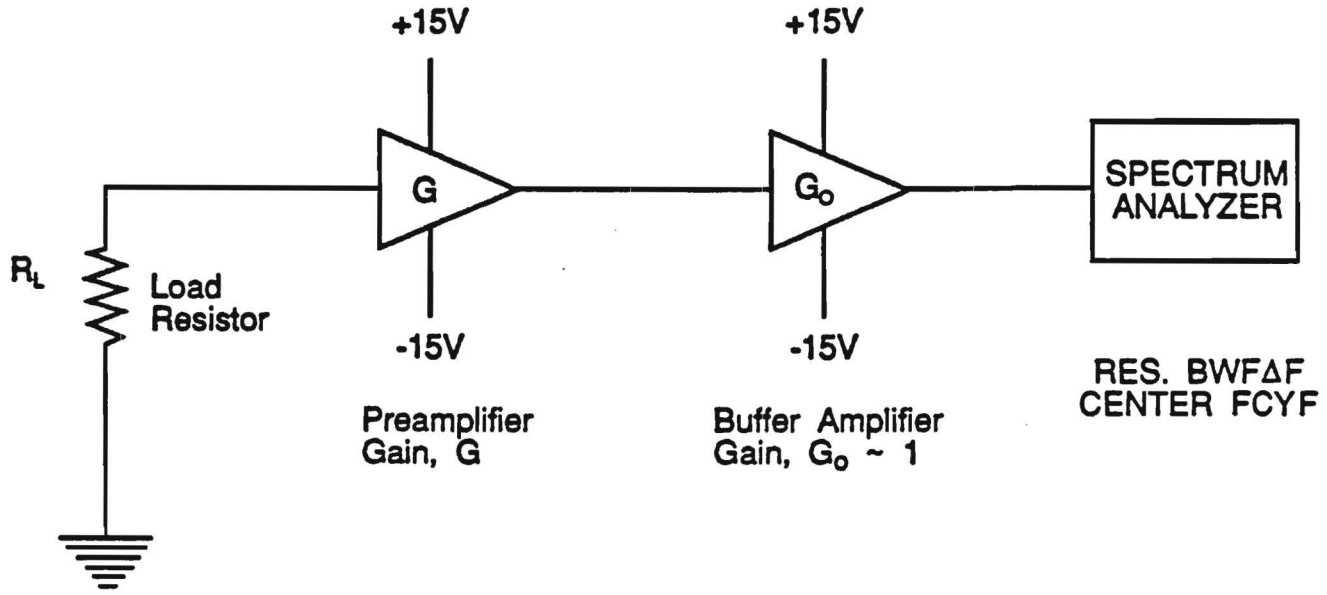

B. Equivalent Circuit

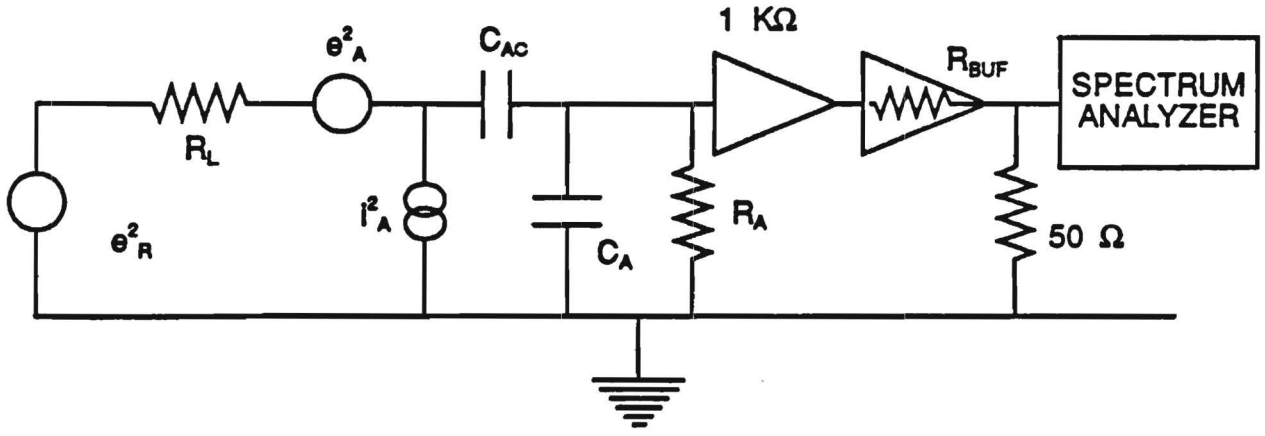

Figure 4. Equivalent Electrical Circuit for Calibration of Measurement System.

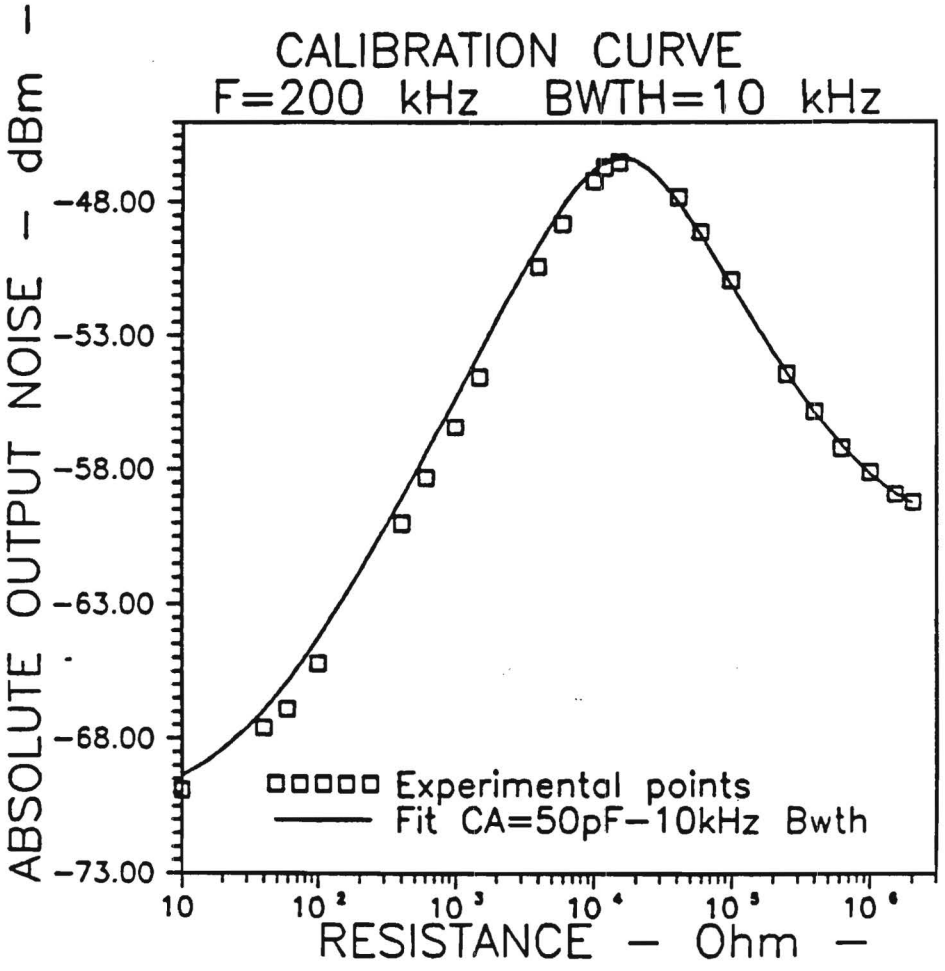

Figure 5. Output Noise for Various Resistors-Theoretical and Experimental Results.

Part 3. Calibration Using a Si PIN Photodiode

The photodiode chosen for a test calibration was a Si PIN photodiode model S1190 from Hamamatsu. Noise measurements were performed for diode bias voltages of 5 volt and 8 volt.

The results shown in Figure 6 represent the variation of the output circuit noise for increasing photocurrent at a constant diode bias voltage. At a constant bias, the output noise increased linearly with the current. The gradient of the output noise is proportional to the ratio of the photodiode shot noise current over the photocurrent, according to the relationship:

$$g = \frac{2 * q * I_{ph} * B}{I_{ph}} * (G+G_O)^2 * \frac{50}{(50+R_{buf})^2} * |Ze|^2$$

where g is the gradient of the output noise, q is the coulomb charge of a carrier, Z_e is the equivalent impedance of the circuit, I_{ph} is the photocurrent, and $2 * q * I_{ph} * B = \langle i^2 \rangle$ is the mean square shot noise value.

The PIN photodiode exhibited only shot noise at 5 or 8 volts, because there was no current gain. In Figure 6, the intercept of the linear fit with the y-axis represents the noise of the circuit itself including the preamplifier noise, the thermal noise of the diode resistance and the thermal noise of the load resistor.

C-V measurements were performed to accurately measure the capacitance of the diode at these two voltages. Then using the theoretical circuit equation, the value of the gradient, g, was

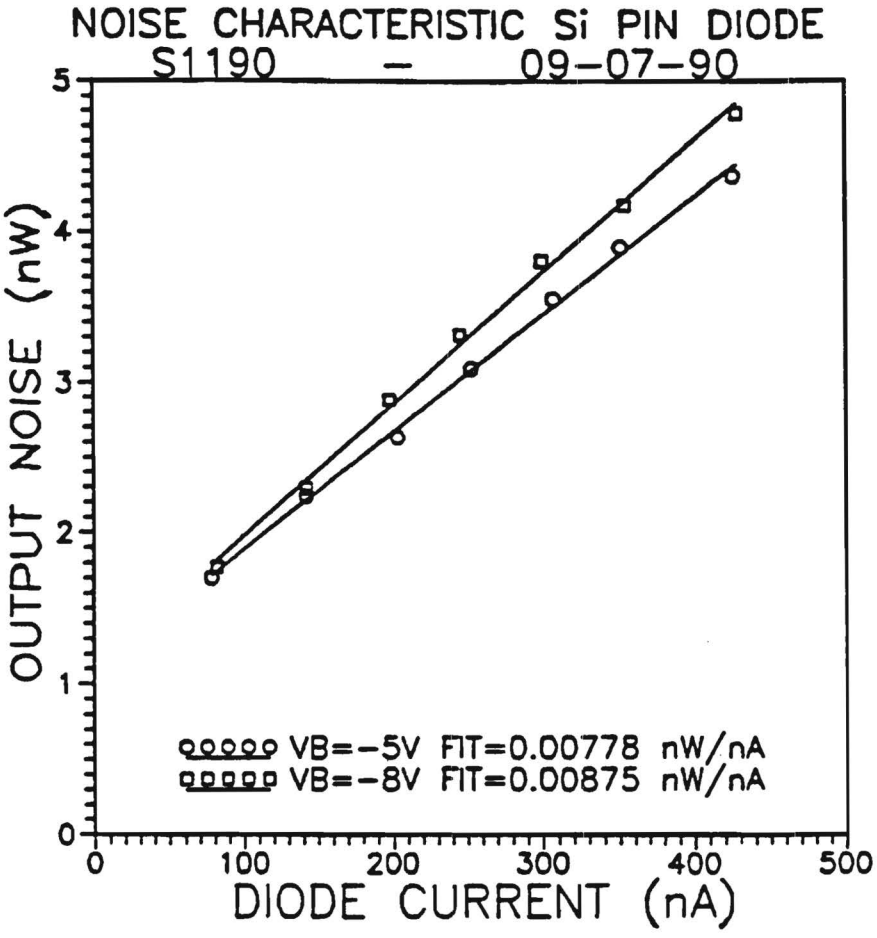

Figure 6. Output Noise Measured for a Si PIN Photodiode.

calculated and compared to the experimental value. For both bias voltages, the experimental results were within 0.5 % of the theoretical calculation. This last step confirmed that the calibration of the circuit was complete and that the noise measurement circuit was sensitive enough to measure the absolute noise of the SL APDs.

III. Theory of the Measurements

The measurement procedure developed to characterize the APDs can also be divided in three steps: I-V measurements and avalanche gain calculation, excess noise factor determination, and quantum efficiency calculation.

A. I-V Measurements and Multiplication Gain Calculation

To determine the avalanche gain of the photodiode, it is necessary to know the pure photocurrent injected after absorption of incident photons. The pure injected photocurrent is obtained by subtracting the I-V characteristics of the diode in the dark, from those obtained when the diode is illuminated by of a He-Ne laser.

The I-V measurements were performed with the dc part of the circuit presented in Figure 2. The current generated under the dark condition was first measured as a function of the total bias voltage. The total bias of the circuit was increased in multiples steps of 0.02 times the value of the breakdown voltage of the diode (from zero volt to the critical voltage value where the diode bias has reached the breakdown voltage). The bias current was always maintained below 1.5 μA to protect the device from being destroyed. The same measurements were then performed for photodiode illuminated with a He-Ne laser. The optical power of the laser beam was set at zero bias voltage to obtain less than 100 nanoamperes of photocurrent. This was done to avoid gain saturation of the photodiode.

For each series of I-V curves and at each value of the current

measured, the diode bias voltage is calculated by

$$V_d = V - R_L * I,$$

where I was the measured current, and R_L the value of the precision resistor in series with the diode.

A computer program was then used to separate the contribution of the dark current and the contribution of the photocurrent at each diode bias voltage. The pure generated injected, I_d, was thus plotted as function of the diode bias,

$$I_{ph} = I_{ph1}(V_d) - I_d(V_d),$$

where I_{ph} was the pure injected photocurrent at a diode bias voltage, V_d, I_{ph1} was the photocurrent measured at V_d on the picoammeter, and I_d is the dark current measured at V_d. The photocurrent variation at low bias voltage was then used to calculate the primary (or unmultiplied) photocurrent. The avalanche gain was plotted as a function of the diode bias voltage by taking the ratio of the photocurrent over the primary photocurrent,

$$M\ (V_d) = I_{ph}(V_d) \ / \ I_{po},$$

where M was the gain obtained at a diode bias voltage V_d, I_{ph} was the pure induced photocurrent at V_d, and I_{po} was the primary photocurrent.

B. Determination of the Excess Noise Factor

The excess noise factor is a measure of the increase of the

shot noise of the photodiode due to the multiplication process. It is calculated from measurements of the circuit output noise power versus the photocurrent for a constant diode bias voltage, i.e. a constant gain.

At a constant diode bias voltage, the circuit output noise power was first measured for increasing values of the photocurrent. The value of the photocurrent was changed by increasing the intensity of the laser light. Thus, for each photocurrent setting, the applied voltage V had to be changed to keep the diode bias voltage constant. V has to satisfy the relation,

$$I = (V - V_d) \; / \; R_L,$$

where I was the measured photocurrent, V was the applied bias voltage, V_d is the diode bias voltage, and R_L is the resistor in series with the diode.

The measurement procedure was repeated for different values of diode gain. At a constant gain, the output noise power is a function of the mean square diode current,

$$< i^2 > = 2 * q * I_{pO} * M^2 * F(M) * B$$

where I_{p0} is the primary photocurrent, M is the diode gain, q is the coulomb charge, B is the equivalent noise bandwidth, and F(M) is the excess noise for a gain M.

If Z_e is the equivalent circuit impedance, the output noise power measured was proportional to $< i_2 > * Z_e$. All the measured values fall on a line which has a slope equal to P over I_{ph} with

shot noise of the photodiode due to the multiplication process. It is calculated from measurements of the circuit output noise power versus the photocurrent for a constant diode bias voltage, i.e. a constant gain.

At a constant diode bias voltage, the circuit output noise power was first measured for increasing values of the photocurrent. The value of the photocurrent was changed by increasing the intensity of the laser light. Thus, for each photocurrent setting, the applied voltage V had to be changed to keep the diode bias voltage constant. V has to satisfy the relation,

$$I = (V - V_d) \; / \; R_L,$$

where I was the measured photocurrent, V was the applied bias voltage, V_d is the diode bias voltage, and R_L is the resistor in series with the diode.

The measurement procedure was repeated for different values of diode gain. At a constant gain, the output noise power is a function of the mean square diode current,

$$< i^2 > = 2 * q * I_{pO} * M^2 * F(M) * B$$

where I_{p0} is the primary photocurrent, M is the diode gain, q is the coulomb charge, B is the equivalent noise bandwidth, and F(M) is the excess noise for a gain M.

If Z_e is the equivalent circuit impedance, the output noise power measured was proportional to $< i_2 > * Z_e$. All the measured values fall on a line which has a slope equal to P over I_{ph} with

shot noise of the photodiode due to the multiplication process. It is calculated from measurements of the circuit output noise power versus the photocurrent for a constant diode bias voltage, i.e. a constant gain.

At a constant diode bias voltage, the circuit output noise power was first measured for increasing values of the photocurrent. The value of the photocurrent was changed by increasing the intensity of the laser light. Thus, for each photocurrent setting, the applied voltage V had to be changed to keep the diode bias voltage constant. V has to satisfy the relation,

$$I = (V - V_d) / R_L,$$

where I was the measured photocurrent, V was the applied bias voltage, V_d is the diode bias voltage, and R_L is the resistor in series with the diode.

The measurement procedure was repeated for different values of diode gain. At a constant gain, the output noise power is a function of the mean square diode current,

$$< i^2 > = 2 * q * I_{pO} * M^2 * F(M) * B$$

where I_{p0} is the primary photocurrent, M is the diode gain, q is the coulomb charge, B is the equivalent noise bandwidth, and F(M) is the excess noise for a gain M.

If Z_e is the equivalent circuit impedance, the output noise power measured was proportional to $< i_2 > * Z_e$. All the measured values fall on a line which has a slope equal to P over I_{ph} with

$$\frac{P(VD,M)}{I_{ph}} = \frac{\langle i_2 \rangle * |Z_e|^2}{I_{pO} * M} = 2 * q * F(M) * |Z_e|^2 * B * A$$

and

$$A = (G+G_O)^2 * 50 \; / \; (50 + R_{buf})^2,$$

where F is the excess noise factor for a gain M, and Z_e is the circuit equivalent noise bandwidth. When the diode has no gain, the mean square diode current becomes equal to the well known shot noise equation,

$$< i^2 > = 2 * q * I_{pO} * B$$

and the ratio of P (Vd,M) over I_{ph} becomes

$$\frac{P(Vd,1)}{I_{ph}} = \frac{< i^2 > * |Z_e|^2}{I_{pO}} = 2 * q * B * |Z_e|^2 * A$$

From the previous equations, the excess noise factor F(M) is defined by the relation

$$F(M) = \frac{P(Vd,M)}{I_{ph}} * \frac{I_{pO}}{P(Vd,M)} * \frac{1}{M}$$

To verify the measurement accuracy, the experimental value of P (Vd,1) over I_{p0} is compared to its theoretical value 2 * q * B * Z^2_e with Z_e, the equivalent circuit impedance defined by

$$Z_e = (Z_A // (Z_{AC}+R_L // (R_D+Z_{CD}))),$$

where Z_A is the preamplifier input impedance, Z_{AC} is the impedance of the coupled capacitance, R_D is the resistance of the diode, and

Z_{CD} is the capacitance of the diode. When Z_{CD} is higher than 2 Pf and changes with the diode bias voltage, Z_e also changes. Thus an accurate knowledge of the photodiode C-V characteristic becomes necessary as the calculation of F(M) will have to take into account the change of Z_e.

C. Quantum Efficiency Measurements

The quantum efficiency is defined as the number of electron-hole pairs generated per incident photon and, thus, is the quantity used to evaluate the sensitivity of the photodiode. The quantum efficiency, n_L, is by definition

$$\eta = (I_p/q) \; / \; (P_{opt}/hv),$$

where I_p is the photogenerated current by the absorption of incident optical power, P_{opt}, at a wavelength, (corresponding to a photon energy $h\sqrt{}$). In these studies the optical power was measured using a calibrated silicon model 818-ST detector from Newport. The optical power, P_{opt}, was measured at a low diode bias voltage, so that the current was still unmultiplied. The quantum efficiency η was then calculated using the previous equation.